Element fractionation in the petrogenesis of ocean island basalts

Thesis

Element Fractionation in the Petrogenesis of Ocean Island Basalts

A thesis presented for the degree of

Doctor of Philosophy

by

TIMOTHY RICHARD ELLIOTT

B.A. (Hons.) *Cantab*. 1987

Department of Earth Sciences,

The Open University.

September 1991

DATE of submission : SEPT 1991

DATE of AWARD : 23 FEB 1992

Acknowledgements

Firstly, and most importantly I would like to thank my parents, for bringing me up proper; always being interested in my education and of late showing a surprising interest in U-Th disequilibrium. I am also very grateful for the support given me throughout my thesis by Sarah. Liberal doses of sarcasm from Paula have sped me on my way this year, and many thanks are due for keeping my spirits up.

On the work front, I am indebted to:

My supervisors Chris and Peter. C.J. for always being the unflappable boss, teasing out answers, touching base and sporting a fine selection tank-tops and Clarky specials, and Peter for Bhudda-like calm in the lab and initiating me into the world of mass-spectrometry.

The Isotope Lab Posse: especially Mabs for making the lab (dare I say) a happening place, Frank for being such a fine torium soul-mate and Janet, for candid opinions, cakes and Neighbourly good humour, Phil and Béatrice for saving the occassional sample, and not forgetting Dave Wright for much software writing and top tips.

Nick Rogers, a man of many parties, for generous helpings of INAA analyses, and being an ever willing ear for the post-grads.

Janet Dryden, the driest wit west of cynicism city.

The Downstairs Crew: John Holbrook, the provider, and Chappers, Brian, Kay & Mich, the suppliers (of many sections) and Andy Tindle (for probe & Mac advice).

Godfrey Fitton and Dodie James for a wadge of XRF analyses and two very enjoyable weeks in Edinburgh, in which Simon Rackam, Faergal Fitzsimmons, Hugh Nicholson, Dave Latin and the university security guards also played important, entertaining roles.

Eva Meenen and Alberto Duce (I think that's the right spelling), who on my fieldwork in the Canaries (where contrary to departmental wisdom, English was no lingua franca) generously helped me out.

The staff at the Nordic Volcanological Institute for samples and hospitality, especially Karl Grönvold for many interesting discussions on Iceland (& life), and Niels Oskarsson. I would also particularly like to thank the Sigurdsson family for feeding, housing and making me at home for much of my Icelandic trip, and Ingrar himself for showing me what a wild and wonderful place Iceland is.

Back on the home front, there have been many people to thank for brightening the drab tedium of life in Milton Keynes, of which I can mention only a few:

El Boys Jon (a fellow traveller with a little bit of white magic), Steve (everybodies' favourite cubist and spinner of yarns), Chukka (for being Chukka as well as Jo le T), Chris (for more sayings than you could shake a stick at), Mattey (poet ruffian) and Sigi (the token Northerner), Jonny M. (for almost turning up once) and Melchett (who couldn't handle his ales).

Office chums Dentiñho (the man with a cigarette and garnet analysis or two), Sian (a perveyor of wicked herbal brews), and Fiona (for many sage words of advice).

The Football team Frankie (for the occassional sniff of whiskey), Kev Butt (aka Bob) and Nick Watson (for my first ever set of wheels).

And finally, when on the shoestring that is a student grant, a snappy cut at a thrifty price is an all important requisite for today's post-grad, so I tip a wink to the lad, the middle man and of course Raymonde himself.

"Preposterous tales"

I, Ludicrous.

('Blah, Blah, Blah' flexi-disc, 1986)

Abstract

Analytical techniques have been developed to measure the very small [$^{230}Th/^{232}Th$] atomic ratios ($3\text{-}8x10^{-6}$) typical of basaltic lavas using a single focussing mass spectrometer. Compared to conventional alpha-counting methods, the technique presented typically gives a 2-5 fold improvement in reproducibility of $^{230}Th/^{232}Th$ ratios, and furthermore uses ~5x less sample, has a simpler chemical prepartion and a data aquisition time ~100x shorter.

The above technique was used in investigating a suite of historic (<1000a) basanites from La Palma, Canaries. The lavas have undergone significant post melt segregration processes, involving residence in deep (>4kbar) magma chambers, that are inferred to persist for at least 30ka. The basanites show geochemical variations related to differences in the degree of partial melting, that are estimated to be between 0.3-2%. Rare earth element (REE) modelling suggests clinopyroxene, rather than garnet control during melting, contrary to expectations from recent geophysical models (McKenzie & O'Nions, in press). The La Palma mantle source is inferred to be LREE enriched, K & Rb depleted, and shows many incompatible element ratios characteristic of 'himu' basalts (Weaver 1991). In contrast, the $^{206}Pb/^{204}Pb$ ratios of the La Palma basanites (19.6±0.05) are lower than the isotopically defined 'high μ' basalts (Zindler & Hart 1986) which suggests that the La Palma source is geochemically similar, but younger than a typical 'high μ' source.

A suite of young (<10,000a) high MgO tholeiites from Iceland show order of magnitude variations in highly incompatible element concentrations that correlate with FeO contents. Variations within these lavas is primarily attributable to sampling of instantaneous melts from different depths within a dynamic melting column. However, additional correlations of radiogenic isotope ratios with major and trace element contents highlights mixing of various plume melts with some 20% mid-ocean ridge basalt, derived from melting of upper mantle material entrained during plume upwelling.

Table of Contents

List of Figures

Chapter 2

Chapter 3

Chapter 4

Chapter 5

List of Tables

Chapter 2

Chapter 3

Chapter 1

Introduction.

Magmatism on ocean islands provides windows to the composition of asthenospheric mantle in numerous places within the ocean basins. Compared with volcanics erupted on the continent, ocean island basalts (OIBs) are much more likely to retain a 'primitive' geochemical signature that carries information on the composition of its source. The lithosphere through which OIBs erupt is nowhere older than 200Ma, so that any enrichment that may have occured within it, in the short time since its isolation from the asthenosphere, has had little chance to develop associated radiogenic isotopic signatures. Furthermore, the overlying MORB crust is generally thinner, denser, more refractory and more depleted in potentially contaminating incompatible elements than the continental crust, so that both the probability and the effects of crustal contamination in OIBs is less than for continental volcanics.

The radiogenic isotope signatures of OIBs are therefore generally inferred to be the same as their source. Extensive radiogenic isotopic studies of OIBs have hightlighted major heterogeneities in the asthenosphere (e.g. Dupré and Allegre 1983, Hart 1984), and the combined analysis of several isotope systems has lead to the postulation of various enrichment and recycling processes occurring within the asthenosphere (e.g. Hawkesworth et al. 1979, Cohen & O'Nions 1982a, Hofmann & White 1982, Zindler & Hart 1986). However, such hypotheses are equivocal, and characteristic isotopic signatures have been interpreted to be the result of several different processes (Hofmann & White 1982, Hawkesworth et al. 1990). Ambiguity in the information carried by radiogenic isotope ratios results both from their reflecting the time-integrated parent-daughter ratios of the source, rather than the parent-daughter ratios of the source prior to melting, and from different processes producing similar parent-daughter fractionations. A more complete knowledge of the incompatible element contents of the source, than that provided by just the time-integrated parent daughter ratios of the radiogenic isotope systems alone, is important in resolving the nature of asthenospheric heterogeneities and hence the processes producing them.

Incompatible element concentrations of the OIBs are a *function* of the composition of the source immediately prior to melting, but they are fractionated by the melting process, and also, although generally to a lesser extent, by fractional crystallisation. However, geochemical variations within a cogenetic lava suite may be used simultaneously to constrain melting and source parameters. Suites of basic rocks, closely related in space and time are most useful for this purpose, as the chances of different sources contributing to the melts are minimised, and geochemical variations between the lavas are most likely to be attributable to magmatic processes. To this end, two such suites were sampled; one from Iceland and another from La Palma, Canary Islands.

In addition to using the systematic variations in incompatible elements within a sample suite to study the partial melting processes, the U/Th isotope systematics also provide constraints on the melting process. Unlike 'conventional' Sr, Nd and Pb isotope ratios, $^{230}Th/^{232}Th$ isotope ratios vary on a timescale of 300ka, which is useful in studying the process of melt production and *recent* incompatible element fractionation (Allègre & Condomines 1982). U/Th isotope studies of OIBs have highlighted disequilibrium, reflecting the fractionation of U and Th during melting (Oversby & Gast 1968, Allègre & Condomines 1982, Krishnaswami et al. 1984, Newman et al. 1984), but only a few samples from any one island have been analysed, and the U/Th data has not been used in conjunction with other incompatible element and isotopic data to study the process of elemental fractionation in more detail. Conversely, studies that have investigated incompatible element fractionation during melting from suites of closely related lavas (Feigenson et al. 1983, Hofmann et al. 1984, Albarède & Tamagnan 1988), have no U-Th data to further constrain the problem.

U-Th isotopic data in this work have been obtained using mass spectrometric techniques. Until very recently (Goldstein et al. 1989), the $^{230}Th/^{232}Th$ ratios of silicate samples have been measured by alpha counting methods only. Alpha counting techniques are limited in precision by the very low count rates of the Th isotopes in the quantities present in silicate samples. Mass spectrometric techniques are not limited by the Th decay constants, but must be able to measure the very low $^{230}Th/^{232}Th$ ratios ($3\text{-}8\times10^{-6}$) in most silicate rocks. Chapter 2 describes techniques developed for a single focussing magnetic

sector mass spectrometer, to measure accurately $^{230}Th/^{232}Th$ ratios.

Data collected using the technique described in Chapter 2 are presented in Chapter 3, together with 'conventional' radiogenic isotope, trace and major element data on a historic (<1000a) suite of basanites from La Palma. Analytically identical radiogenic isotopic ratios in these samples strongly suggest a common source for the lavas. Unfortunately the lavas show a complex, post-melt segregation history, but after correction for these 'secondary' effects, the partial melting process can be analysed, and a source composition inferred.

Chapter 4 presents data analysed on a suite of <10,000a, high MgO lavas from Iceland. In contrast to the La Palma lavas, these samples show a very wide range of incompatible element concentrations and small but significant radiogenic isotopic variation. The variations in incompatible element concentrations and ratios cannot be explained using 'single-stage' melting equations, and Chapter 4 develops a dynamic melting approach to account for the geochemical variations. The mathematical formalisation of dynamic melting is much more complex than the modelling used in Chapter 3, and inverting the data is difficult. Instead, Chapter 5 attempts to forward model the data in Chapter 4, and compares the geochemical constraints thus obtained on the melting column beneath Iceland with those inferred from geophysical arguments.

Iceland and La Palma are the result of plume related volcanism, but produce contrasting magmatic products that largely reflect the influence of their different tectonic regimes on the underlying melting column. Chapter 6 presents a brief synthesis of the common partial melting processes beneath the two islands, and points to future work that may resolve some of the problems highlighted by this study.

The chapters in this study are presented in the style of papers so that they are entities in themselves, although clearly they draw from the conclusions of the other chapters.

Chapter 2

Measurement of silicate $^{230}Th/^{232}Th$ ratios by multicollector mass spectrometry.

A technique is described for measuring the very low [$^{230}Th/^{232}Th$] atomic ratios (~3-8x10^{-6}) found in young volcanic rocks using a single focussing, multicollector mass spectrometer. Compared with alpha-counting methods, this technique offers a two to five fold improvement in precision and reproduciblity, considerably shorter data aquisition times (~1.5 hours as against several days), and smaller sample size needed (~0.2μg Th as against ~1μg), which result from the favourable counting statistics achieved by mass spectrometry. The accuracy of the technique is verified by analysing rock standards that have been measured by different techniques in other laboratories, and also by demonstrating secular equilibrium for a set of old (>350ka) rock samples.

2.1 Introduction

Due to the short half-lives of the daughter nuclides with respect to the parent in the ^{238}U-^{206}Pb decay series, the system evolves to secular equilibrium. (Notable nuclides and their half-lives within this decay series are shown in Table 2.1). In secular equilibrium, the atomic ratios of nuclides are solely controlled by their relative half-lives, and hence with half lives of 7.5x10^4 and 4.47x10^9 respectively, the equilibrium atomic [$^{230}Th/^{238}U$] ratio is 1.678x10^{-5}. Most silicates have [$^{238}U/^{232}Th$] atomic ratios of 2-5, which correspond to equilibrium [$^{230}Th/^{232}Th$] atomic ratios of ~3-8x10^{-6}, and since magma genesis does not greatly affect $^{230}Th/^{232}Th$ ratios, silicate lavas characteristically show such low $^{230}Th/^{232}Th$ atomic ratios (Condomines et al. 1988, Gill & Williams 1990, McDermott & Hawkesworth 1991).

Several geological processes disturb the secular equilibrium of the U decay series, and the time taken for various nuclides in the chain to restablish equilibrium is determined by their half-lives. The study of $^{238}U/^{230}Th$ disequilibrium, which persists for ~350ka, provides a chronometer that yields information on recent geological processes, as opposed to studies of 'conventional' Sr, Nd and Pb isotope systems that record the effect of processes

Nuclide	Half-Life (a)
$^{238}U \rightarrow \rightarrow ^{234}U \rightarrow ^{230}Th \rightarrow ^{226}Ra - - - \rightarrow ^{210}Pb \rightarrow ^{206}Pb$	
^{238}U	4.469×10^9
^{234}U	2.445×10^5
^{230}Th	7.538×10^4
^{226}Ra	1600
^{210}Pb	22.3
^{206}Pb	Stable

Table 2.1 Principal nuclides of interest in the ^{238}U-^{206}Pb decay series. Double arrows indicate decay via a single intermediate nuclide, whilst the dashed arrow indicates multiple intermediate nuclides.

that have occurred several hundred million years previously. The time-scales over which $^{238}U/^{230}Th$ disequilibrium persists is similar to those of melt segregation and fractional crystallisation, and consequently it is an important tool in studying these processes. The numerous petrogenetic applications of $^{238}U/^{230}Th$ disequilibrium are reviewed by Harmon and Rosholt (1982) and Condomines et al. (1988). $^{238}U/^{230}Th$ disequilibrium also has many important applications in studying proceses recorded in carbonate systems (Ivanovich & Harmon 1982), but this study is concerned only with silicate systems.

Measurement of $^{230}Th/^{232}Th$ ratios has largely relied on alpha-counting techniques, the precision of which is dependent on the number of alpha particles produced by decay of their respective nuclides. The rate of nuclear decay (activity) is a product of the decay constant and atomic abundance of a nuclide, and both the very low decay constant of ^{232}Th and the very low abundances of ^{230}Th are limiting factors in the precision of silicate $^{230}Th/^{232}Th$ ratios measured by alpha spectrometry. For example, in one week of alpha-counting of a typical 1g volcanic sample (1ppm Th, by weight), ~1300 counts from ^{232}Th decay and a similar number from ^{230}Th will be detected, giving a combined 2 σ counting error ($\sqrt{N}/N$) of ~7.8% for the $^{230}Th/^{232}Th$ ratio. Since alpha-counting measures the activities of ^{230}Th and ^{232}Th, $^{230}Th/^{232}Th$ ratios are conventionally expressed as activity ratios, written as $(^{230}Th/^{232}Th)_a$. In mass spectrometry both $^{230}Th^+$ and $^{232}Th^+$ ions are produced with almost equal efficiency, and it is solely the low abundances of ^{230}Th which limits the precision due to counting statistics. For the same sample as above, using a conservative estimate of ionisation efficiency of $1x10^{-5}$, the 2 σ counting error on ^{230}Th, and hence for $^{230}Th/^{232}Th$ (since the error on ^{232}Th is much smaller), is only 0.5%. The favourable counting statistics obtainable from mass spectrometry hence gives the potential for the analysis of smaller samples with greater precision. Since mass spectrometry measures atomic ratios, written $[^{230}Th/^{232}Th]$, they must be converted to activity ratios using appropriate decay constants. This not only makes data consistent with the alpha-counting studies in the literature, but also, since $(^{230}Th/^{232}Th)_a$ ratios for silicates are close to unity, they are easier to work with than $[^{230}Th/^{232}Th]$ ratios, that are typically $3\text{-}8x10^{-6}$.

Recent studies have used such advantages of mass-spectrometry to measure $^{230}Th/^{232}Th$ ratios for small carbonate samples (Edwards et al. 1987, Li et al. 1989, Bard et

al. 1990). Carbonates have very low Th contents, high U/Th ratios and consequently high [$^{230}Th/^{232}Th$] ratios (0.001-1.0). Although the low total Th abundances in carbonates presents analytical problems, this is in part off-set by higher ionisation efficiencies for small sample loads (Edwards et al. 1987). Furthermore the $^{230}Th/^{232}Th$ ratios of carbonates are several orders of magnitude greater than $^{230}Th/^{232}Th$ ratios in silicates, which are so low that interference of the main $^{232}Th^+$ beam at mass 230 (the abundance sensitivity) becomes significant with respect to the minor $^{230}Th^+$ beam (Fig. 2.1). Correction for this background contribution, rather than solely the counting statistics on the very small $^{230}Th^+$ beam itself, limits the accuracy of $^{230}Th/^{232}Th$ ratios for silicate samples measured by mass spectrometry, which have to date only been reported using a low abundance sensitivity, double focussing machine (Goldstein et al. 1989). The technique presented here however uses a conventional, single focussing, multicollector mass spectrometer, without additional hardware to reduce abundance sensitivity.

2.2 Chemical separation of Th and U, and basic mass spectrometry

Rock powder dissolutions and subsequent anionic exchange resin procedures are similar to those already documented in the literature (Chen & Wasserburg 1981, Edwards et al. 1987). Powders are digested using a HF-HNO_3-$HClO_4$ mixture in teflon bombs, and evaporated to dryness. Cycles of conversion to nitrate, followed by dissolution in 6M HCl, are repeated until dissolution of the whole sample is complete. After final conversion to nitrate form, the sample is dissolved in 7M HNO_3 and loaded onto 4ml of DOWEX AG 1x8 anionic exchange resin, pre conditioned with 7M HNO_3. All cations other than actinides are eluted using 7M HNO_3 (this fraction can be collected for further purification, if Sr and Nd isotopic analyses are required for the same sample). Th is then eluted using 6M HCl, and finally the U fraction is eluted with 1M HBr. All reagents used are once, sub-boiling distilled.

The eluted Th is converted to nitrate form and loaded in 2µl of twice, sub-boiling distilled 0.1M HNO_3 onto a zone refined Re double filament. Several experiments were made into loading techniques documented in the literature (Arden & Gale 1974, Smith & Carter 1981, Chen & Wasserburg 1981, Rokop et al 1982, Smith et al 1982, Edwards et

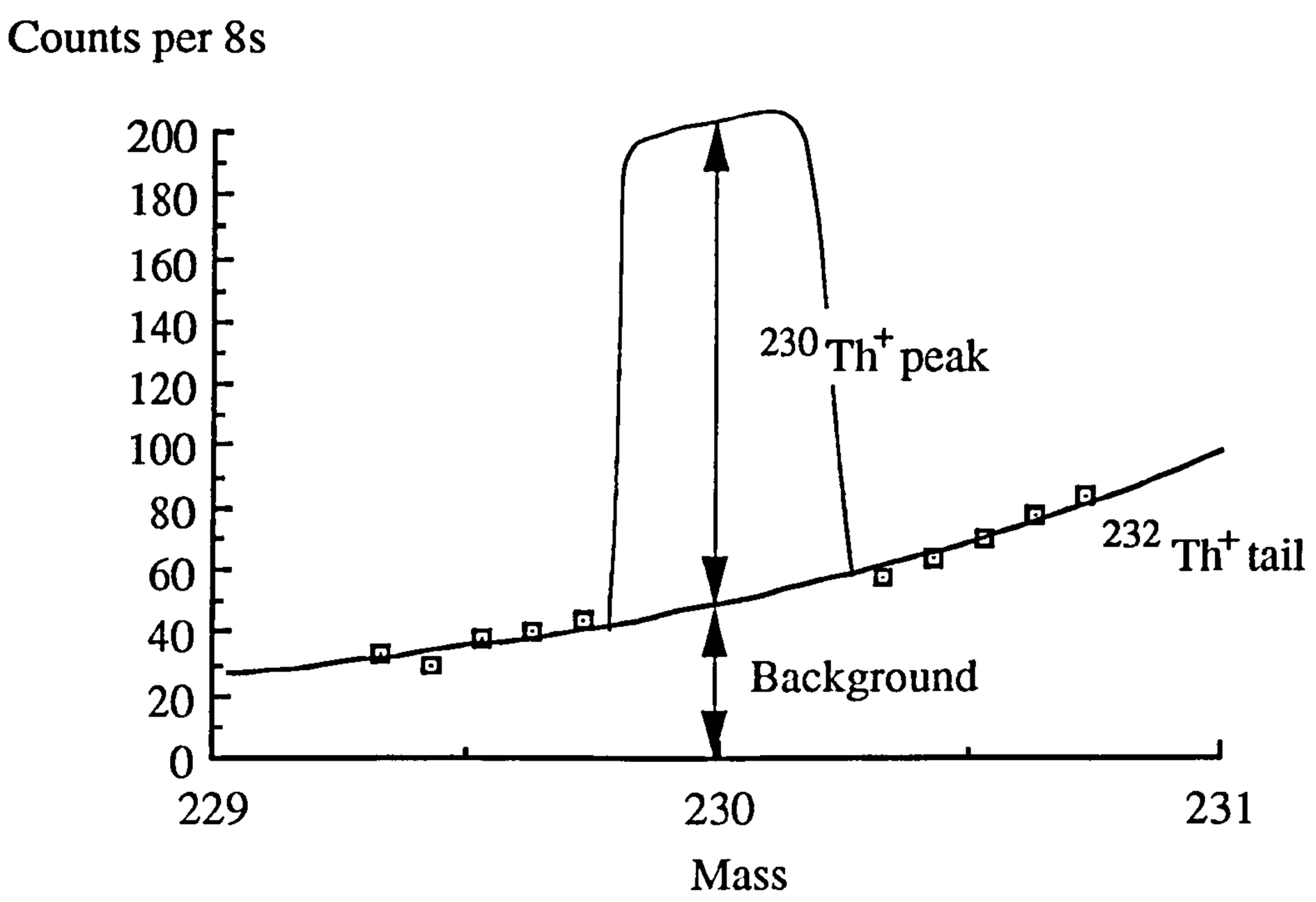

Figure 2.1 Measurements of background counts between mass 229.3 and 230.7, illustrating the $^{232}Th^{+}$ 'tail' and its interference on the $^{230}Th^{+}$ peak.

al. 1987). Most efficient ionisation was achieved by first evaporating colloidal graphite onto a Re filament to produce a thin graphite layer before loading the sample. For a typical sample, 0.2μg Th produced a steady 1pA beam for 1-1.5hr. This represents an ionisation efficiency of ~$4x10^{-5}$, and such characteristically low values (Edwards et al. 1987) are a further constraint on the potential precision of the technique. U is loaded in the same way as Th but run at lower filament temperatures. Total blanks are very low and difficult to determine precisely, but are <$1x10^{10}$ and <$1x10^{6}$ atoms of ^{232}Th and ^{230}Th respectively, and negligible for typical loads of $5x10^{14}$ atoms ^{232}Th. Likewise ^{238}U blanks of <$1x10^{11}$ atoms are therefore negligible.

Measurement of ^{238}U/^{230}Th disequilibrium requires analysis Th and U concentrations in addition to ^{230}Th/^{232}Th ratios, and so isotope dilution techniques were developed for these elements using a mixed ^{229}Th-^{235}U spike. U&Th concentrations and ^{230}Th/^{232}Th ratios were determined on separate dissolutions, because of the significant but uncertified ^{230}Th content of the ^{229}Th tracer.

All mass spectrometric measurements were performed on a Finnigan 261 multicollector machine. Data is collected over 8s intergration times and reported as sets of ten readings. Isotope dilution runs measure ^{229}Th/^{232}Th and ^{235}U/^{238}U ratios on faraday collectors in static mode. Concentrations are reproducible to 1.5% (2 σ standard deviation). ^{230}Th/^{232}Th isotopic ratios are also measured statically. The ^{232}Th beam is measured on a faraday cup, whilst the ^{230}Th beam (Fig. 2.2a), or backgrounds (Fig. 2.2b), are measured simultaneously with a secondary electron multiplier (SEM). ^{230}Th beam intensities (~$1x10^{-5}$ pA) are too low to measure precisely as an analogue signal, so the SEM output is fed into an ion counting system, consisting of EG&G ORTEC 9305 fast pre-amp, EG&G ORTEC 9302 amplifier-discriminator and Hewlett Packard 5316B ion-counter. Some low energy pulses from the SEM are not counted since they are of similar energy to electronic noise in the system and thus below the set descrimination level. Hence the gain between faraday and SEM had to be determined. The gain is measured using certified NBS uranium standards with [^{234}U/^{238}U] ratios ranging from $1.17x10^{-3}$ to $3.49x10^{-2}$ (Garner et al. 1971), and a autentite standard, in which the uranium isotopes are assumed to be in secular equilibrium and hence in the ratio [^{234}U/^{238}U]=$5.472x10^{-5}$. The ion counting system is linear

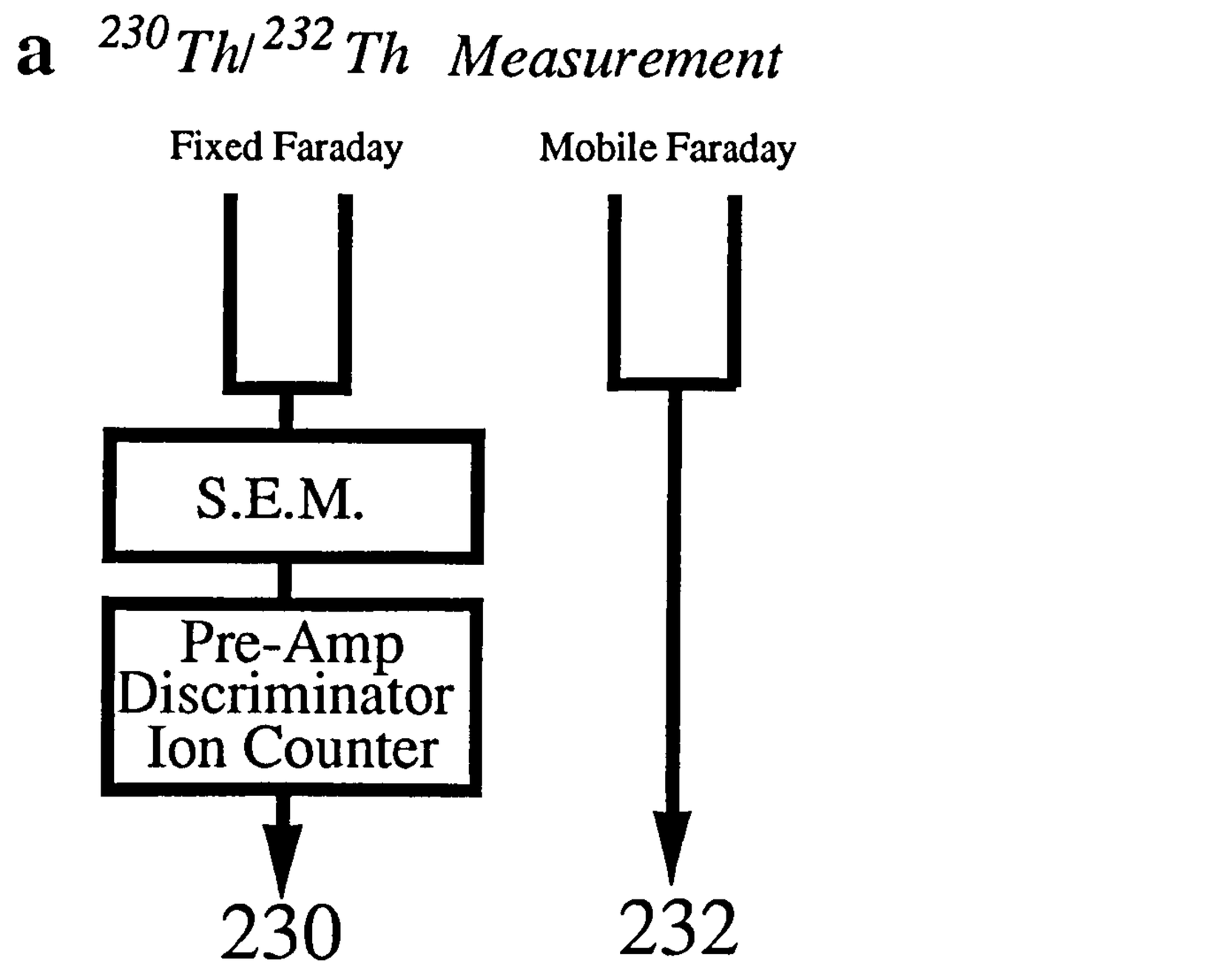

Figure 2.2 Cup configurations for a) $^{230}Th/^{232}Th$ ratio measurement and b) for background measurements at mass 230.7 and 229.7, interpolated to give the background at mass 230.

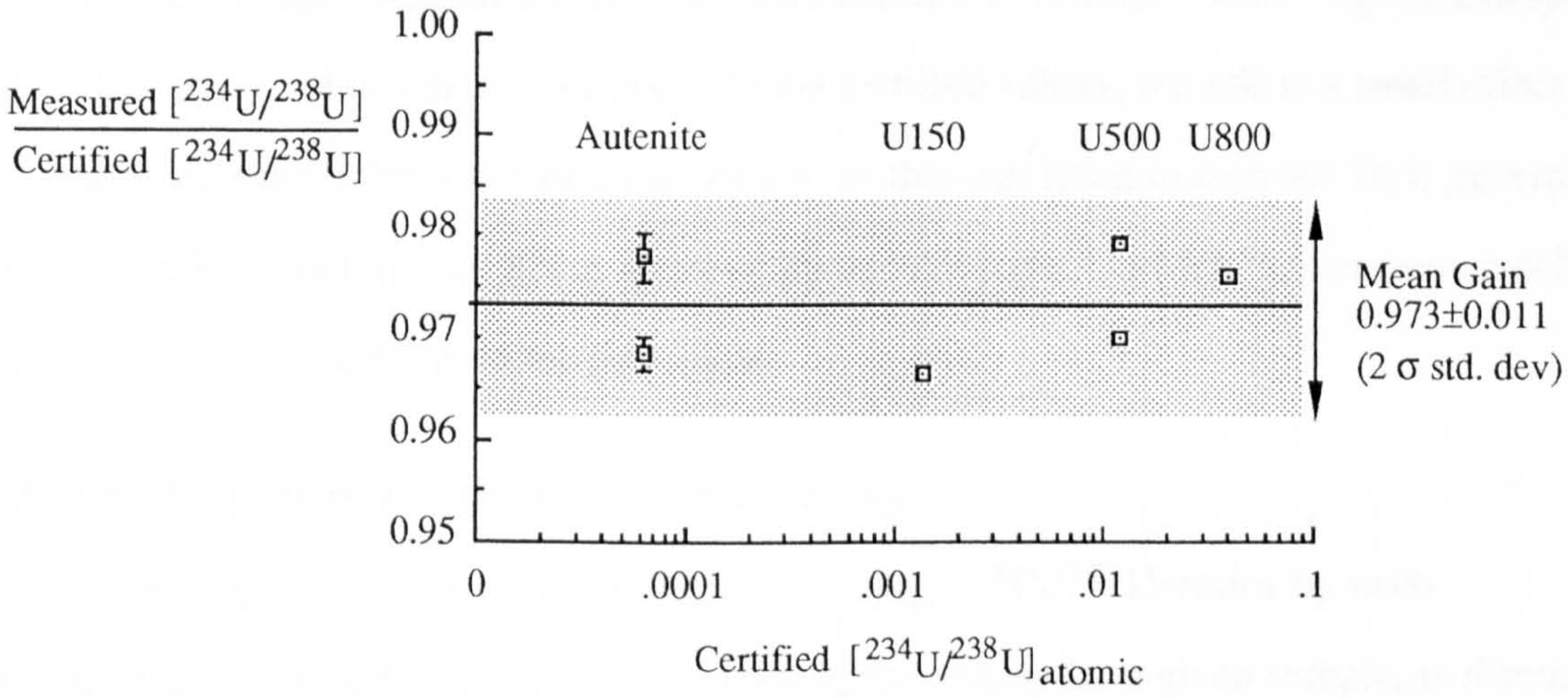

Figure 2.3 Results of gain determinations for SEM/faraday cup for a series of NBS certified U isotopic standards and a natural autenite. The shaded band shows 2σ errors on the mean gain from all determinations. Error bars on the autenite samples show internal precision (1σ) for the two runs. Within-run errors are less than the size of the data points for the other standards measured, with higher $^{234}U/^{238}U$.

over this range of isotope ratios (Fig 2.3) and it had a gain of 0.973±0.011 (2 σ standard deviation) relative to the faraday cup for the period of analysis reported here. Before making $^{230}Th/^{232}Th$ analyses the gain was checked using the autunite standard, but it was found not to vary beyond the uncertainty of the gain determination. The uranium standards with $[^{234}U/^{238}U]<1x10^{-4}$ have ^{234}U intensities corrected for background using the background measurement routine used for $^{230}Th/^{232}Th$ ratios, which is described below.

NBS certified uranium standards were also used to investigate mass fractionation over this mass range. Measured ratios showed a mean 0.13% amu^{-1} bias to lighter isotopic values for a range of standards, compared to the certified values, but this is a small effect and is also accounted for in the gain calibration. Within-run fractionation for Th is generally not evident, but when it does occur it can be up to 0.1% amu^{-1}, which is, however, much less than the reproducibility of the technique.

2.3 Tailing and abundance sensitivity

Although the counting statistics for measuring $^{230}Th/^{232}Th$ ratios by mass spectrometer are significantly better than alpha spectrometry for a given sample, as discussed above, accurate determinations rely on the correction for background interference at mass 230 from the $^{232}Th^+$ beam (Fig. 2.1). The interference is a result of elastic and inelastic scattering of $^{232}Th^+$ ions. A scan of the 236.3-238.7 mass range shows this scattering effect for a U beam (Fig.2.4). There is some mathematical treatment of elastic scattering in mass spectrometers (Menat 1964, Ruedenauer 1970), but inelastic models are poorly developed, and a largely empircal approach was taken in this study. To assess accurately the background interference of the $^{232}Th^+$ beam at mass 230, requires a knowledge of the shape of the main beam tail, which was hence investigated using stable Th, Ta and Re beams.

Mass positions on the tail were measured on the stationary SEM, as the main beam was collected on a mobile faraday cup that was moved incrementally across the mass spectrum. Collecting the main beam and background counts simultaneously had two important advantages. It was found that if the main beam was not 'caught' in a faraday cup, the tail was both larger, and also somewhat erratic, presumably due to additional scattering

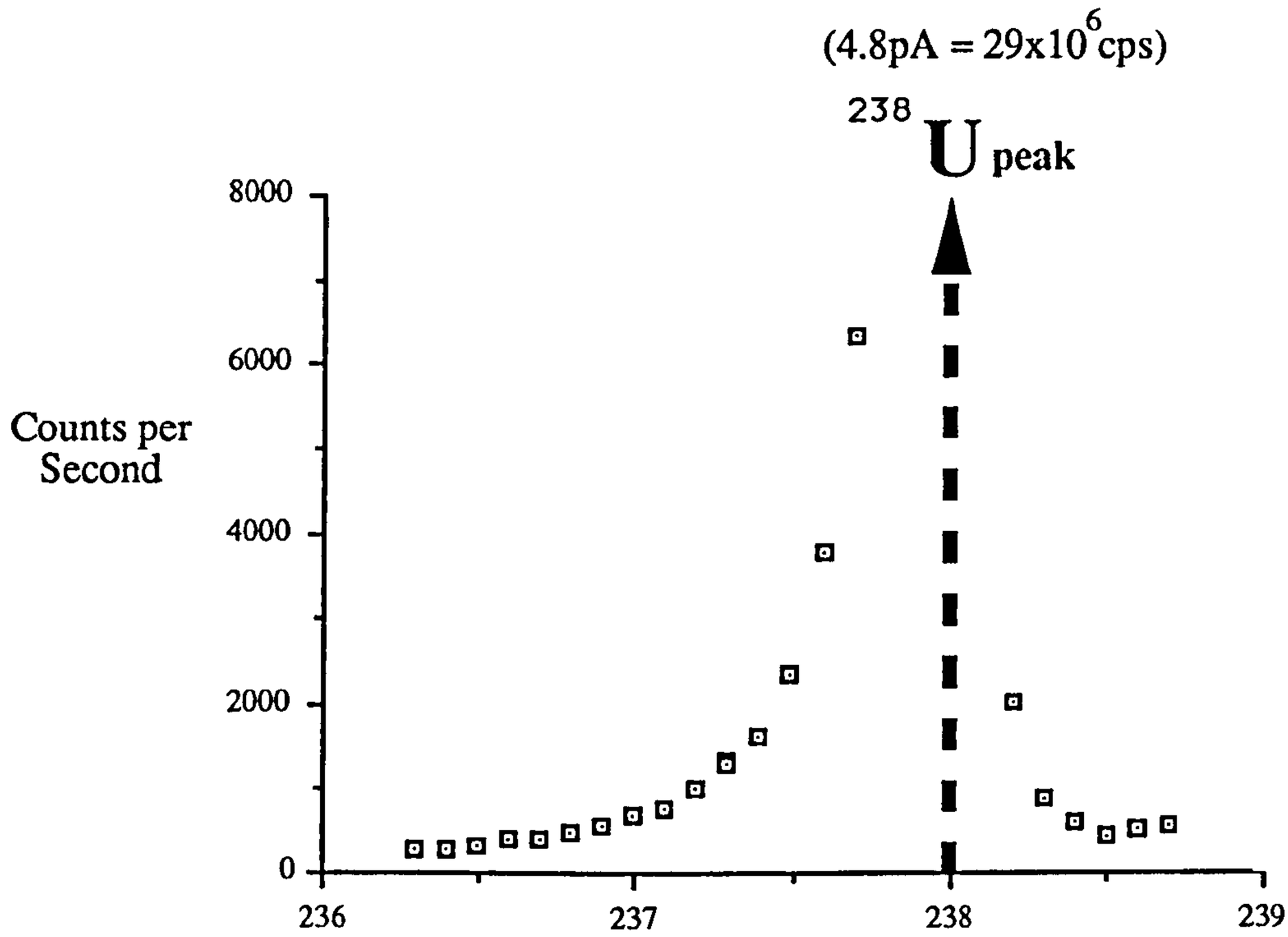

Figure 2.4 Scan of the mass range 236.3-238.7 (excluding ^{238}U peak) illustrating the assymetric nature of the $^{238}U^{+}$ tail, which is clearly greater on the low mass side of the peak.

from collisions with collector edges and scaffolding. Secondly, beam growth during the mass scan can be monitored, and so tail measurements could be normalised to a constant main beam current. The variations of background intensity (tail contribution) with mass were found to be adequately described by curves of the form $e^{(a+bM)}$, although slightly better fits were achieved using functions of the form $e^{(a+bM+cM^2)}$, where a, b and c are constants and M is the mass.

The abundance sensitivity at two mass units below mass 232 ($\Delta m/m=-2/232$), namely the background beneath the $^{230}Th^+$ beam, is calculated from an interpolation of background measurements at masses 229.7 and 230.7, that is corrected for the shape of the tail and is described in detail in the next section. The variation of the abundance sensitivity at $\Delta m/m=-2/232$ was investigated for a range of running conditions. Since the major $^{232}Th^+$ tailing is thought to be due to inelastic scattering in the source, the source pressure is expected to have a significant effect on abundance sensitivity, as is observed in Fig. 2.5a. Some of the scatter on Fig. 2.5a is due to uncertainty in the pressure measurement, but there is also a secondary variation of abundance sensitivity with main beam intensity.

Measurements on Ta beams over a wide range of intensities show this phenomenon more clearly (Fig. 2.5b). At low pressures and hence lower overall abundance sensitivities, variation of abundance sensitivity with beam intensity is much less marked than at higher pressures. Hence to minimise both the magnitude and potential variation of the background at mass 230, $^{230}Th/^{232}Th$ isotopic runs were made with source pressures $<1.5\times10^{-5}$Pa.

2.4 Background Correction

The background measurement routine drives the faraday cups from positions for collection of $^{230}Th/^{232}Th$ data (Fig 2.2a) to the configuration shown in Fig 2.2b, enabling collection of the $^{232}Th^+$ beam simultaneously with background measurement. Using two adjacent faraday cups in the background routine allows both background readings to be made using a single cup configuration by simply changing the magnetic field. This saves time over driving a single faraday cup to two positions, but limits the minimum mass separation between the two background positions. This is determined by the smallest distance allowed between mobile faraday cups, which is one mass unit at this mass range for

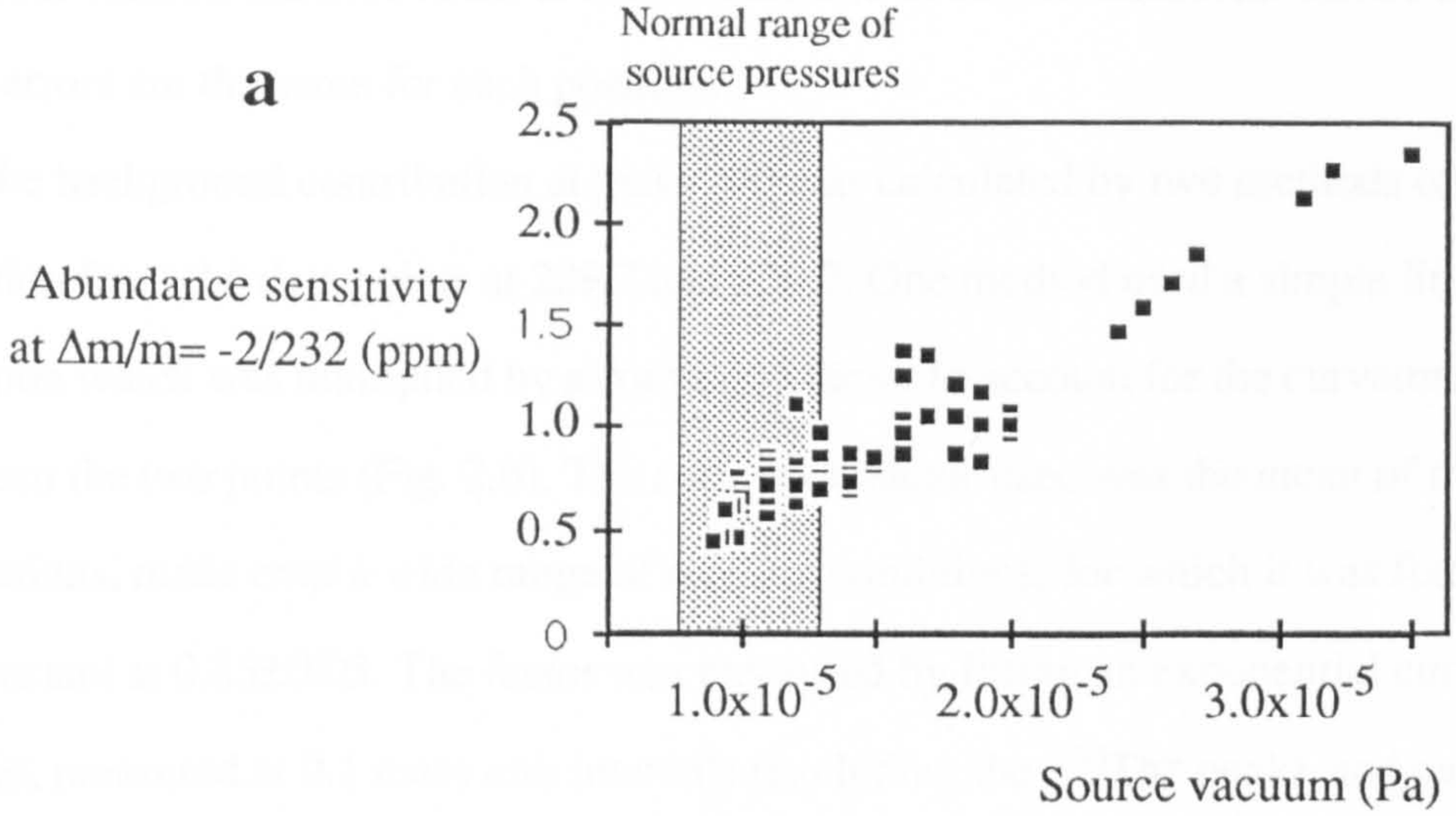

Figure 2.5 a) The variation of abundance sensitivity (ppm) at two mass units below mass 232 with source pressure. Shaded zone indicates normal source pressures during analysis. **b)** The variation of abundance sensitivity (ppm) two mass units below mass 181, with beam intensity, for three different source pressures. Shaded zone indicates normal beam intensities of Th analyses.

the mass spectrometer used in this study. The low mass measurement position was chosen to be at as high a mass as possible, without overlapping the $^{230}Th^{+}$ beam, so as to maximise count rates measured and hence minimise the overall background counting statistics. These considerations determined the measurement of backgrounds at masses 229.7 and 230.7. At each of these masses, the time taken to accumulate 500 counts is measured. Hence the counting errors are the same for each position.

The background contribution at mass 230 was calculated by two methods of interpolation from the data points at 229.7 and 230.7. One method used a simple linear interpolation which was multiplied by a correction factor to account for the curvature of the tail between the two points (Fig. 2.6). The correction factor used was the mean of nine determinations, made over a wide range of running conditions, for which it was found to be nearly constant at 0.85±0.05. The factor was measured by fitting an exponential curve to a $^{232}Th^{+}$ tail, measured at 0.1 mass unit intervals (excluding the $^{230}Th^{+}$ peak), and calculating the intensity at mass 230 from the best fit equation derived for the curve (Fig. 2.6).

A second interpolation method fitted an exponential form between the two background readings. Since there are only two data points, only curves of the form $y=e^{(a+bM)}$ could be fitted. However, as described above, the initial studies on the shape of tails for Th, Re and Ta showed this to be quite adequate. Six standard runs were corrected using both correction routines, and the two methods gave very similar mean [$^{230}Th/^{232}Th$] ratios and 2 σ standard deviations; $(8.389\pm0.21)\times10^{-6}$ using the linear interpolation with constant correction factor, and $(8.367\pm0.21)\times 10^{-6}$ for the exponential interpolation. Since the latter is not specifically determined on the Th tail, it can be used, for example, to correct for background in the measurement of low $^{234}U/^{238}U$ ratios.

In order to monitor to potential variations of abundance sensitivity within run, background measurements must be made at intervals during an analysis. The amount of time spent collecting backgrounds during an analysis is in proportion to the contribution of the background to the total number of counts at mass 230. Since the background represents some 15-25% of the total signal at mass 230, for the low $^{230}Th/^{232}Th$ ratios of silicate samples (Fig 2.7), the background need only be known to ~1/5th of the precision of the 230

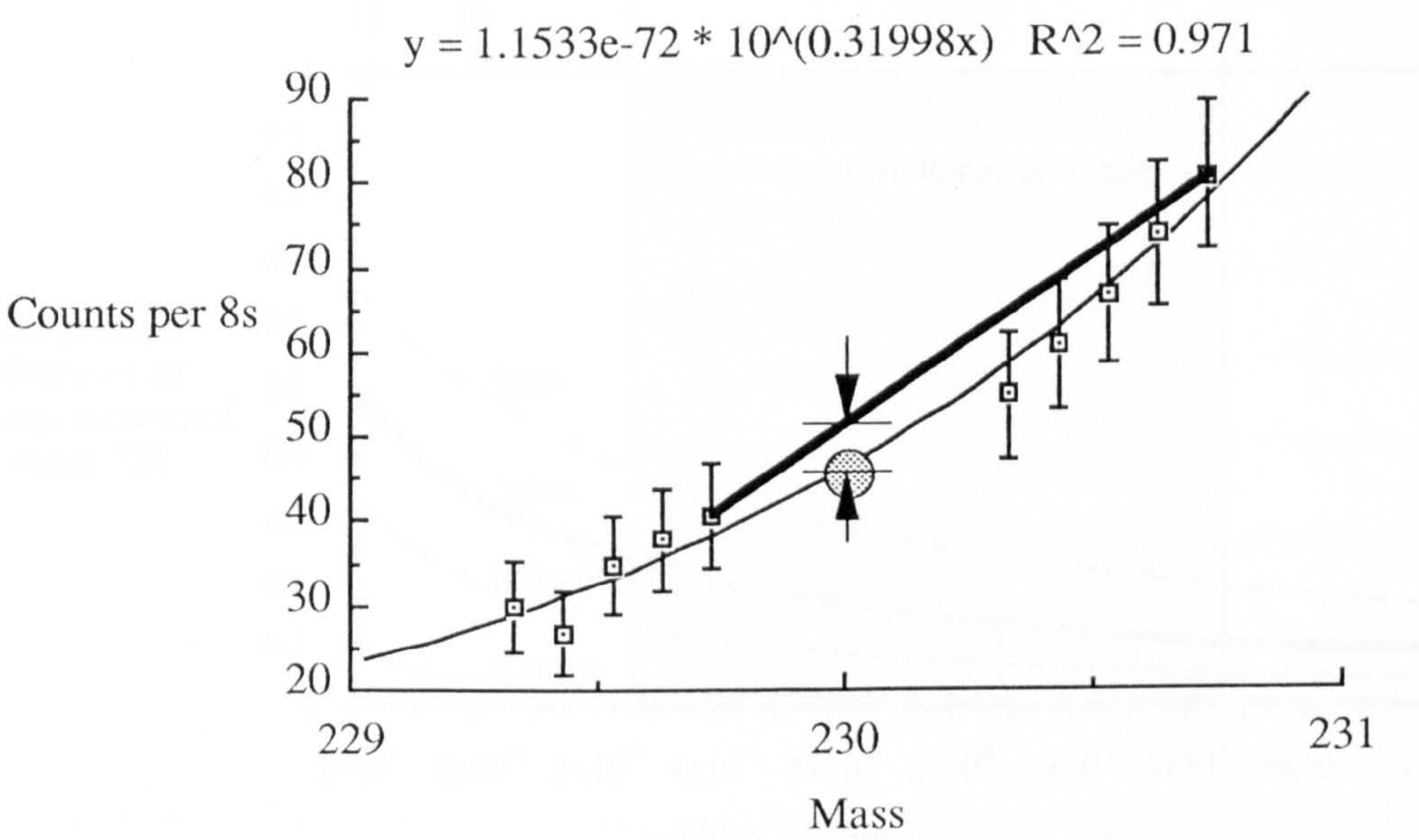

Figure 2.6 An illustration to show the calculation of the correction factor applied to linear interpolations of background intensity at mass 230. A series of beam intensity measurements at 0.1amu steps across the mass range 229.3-230.7 are shown (excluding the $^{230}Th^{+}$ peak). Measurements are corrected for beam growth during the scan, and 1σ counting errors are shown for individual measurements. A curve has been fitted to these points to model the $^{232}Th^{+}$ tail beneath the $^{230}Th^{+}$ peak. Using the equation of the fitted curve (shown above graph), the beam intensity due to $^{232}Th^{+}$ tailing at mass 230 can be calculated (shaded circle). The difference between this value and that obtained from linear interpolation between mass 229.7 and 230.7 (the heavy line) is indicated. A ratio of calculated intensity from the best fit curve at mass 230 to that from linear interpolation gives the correction factor.

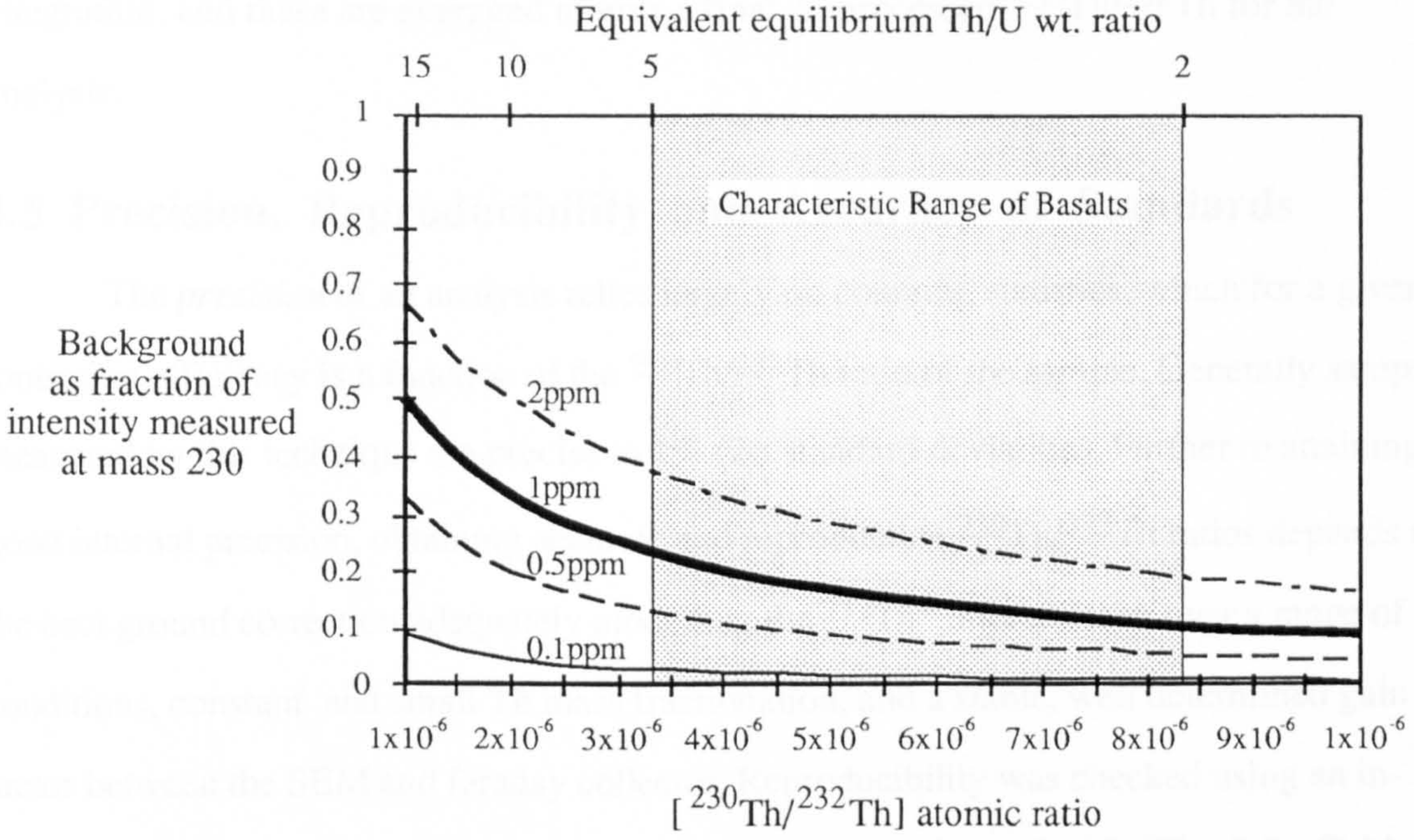

Figure 2.7 Background interference at mass 230, as a fraction of total beam intensity measured at mass 230, as a function of sample [$^{230}Th/^{232}Th$] ratio. Variation is shown for a maximum probable range of abundance sensitivities. Machine conditions during this study generally resulted in an abundance sensitivity of close to 1ppm (shown as a bold line on the diagram). A characteristic range of [$^{230}Th/^{232}Th$] ratios found in basaltic rocks is indicated.

peak. A rigorous calculation to minimise the combined counting error in $^{230}Th/^{232}Th$ as a function of the relative time spent collecting backgrounds was not undertaken, but measurement of backgrounds after every 4 sets of $^{230}Th/^{232}Th$ ratios collected proved adequate.

At the end of a sample run, a background at mass 230 is calculated from all the background measurements. This is used to recalculate the $^{230}Th/^{232}Th$ of each 8s integration, and these are averaged to give a final, 'reprocessed' $^{230}Th/^{232}Th$ for the analysis.

2.5 Precision, Reproducibility and Accuracy of Standards

The *precision* of an analysis relies largely on counting statistics, which for a given ionisation efficiency is a function of the $^{230}Th/^{232}Th$ ratio of the sample. Generally samples measured by this technique are precise to 1% (2σ standard deviation). Further to attaining good internal precision, obtaining accurate and reproducible $^{230}Th/^{232}Th$ ratios depends on the background correction adequately modelling the $^{232}Th^{+}$ intereference over a range of conditions, constant and small Th mass fractionation, and a stable, well determined gain factor between the SEM and faraday collector. Reproducibility was checked using an in-house standard that gave a 2σ standard deviation on 8 readings of $\pm 2\%$ (Fig. 2.8a, Table 2.2).

There are no currently available NBS certified Th isotopic standards, and so accuracy has been assessed by measurement of the Table Mountain Latite (TML) rock standard, that has been analysed by both alpha-counting at Santa Cruz and by mass spectrometry at Los Alamos (Goldstein et al. 1989). Table 2.3 and Fig. 2.8b report measurements made in this study on TML over a nine month period compared with a grand mean for 4 alpha-counting analyses from Santa Cruz, and a single determination by the Los Alamos group (Goldstein et al. 1989). The reproducibility of $\pm 2\%$ ($2\ \sigma$ standard deviation) is similar to the in-house standard. The absolute value obtained is within error of the mean of the Santa Cruz group, but statistically different from the Los Alamos determination. The cause of this discrepency is uncertain, but another group using a low abundance sensitivity mass-spectrometer also reports lower values for TML than Los Alamos (Palacz pers. comm.). The TML standard is an evolved rock that contains accessory phases that concentrate U and Th, which may lead to

In-house standard

	$[^{230}Th/^{232}Th]$	1 σ within-run error
Single runs	8.317E-06	3.9e-08
	8.377E-06	3.9e-08
	8.277E-06	3.9e-08
	8.417E-06	4.0e-08
	8.315E-06	3.2e-08
	8.376E-06	3.9e-08
	8.576E-06	4.0e-08
	8.383E-06	3.8e-08
	8.351E-06	2.1e-08
		2 σ std. dev.
Mean	**8.377e-06**	**1.7e-07**

Table 2.2 $[^{230}Th/^{232}Th]$ analyses of an in-house standard.

TML rock standard

	$[^{230}Th/^{232}Th]$	1 σ within-run error	$(^{230}Th/^{232}Th)_a$	1 σ within-run error
Single runs	5.619e-06	9.0e-08	1.044	0.017
	5.647e-06	3.0e-08	1.049	0.006
	5.724e-06	3.0e-08	1.064	0.006
	5.673e-06	3.0e-08	1.054	0.006
	5.628e-06	3.0e-08	1.046	0.006
	5.759e-06	4.0e-08	1.070	0.007
	5.702e-06	4.0e-08	1.060	0.007
	5.723e-06	4.0e-08	1.064	0.007
	5.637e-06	4.0e-08	1.048	0.007
		2 σ std. dev.		2 σ std. dev
Mean this study	**5.679e-06**	**1.0e-07**	**1.055**	**0.019**
Los Alamos			**1.084**	**0.005**
Santa Cruz			**1.070**	**0.007**

Table 2.3 $[^{230}Th/^{232}Th]$ analyses of the Table Mountain Latite rock standard over a nine month period. Atomic ratios are converted to activity ratios using the values given in Table 2.5, and compared to other analyses of TML reported in Goldstein et al. (1989).

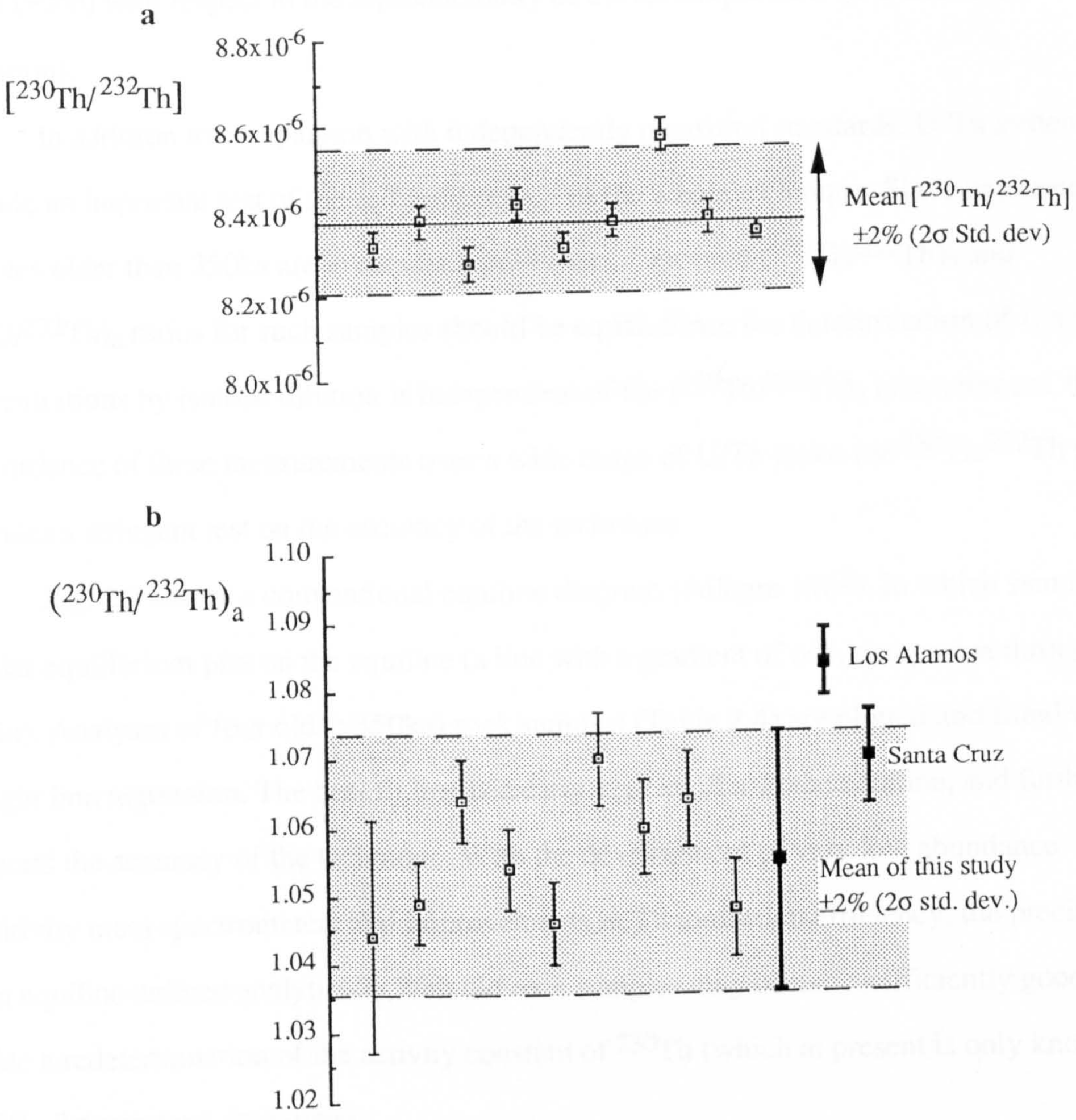

Figure 2.8 a) [$^{230}Th/^{232}Th$] analyses of an in-house standard, showing the mean and 2σ standard devaiation. Within run 1σ errors are shown on individual analyses. **b)** Analyses of rock 'standard' TML, run over a nine month period, expressed as activity ratios. 1σ within-run errors are shown on individual measurements, and the 2σ standard deviation is illustrated for the whole data set. A single measurement of the same standard by mass spectrometry from the Los Alamos laboratory (Goldstein et al. 1989) and an average value obtained by alpha -counting from the Santa Cruz laboratory are also plotted.

heterogeneity in processing and splitting the sample, although inter-laboratory differences may be real and require further investigation. However it is important to stress that the difference between our mean $^{230}Th/^{232}Th$ ratio for TML and the Los Alamos result is still small (~3%) with respect to the reproducibility of the technique ±2% (2 σ standard deviation).

In addition to comparison with independently measured standards, U-Th systematics provide an important test of the self consistancy of the whole technique. Since unaltered samples older than 350ka are in secular equilibrium, measured $(^{230}Th/^{232}Th)_a$ and $(^{238}U/^{232}Th)_a$ ratios for such samples should be equal. Since the determination of U and Th concentrations by isotope dilution is independent of the $(^{230}Th/^{232}Th)_a$ measurement, the concordance of these measurements over a wide range of U/Th ratios (or $^{230}Th/^{232}Th$ ratios) provides a stringent test on the accuracy of the technique.

Fig. 2.9 shows a conventional equiline diagram (Allègre 1968), in which samples in secular equilibrium plot on the equiline (a line with a gradient of one, that passes through the origin). Analyses of four old (>350ka) rock samples (Table 2.4) are plotted and fitted with a straight line regression. The best fit line is clearly very similar to the equiline, and further supports the accuracy of the technique. With the development of very low abundance sensitivity mass spectrometers and improvements in Th ionisation efficiency, the precision of an equiline defined analytically with old rock samples may become sufficiently good to enable a redetermination of the activity constant of ^{230}Th (which at present is only known to ±0.8%, 2σ standard deviation).

2.6 Comparison with Alpha-Counting

For routine alpha-counting analysis, sample size and counting times are varied from 1-5g and several days to several weeks respectively, depending on sample Th concentration, to obtain reasonable counting statistics. For a typical basaltic sample (1ppm Th), 1g of sample (1μg Th), counted for a week (at a maximum possible 50% efficiency) will give ~1300 counts of both ^{230}Th and ^{232}Th, resulting in 2 σ counting error on $^{230}Th/^{232}Th$ of 7.8%. For mass spectrometry there is not quite the same trade-off between sample size, analysis time and precision. The principal control on beam size, and hence precision, is

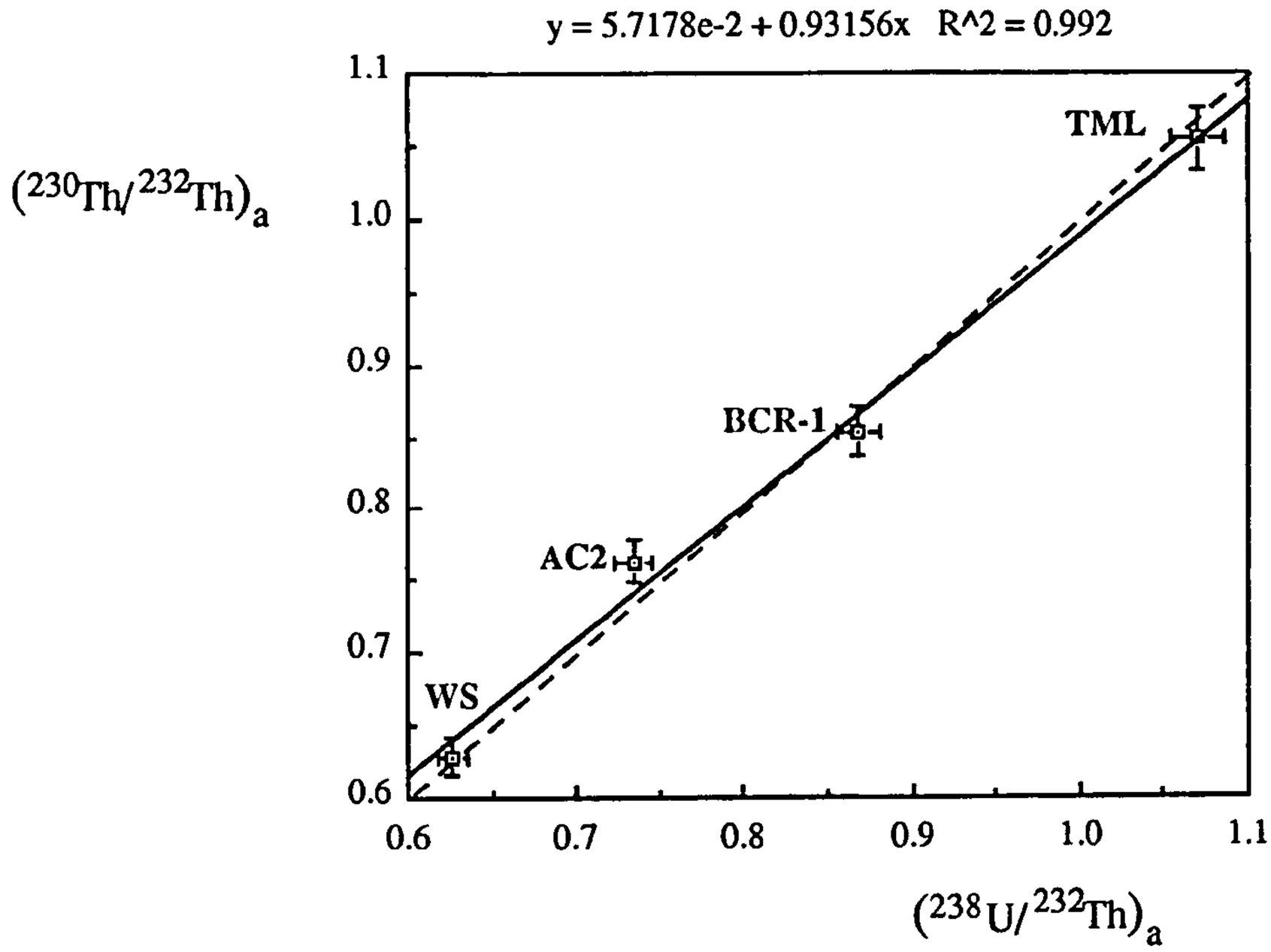

Figure 2.9 An equiline diagram (Allègre 1968) for analyses of international and internal rock standards. All standards are older than 350ka, and should thus be in secular equilibrium and plot on a line with a gradient of unity that passes through the origin (i.e. the equiline, shown as a dashed line). A regression line (solid line) has been fitted to the analyses (the equation of which reported above the figure) and is very close to the equiline. The error bars on the samples are 1.5% and 2% for $(^{238}U/^{232}Th)_a$ and $(^{230}Th/^{232}Th)_a$ respectively, and represent 2σ sample reproducibility ascertained from replicate analyses of standards and samples.

Equiline data

	Th (ppm)	U (ppm)	Th/U	$(^{238}U/^{232}Th)_a$	$(^{230}Th/^{232}Th)_a$
TML	29.71	10.4	2.86	1.070	1.055±0.021
BCR-1	5.81	1.65	3.52	0.868	0.854±0.017
AC2	17.28	4.15	4.16	0.734	0.763±0.015
WS	2.83	0.58	4.88	0.626	0.629±0.012

Table 2.4 U-Th data for the rock standards plotted in Fig. 2.9.

ionisation efficiency, which tends to decrease with the amount of sample loaded. Furthermore, Th beams have a finite life span of 1-2 hours and cannot be measured indefinitely as with alpha counting. However in this study, 0.2μg Th generally produces a 1pA beam for 1.5 hours, that results in ~50 counts per second of $^{230}Th^{+}$. The routine measures 20 sets of ten 8s integration times, which results in 2 σ counting errors of 0.6% on ^{230}Th, and hence for $^{230}Th/^{232}Th$, since the errors on the much larger $^{232}Th^{+}$ beam measured on the faraday cups are insignificant by comparison. The precision obtained for single samples in this study of ±1% (2σ standard deviation), shown in Tables 2.2 & 2.3, illustrate the additional affects of background determination in the overall precision.

Although the relative precision of $^{230}Th/^{232}Th$ obtained from alpha-counting and mass spectrometry will change with Th content of the sample analysed, for the representative example above, an eight-fold increase in precision is obtained using $1/5^{th}$ the sample weight and less than $1/100^{th}$ of the analysis time. It is more difficult to compare the reproducibilities of the two techniques, since alpha-counting studies generally report only counting errors. Gill & Williams (1990) cite ±5-10% reproducibility (2σ standard deviation) for routine alpha-counting analyses, and hence the technique present here respresents a 2-5 fold improvement on this. (The errors shown for the alpha-counting analysis of TML (Fig. 2.8b) implies much lower reproducibilities, but this measurement may represent standard *errors* of analyses counted for very long periods of time, although the derivation of the error quoted is not clarified. Furthermore, TML has very high Th contents (~30ppm) and so errors on this sample are not representative of typical analyses).

The advantages discussed above make it likely that mass spectrometric measurements will become increasingly common. Since alpha-counting measures $(^{230}Th/^{232}Th)_a$ (activities), whilst mass-spectrometry measures $[^{230}Th/^{232}Th]$ (atomic ratios), comparison of data measured by the different techniques requires conversion using the appropriate decay constants. This also applies to the conversion of uranium concentrations measured mass spectrometry to activities that may be plotted on an equiline diagram. Consequently, as mass spectrometric measurements of $^{230}Th/^{232}Th$ become more prevalent, it is important to standardise the decay constants used to facilitate inter-laboratory comparisons. In this study we have used the decay constants used by Goldstein et al.

(1989), reproduced in Table 2.5, and we recommend any future mass spectrometric studies do likewise.

Nuclide	Decay Constant (a^{-1})
^{232}Th	4.948×10^{-11}
^{230}Th	9.195×10^{-6}
^{238}U	1.551×10^{-10}
^{234}U	2.835×10^{-6}

Table 2.5 Decay constants used in this study (after complation in Goldstein et al. 1989)

The development of mass spectrometric techniques for measuring $^{230}Th/^{232}Th$ has given rise to unnecessary complication over notation used in expressing Th isotope ratios. Some workers to report the very large $^{232}Th/^{230}Th$ atomic ratios, rather than the very small $^{230}Th/^{232}Th$, presumably for aesthetic reasons. This is both contrary to the convention of using the stable isotope as the denominator in isotopic ratios (^{232}Th is effectively stable over the timescales of U-Th disequilibrium systematics), and moreover, it is $^{230}Th/^{232}Th$ activity ratios, not the inverse, that are plotted on equiline diagrams. Since the equiline diagrams are the most convenient way of displaying U-Th disequilibrium data, and use $(^{230}Th/^{232}Th)_a$ activity ratios, it is reasonable to report Th isotope ratios measured by mass spectrometry as activity ratios, using standardised decay coefficients, instead of the measured atomic ratios.

Finally, Gill & Williams (1990) have suggested a β notation to express Th isotope measurements. βTh is analagous to εNd, which expresses $^{143}Nd/^{144}Nd$ relative to an evolving chondritic reservoir. Although the $(^{230}Th/^{232}Th)_a$ of a chondritic reservoir does change over earth history, because U-Th disequilibrium only persists for 350ka, there is no need for reference to an evolving reservoir since *all* measurements of $(^{230}Th/^{232}Th)_a$ ratios are relative to the $(^{230}Th/^{232}Th)_a$ ratio of the present day reservoir. Furthermore the $(^{230}Th/^{232}Th)_a$ of a chondritic reservoir is calculated from an estimate of chondritic U/Th, which, unlike chondritic Sm/Nd, is not well constrained. For these reasons we do *not* use the β notation.

2.7 Conclusions

With careful analysis of background intereference due to scattering of the main $^{232}Th^{+}$ beam, $^{230}Th/^{232}Th$ ratios can be measured with a conventional, single focussing mass spectrometer with a reproduciblity of ±2% (2σ standard deviation). This represents a 2-5 fold improvement over traditional alpha-counting methods, and furthermore, the technique requires smaller sample size and significantly shorter analysis time. The concordance of $(^{230}Th/^{232}Th)_a$ and $(^{238}U/^{232}Th)_a$ data for samples >350ka, and analyses the TML rock standard verify the accuracy of the technique.

Chapter 3

Petrogenesis of the historic basanites of La Palma. Implications for source composition and melting of the Canary plume.

The historic basanites of La Palma show small but significant variations in incompatible trace element ratios, but they have analytically indistinguishable radiogenic isotope signatures. The comparatively evolved (Mg#<55) compositions of the basanites indicate moderate degrees of crystal fractionation, and some samples also show accumulation of an actinide/LREE rich accessory phase, probably monazite, from coexisting evolved lavas. Identification of these post melt segregation processes enables lavas with comparatively primitive signatures to be identified, in which geochemical variation is due to partial melting alone. Analysis of these samples suggests small degrees of melting (~0.3-2%) from a source that is light rare earth enriched, and in which the controlling mineralogy is dominantly clinopyroxene, and not garnet as predicted by recent geophysical models. The small degrees of melting fractionate even highly incompatible trace element ratios, as is also clear from large $^{238}U/^{230}Th$ disequilibrium (~0.75). However such trace element fractionation on melting cannot account for the very low K/Ba and Rb/Ba ratios of the basanites, that are shown to be source features, and suggest source enrichment by small degree melts derived from phlogopite bearing mantle. Whilst the La Palma basanites have incompatible trace element ratios very similar to those of the isotopically defined 'high μ' basalts, their Pb isotopic ratios are not as extreme, implying that the Canary plume has a similar but younger source than the 'high μ' basalts of St. Helena and the Austral Islands.

3.1 Introduction

Since ocean island basalts are not erupted through continental crust, which is a potential source of contamination, variations in trace element ratios and isotopic signatures are generally presumed to reflect mantle sources and melting processes.Variations in incompatible trace element ratios in ocean island basalts have therefore been used both to assess mantle heterogeneity (Weaver et al. 1987, Loubet et al. 1988, Joron & Treuil 1989,

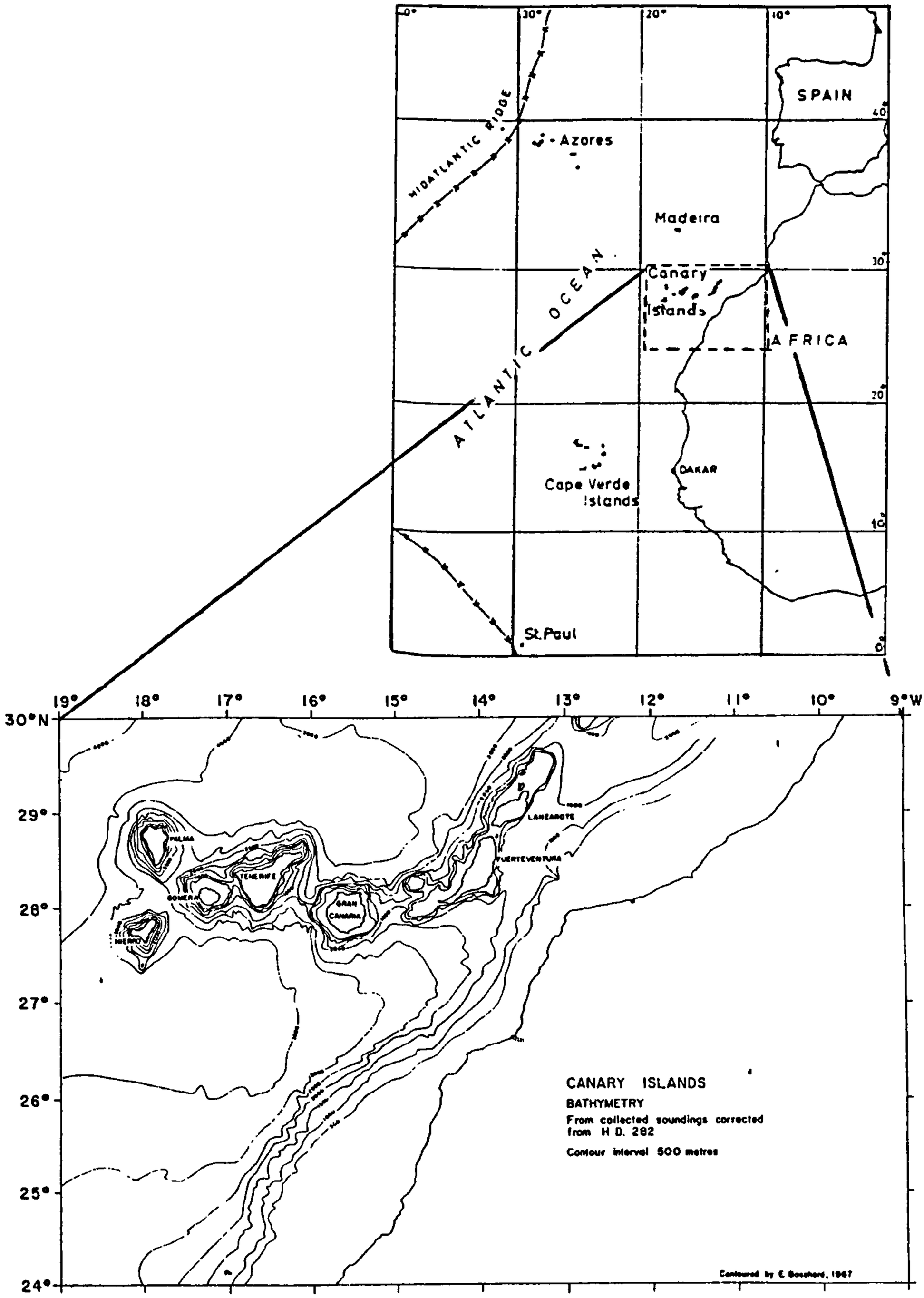

Figure 3.1 Map showing the position of the Canary Islands in the Atlantic, and the position of individual islands within the archipelago (after Rothe & Schmincke 1968 and Bosshard & MacFarlane 1969 respectively).

Weaver 1991) and to quantify degrees of mantle melting (Gast 1968, Liotard et al. 1986, McKenzie & O'Nions, in press). Within a given suite of ocean island lavas, combining major, trace element and radiogenic isotopic data can best resolve whether differences in incompatible element ratios are caused by source or melting effects, and U-Th isotope systematics provide an additional powerful tool in identifying recent elemental fractionations associated with magma genesis (Allègre & Condomines 1982). Such an integrated geochemical approach has been used on a suite of fourteen historic basanites from La Palma. The very close temporal and spatial association of the flows studied minimises potential source variation between events and provides an excellent opportunity to assess processes producing trace element fractionation, and hence to infer the unfractionated source composition.

3.2 Geological Setting

La Palma lies at 17°50'W 28°40'W at the western end of the Canary Archipelago in the Atlantic Ocean (Fig. 3.1) and rises 6500m from 155Ma old oceanic crust (Hayes & Rabonwitz 1975, Kent & Gradstein 1984). Although the nature of the crust underlying the eastern-most Canary Islands has been debated (Rothe & Schmincke 1968, Dietz & Sproll 1970, Roeser et al. 1971), the crust beneath the western Canaries is almost certainly oceanic (Dash & MacFarlane 1969, Bosshard & MacFarlane 1970). Volcanism in the Canary Islands has been continously active during the last 19Ma (Abdel Monem et al. 1971, 1972), and though in general the eastern islands are older and more eroded, all the islands (except La Gomera) have had historic or prehistoric (<50,000a) eruptions. The Atlantic plate has a small relative motion with respect to the Canarian plume (Schmincke 1973), in contrast to the clearer migration, for example, of the Pacific plate over the Hawaiian plume (McDougall 1964).

General reviews of the geology of La Palma are given by Hausen (1969) and Middlemost (1970). The island is very young, one of the stratigraphically oldest sub-aerial basalts being dated at 1.57Ma (Abdel Monem et al. 1972), and activity appears to have been continuous since then, producing ~800km^3 of sub-aerial volcanics (Schmincke 1982). After submarine emergence, recorded in a pillow basalt sequence that forms the island's basement complex (Gasteri et al. 1966, Staudigel & Schminke 1984), the earliest activity produced a

large basanitic strato-volcano (Taburiente) at the North of the island (Fig. 3.2a). Quaternary eruptions (<0.5Ka) have produced small monogenetic cones across the whole island, but have more commonly issued from the major volcanic ridge (the Cumbre Vieja) running south from the now extinct Taburiente (Fig. 3.2a). The eruptive products of La Palma are very dominantly basanitic (Hausen 1969), but more evolved products, up to phonolitic composition (Middlemost 1972), are found as plugs (now exposed as spines) and occasionally as flows.

3.3 Sampling and Field Evidence

U-Th disequilibrium work requires samples to be <350ka (after which time equilibrium is restablished in any sample that initially showed disequilibrium), and within this first order constraint, the age of a sample must be known in order to correct for in situ decay (or growth) of ^{230}Th since eruption. Uncertainties in the ages of samples leads to uncertainty in the correction of measured, present-day $(^{230}Th/^{232}Th)_a$ ratios to initial erupted values. Thus historically documented eruptions are ideal for U-Th disequilibrium studies since no uncertainty in $(^{230}Th/^{232}Th)_a$ arises from age correction. La Palma has five recorded volcanic events, at 1585, 1646, 1677, 1949 and 1971, that erupted flows from fissures and cones on the flanks of the Cumbre Vieja (Fig. 3.2b). The eruptive events comprise several distinct flows from different phases of activity. Fourteen distinct basanite flows, from the five historic events, were analysed in this study: seven from the 1712 event, two from both of the 1646 and 1971 events, and one from each of the 1585, 1677 and 1949 events (locations shown in Fig. 3.2b).

Although the great majority of the historic flows are basanitic, the 1949 events erupted both evolved (tephritic) and basanitic lavas (Kaiser & Schmincke 1987), and rhyolitic pumices were produced in the 1971 event (Araña and Ibarrola 1973). The basanitic Jedey flow (of the 1712 event) also contains highly vesicular phonolitic blebs that suggests mixing of contemporaneous evolved and basic lavas. Many of the historic flows contain nodules of various sizes (0.5-30cm), that range in mineralogy from harzburgites, to pyroxenites/amphibolites and alkalic gabbros. Kaersutite megacrysts are observed in some flows. In order to assess the potential variation produced within an individual flow, by heterogeneous inclusion of such xenocrystic material, each of the fourteen flows was

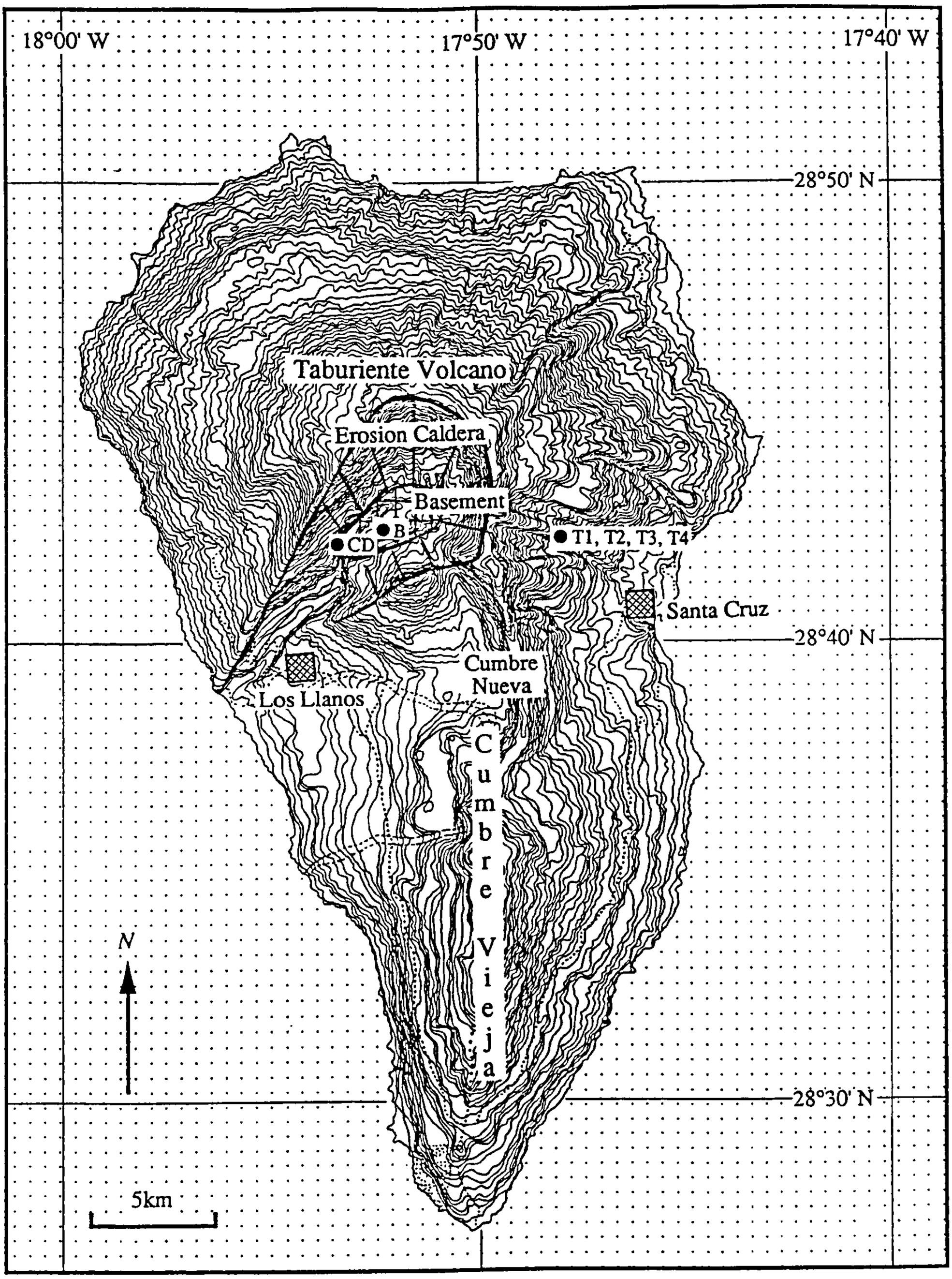

Figure 3.2a A map of La Palma showing the relief and principal geological features (after Hausen 1969). Localities are indicated for the older samples analysed in this study (Table 3.1, Appendix A).

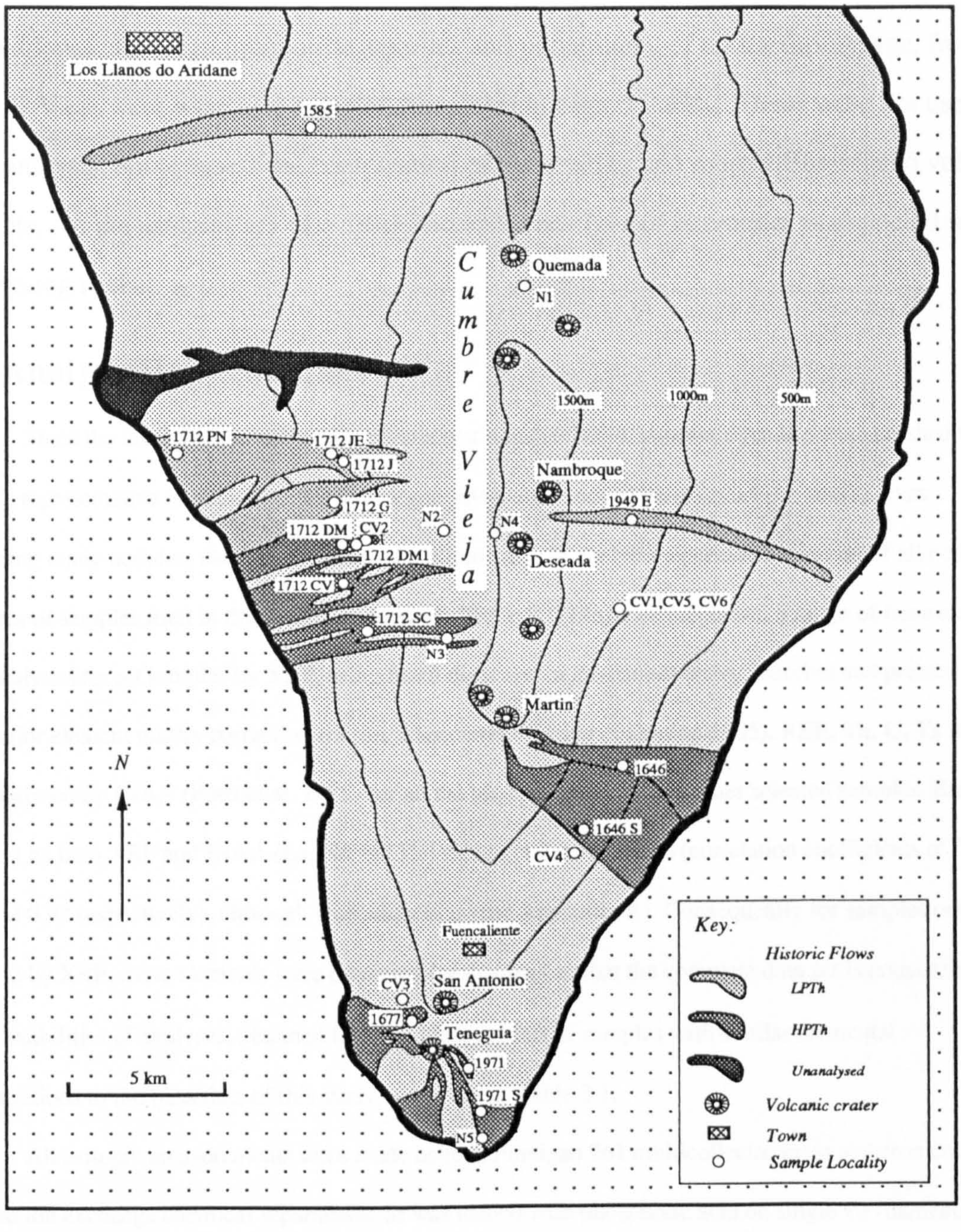

Figure 3.2b A detailed map of the southern part of La Palma, showing the historic flows (sub-groups defined later in the text) and additional sampling localities of this study (Table 3.1, Appendix A). Compiled from field mapping on 1:50,000 base maps.

sampled in several places. However analyses of different samples from the same flow were subsequently found to be very similar and generally within analytical uncertainty (Appendix A).

A small selection of lavas (>500Ka?) from the Taburiente volcano and some evolved lavas and plugs (phonolitic tephrites and phonolites), of undetermined age, from the Cumbre Vieja were were also sampled (localities in Figs. 3.2a&b). These were not used for U-Th analysis, but to assess the composition of both earlier and more differentiated volcanic products. All the samples are very fresh and show no signs of alteration, as expected for such young rocks.

3.4 Analytical Techniques

Since the lavas are generally quite phenocryst rich (10-20%), samples over 1kg were crushed to ensure a representative sample. Nodules and megacrysts were removed before crushing, and in lavas containing many nodules, the sample was first cut into slabs to enable a systematic removal of all nodules. Analyses of samples used in this study are shown in Table 3.1. Major elements and a range of trace elements were analysed for all samples by XRF, using fused discs with a lanthanum heavy absorber and pressed pellets with major element matrix correction routine respectively (Fitton & Dunlop 1985). REE, Th, U, Ta and Hf were analysed by INAA (Potts et al. 1985) for all the historic basanites and other selected samples. Elements analysed by both XRF and INAA (La, Nd and Ce) show good correlations (correlation coefficients of 0.92, 0.85 and 0.92 respectively), although with some bias (see Appendix A). Consequently for samples only analysed by XRF, these elements were corrected for this bias so that the complete data set is consistent. Reproducibilities of analyses, obtained from multiple repeats of samples with similar elemental concentrations to the basanites of this study, are given in Table 3.1.

All isotopic measurements were made using a Finnigan 261 multicollector mass spectrometer, after standard ion exchange chemical separations. Sr was loaded with phosphoric acid on single Ta filaments. $^{87}Sr/^{86}Sr$ ratios were exponentially fractionation corrected within run to $^{86}Sr/^{88}Sr=0.1194$. During the period of analysis some runs were measured statically and others dynamically, although no systematic bias was noted between these methods, with a mean value for NBS 987, using analyses from both types of collection routines, of $^{87}Sr/^{86}Sr=0.71024\pm0.00004$ (2σ standard deviation on 7 measurements). Nd was loaded on double Re filaments, run as metal ions and collected in a dynamic collection routine. $^{143}Nd/^{144}Nd$ ratios were exponentially fractionation corrected within run to $^{146}Nd/^{144}Nd=0.72190$. Four analyses of a

HISTORIC LAVAS

		S.D. 1σ%	LP45D 1585	LP43E 1646	LP63C 1646 S	LP65C 1677	LP95D 1712 J	LP4 1712 SC	LP29D 1712 CV	LP30A 1712 DM	LP32B 1712 DM	LP51C 1712 G	LP48B 1712PN	LP69A 1949 E	LP40E 1971	LP41C 1971S	LP 95en 1712 JE
SiO_2	XRF	0.2	43.15	42.7	42.45	43.29	44.01	43.04	42.69	42.68	42.34	43.57	43.37	43.96	43.99	42.96	55.18
Al_2O_3	XRF	0.4	13.91	13.11	12.84	13.75	13.99	14.62	14.18	12.93	13.87	14.26	13.51	13.87	15.35	13.76	20.37
Fe_2O_3T	XRF	0.2	13.2	13.43	13.55	13.29	13.09	13.06	13.4	13.59	13.49	13.31	13.34	13.71	13.07	14.05	4.63
Fe_2O_3	Calc.		1.98	2.01	2.03	1.99	1.96	1.96	2.01	2.04	2.02	2.00	2.00	2.06	1.96	2.11	0.69
FeO	Calc.		10.10	10.28	10.37	10.17	10.02	9.99	10.25	10.40	10.32	10.18	10.21	10.49	10.00	10.75	3.54
MgO	XRF	0.4	7.29	8.24	8.48	7.81	7.65	6.39	6.91	8.68	7.47	7.15	7.97	8.35	5.84	8.14	0.94
CaO	XRF	0.3	10.6	12.22	12.26	10.8	10.9	10.84	11.15	11.47	11.19	10.68	11.28	10.83	10.15	11.04	3.95
Na_2O	XRF	1.1	4	3.54	3.39	3.95	3.71	4.39	3.98	3.57	3.83	4.08	3.72	3.47	4.28	3.54	8.27
K_2O	XRF	0.4	1.83	1.54	1.49	1.83	1.73	1.95	1.82	1.63	1.78	1.71	1.52	1.26	1.75	1.39	4.06
TiO_2	XRF	0.2	3.75	3.76	3.75	3.6	3.68	3.82	3.88	3.74	3.82	3.71	3.74	3.35	3.72	3.7	1.05
MnO	XRF	3.3	0.21	0.2	0.2	0.21	0.21	0.21	0.21	0.2	0.21	0.21	0.2	0.19	0.2	0.2	0.17
P_2O_5	XRF	0.3	0.87	0.87	0.84	0.84	0.76	1.1	1.02	0.87	1	0.83	0.76	0.7	0.97	0.82	0.24
Total	Calc.		97.7	98.5	98.1	98.2	98.6	98.3	98.1	98.2	97.9	98.4	98.3	98.5	98.2	98.4	98.5
Mg#	Calc.		56.3	58.8	59.3	57.8	57.6	53.3	54.6	59.8	56.3	55.6	58.2	58.7	51.0	57.4	32.1
Co	INAA	2.1	43.7	51.5	52.3	48.8	48.4	42	46.1	53.3		46.8	50.2	52.4	41.1	52.9	6.1
Ni	XRF	0.2	101	112	118	110	100	56	70	124	87	89	105	122	49	102	7
Cr	XRF	0.8	250	292	307	244	252	93	141	297	206	195	260	307	66	207	1
V	XRF	1.5	303	331	334	305	291	304	322	321	322	291	309	296	278	307	67
Sc	XRF	1.6	21	23	24	20	20	18	20	22	18	21	20	26	17	22	2
Ba	XRF	0.8	709	694	697	704	677	832	776	737	768	706	632	473	639	546	1277
Rb	XRF	1.1	44	35	32	42	40	44	42	36	40	42	35	25	37	28	125
Sr	XRF	0.4	1172	1174	1152	1246	1166	1447	1351	1155	1285	1243	1091	924	1224	1018	1633
Nb	XRF	0.5	91	79	76	90	89	100	94	80	90	94	82	66	81	66	120
Ta	INAA	3.6	5.95	5.1	5.15	5.67	5.68	6.27	5.75	5.62		5.99	5.22	4.62	5.7	4.25	5.04
Zr	XRF	0.3	427	354	348	399	387	459	433	379	411	416	369	320	427	361	741
Hf	INAA	2.4	7.82	6.83	6.86	7.42	7.53	8.02	7.56	7.09		7.8	7.29	6.47	7.77	6.81	11.4
Th	I.D.	0.2			8.62	9.48	7.67	11.35	10.36	8.37		8.33			7.73	6.40	20.24
	INAA	3.1	7.65	9.18									7.12	5.91			
U	I.D.	0.4			2.25	2.71	2.04	3.08	2.76	2.28		2.30			2.26	1.79	6.49
	INAA	10.0	2.14	2.47									1.89	1.77			
La	INAA	2.0	81	92	90	97	84	113	105	88		92	79	64	86	74	131
	XRF	1.0									95						
Ce	INAA	1.9	163	177	172	179	161	201	196	174		168	143	133	176	134	183
	XRF	1.0									183						
Nd	INAA	4.4	73	77	74	78	72	88	84	80		77	69	64	79	65	54
	XRF	0.9									79						
Sm	INAA	1.9	13.4	14.1	14	14.2	13.5	15.9	15.2	14.3		14	12.9	11.8	14.7	12.3	8.24
Eu	INAA	2.0	4.18	4.06	4.18	4.12	3.93	4.53	4.37	4.24		4.06	3.79	3.63	4.4	3.68	2.25
Tb	INAA	3.9	1.55	1.49	1.5	1.44	1.39	1.62	1.5	1.71		1.46	1.34	1.55	1.75	1.37	0.89
Yb	INAA	4.3	2.46	2.24	2.35	2.51	2.36	2.53	2.48	2.46		2.45	2.26	2.22	2.5	2.07	2.32
Lu	INAA	4.2	0.35	0.38	0.34	0.36	0.37	0.41	0.4	0.41		0.4	0.35	0.33	0.37	0.3	0.4
Y	XRF	1.2	37	35	34	36	35	39	38	34	37	36	34	32	35	32	26
		S.D. 2σ%															
$^{87}Sr/^{86}Sr$	TIMS	0.005	0.70308	0.70308	0.70309	0.70311	0.70307	0.70309	0.70311	0.70308	0.70311	0.70309	0.70305	0.70313	0.70306	0.70311	
$^{143}Nd/^{144}Nd$	TIMS	0.003	0.51289	0.51288	0.51289		0.51289		0.51291		0.51289		0.51291			0.51289	
$^{206}Pb/^{204}Pb$	TIMS	0.080		19.611			19.668	19.622	19.615		19.619	19.614					19.662
$^{207}Pb/^{204}Pb$	TIMS	0.100		15.600			15.617	15.604	15.615		15.610	15.498					15.618
$^{208}Pb/^{204}Pb$	TIMS	0.140		39.411			39.459	39.434	39.466		39.446	39.410					39.511
$(^{230}Th/^{232}Th)_a$	TIMS	1.80			1.03	1.09	1.11		1.05	1.04		1.10			1.07	1.07	1.10
$(^{238}U/^{232}Th)_a$	Calc.	1.400			0.798	0.873	0.811	0.830	0.815	0.831		0.843			0.892	0.855	0.979

Table 3.1a Whole rock analyses of the historic lavas of La Palma; fourteen basanites and a phonolitic enclave from within one of the basanitic flows. The lavas are ordered in age of eruption (except the phonolite that is on the far right of the table), and are also distinguished by letters, when flows are from the same eruptive event. The age codes are used to identify the sampling localities on Fig. 3.2b, but sample cataloguing numbers are also shown above. The LPTh series (defined later in the text) are indicated by bold sample names. Estimates of 1σ sample reproducibility (relative standard deviation) of major and trace element contents, and 2σ reproducibilities (relative standard deviation) of isotopic ratios are shown (see section 3.4 for details).

			OLDER BASIC LAVAS						OLDER EVOLVED LAVAS				
		S.D. 1σ%	LP9 T1	LP12 T2	LP16 T3	LP19 T4	LP73A CV1	LP61D CD	LP34C CV2	LP64D CV3	LP74A CV4	LP71C CV5	LP72E CV6
SiO_2	XRF	0.2	48.31	43.31	41.15	42.68	45.36	42.82	53.33	54.88	56.7	52.52	49.67
Al_2O_3	XRF	0.4	16.6	14.7	11.66	13.92	14.66	16.82	19.25	20.35	20.45	19.53	17.94
Fe_2O_3T	XRF	0.2	11.2	13.6	13.98	15.78	12.08	9.14	5.77	4.32	3.77	6.24	8.36
Fe_2O_3	Calc.		1.68	2.04	2.10	2.37	1.81	1.37	0.87	0.65	0.57	0.94	1.25
FeO	Calc.		8.57	10.41	10.70	12.07	9.24	6.99	4.41	3.31	2.88	4.77	6.40
MgO	XRF	0.4	3.52	6.09	10.27	7.23	7.03	3.62	1.85	1.05	0.63	1.57	2.85
CaO	XRF	0.3	8.3	10.16	13.11	10.94	10.2	8.58	3.84	2.79	2.83	4.78	6.47
Na_2O	XRF	1.1	4.5	3.56	2.49	2.85	3.99	6.71	8.09	8.81	8.66	7.98	6.87
K_2O	XRF	0.4	2.13	1.79	1.21	0.89	1.8	2.48	4.16	4.54	4.63	3.59	3.26
TiO_2	XRF	0.2	2.75	3.86	3.98	4.33	3.31	2.65	1.3	0.91	0.74	1.75	2.44
MnO	XRF	3.3	0.24	0.21	0.19	0.19	0.18	0.19	0.18	0.15	0.17	0.19	0.19
P_2O_5	XRF	0.3	1.26	1.07	0.63	0.52	0.77	0.77	0.42	0.21	0.21	0.47	0.77
Total	Calc.		97.9	97.2	97.5	98.0	98.4	93.0	97.7	97.6	98.5	98.1	98.1
Mg#	Calc.		42.3	51.0	63.1	51.6	57.5	48.0	42.7	36.1	28.0	36.9	44.3
Co	INAA	2.1	22	42.1	56.4	56.6		23.5	11.5	6.2	4.5		
Ni	XRF	0.2	6	48	140	89	96	17	13	9	4	8	13
Cr	XRF	0.8	2	59	342	115	211	20	11	9	1	1	11
V	XRF	1.5	137	287	354	373	252	245	75	57	42	97	146
Sc	XRF	1.6	7	20	26	25	16	5	2	1		1	3
Ba	XRF	0.8	769	575	507	282	716	1123	1353	1743	1457	1184	1183
Rb	XRF	1.1	58	41	26	15	45	65	162	166	147	109	99
Sr	XRF	0.4	1305	1033	839	679	1078	1512	1634	1980	1013	1468	1530
Nb	XRF	0.5	128	93	55	41	84	141	246	219	117	184	172
Ta	INAA	0.0	8.8	6.31	3.64	2.91		8.29	11.4	9.09	4.07		
Zr	XRF	0.3	675	477	294	287	358	484	972	1099	801	660	676
Hf	INAA	0.0	12.5	9.09	5.93	6.34		6.87	16	16.2	12.6		
Th	I.D.	0.2											
	INAA	0.0	10.15	6.51	4.55	2.76		10.97	44.15	42.76	21.69		
U	I.D.	0.4											
	INAA	0.0	2.51	2.20	1.17	1.22		3.10	15.65	19.44	7.71		
La	INAA	0.0	109	75	44	34		88	212	170	129		
	XRF	1.0					72					145	137
Ce	INAA	0.0	214	153	92	78		166	276	218	181		
	XRF	1.0					150					240	243
Nd	INAA	0.0	92	72	51	44		68	76	60	45		
	XRF	0.9					62					80	84
Sm	INAA	0.0	16	13.3	9.71	9.13		12.3	12.5	10.2	5.67		
Eu	INAA	0.0	4.87	4.13	3.1	2.95		3.7	3.04	2.24	1.69		
Tb	INAA	0.0	1.92	1.47	1.23	1.15		1.34	1.34	1.1	0.68		
Yb	INAA	0.0	3.13	2.33	1.92	2		2.31	2.84	2.49	2.43		
Lu	INAA	0.0	0.5		0.3	0.29		0.34	0.48	0.42	0.36		
Y	XRF	1.2	41	35	27	28	32	34	35	28	24	38	38

Table 3.1b Whole rock analyses of the older La Palma samples. Sample localities are indicated in Fig. 3.1 and 3.2 using the codes given beneath the cataloguing numbers.

J&M Nd standard over the complete period of analysis gave a mean value of $^{143}Nd/^{144}Nd=0.511820\pm0.000034$ (2σ standard deviation). Pb was run on single Re filaments using a silica gel technique adapted from Manhès et al. (1978), and collected statically. Sample fractionation corrections were made using mass dicrimination coefficients calculated from mean values for NBS 981 of $^{206}Pb/^{204}Pb=16.892\pm0.013$, $^{207}Pb/^{204}Pb=15.432\pm0.016$, $^{208}Pb/^{204}Pb=36.517\pm0.050$ (2σ standard deviation from 6 runs) relative to 'accepted' NBS 981 values of $^{206}Pb/^{204}Pb=16.937$, $^{207}Pb/^{204}Pb=15.491$, $^{208}Pb/^{204}Pb=36.700$. Repeats analyses of *samples* for Sr, Nd and Pb all fell within the reproducibility indicated by repeat runs of standards. Blanks were ~1ng, <1ng and <0.5ng for Sr, Nd and Pb respectively and consequently insignificant.

$^{230}Th/^{232}Th$ ratios were measured by mass spectrometry using the technique described in Chapter 2. A mean SEM efficiency relative to the faraday cups of 0.96 for the period of analysis, together with decay constants from the compliation of Goldstein et al. (1989) were used to convert measured $[^{230}Th/^{232}Th]$ to $(^{230}Th/^{232}Th)_a$ ratios. Three analyses of the TML standard gave $(^{230}Th/^{232}Th)_a=1.061\pm0.019$ (2σ standard deviation) and comparable reproducibility, given its higher isotope ratio, was obtained for an in-house standard solution $(^{230}Th/^{232}Th)_a=1.741\pm0.021$ (2σ standard deviation on 4 runs) over the same period. Samples with measured $(^{230}Th/^{232}Th)_a$ ratios had U and Th concentrations precisely determined by isotope dilution mass spectrometry. The Th/U ratios on four seperate dissolutions of the same basanite sample were reproducible to better than 1.5% (2σ standard deviation). There was a systematic bias between isotope dilution and INAA data for Th and U concentrations (see Appendix A), and for samples with just INAA data, concentrations were corrected (as with XRF La, Ce and Nd concentrations), using regression lines from data measured by both techniques, to be consistent with the samples determined by isotope dilution.

Electron microprobe analyses were made on a wavelength dispersive, Cambridge microscan Mk 9 machine, using a ZAF matrix correction, an accelerating potential of 20KV, beam current of 3.05nA and typical spot size of 10-15microns. The instrument was calibrated using mineral standards and drift monitored with an internal, basaltic glass standard.

3.5 Petrography and Mineral Chemistry

The basanites are generally quite porphyritic and have 10-20% phenocrysts of clinopyroxene (largely titaniferous augite), olivine (~Fo 80) and titanomagnetite, and their microcrystalline groundmass contains a similar assemblage together with small plagioclase laths. The presence of only olivine and clinopyroxene phenocrysts in the basanites has

important implications for the depth of fractionation. Experimental studies of alkalic basalts from Réunion (Fisk et al. 1988), show that clinopyroxene rather than plagioclase, becomes cotectic with olivine only at pressures greater than 4kbar. Not only does the basanite phenocryst assemblage suggest that plagioclase is not on the liquidus during fractionation of the basanites, but furthermore, contacts of plagioclase from gabbroic nodules within basanite lavas are marked by strong resorption. Phonolitic tephrites have large (~10mm) plagioclase laths (An 45), titaniferous augites, hauyne, apatite, kaersutite and titanomagnetite phenocrysts. Phonolites are more sparsely porphrytic, generally with small phenocrysts (<1mm) which include aegirine augite, anorthoclase, kaersutite, titanomagnetite, hauyne and sphene. Representative mineral compositions are shown in Table 3.2 (other analyses are presented in Appendix B, and brief petrographic descriptions of samples are given in Appendix C).

The harzburgite nodules contain highly magnesian olivines (Fo 90-91), that show dislocation boundaries, sweeping extinction and neoblasts, indicating recrystallisation, together with minor amounts of orthopyroxene (En 90-91) and chrome spinel. The mineralogy and very refractory nature of these nodules suggest they represent fragments of melt depleted mantle that is thought to form part of the oceanic lithosphere. Furthermore, the olivine deformation indicates shock from forceful entrainment, or rapid pressure release, as would be expected for fragments of mantle entrained during the ascent of melts through the overlying lithosphere. The contact between dunite nodules and the basanitic lava is usually characterised by a rim of fine grained titanaugites that have crystallised from the basanite.

Other nodules appear cumulate in origin, with mineralogies consistent with phenocrysts observed in the volcanics. Pyroxenite nodules of titaniferous augite are common, although the pyroxenes often show extensive reaction to kaersutite. Gabbroic nodules of various mineralogies are found from 'basic' assemblages of titanaugite, olivine and plagioclase to more evolved assemblages that include sodic pyroxene, kaersutite, hauyne, apatite, sphene and plagioclase.

In detail the basanites show a large range of non-equilibrium features that indicate mixing processes. Most notable and ubiquitous are clinopyroxenes with compositionally distinct, anhedral (sometimes melt sieved) cores. The composition of the cores varies

CLINOPYROXENES

	Basanite LP65d core 1	Basanite LP65d rim 1	Basanite LP65d core 2	Basanite LP65d rim 2	Basanite LP65d core 3	Basanite LP65d rim 3	Phonolitic Tephrite LP72	Phonolitic Tephrite LP71	Phonolite LP34	Phonolite LP64
SiO_2	46.11	***47.57***	46.93	43.92	44.91	46.04	47.19	46.65	50.20	49.04
TiO_2	1.78	***2.74***	2.37	3.37	3.30	3.15	2.97	3.10	1.52	1.22
Al_2O_3	6.30	***6.27***	6.75	8.58	8.11	7.22	6.78	7.46	3.90	4.26
FeO^T	11.90	***7.48***	9.76	10.16	9.51	8.52	9.12	9.20	8.55	13.78
MnO	0.51	***0.14***	0.33	0.27	0.25	0.20	0.34	0.30	0.38	0.75
MgO	9.08	***13.10***	10.38	9.55	10.13	11.31	11.18	10.89	11.98	8.19
CaO	21.46	***22.70***	22.64	22.58	23.00	23.44	22.51	22.69	22.12	20.42
Na_2O	1.45	***0.53***	0.98	0.92	0.95	0.73	1.15	0.94	1.08	2.14
Total	98.59	***100.53***	100.14	99.36	100.16	100.61	101.24	101.25	99.73	99.80
Wo	55.6	***51.3***	54.4	56.7	56.7	55.3	49.8	53.9	50.6	53.3
En	32.7	***41.1***	34.7	33.4	34.7	37.1	34.4	36.0	38.1	29.8
Fs	11.8	***7.6***	11.0	9.9	8.6	7.6	15.8	10.1	11.3	16.9

FE/TI OXIDES

	Basanite LP29	Phonolitic Tephrite LP71	Phonolite LP34
SiO_2	***0.13***	0.03	0.05
TiO_2	***15.81***	14.11	14.34
Al_2O_3	***5.94***	3.04	2.13
Cr_2O_3	***0.69***	0.13	0.01
Fe_2O_3	***33.45***	39.37	39.80
FeO	***36.39***	38.39	37.43
MnO	***0.5***	1.44	1.56
MgO	***6.4***	3.09	3.53
Total	***99.31***	99.60	98.87
Us	***32***	26	26
Mt	***68***	74	74

AMPHIBOLES

	Basanite LP45e	Phonolitic Tephrite LP71	Phonolite LP34
SiO_2	39.83	40.72	40.98
TiO_2	6.12	5.84	4.41
Al_2O_3	12.81	12.95	11.85
FeO^T	10.05	13.42	12.32
MnO	0.12	0.4	0.31
MgO	13.27	11.58	12.01
CaO	12.35	11.82	11.32
Na_2O	2.63	3.32	2.92
K_2O	1.14	1.08	1.17
Total	98.32	101.13	97.29

FELDSPARS

	Phonolitic Tephrite LP71	Phonolite LP64
SiO_2	57.55	63.06
TiO_2	0.11	0.13
Al_2O_3	26.32	23.34
FeO	0.38	0.34
CaO	8.6	2.95
Na_2O	6.68	7.97
K_2O	0.47	2.07
Total	100.11	99.86
An	40	15
Ab	57	73
Or	3	12

OLIVINES

	Basanite LP65d	Basanite LP65d
SiO_2	***38.87***	39.19
TiO_2	***0.04***	0.04
FeO	***18.05***	18.39
MnO	***0.28***	0.26
MgO	***42.42***	42.61
NiO	***0.12***	0.13
CaO	***0.3***	0.26
Total	***100.08***	100.88
Fo	***80.7***	80.5
Fa	***19.3***	19.5

Table 3.2 Representative mineral analyses for the La Palma sample suite. The analyses in bold italics are used in the major element fractionation calculation shown in Table 3.3. Fe_2O_3 contents for the Fe/Ti oxides are calculated from a charge balance algorithm. Proportions of compositional endmembers are shown; wollastonite, enstatite and ferrosilite for clinopyroxene (after charge balance calculations, in which a significant proportion of FeO^T is allocated as Fe_2O_3), ulvöspinel and titanomagnetite for Fe/Ti oxides (assuming this is the only solid solution, although these spinels are clearly more complex), anorthite, albite and orthoclase for the feldspars, and forsterite and faylite for the olivines.

considerably, from titaniferous to aergirine augite (that sometimes have small apatite inclusions), but most have a euhedral rim of titaniferous augite. The diversity of core compositions is illustrated in Fig. 3.3, in a plot used by Duda &Schmincke (1985) to distinguish between varied pyroxene compositions, and analyses of pyroxene rims and cores from a single basanite sample are compared with analyses of pyroxenes from phonolites and various nodules. Cores have both higher and lower Mg than rims (Fig. 3.3), suggesting encorporation of pyroxenes that crystallised from more and less fractionated melts, although generally cores are less Mg rich. Duda & Schminke (1985) explain a similar variety of pyroxene core compositions in alkali basalts from the Eifel, Germany as the result of mixing fresh magma batches with stagnated magmas at different levels in the lithosphere. Alternatively, xenocrysts in the basanites may represent phenocrysts that have settled from evolved, overlying magma layers within a zoned magma chamber. Extensive zoned magma chambers are proposed to have existed beneath several ocean islands, from the identification of chemical zonation within eruptive sequences on Tenerife, Canaries and San Miguel and Faial, Azores (Booth 1973, Booth et al. 1978, Wolff 1984); and also from distinctive geochemical signatures within basalts in the Azores, that are attributed to mixing with crystal rich density currents from evolved layers of a zoned magma chamber (Storey et al. 1989).

Further evidence of mineral disequilibrium in the basanites include corroded kaersutite megacrysts in some of the basanitic lavas and although most olivine crystals are normally euhedral or skeletal, resorbed and anhedral olivines rimmed by fine titanaugite crystals are sometimes observed. Thus, further to the field evidence of phonolite/basanite mixing and nodule entrainment, such petrographic features also suggest a complex mixing history for the basanite lavas, involving perhaps the addition of partially disagregated nodules, settled phenocrysts from overlying phonolites in a zoned magma chamber and mixing with other basanitic melts.

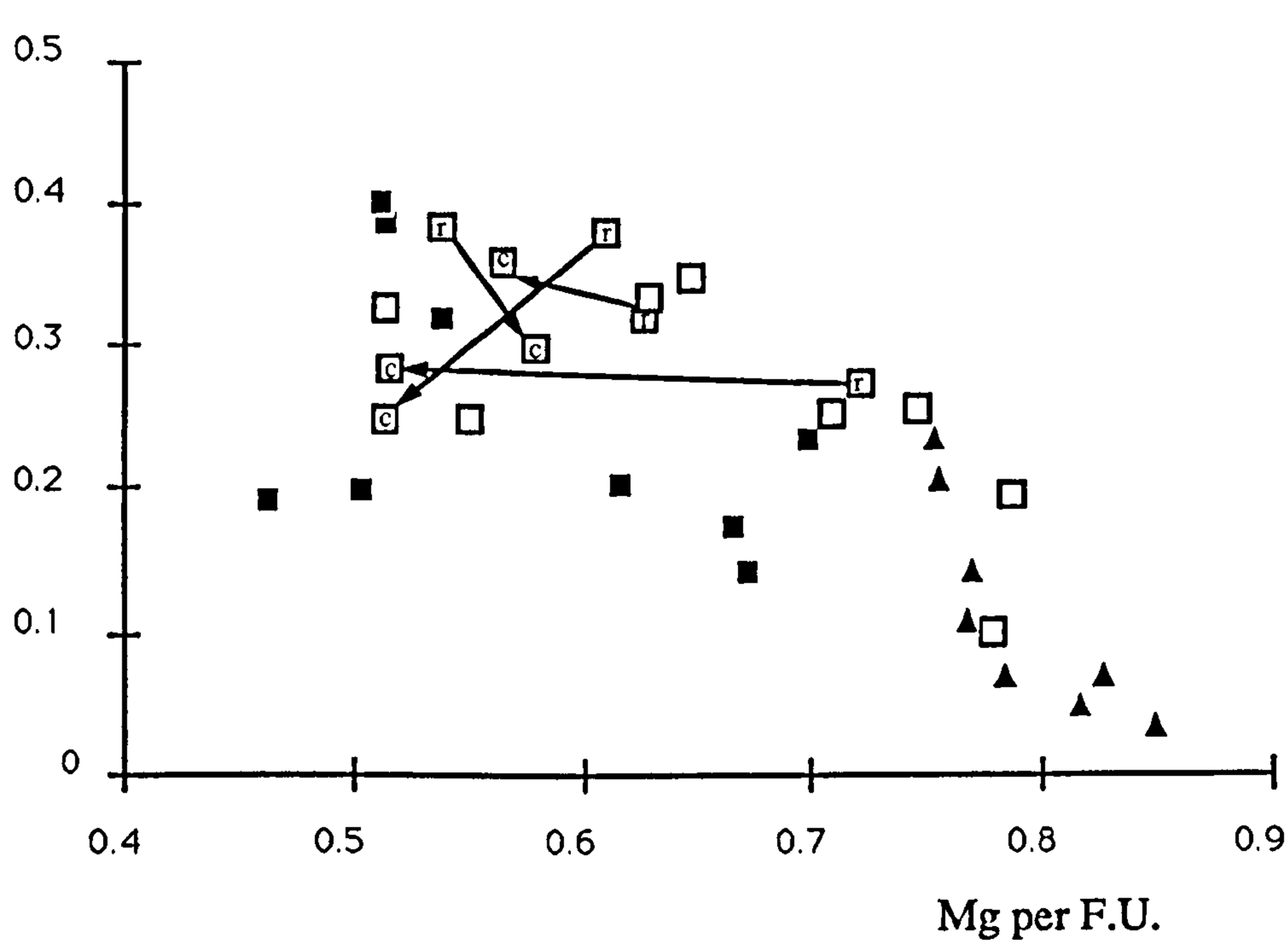

Figure 3.3 Variation of atomic Mg and Al (atoms per formula unit) for clinopyroxenes from a single basanite LP 65 (large open squares), 'basic' cumulate nodules (small filled triangles), and phonolites and 'evolved' cumulate nodules (small filled squares). Arrows link multiple analyses of single pyroxene crystals, with the arrow pointing from the composition of the rims (r) to that of the cores (c).

3.6 Major and Trace Element Variation

Variation diagrams are shown for the full range of rock types sampled, including the lavas from Taburiente and more evolved samples from the Cumbre Vieja Ridge (Fig. 3.4). Overall, the coherent variation of major elements is compatible with evolution of the suite by crystal fractionation. Steady decreases in CaO and increases in Al_2O_3 with decreasing MgO suggest the importance of clinopyroxene as a major fractionating phase throughout the suite. Likewise titanomagnetite appears to be an important liquidus phase for all the compositions sampled, as implied by steady decreases in TiO_2 and FeO from basanite to phonolite. These observations are consistent with the phenocryst and nodule phases observed.

There appears to be a major change in fractionating assemblage at around 4-5% MgO, as has been observed in other alkalic suites (Le Roex 1985, Maaløe et al. 1986, Storey et al. 1989), which results in an inflexion in most of the major element trends. This probably represents a reaction point, at which olivine, observed as a phenocryst phase only in the basanites, disappears from the fractionating assemblage, resulting in a more rapid increase of K_2O and SiO_2, and more rapid decrease of FeO and TiO_2 with MgO. At this point, plagioclase (and kaersutite?) also become liquidus phases, and apatite starts fractionating, resulting in a rapid decrease in P_2O_5. Although plagioclase is observed as a phenocryst phase in the more evolved rocks, a steady increase in Al_2O_3 argues against its extensive fractionation, which may be hindered by density considerations. This is however puzzling considering the abundance of gabbroic cumulates observed in the eroded centre of the Taburiente caldera. However this plutonic complex probably resulted from *shallow* level *basanitic* fractionation, in which plagioclase became cotectic before clinopyroxene (Fisk et al. 1988), during an earlier phase of activity.

Fig. 3.5 shows the variation of MgO with trace elements, which are normally incompatible during mantle melting, within the basanites and evolved samples of this study. In the fractionation sequence Rb is the most incompatible element, with concentrations ranging from ~30ppm in a typical historic basanite to ~170ppm in some of the phonolites.

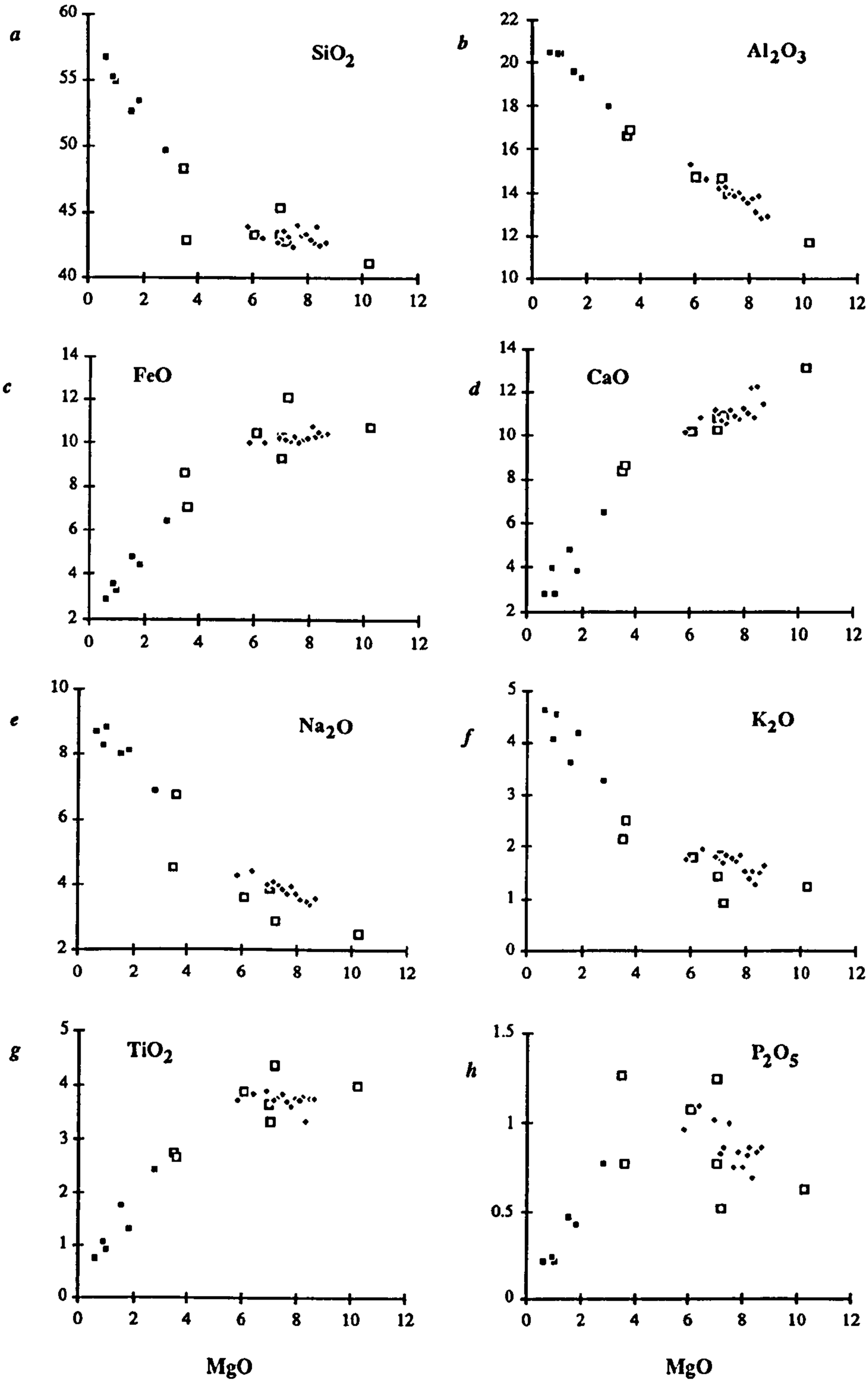

Figure 3.4 Variation of major and minor element contents against MgO for the whole La Palma suite. The historic basanites are shown as filled daimonds, the older, basic lavas as open squares and the more evolved rocks as filled squares.

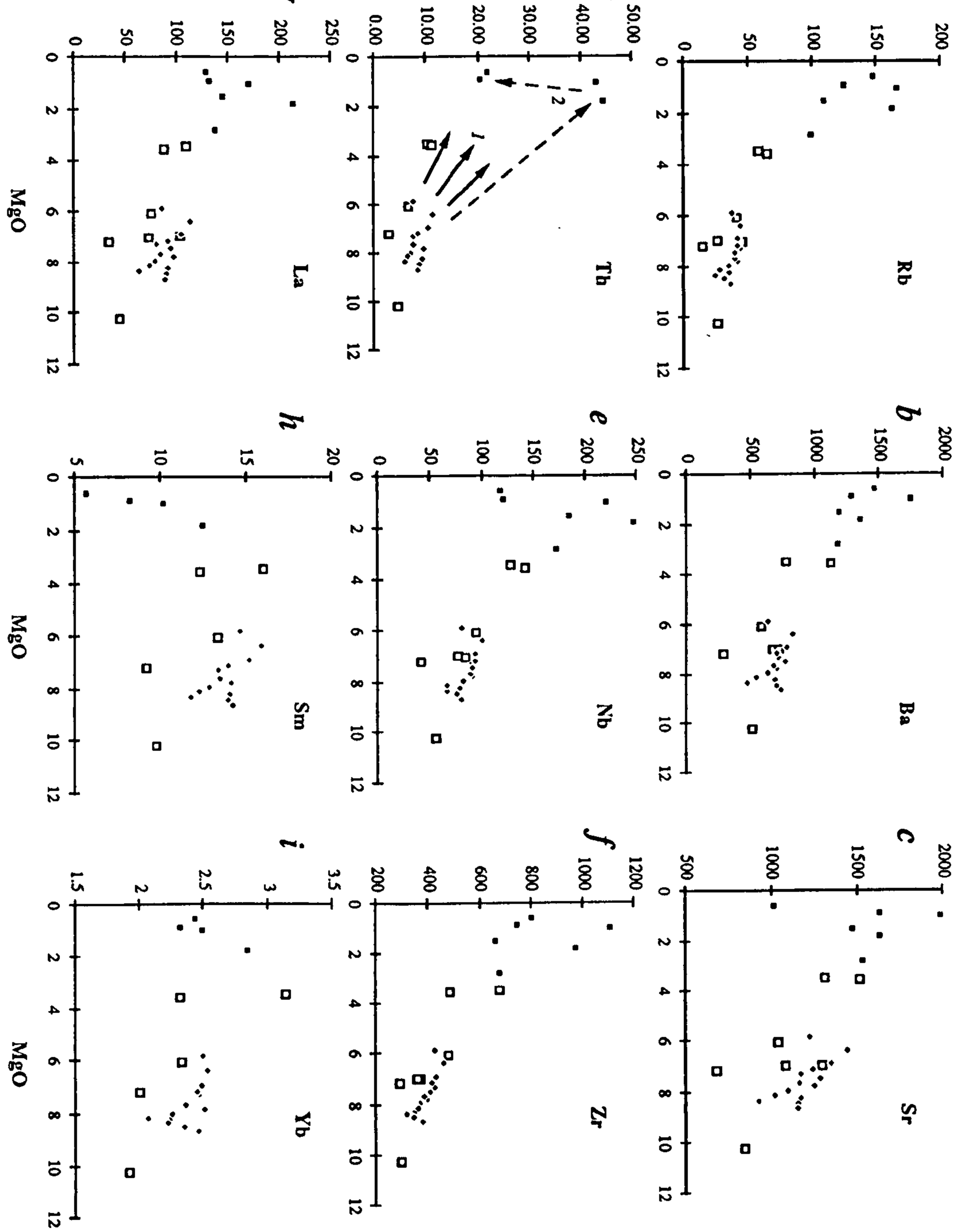

Figure 3.5 Variation of contents of trace elements, that are normally incompatible during mantle melting, against MgO for the whole La Palma suite. Symbols as in Fig. 3.4. Diagram **d)** shows possible interpretations of chemical variation in terms of multiple fractionation trends (1) or late appearence of an accessory phase that strongly controls various trace element contents (2).

Assuming Rb remains completely incompatible with respect to all fractionating phases, this suggests ~80% fractionation to evolve a phonolite from a basanite. This is a minimium value since although Rb remains incompatible throughout the lava series, it is not necessarily *totally* incompatible, and indeed it is clear that several elements that are characteristically incompatible during mantle melting become less incompatible or even compatible in the more evolved fractionation assemblages of La Palma (e.g. Fig. 3.4g & 3.5h). Although major element variation suggests a single fractionation trend for the whole suite of rocks, this is less apparent from plots of trace element concentrations against MgO. The small number of evolved samples analysed makes the issue difficult to assess comprehensively, and it is unclear in plots such as Fig. 3.5d whether the variation is best accounted for as multiple fractionation trends (model 1 Fig. 3.5d) or the very late stage crystallisation of an accessory phase(s) into which Th (and other normally incompatible elements) are partitioned (model 2 Fig. 5d). Trace elements concentrations are susceptible to small variations in the proportion and composition of minor phases fractionated, that might result from variable oxygen and water fugacities. Hence different fractionation trends implied by trends in trace elements may not signify volumetrically major differences in bulk fractionating assemblage, but simply small differences in the minor phases fractionated. Likewise differences in degree of melting may have little effect on major element compositions, but result in a range of primary incompatible element concentrations, for different degree melts, and hence multiple (parallel) fractionation trends.

Apatite fractionation is evident from the decrease in P_2O_5 with MgO, as discussed above, and it can also account for the compatible behaviour of Nd and Y and only modest increases in La and Sr with respect to Zr, for example, within the phonolites (Fig. 3.5). The geochemical signature of sphene fractionation is most readily identified in increasing Nb/Ta with indices of fractionation in the La Palma phonolites (see Fig. 3.6, in which FeO is plotted as fractionation index instead of MgO to exemplifiy an additional point which is discussed later). The geochemical behaviour of Nb and Ta is usually almost identical, but experimental determinations of the melt distribution coefficients of Nb and Ta with sphene (Green & Pearson 1987) indicate that it can fractionate these elements, as suggested by

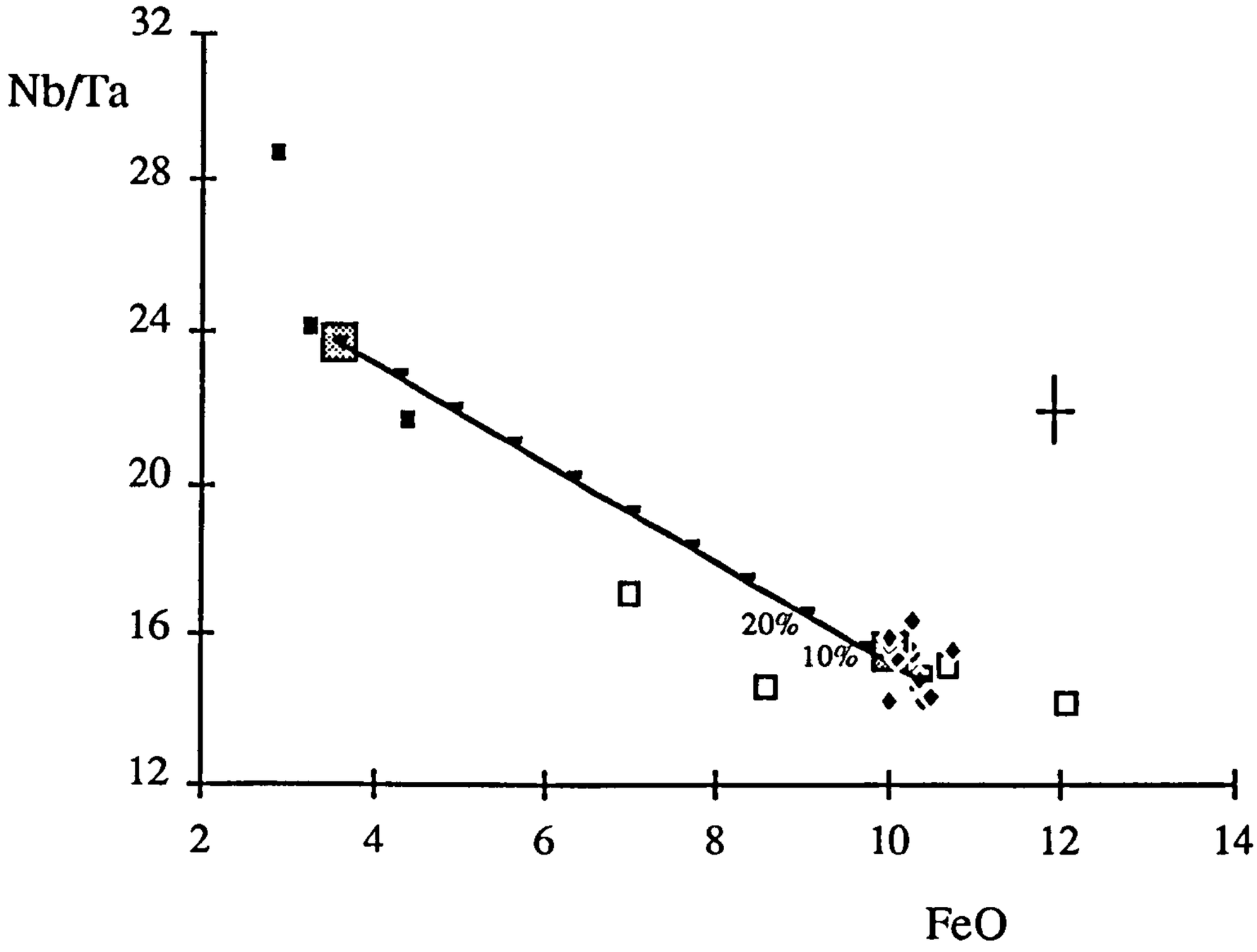

Figure 3.6 Nb/Ta against FeO for the La Palma suite, with symbols for different rock types as in Fig. 3.4. The two grey filled large squares are a basanite of the 1712 eruption and a phonolitic enclave found within this basanite flow. A mixing line, with ticks every 10%, is shown to illustrate the effects of mixing the phonolite with another more FeO rich basanite, to assess the extent of any chemical mixing the 1712 basanite may display, is discussed later in the text. 2σ errors are indicated by the cross.

Wolff (1984) to explain significant Nb/Ta variations in syenitic pumices of Tenerife. The general increase in Nb/Ta with decreasing FeO (or MgO) within the evolved magmas suggests that sphene fractionation occurs throughout these compositions, as was observed by Wolff (1984) for the Tenerife samples. As with apatite, sphene fractionation will have a significant affect on rare earth element concentrations of the evolving magma.

The lowest MgO phonolites show marked decreases in Th, U, Nb &Ta concentrations, which may represent the endmembers of a particular fractionation trend, or the late appearance of another minor phase in which these elements are compatible (illustrated by model 2 in Fig. 3.5d). Sphene might produce such variations, but it has has been argued above that it fractionates throughout the phonolite sequence. Loparite (a Nb rich perovskite), which is thought to be a very late stage liquidus phase and is found interstitially in syenitic blocks within phonolitic pumices on Tenerife (Wolff 1983), contains large amounts (weight percents) of Th, Nb and Ta oxides. Although it is unlikely physically to fractionate from a magma chamber (Wolff 1983), the geochemical signature of its *in situ* fractionation may be recorded in the compositions of the lowest MgO phonolites. Monazite frequently crystallises with apatite in phosphorous saturated systems and may also be an important phase for controlling the Th, U and LREE contents of the evolved magmas.

3.7 Chemical Variation within the Historic Basanites

The basanites are 10 to 17% nepheline normative (assuming $Fe^{2+}/(Fe^{2+}+Fe^{3+})=0.85$) and as such, they are some of the more alkaline basalts from Atlantic ocean islands (McBirney & Gass 1967, Weaver et al. 1987). Despite the quite high MgO contents of the basanites (6-8.5%), the low Ni contents (50-130ppm) and Mg# (53-60, assuming $Fe^{2+}/(Fe^{2+}+Fe^{3+})=0.85$) indicate that they are not primitive mantle melts.

3.7.1 Crystal Fractionation within the Historic Basanites

Fig. 3.7 shows the Rb and FeO contents of the basanites plotted against Ni. The majority of the samples form a shallow trend of decreasing Ni with decreasing FeO and increasing Rb, whilst outliers have significantly lower Ni contents. Crystallisation of a clinopyroxene/ olivine/ titano-magnetite assemblage, expected from the basanite phenocryst assemblage, results in rapid Ni (and Cr) depletion, as shown by representative trajectories

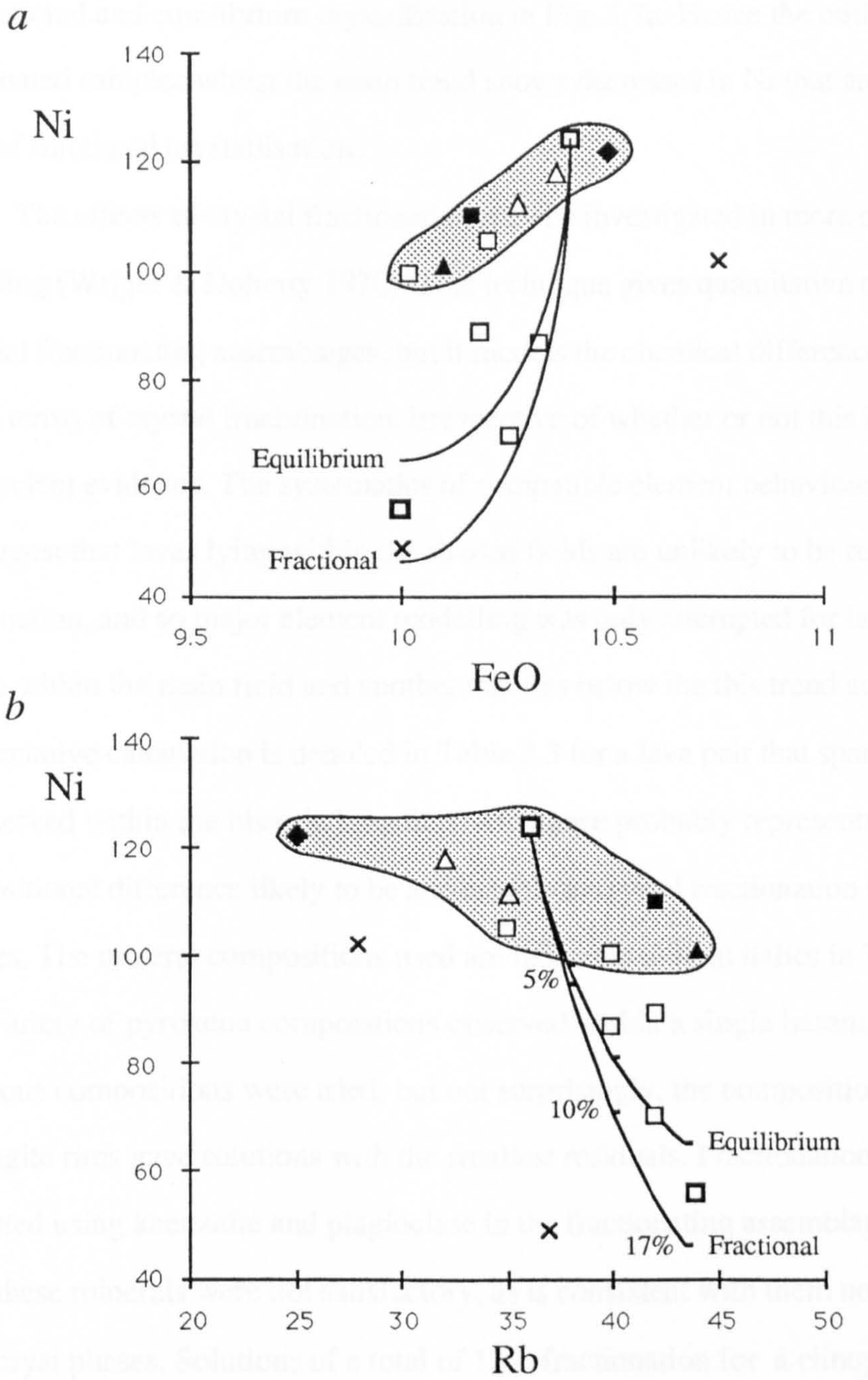

Figure 3.7 a) Ni against FeO and **b)** Ni against Rb for the historic basanites. Symbols show historic lavas of different eruptive events. Equilibrium and fractional crystallisation trends are shown for the two lavas (from the 1712 event, indicated as bold open squares) modelled in Table 3.3, using the fractionating mineral assemblage calculated in Table 3.3. Distribution coefficients used for Ni are $D^{ol} = 15.6$ (from Hart & Davis 1978, $D^{ol} = 124/MgO-0.9$, taking a mean MgO of 7.5%), $D^{cpx} = 2.2$ (Le Roux 1984) and $D^{titmag} = 10$ (Le Roux 1985) and Rb is assumed to be totally incompatible. In **a)** the trends are schematic between two calculated endmembers whilst in **b)** the trends show tick marks for increments of fractionation. The shaded fields highlight historic basanites in which the main chemical variation cannot be accounted for by crystal fractionation, and it is apparent that within this field there is no progressive change in lava composition with age of eruption.

for fractional and equilibrium crystallisation in Fig. 3.7a. Hence the outliers appear to be the fractionated samples whilst the main trend shows decreases in Ni that are too small to be the result of fractional crystallisation.

The effects of crystal fractionation may be investigated in more detail by least squares modelling (Wright & Doherty 1970). This technique gives quantitative constraints on potential fractionating assemblages, but it models the chemical difference between any lava pair in terms of crystal fractionation, irrespective of whether or not this is likely from independent evidence. The systematics of compatible element behaviour illustrated in Fig. 3.7 suggest that lavas lying within the shaded fields are unlikely to be related by crystal fractionation, and so major element modelling was only attempted for lava pairs with one sample within the main field and another that lies below the this trend at lower Ni. A representative calculation is detailed in Table 3.3 for a lava pair that spans the entire range of Ni observed within the historic basanites, and hence probably represents the greatest compositional difference likely to be attributable to crystal fractionation between the basanitic samples. The mineral compositions used are indicated in bold italics in Table 3.2. Due to the wide variety of pyroxene compositions observed within a single basanite flow (Fig. 3.3) numerous compositions were tried, but not surprisingly, the compositions of the euhedral titanaugite rims gave solutions with the smallest residuals. Fractionation schemes were also attempted using kaersutite and plagioclase in the fractionating assemblage, but solutions using these minerals were not satisfactory, as is consistent with them not appearing as phenocryst phases. Solutions of a total of 17% fractionation for a clinopyroxene/ olivine/ titanomagnetite assemblage (in the ratio 8.2:3.2:1) gives an acceptable calculated sum of the squares of the residuals of 0.02. Using the partition coefficients cited in the caption of Fig. 3.7, the effects of fractionation of this best fit assemblage (Table 3.3) are calculated for incompatible and compatible element contents, and are illustrated in Figs. 3.7a & b. These calculations show that the proportions of fractionating phases and the overall degree of crystal fractionation constrained from major element mass balance considerations are also consistent with trace element variations observed between the same lava pair.

Fig. 3.7b shows there is a variation of Rb from 25-40ppm within the samples that show little difference in compatible element concentrations (i.e. those of the main trend) and

Table 3.3 The most reasonable, least squares major element and minor element modelling solution for the lava pair highlighted in Fig. 3.7. Mineral compositions used are from the analyses indicated by bold italics in Table 3.2.

LP30a ⇒ 83.06LP4 + 11.18cpx + 4.39ol + 1.37 titanomag.

		SiO_2	TiO_2	Al_2O_3	FeOT	MnO	MgO	CaO	Na_2O	K_2O	P_2O_5		Total
LP 30a	Obs.	42.95	3.76	13.01	13.68	0.20	8.74	11.54	3.59	1.64	0.88		99.99
	Calc.	42.93	3.7	12.99	13.69	0.21	8.75	11.58	3.73	1.63	0.92		100.13
	Residual	*-0.017*	*-0.055*	*-0.020*	*0.013*	*0.009*	*0.010*	*0.035*	*0.140*	*-0.120*	*0.042*	$\Sigma r^2 =$	*0.027*

which cannot therefore have experienced significantly different degrees of fractional crystallisation (<5%, Fig 3.7b). Moreover, if the observed variation in Rb was due to fractional crystalliastion it would require ~50% fractionation, which is clearly inconsistent with the Ni data and major element considerations, and so it must be attributable to a different process. Mixing with more Rb rich lavas, such as the phonolites, accumulation of accessory phases, differences in source composition or degree of melting may potentially account for the large Rb (and other incompatible element) variations, and these processes are considered in the next sections.

3.7.2 Chemical Variation due to Magma Mixing?

Some of the xenocrystic pyroxenes within the basanites overlap in composition with pyroxene phenocrysts found within the phonolites (Fig. 3.3), and this perhaps suggests mixing of phonolitic and basanitic magmas, resulting in a hybrid, disequilibrium phenocryst assemblage. However, the geochemical effects of magma mixing between samples in Figs 3.4 & 3.5 are represented by straight lines, and as is clear in Figs 3.4c&g and 3.5h&c, for example, there are no evolved lavas that lie at the end of the basanite trends in these plots that could represent suitable mixing endmembers to explain the chemical variation in the basanites. Not only does bulk mixing with the phonolites not explain the geochemical trends observed within the basanite lavas, but even in the Jedey 1712 flow where phonolitic enclaves are actually observed within the basanite, and clearly some *physical* mixing of magmas has occurred, there is little geochemical evidence for magma homogenisation. This is illustrated in Fig. 3.6, where Nb/Ta ratios (that are anomalously high in the phonolites) are plotted against FeO. Analyses of the phonolitic enclave and host basanite are highlighted, and a mixing line is shown from another, higher FeO basanite, arbitarily chosen to give the best possible fit for a mixing line to the phonolite enclave. Even in this scenario any potential mixing is less than 10%, and thus it appears that even where there is field evidence for coexisting basanitic and phonolitic magmas, they are not intimately mixed to produce chemically homogeneous hybrids. This is consistent with studies of Sparks & Marshall (1986) and Campbell & Turner (1986), that show that contrasts in temperature and viscosity between evolved and basic melts make complete mixing difficult.

3.7.3 Mixing by Crystal Accumulation

As discussed above, the xenocrystic pyroxenes commonly observed in the basanites need not represent the mixing of magmas but instead may result from the settling of phenocrysts from stratified layers of evolved magmas into underlying basanitic layers, in a zoned magma chamber. This would also account for the large range in xenocrystic compositions observed in a single basanite, rather than two distinct mixed populations (Fig. 3.3). Furthermore, the variations of certain incompatible element concentrations within the basanites also are consistent with accumulation of fractionating phases from the more evolved magmas. Fig. 3.8 shows the variation of some incompatible elements with Rb for the historic basanites. Whilst for elements such as K_2O, Nb and Yb (Figs. 3.8f,g & h), a single trend for the whole suite of basanites is observed, in plots of Rb against Th, U, P, LREE and MREE, and to a lesser extent Sr (Figs. 3.8a-e & i), the basanites show considerable scatter, with a group depicted by open symbols showing significantly higher concentrations of these elements than those of the group shown with filled symbols, at a given Rb content. (The two samples from the 1971 eruption shown as crosses do not consistently fit in either group. However rhyolitic pumices, that are geochemically quite distinct from the other alkalic products of La Palma, are associated with this eruption and may help account for their anomalous behaviour).

Figure 3.9a shows the Nb/U ratios of samples within the groups indicated in Fig. 8 are fairly constant (one of the filled symbols appears to plot to somewhat low Nb/U, but the U content, measured by INAA on this sample, is imprecise and has much greater uncertainty than U contents measured by isotope dilution. Notably, all samples with U measured more precisely by isotope dilution (circled), plot within the two distinct groups). However, the basanites with higher P_2O_5, U, Th and LREE concentrations have anomalously *low* Nb/U ratios with respect to the near constant ratio of 47±10 found by Hofmann et al. (1986) for nearly all MORBs and OIBs, whilst the 'low U' basanite group plot within this range (Fig. 3.9a). This implies that the high U/Th/P/LREE (HPTh) basanites have been preferentially *enriched* in U (and by inference the other associated elements), and that the low U/Th/P/LREE (LPTh) basanites represent more typical asthenospheric melts.

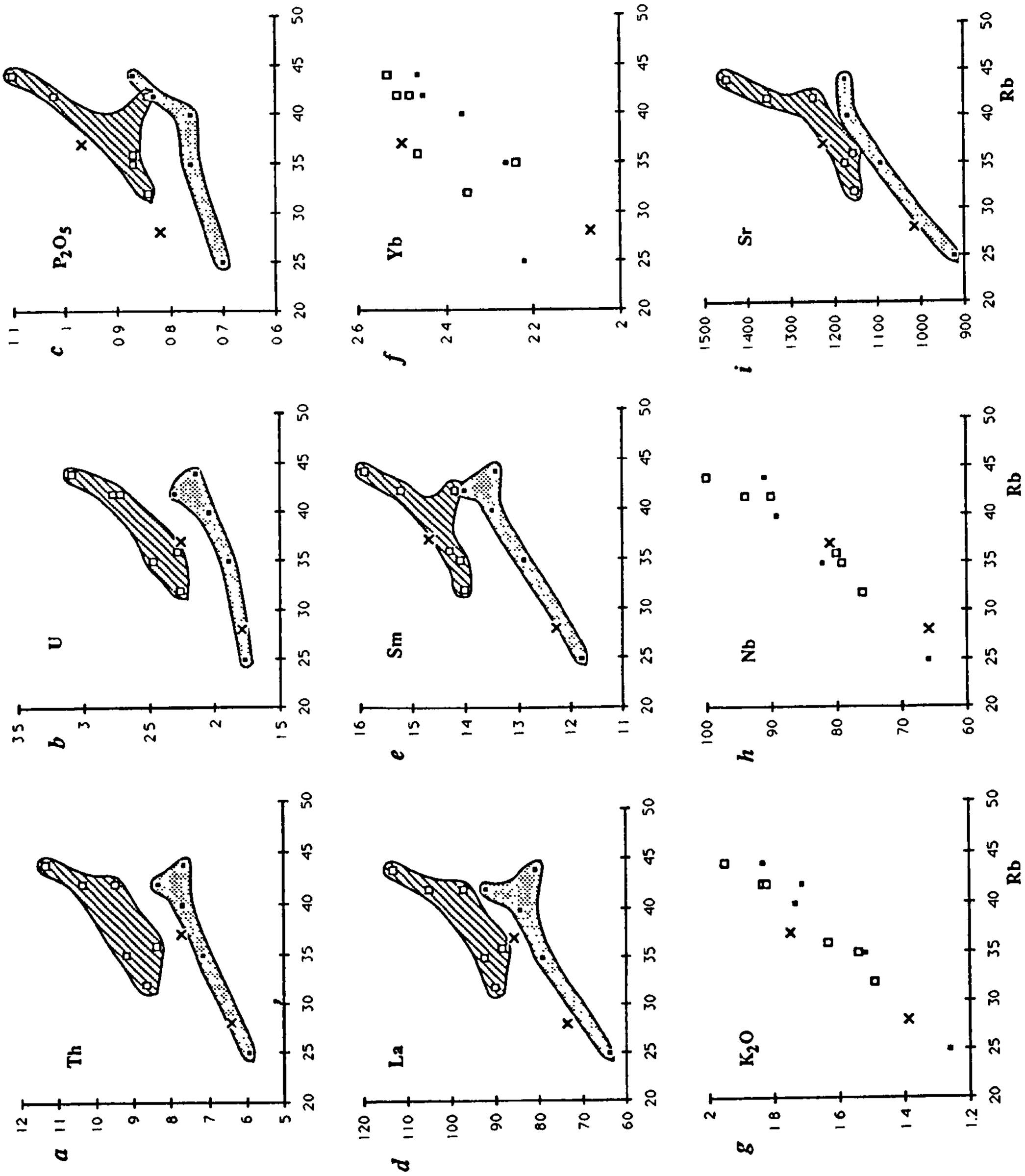

Fig. 3.8 Variation of trace elements normally incompatible during mantle melting, against Rb for the historic basanites. The diagonally shaded field and associated open squares represent basanites (the HPTh group) with elevated contents of certain trace elements e.g. Th & U, at a given Rb content, with respect to the basanites shown as filled squares in the dotted, shaded field (the LPTh basanites). The two basanites from the 1971 eruption do not systematically fall in either field, see text, and are shown as crosses.

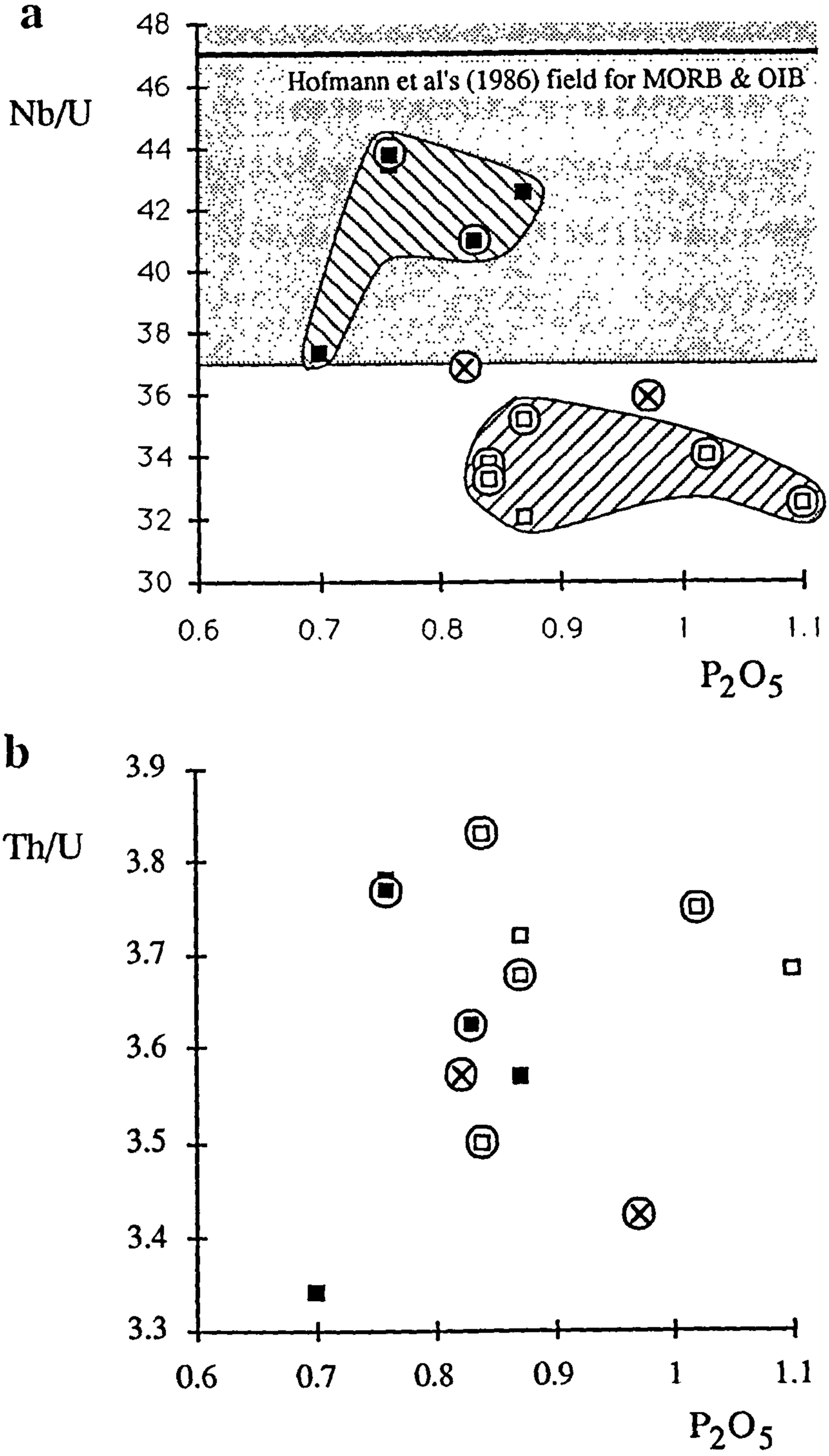

Figure 3.9 a) Nb/U and **b)** Th/U against P_2O_5 content (weight percent) for the historic basanites. The sample symbols are the same as in Fig. 3.8. Samples ringed have U and Th contents measured by isotope dilution.

It is unlikely that the two basanite group have different mantle sources, since the preferential metasomatic enrichment of only Th, U and LREE, and not other incompatible elements in the HPTh source is not compatible with the commonly inferred geochemical behaviour of incompatible elements in *either* hydrous fluids *or* small degree melts (Hawkesworth et al. 1984). However the association of P/Th/U and rare earth elements is characteristic of apatite (Irving & Frey 1984). Different amounts of residual apatite during melting could result in basanite groups with high and low concentrations of elements compatible in this mineral. However, such a scenario would be expected to produce a LPTh group (with most residual apatite) that had anomalously *high* Nb/U, rather than a HPTh group with low Nb/U ratios, as found in the La Palma basanites. Furthermore, experiments by Watson et al. (1979) have shown that it is very unlikely for apatite to be residual during mantle melting. It is thus improbable that apatite is a controlling phase during melting, although it might then be invoked to control the compositions of small degree melts in an (unusual) intra-mantle enrichment process. Not only are enrichment scenarios for such closely temporally and spatially associated lavas as the historic basanites difficult to envisage, but any enrichment must have been very recent, since the radiogenic isotopic ratios of HPTh and LPTh basanites are analytically indistinguishable (Table 3.1). This suggests the *addition* of an apatite mineral to the HPTh melts after melt segregation, rather than a role of residual apatite during mantle processes, is important in explaining the differences between the HPTh and LPTh basanites.

Apatite is observed both petrographically and geochemically to be involved in the fractionation sequence of the La Palma lavas, and it is also seen as inclusions within sodic, xenocrystic cores of pyroxene phenocrysts in the historic basanites. Apatites enclosed within pyroxenes are petrographically preserved, but free crystals that settle from overlying evolved magmas into a basanite are likely to dissolve (basanite pairs that can be related by fractional crystallisation, Table 3.3, show P_2O_5 behaving incompatibly and hence are under-saturated in phosphorous) and thus the effects of apatite accumulation may be evident only in the geochemistry of the host basanite. Clearly settling of other phases, such as clinopyroxene, may also occur, but the very high actinide, LREE and P contents of phosphate minerals, compared with the much smaller contents of 'mantle incompatible' trace

elements in most other likely settling phases results in the effects of phosphate mineral settling being most obvious in the geochemical signatures of the basanites.

It thus appears that the HPTh are related to the LPTh basanites by addition of a phosphate mineral, since the chemistry of the groups, apart from contents of Th, U, P and light to middle REEs is very similar. However addition of <<1% apatite to an LPTh basanite raises the P_2O_5 content to that of an HPTh lava (of similar Rb content), but barely affects the Th, U and LREE contents, even if the Th, U and LREE contents of the apatite are calculated to be in equilibrium with the phonolite in this study with the *highest* contents of these elements (using distribution coefficients taken from Irving & Frey 1984). Addition of apatite would also be expected to produce more significant differences in HREE and Sr between the basanite groups (c.f. Fig. 3.8f & i). Monazite, which frequently crystallises together with apatite, contains much larger proportions of Th and LREE (weight percents) than apatite and is thus a more reasonable choice of 'contaminating' phosphate mineral. Furthermore, monazite is very dense (~5gcm^{-3}) and so is likely to settle rapidly from an overlying phonolitic layer. Generally monazite has high Th/U ratios (>10) and would be expected to cause systematic differences in Th/U ratios between the HPTh and LPTh basanites. Figure 3.9b shows that this is not observed, and suggests that U rich monazites (Overstreet et al. 1970) have settled into the HPTh lavas.

In summary, some of the historic basanites may be related by minor degrees of crystal fractionation (~15%), but in basanites with similar Ni contents variations of Rb content, from 25-45ppm are too great to be explained by crystal fractionation alone. Mixing of evolved and basic magmas could produce such a variation in Rb, but cannot explain the associated variations in other major and incompatible elements, and is also physically unlikely. Contamination of some basanites with an accessory phase settling from coexisting phonolites accounts for variable Th, U, P_2O_5 and LREE contents of basanites with similar Rb, but not the variations in Rb itself. Thus there are significant and coherent geochemical variations within the basanites which cannot be explained by crystal fractionation or mixing processes, and hence may be attributable to variations in degree of partial melting or variations in source composition. Potential source variations are most readily identified, in

the absence of contamination, by variations in radiogenic isotope ratios. However, as is evident from Table 3.1, $^{87}Sr/^{86}Sr$ and $^{143}Nd/^{144}Nd$ show no variations greater than the reproduciblity of standards, and likewise $^{206}Pb/^{204}Pb$ ratios are analytically indistinguishable, except for a single sample that is only just outside the 2 σ error. This does not eliminate the possibility of recently produced source heterogeneity, but this is likely to result in similar geochemical variations to those produced by the immediate melting processes, and so potential compositonal variations due to partial melting processes are first investigated (using the uncontaminated LPTh lavas).

3.7 Melting Beneath La Palma

Minster & Allègre (1978) proposed plots of C_H/C_i against C_H (where C_H is the concentration of the most incompatible element within a cogenetic suite and C_i is the concentration of other incompatible elements) to identify variations due to partial melting within cogenetic lava suites. Although it is very difficult to prove a common source for any lava suite, the close temporal relationship and identical radiogenic isotope ratios of the historic La Palma basanites make such inferences reasonable for these lavas. Figure 3.10 shows Rb/C_i plots for the LPTh basanites, in which all elements are normalised to primitive mantle concentrations to facilitate comparisons. (All normalisations in this chapter are relative to the primitive mantle values of Sun & McDonough (1989) and denoted by a subscript n). Significant variations of Rb/C_i ratios with Rb are evident, even for other highly incompatible elements (Fig. 3.10a) that indicate differences in degrees of partial melting between the basanites. The steeper gradients on such plots for the middle and heavy REE (Fig. 3.10b) is consistent with their higher distribution coefficients for mantle assemblages, and hence greater fractionation with respect to more highly incompatible elements for variable degrees of melting. The HPTh basanites show similar positive trends to the LPTh basanites, but they add scatter on many of the plots, due to monazite accumulation outlined in the model above, and so are not shown.

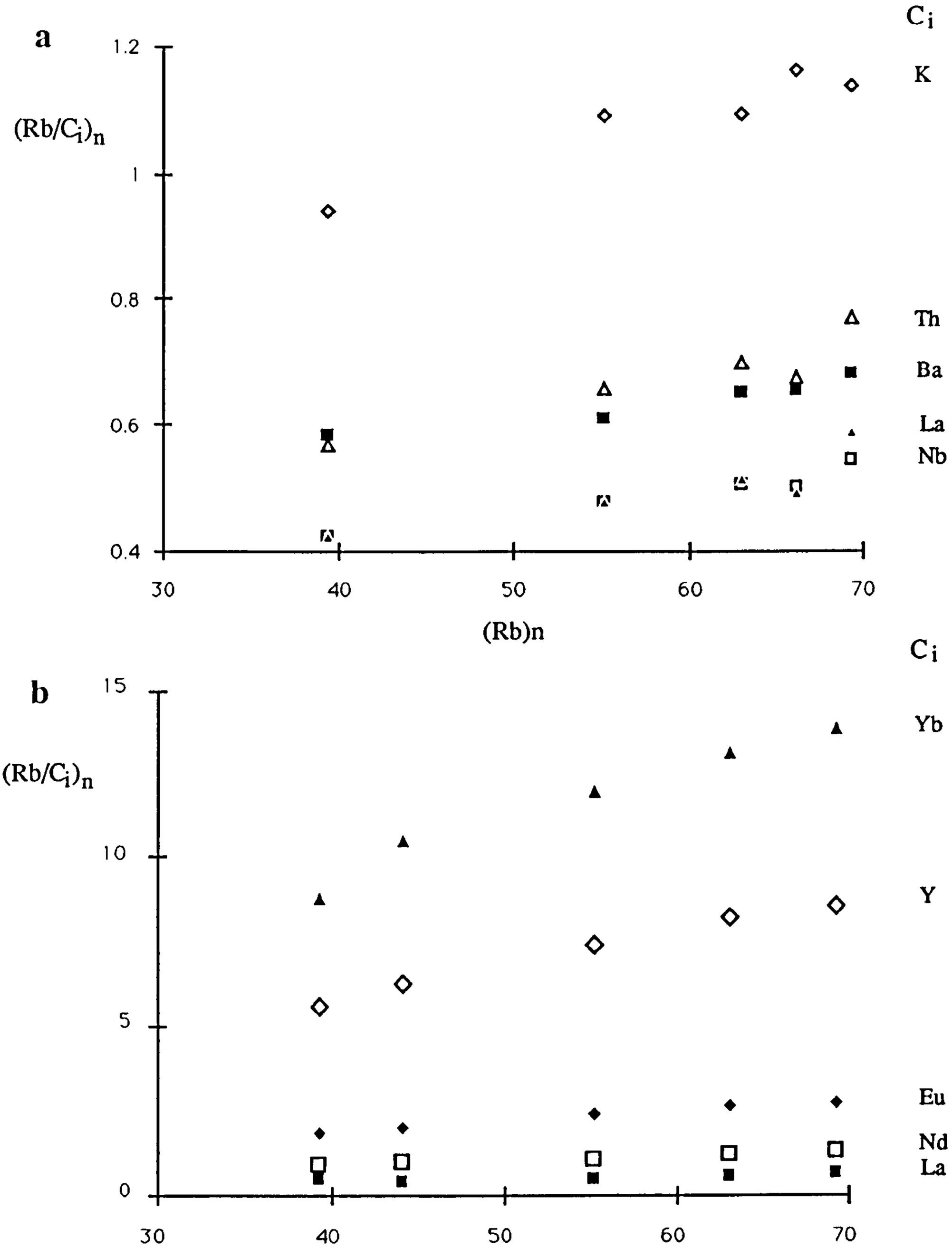

Figure 3.10 Variation in the LPTh basanites of primitive mantle normalised Rb contents against primitive mantle normalised ratios of Rb over **a)** various elements normally highly incompatible during mantle melting and **b)** various rare earth elements (and Y).

3.7.1 Modelling of Melting Processes

Minster & Allègre (1978) and Hofmann & Feigenson (1983) discussed inversion techniques for data arrays of rare earth elements from cogenetic lava suites, similar to those in Fig. 10b, to infer the mineralogy and relative REE compositions of mantle sources. The inversion procedure to obtain source *mineralogy* relies critically on values used for the melt norms (the proportions of minerals that enter the melt). Melt norms may be estimated by least squares modelling of major element contents using reasonable mantle mineral compositions together with the inferred composition of the primitive melt. None of the La Palma basanites have near primitive Ni contents nor Mg#, and assuming a primary melt Mg# of 71 and olivine as the only liquidus phase (for simplicity), most of the basanites have undergone some 15-20% fractionation. Whilst a simple olivine addition correction may be adequate for calculating primitive incompatible element contents, because the basanites have probably also fractionated significant proportions of clinopyroxene, back calculating a reliable, primitive major element composition is difficult, and hence melt norms cannot be easily obtained by such an approach. Instead a forward modelling method has been used to investigate melting parameters for the La Palma basanites. Although a forward approach does not provide a unique solution for the melting assemblage and composition, it can still provide strong constraints on the melting process.

A dynamic melting model is probably most appropriate for melting during asthenospheric upwelling (McKenzie 1984, Klein & Langmuir 1987), but useful information can be obtained from simple melting equations that reasonably reproduce the effects of more complex melting scenarios for many situations (Langmuir & Plank 1988). A batch melting equation (Shaw 1970) has been used in this study:

$$C_l^i = C_o^i / (D_o^i + X(1-P^i)) \qquad (1)$$

where C_o^i and D_o^i are the initial concentration and bulk distribution coefficient respectively of a trace element i in the unmelted source, X is the degree of melting (F^{liq} in Hofmann & Feigenson's (1983) nomenclature), P is the bulk distribution coefficient of the melt norms and C_l^i is the concentration of the trace element i in the resulting melt. Hence for a source with n mineral phases, each of which represents a fraction F^n of the bulk source and enter the melt in a constant proportion p^n, having melt partition coefficients K_n^i, then $D_o^i = {}_o\Sigma^n$

$F^n.K_n^i$ and $P_o^i = {}_o\Sigma^n p^n.K_n^i$. Very similar incompatible element fractionations are generated using an accumulated fractional melting equation (Williams & Gill 1989).

Rare earth elements have the best characterised distribution coefficients of the incompatible elements and so they are probably the most reliably modelled. Variations in highly incompatible elements (such as La and Ce) provide important information on degree of melting whilst less incompatible elements (such as Yb) yield information on source mineralogy. Thus the Ce and Yb variations of the LPTh basanites are modelled in an attempt to constrain both the source mineralogy and degree of melting beneath La Palma. (Ce is used rather than La in order to be consistent with other studies e.g. Hofmann & Feigenson 1983, Feigenson et al. 1983).

Fig. 3.11 shows various melting trajectories calculated from melting equation parameters given in Table 3.4. Since the basanites are somewhat fractionated, in all the plots in Fig. 3.11, calculated melt compositions have both Ce and Yb concentrations increased to account for a nominal 15% olivine fractionation, which affects only absolute abundances and not the relative proportions of the elements nor the melting trajectories. Since the HPTh basanites have been shown to have elevated LREE concentrations due to accumulation of monazite, the melting paths model the compositional variation within the LPTh lavas, which are shown as open squares in Fig. 3.11. Nevertheless, the HPTh and LPTh lavas show similar trends, although the former are more erratic and clearly have higher Ce.

The most significant aspect of the Ce-Yb variation in the basanites is the overall positive correlation (Fig. 3.11). A positive Ce-Yb trend may be generated by fractional crystallisation of the basanite mineral assemblage. However, the five LPTh samples plotted in Fig. 3.11 have Ni contents that vary only from 122-90ppm, which can be accounted for by just 6% fractional crystallisation (of an olivine, clinopyroxene and titanomagnetite assemblage calculated in 3.7.1) between the samples (Fig. 3.7b), and the effect of this 6% fractional crystallisation is indicated in Fig. 3.11a. Three of the LPTh samples, which by themselves still clearly define a positive Ce-Yb trend in fact have identical Ni contents. Furthermore, crystal fractionation cannot explain the variation of highly incompatible element ratios (Fig. 3.10a) that is also evident in these samples, and thus the Ce-Yb variation appears to be primarily due to partial melting processes.

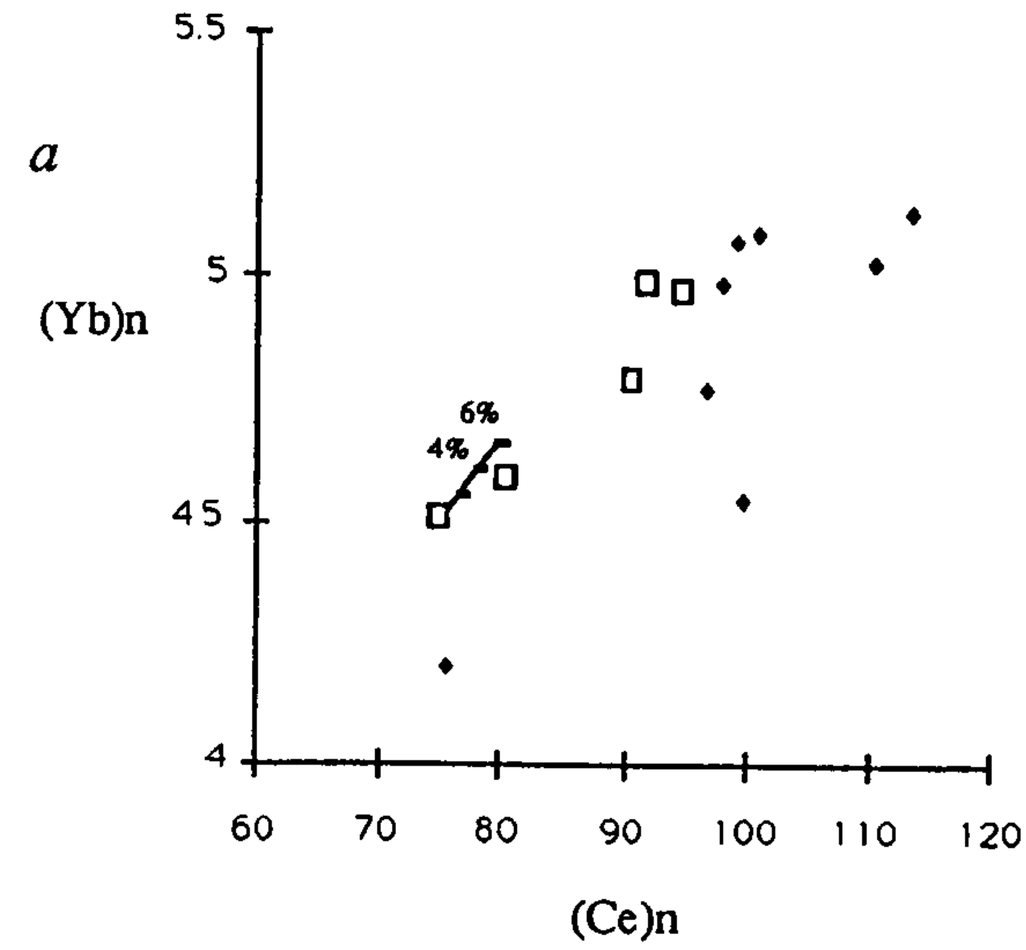

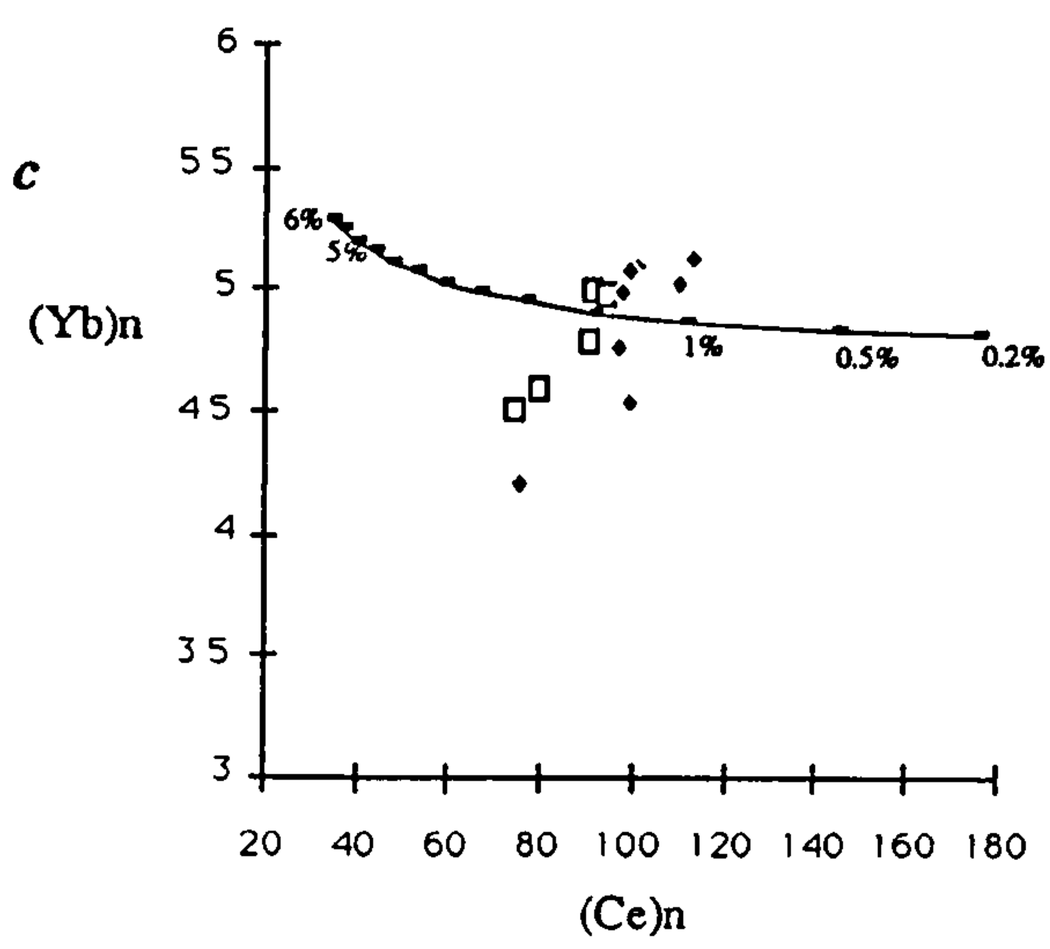

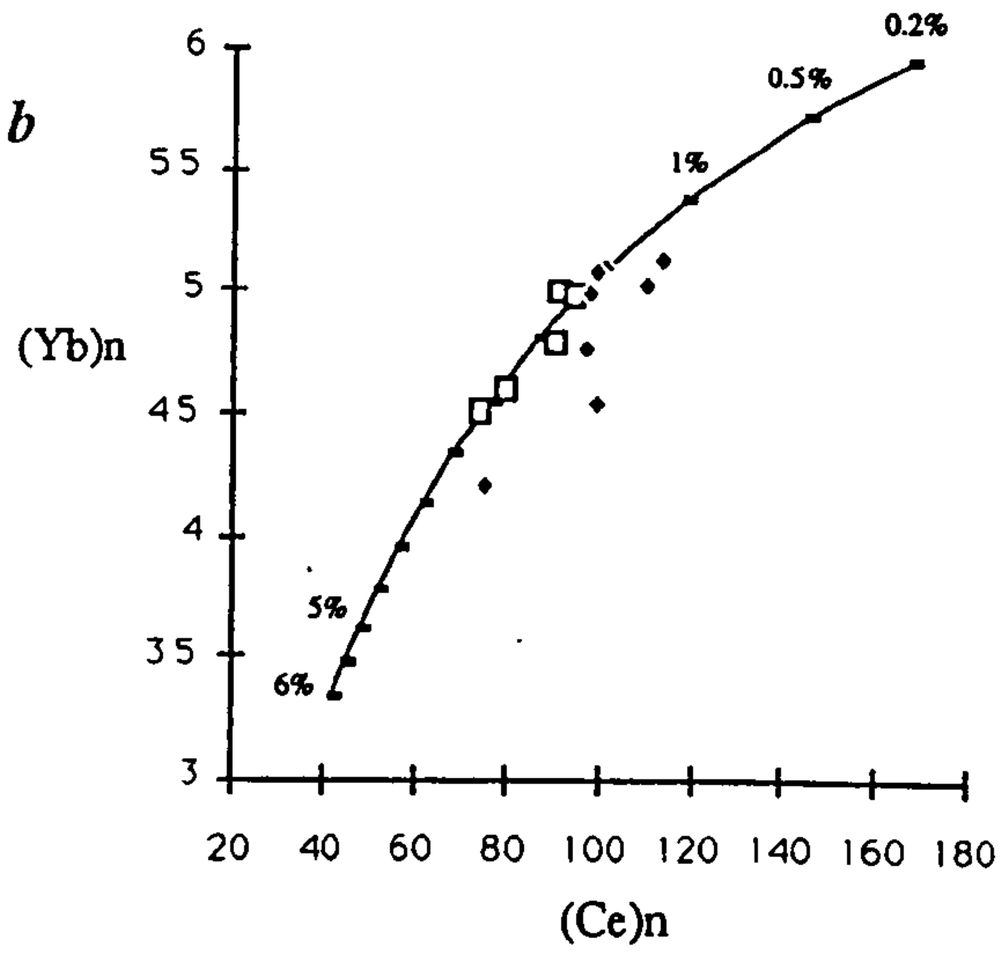

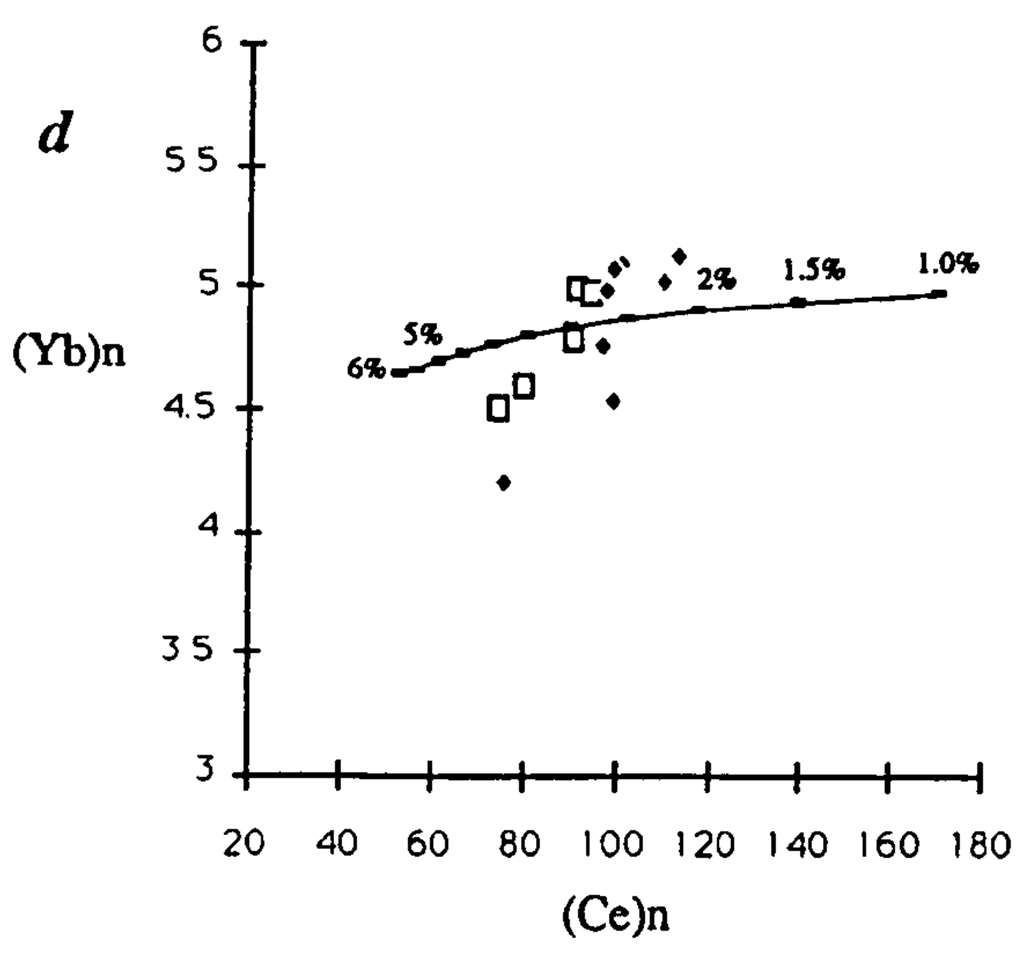

Fig. 3.11 Variation of mantle normalised Ce and Yb contents of the historic basanites. The LPTh basanites are shown as open squares and the HPTh basanites (and 1971 lavas) as filled diamonds. **a)** shows the effect of 6% fractional crystallisation (with ticks at 2% increments) of the mineral assemblage shown in Table 3.3 using the distribution coefficients given in Table 3.4. **b)** shows various degree batch melts, up to a maximum of 6%, from a spinel lherzolite mantle and **c&d)** show various degree batch melts from a garnet bearing source, with different garnet melt norms (tick marks after 0.5% melting, show 0.5% melt intervals). The data used in melting calculations (e.g. mineralogies, partition coefficients, melt norms and source Ce and Yb contents) for the models **b-d)** are given in Table 3.4.

Table 3.4 Partition coefficients and batch melting equation parameters used for modelling Ce and Yb contents for different degree partial melts, illustrated in Figs. 3.11 and 3.12. Batch melting equation parameters are defined in the text.

Partition coefficients

Element	K^{ol}	K^{opx}	K^{cpx}	K^{gnt}	K^{sp}
Ce	0.0005	0.0003	0.098	0.021	0.01
Yb	0.0015	0.049	0.28	4.03	0.01

Batch melting equation parameters

Model	$(C_o)_n^{Ce}$	$(C_o)_n^{Yb}$	F^{ol}	F^{opx}	F^{cpx}	F^{gnt}	F^{sp}	P^{ol}	P^{opx}	P^{cpx}	P^{gnt}	P^{sp}
Fig. 3.11b	2.6	0.3	0.55	0.27	0.15		0.03	0.1	0.13	0.75		0.02
Fig. 3.11c	2	2	0.55	0.26	0.08	0.11		0.05	0.05	0.5	0.4	
Fig. 3.11d	3	2.1	0.55	0.26	0.08	0.11		0.1	0.1	0.78	0.02	
Fig. 3.12	0.6	0.33	0.55	0.27	0.15		0.03	0.1	0.13	0.75		0.02

Melting in the spinel peridotite facies, in which clinopyroxene is the only controlling mineral for melt concentrations of the REE elements, readily produces a positive Ce-Yb trend for different degrees of partial melting, since both elements are incompatible in clinopyroxene. For primitive mantle source concentrations of Yb, melting in the spinel facies results in melt Yb contents that are higher than in the basanites, and for a source with flat primitive mantle normalised REE concentrations, fractionation during melting of a spinel peridotite is not sufficient to produce the highly enriched $(Ce/Yb)_n$ ratios of 17-19 in the basanites, even in limit of the melting equation, where X=0. Consequently a LREE enriched source must be invoked for melting models of spinel peridotite to account for La Palma basanite compositions. 1-2% melting of a source with 0.3x primitive mantle (~1x chondrite) Yb content and $(Ce/Yb)_n$ ~8 (Table 3.4) models the Ce and Yb variations shown by the LPTh basanites quite well (Fig. 3.11b). Such a source composition is similar to, although slightly more LREE enriched than some spinel harzburgites and lherzolites nodules from Salt Lake Crater, Oahu, Hawaii (Frey 1980).

The presence of small amounts of garnet in the source results in greater Ce-Yb fractionation during melting (since Yb is more compatible in a garnet bearing source) and consequently requires a less LREE enriched source for a given degree of melting to produce the high Ce/Yb ratios of the La Palma basanites. Fig. 3.11c shows various degrees of melting of a source with mineral compositions typical of a garnet peridotite (11% garnet) and a flat primitive mantle normalised REE pattern. The trajectory of the melting curve in Fig. 3.11c clearly does not adequately reproduce the positive Ce-Yb trends observed in the LPTh lavas, since the Yb contents of the melts are largely buffered by the presence of garnet. The negative Ce-Yb trend evident at higher degrees of melting in Fig. 3.11c results from increasing incompatibilty of Yb as garnet becomes exhausted, whilst over the same melting interval, Ce, that is concentrated into the melt phase at the onset of melting, is simply diluted. Solely decreasing the amount of garnet present in the source hence only heightens the negative correlation. Decreasing the amount of garnet that enters the melt flattens the melting trend, and for very low garnet melt norms (~5%) a positive Ce-Yb variation is evident at higher degrees of melting, 4-6% (Fig. 3.11d). However, such small garnet melt

norms are improbable, and they would also lead to very high CaO/Al_2O_3 (≥0.9) ratios in the basanites that are not observed (CaO/Al_2O_3 of LPTh basanites range from 0.75-0.84).

Thus from the forward modelling of Ce and Yb contents of the LPTh lavas, melting beneath La Palma appears to be controlled by clinopyroxene, with very little, if any garnet present. This suggests that melting occurs above the depth at which garnet has reacted to produce spinel.

3.7.2 Comparison with other OIB suites

The presence or absence of garnet during melting has been an important and contentious issue in studies of the petrogenesis of OIBs, especially with respect to Hawaiian basalts. Leeman et al. (1980) explained chemical differences between various Hawaiian lavas using a source with residual garnet, but as stressed by Feigenson et al. (1983), these were from averaged compositions of various volcanoes rather than an assessment variation within lavas that could be more reasonably inferred to be derived from a uniform source. Lavas from the 1969-71 eruptions of Mauna Ulu, Kilauea have very constant Yb contents with varying Ce contents (Fig. 3.12a), that strongly suggest a garnet control during melting (Hofmann et al. 1984). However, the source mineralogy responsible for the larger geochemical variations from tholeiites to transitional and alkalic lavas from Kohala, Hawaii, has been the subject of much greater debate (Feigenson et al. 1983, Albarède 1983, Liotard et al. 1986, Lanphere & Frey 1987, Hofmann & Feigenson 1987). Feigenson et al. (1983) concluded that the controlling mineralogy was dominantly and possibly exclusively clinopyroxene: garnet might be present, but there was ambiguity because of the large errors on the inversion of the heavy rare earth element data. The fractionation corrected data for these lavas are shown on a Ce-Yb diagram in Fig. 3.12b. Although the field is quite scattered, which presumably accounts for the propagated uncertainties on inversion, there is, for some of the samples at least, a sense of increasing Ce and Yb.

These data were modelled with the same spinel peridotite source mineralogy and melting norms that were used for the La Palma data (Fig. 3.11b, Table 3.4), although the Kohala lavas are less LREE enriched than the La Palma basanites, and the model require a less LREE enriched source (see Table 3.4). This modelling reproduces the upper band of increasing Ce and Yb quite well, and suggests that the Kohala tholeiites are produced by up

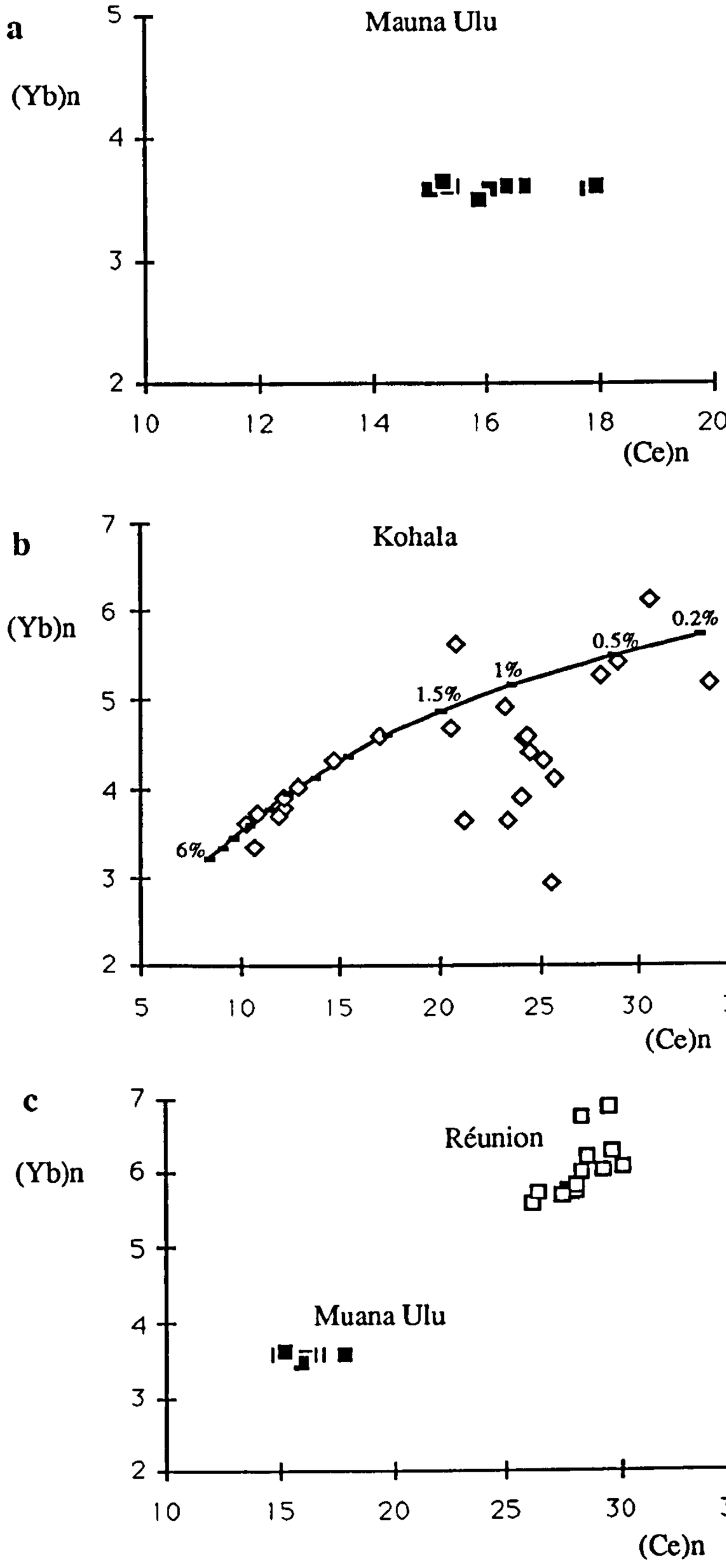

Figure 3.12 Plots of mantle normalised Ce and Yb contents for **a)** Mauna Ulu, Hawaii (Hofmann et al. 1984), Ce and Yb contents are corrected for crystal fractionation **b)** Kohala, Hawaii (Feigenson et al. 1983), Ce and Yb contents are corrected for crystal fractionation. A batch melting trajectory, using the parameters given in Table 3.4, is shown with tick marks at 0.5% melt increments (except for the first increment). **c)** Comparison of data for Mauna Ulu, and data from Réunion (Albarède & Tamagnan 1988). The Réunion data are not corrected for crystal fractionation but all have Ni contents from 70-80ppm.

to 4.5% melting. The higher inferred degrees of melting for the Kohala data, compared to La Palma basanites, are generally consistent with the larger volumes of melt erupted on the Hawaiian Islands and independent estimates, from geophysical constraints, on degrees of melting (Watson & McKenzie 1991). Although the forward modelling techniques used above do not provide necessarily unique solutions, it is encouraging that data for La Palma and Hawaii are reasonably modelled from the same source mineralogy. Some of the data below the clinopyroxene melting control line in Figure 3.12b may be due to garnet control, and/or some source heterogeneity, but as with the La Palma basanites, there appears to be a strong argument for the derivation of some Hawaiian tholeiites from melting of spinel peridotite in the absence of residual garnet.

There are few available data from other ocean islands that can be readily used to further assess mineralogical control during OIB genesis, due to a lack of high quality data sets on closely temporally and spatially related lavas, that from isotopic considerations, may reasonably presumed to be cogenetic. Nevertheless, a recent study of Réunion by Albarède & Tamagnan (1988), shows a suite of historic lavas that clearly show parallel REE profiles (i.e. increasing Yb with increasing Ce), indicative of clinopyroxene control, rather than REE profiles 'anchored' at Yb, that would be expected for sources containing residual garnet. Lavas from Réunion (Albarède & Tamagnan 1988), with Ni contents within the narrow range of 70-80ppm, for which Ce-Yb covariation cannot be attributed to fractional crystallisation, are plotted in Fig. 3.12c, which clearly constrasts the positive Ce-Yb trends for the Réunion lavas with the flat trend from the Muana Ulu data. Additionally, although the lavas of St. Helena (Chaffey et al. 1989) and Society Seamounts (Devey et al. 1990) show some isotopic variation, for lavas within a given unit, with similar isotopic ratios (and Ni contents), the REE profiles are also parallel. Thus for several other OIB suites there also appears to be evidence, from positive Ce-Yb correlations, of melting within the spinel peridotite facies with little or no garnet control.

3.7.3 Comparison with geophysical models

Recent geophysical work has lead to estimates of the depth at which mantle plumes start to melt (McKenzie 1984, McKenzie & Bickle 1988), and hence has implications for the mantle mineralogy that is present during melting. From analysis of topographic and geoid

anomalies over the Cape Verde Islands and Hawaii (Courteney & White 1986, Watson & McKenzie 1991), mantle plumes are modelled to have temperatures 200°C hotter than MORB mantle. McKenzie & Bickle (1988) calculated that 'normal' oceanic crust is the result of adiabatic decompression of mantle with a potential temperature of 1280°C, whilst the thick crust at Iceland is the result of a 1480°C plume upwelling beneath the ridge axis. Volumes of magma production beneath Hawaii have also been calulated to be consistent with a plume with a potential temperature of 1480°C (Wason & McKenzie 1991). Using the parameterisation of mantle solidii from peridotite melting experiments (McKenzie & Bickle 1988), a plume with a potential temperature of 1480°C is thought to start melting at ~120km. Using these temperature and pressure constraints from geophysical work, the stable mineralogy during plume melting may be assessed from experimental work on the pressure and temperature dependance of the garnet to spinel reaction (Nickel 1986). Unfortunately the experiments of Nickel (1986) did not reach the conditions predicted for mantle plumes and so the results must be extrapolated. From these combined constraints however, a mantle plume is expected to start melting at 120km within the garnet stability field, and during upwelling, garnet starts reacting to spinel at 100km and the reaction is complete at 80km (McKenzie & O'Nions, in press).

Using such a framework, McKenzie & O'Nions (in press) have attempted to use REE contents of lavas to deduce the variation of melting with depth. They use a model in which the REE content of a lava represents the depth integrated mean of fractional instantaneous melts from all levels of a melting column. The top of the melting column is taken to be the mechanical boundary layer but the bottom is constrained by the inversion. In inverting the data the degree of melting is varied with depth in the column (although it is constrained to continuously increase towards the top of the column) until a minimum is obtained in the fitting parameters that compare the synthetically generated REE pattern and the real data. The same major element mantle composition is used in all inversions and its mineralogy is calculated as a function of depth in the column as described above (e.g. in plumes, the garnet/spinel transition occurs between 80 and 100km). For inverting OIBs, sources with primitive mantle REE contents are assumed, but if the calculated fit between modelled melt and the data is poor the source REE contents are amended.

Averages of REE concentrations within lava suites are inverted using this technique (McKenzie & O'Nions, in press). The Kohala lavas give acceptable solutions using a source with primitive mantle REE contents, in which melting is dominantly in the transition zone between spinel in and garnet out reactions, i.e. from mineralogies with strong garnet control to mineralogies almost totally clinopyroxene controlled. For more alkalic lavas from Hawaii and from the Society Islands (which are closer in REE profiles to the La Palma basanites) solutions suggest ~1% melting entirely within garnet peridotite facies. The solutions for these LREE enriched alkalic lavas furthermore require ~2x primitive mantle source enrichment of *all* REE concentrations (i.e. *not* LREE enriched).

These solutions clearly predict a different residual mantle mineralogy and REE profiles to those inferred for the La Palma basanites in this study. However, one of the main drawbacks in the inversion technique of McKenzie & O'Nions (in press) is that lava analyses are averaged and so the information gained on melting processes from *trends* in lava compositions is lost. As is clear from the simple forward modelling in Fig. 3.11c&d, melting of a garnet bearing source can be constrained to fit a single data *point* and could thus be modelled to fit a single, average composition of the La Palma basanites, but cannot explain the increase in Yb with Ce, over the whole suite suite of cogenetic lavas. The crux of the conflicting conclusions as to the role of garnet in the genesis of highly enriched LREE lavas from McKenzie & O'Nions (in press) and this study is that, by starting with a source with a flat REE profile, the model of McKenzie & O'Nions (in press) can produce melts with suitable LREE enrichment only by melting in the presence of garnet, whilst this study invokes a LREE enriched source, which can melt without residual garnet to produce the melts with highly LREE enriched profiles of the La Palma basanites.

The crucial difference in the modelling techniques is that McKenzie & O'Nions (in press) assume garnet to be present in the plume at depths greater than 80km from geophysical considerations, whilst this study assesses the mineralogy solely from the geochemical trends in the data. Perhaps there is enough uncertainty in the extrapolations of the experiments of Nickel (1986) and in the thermal structure of plumes, for the geophysical data to be consistent with the strong geochemical evidence of this section, but this question clearly requires further detailed work.

3.8 U-Th disequilibrium constraints on mixing and melting processes

Fig. 3.13a shows an equiline diagram (Allègre 1968) displaying U-Th disequilibrium data for some of the historic basanites of La Palma, together with a single analysis for a phonolitic enclave found within the 1712 Jedey flow. Fig. 3.13b compares these data with U-Th disequilibrium data from other ocean island basalts. The La Palma lavas show marked disequilibrium with $(^{238}U/^{230}Th)_a$ from 0.83-0.73. Disequilibrium is believed to be produced during melting and for ocean island and mid-ocean ridge basalts it results in preferential enrichment in Th relative to U (Allègre and Condomines 1982), as is observed in La Palma. A few islands, such as Hawaii erupt lavas that show no disequilibrium.

3.8.1 Interpretation of Disequilibrium Data

Conventionally it has been thought that $^{230}Th/^{232}Th$ ratios are not fractionated during melting (viz. Sr, Nd and Pb isotope ratios), and that the effect of melting can be represented as a horizontal vector on the equiline diagram (Fig. 3.14a). However this assumes an instantaneous melting process which, however, is not consistent with more recent dynamic melting models developed for geophysical reasons (McKenzie 1984), and to explain observed geochemical variations (Langmuir et al. 1977, Wood 1980, Elliott et al. 1991). In a dynamic melting model, a mantle segment passes through a melting column from which melt is continuously extracted. As a given mantle segment is depleted in incompatible elements during melting, the residue is consequently relatively enriched in U with respect to Th, in OIB and MORB melting regimes. Plume upwelling rates are of the order of tens of km/Ma (Davies 1990) and consequently a mantle segment has a residence time of several million years within typical melting columns of 40-120km (McKenzie & Bickle 1988). Over such timescales, excess U in the upwelling matrix will 'in-grow' ^{230}Th in an attempt to restablish secular equilibrium. However since melting occurs continuously throughout upwelling, 'in-grown' ^{230}Th will be preferentially partitioned into the melt phase, preserving excess U disequilibrium in the matrix and resulting in an excess $^{230}Th/^{232}Th$ in the summed

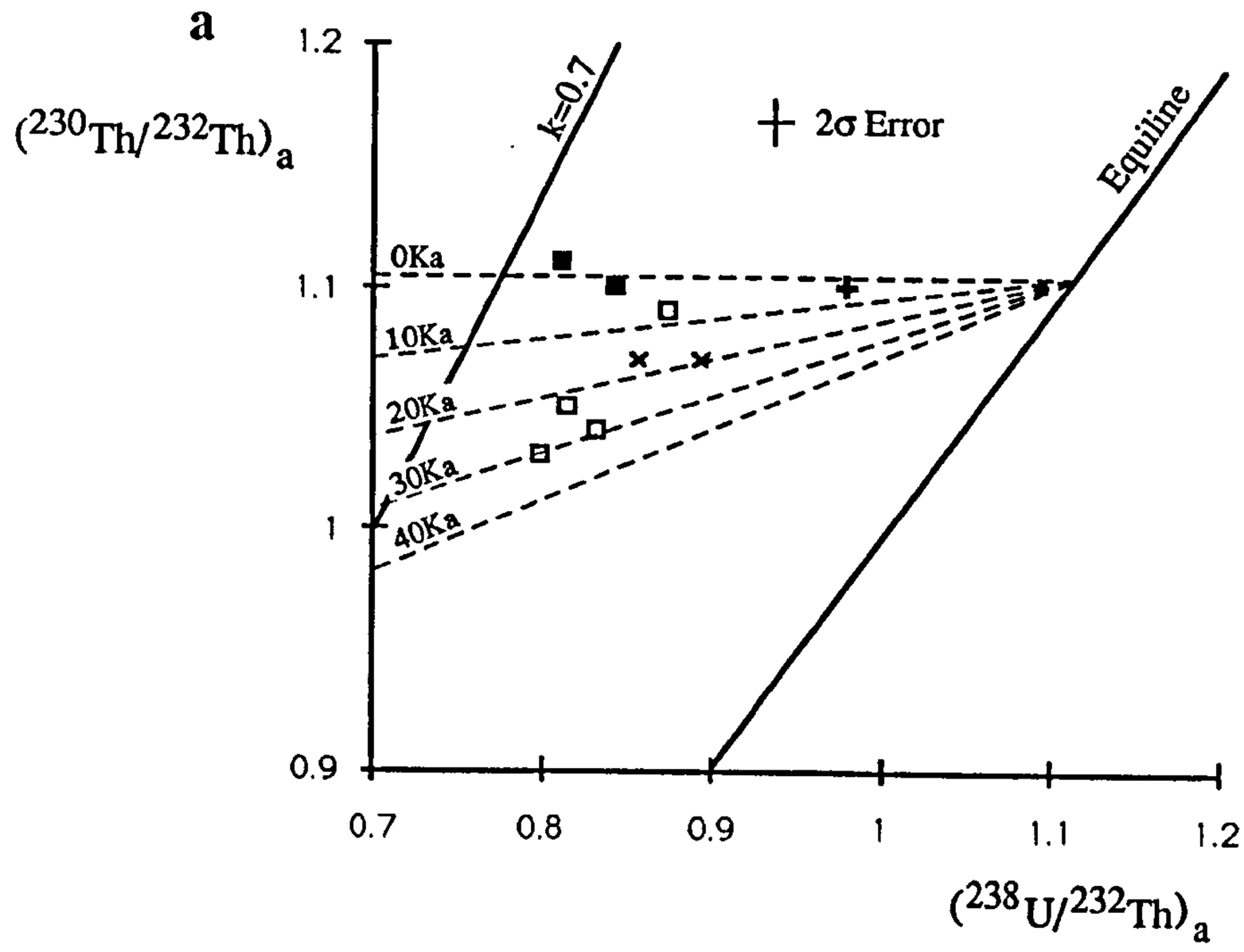

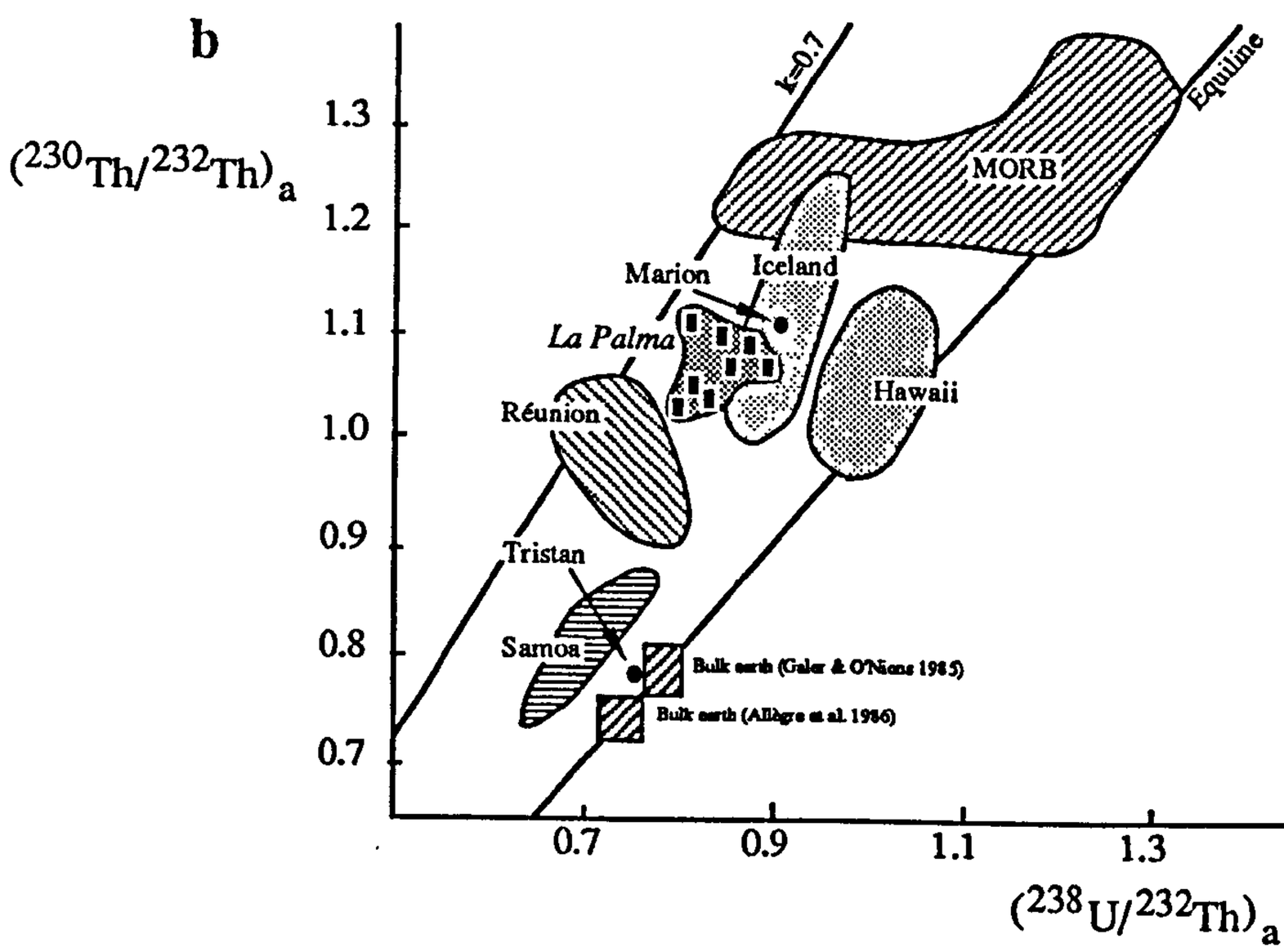

Figure 3.13 Equiline diagrams (Allègre 1968) for **a)** the La Palma samples, symbols for the historic basanites as in Fig. 3.8, and additionally the vertical cross shows the phonolitic enclave in the 1712 basanite. Isochrons, dashed lines, are shown for a samples with initial $(^{230}Th/^{232}Th)_a = 1.1$. $k=(^{238}U/^{230}Th)_a$ and for samples in secular equilibrium, k=1 and such samples lie on the equiline. **b)** the La Palma basanites (filled squares) together with data for MORB and other OIBs (Figure after Condomines et al. 1988, but including additional MORB data from Rubin & McDougall (1988), Ben Othman et al. (1990) and Goldstein et al. (1989).

instantaneous melt compositions erupted from the column. This mechanism for producing disequilibrium during melting (McKenzie 1985) is important in explaining $(^{238}U/^{230}Th)_a<1$ found in many MORBs (Condomines at al 1981, Newman et al. 1983, Rubin & McDougall 1988, Goldstein et al. 1989), because MORBs are thought to represent some 8-15% melts (Klein & Langmuir 1987, McKenzie & Bickle 1988), and such high degree melts would not be expected to have U/Th ratios fractionated relative to source values, as implied by a horizontal vector in Fig 3.14a, but they can show ^{230}Th excesses due to ingrowth during dynamic melting.

Interpreting U-Th disequilibrium data is strongly dependent on the process which is thought to have been responsible for the disequilibrium. If $^{230}Th/^{232}Th$ is unfractionated by the melting process, as envisaged in conventional models, the $^{238}U/^{232}Th$ ratio for the source may be calculated by assuming that the unmelted source was in secular equilibrium, i.e. $(^{230}Th/^{232}Th)_a=(^{238}U/^{232}Th)_a$, and the degree of disequilibrium, $(^{238}U/^{230}Th)_a$, then gives the elemental U/Th fractionation during melting, from which other incompatible element fractionations may be inferred. This is potentially a very powerful tool in geochemistry. However, in a dynamic model, since $(^{230}Th/^{232}Th)_a$ and consequently $(^{230}Th/^{238}U)_a$ are a function of upwelling rates, length, porosity and melt distribution of the melting column (McKenzie 1985, Williams & Gill 1989), disequilibrium data provides constraints on different aspects of magma genesis. The two endmember models that account for U-Th disequilibrium in mantle melts are shown diagramatically on Fig. 3.14. For large degrees of melting, in slow upwelling systems, U/Th elemental ratios of the *depth averaged* melts are unfractionated from source values (or relatively unfractionated for slightly smaller degrees of melting) whilst $^{230}Th/^{232}Th$ ratios increase by in-growth, resulting in a vertical vector of displacement on the equiline diagram (Fig. 3.14b). For small degrees of melting, in fast upwelling sytems the U/Th elemental ratios in the melts are fractionated and there is little time for $^{230}Th/^{232}Th$ in-growth, resulting in a horizontal vector of displacement, as envisaged in traditional models (Fig. 3.14a). In many systems, the vector of displacement of melt from source is likely to be intermediate between these extremes.

Assuming that mantle plumes have a near uniform temperature and similar anhydrous compositions (McKenzie and Bickle 1988, Sleep 1990, Davies 1990), they should intersect

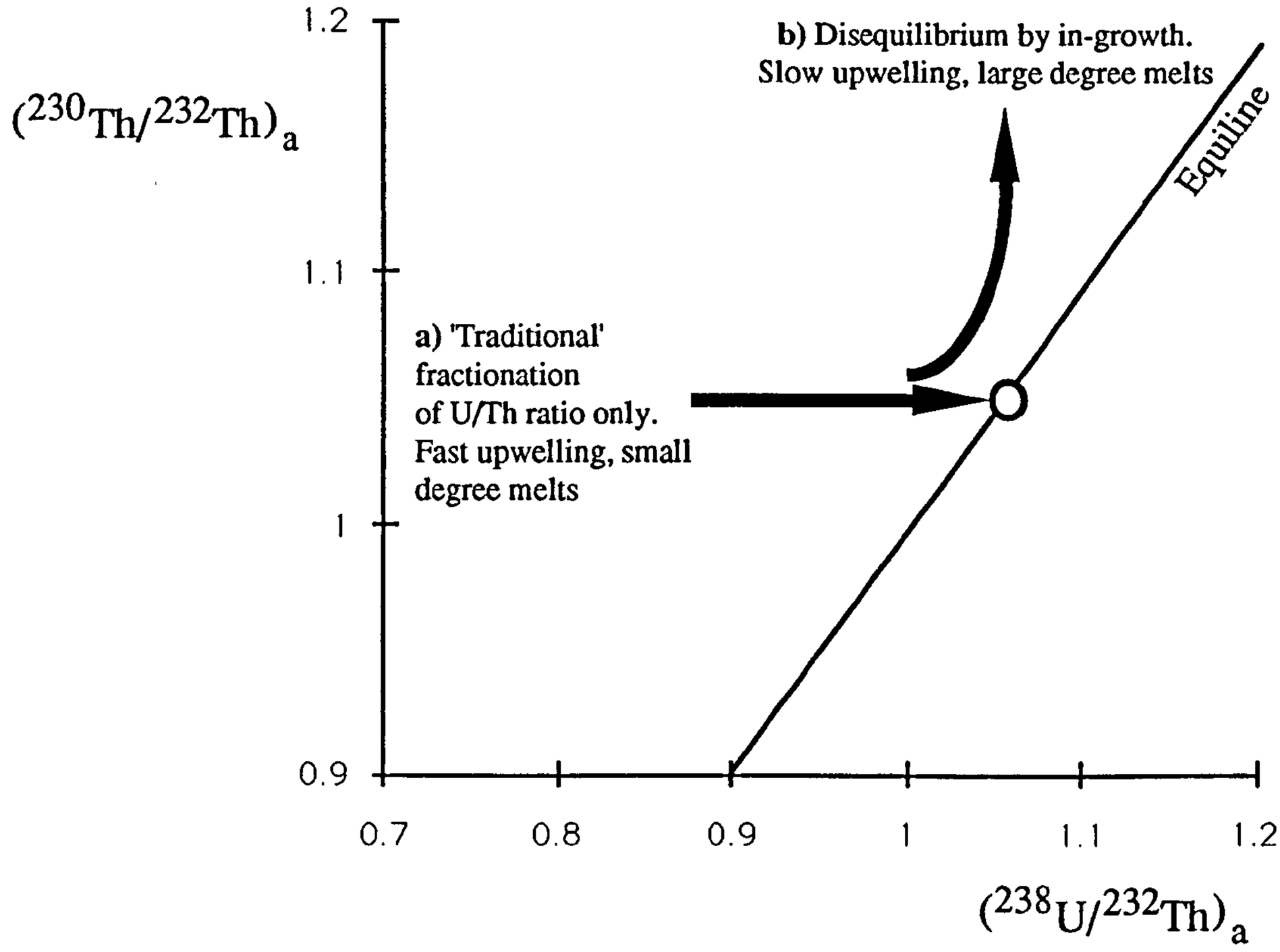

Figure 3.14 U/Th fractionation expected from melting in which **a)** no melt segregation occurs before melting is complete and **b)** dynamic melting occurs. Trajectories represent disequilibrium produced by different degrees of melting for each melt process, with arrows at the end representing the largest degree of melting.

their solidi at similar depths and consequently the length of the melting column is determined by the thickness of the overlying lithosphere (more strictly the depth to the mechanical boundary layer), which physically limits the height to which the plume may upwell. The mechanical boundary layer of oceanic lithosphere thickens with age up to some 80Ma, but subsequently, the onset of thermal instabilities result in small scale convection that prevents further thickening with age (Houseman & McKenzie 1984). La Palma lies on thick, 155Ma oceanic lithosphere and so it is likely to have a minimum melting column length for ocean islands. This is consistent with the small degrees of melting inferred from incompatible element variation, and since Fig. 3.10a shows that even highly incompatible elements are fractionated during melting, U-Th disequilibrium may be best interpreted in terms of the conventional models.

3.8.2 U/Th Disequilibrium Constraints on Magmatic Evolution after Melt Segregation

The historic basanites of La Palma exhibit significant variation in $(^{230}Th/^{232}Th)_a$ (Fig. 3.13a), which may imply a variable component of dynamic ^{230}Th in-growth, due to different degrees of melting, contrary to the arguments of the last section. However, variation in $(^{230}Th/^{232}Th)_a$ may also be due to decay of excess ^{230}Th after melt segregation (Condomines et al. 1982). It is noticeable that the basanites with lower $(^{230}Th/^{232}Th)_a$ are the HPTh basanites, in which anomalously high Th, U and LREE contents have been interpreted in terms of accumulation of monazite from coexisting evolved magma chambers, and consequently a significant proportion of their Th (~25-30%) is not related to melting processes. Rather the $(^{230}Th/^{232}Th)_a$ ratios of the HPTh lavas will have been strongly affected by the $(^{230}Th/^{232}Th)_a$ of the contaminating monazite crystals. It is argued that the monazite crystals settle from a phonolitic upper layer of a zoned magma chamber, and therefore their $(^{230}Th/^{232}Th)_a$ ratios will reflect the time taken for this upper layer to evolve.

Fig. 3.13a shows U-Th disequilibrium data for both an LPTh basanite and entrained phonolitic enclave. The phonolite has a higher U/Th ratio than the basanite, which is consistent with the higher U/Th ratios of the older phonolites analysed, but has identical $(^{230}Th/^{232}Th)_a$ to the basanite. This implies rapid differentiation of the evolved magma (<5000a) from the basanite, and it is clearly inconsistent with entrainment of a phonolite

from a long lived magma chamber. However, Kaiser & Schmincke (1987) presented a detailed study of the 1949 eruption, in which an initial tephritic lava was followed by eruption of a basanite. Fractionation calculations using observed phases are compatible with derivation of the tephrite from the basanite, and they argue for differentiation in a magma conduit, presumably at shallow level. There is a compositional gap between the two magma compositions, and the tephrite is thought to evolve by a compositional convection as proposed by Huppert & Sparks (1984, 1986), which can be a very rapid, as suggested by the U-Th disequilibrium systematics of the phonolitic enclave and its host basanite in this study.

However such shallow level crystallisation may not be representative of the main fractionation process that results in none of the basanites having primary Ni contents or Mg#, since although all basanites record some fractionation, many also contain nodules, both cumulates and presumed fragments of oceanic lithospheric mantle. During stagnation and fractionation, such nodules are expected to settle out (Clague & Dalrymple 1987), and this implies that these nodules have been entrained *after* the main episode of crystal fractionation for the basanites. The presence of mantle nodules therefore suggests that generally such fractionation must have been at depth, within the mantle, rather than at shallow crustal levels. This is also consistent with the presence of olivine and clinopyroxene, but no plagioclase phenocrysts in the basanites, that suggests fractionation depths >4kbar (Fisk et al. 1988). During the alkalic post-shield phase of volcanism in the Hawaiian Islands, the composition of CO_2 inclusions in dunitic nodules suggests depths, and hence entrainment depths of >15km (Roedder 1965) and by inference, magma chambers deeper than this. The range of nodules found in lavas of the alkalic post-shield phase on Hawaii (Jackson 1968) are similar to those found in the historic basanites of La Palma, and hence La Palma may be in a similar phase of magmatic evolution.

Deep magma chambers are likely to have significant lifespans due to elevated ambient temperatures and continual reinjection of hot, basic magma to the base of the chamber. Clearly the basanitic melts must be tapped and erupted from the magma chamber, but due to higher viscosities, the more evolved cap of the chamber may stagnate at depth, and indeed there are no extensive eruptions of evolved compositions on La Palma. The age

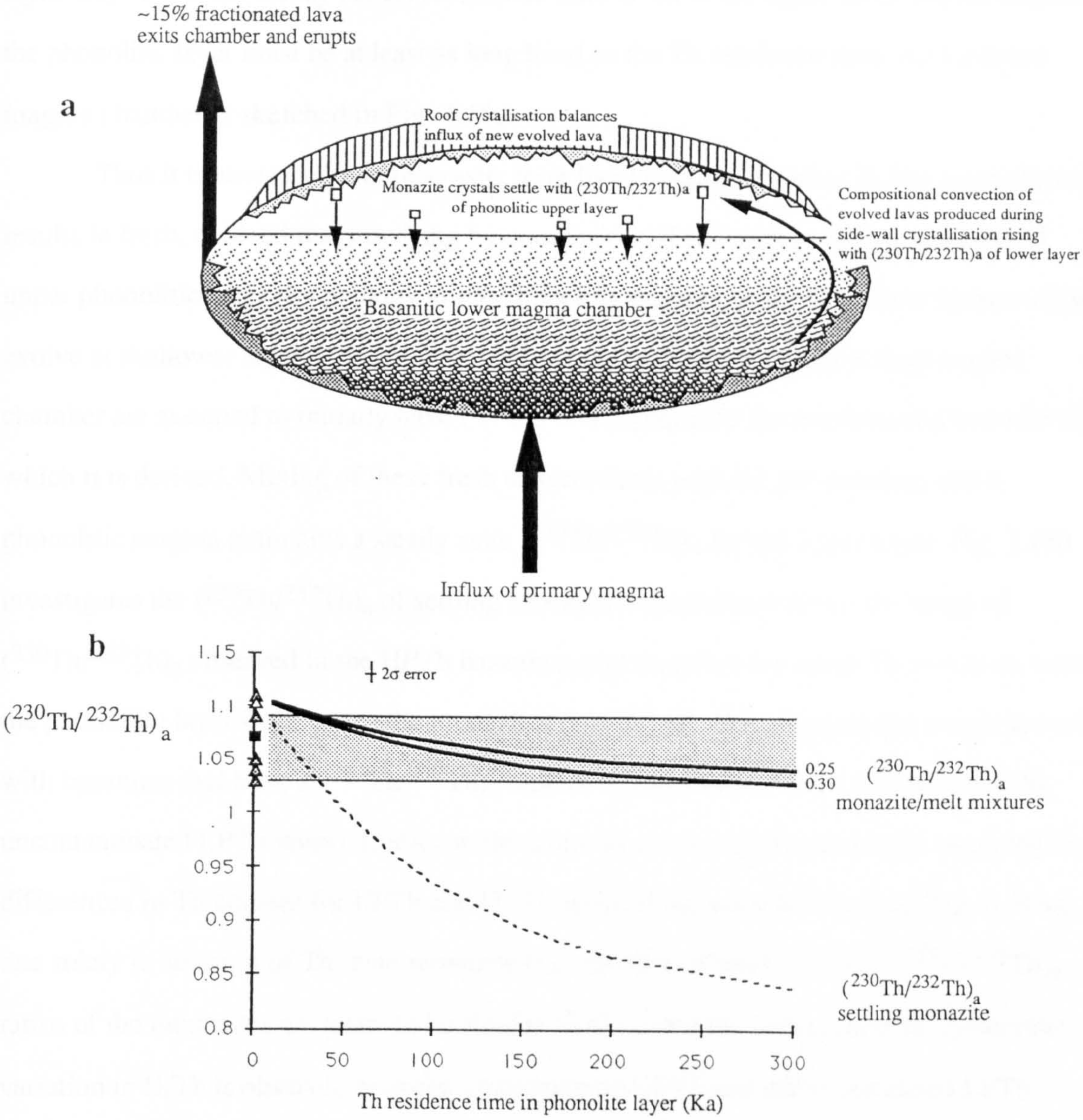

Figure 3.15 a) An idealised magma chamber to account for $(^{230}Th/^{232}Th)_a$ variations in the La Palma basanites. Primitive, dense MgO rich magma feeds the bottom of the magma chamber and fractionates, producing a layer of less dense basanite above it that is tapped and erupted. The upper portion of the chamber is fed by compositional convection from the products of sidewall crystallisation in the lower magma chamber and initially have $(^{230}Th/^{232}Th)_a$ ratios the same as the fractionating basanite. During the residence of Th in the untapped phonolitic upper layer, $(^{230}Th/^{232}Th)_a$ ratios will decay and the mean residence time will be reflected in the $(^{230}Th/^{232}Th)_a$ ratios of monazites that crystallise and settle from the phonolite. The settling monazites dissolve in the upper basanite layer, producing HPTh basanites, which are tapped and erupted with $(^{230}Th/^{232}Th)_a$ ratios that represent a mixture of primitive basanite and monazite $(^{230}Th/^{232}Th)_a$ ratios. **b)** A quantitative assessment of Th residence times in a phonolitic layer of a zoned magma chamber, such as depicted in **a)**. The shaded field represents the range in $(^{230}Th/^{232}Th)_a$ ratios measured in the HPTh basanites, which are shown together with other historic basanites on the vertical axis (open triangles, LPTh basanites, filled squares, 1971 basanites, and shaded triangles, HPTh basanites). The solid lines show the $(^{230}Th/^{232}Th)_a$ of mixtures of LPTh lavas with monazites, in which the monazite contributes 25&30% respectively of Th in resulting the HPTh lava.

of such a cap will depend the relative rates of addition of new magma compared with the rates of crystallisation. The $(^{230}Th/^{232}Th)_a$ of monazite that crystalises from this phonolitic layer may reflect the steady state(?) residence time of Th in the upper layer and consequently, the phonolitic layer must be at least as long lived as the Th residence time. An idealised magma chamber is sketched in Fig. 3.15a.

Thus it is envisaged that in a deep, long lived magma chamber, in situ crystallisation results in fresh, evolved magma rising by compositional convection into an established upper phonolitic layer. By analogy to the phonolitic enclave in the 1712 flow (presumed to evolve at shallower levels), the evolved melts rising to form the cap of a deep magma chamber are assumed to initially have $(^{230}Th/^{232}Th)_a$ equal to the fractionating basanite from which it is derived. Mixing of these fresh differentiates with the pre-existing, older phonolitic magma maintains a steady state $(^{230}Th/^{232}Th)_a$ for the upper layer. Fig. 3.15b investigates the $(^{230}Th/^{232}Th)_a$ of settling monazites needed to produce the range of $(^{230}Th/^{232}Th)_a$ observed in the HPTh basanites, and therefore the mean Th residence time in the phonolitic layer from which the monazites crystallised. This assumes the monazites mix with basanites that have a $(^{230}Th/^{232}Th)_a$ ratio of 1.1±0.1 (taken from the values of the uncontaminated LPTh lavas). Limits on the amounts of mixing are calculated assuming that differences in Th content for LPTh and HPTh lavas of the same Rb content (Fig. 3.8) are due solely to addition of Th from monazite (i.e. 25-30% of total Th). The $(^{238}U/^{232}Th)_a$ ratios of the monazites are taken to be similar (0.82) to the basanites, since no systematic variation in U/Th is observed between contaminated HPTh and uncontaminated LPTh basanites (Fig. 3.9b). A wide range of residence times are required to explain the full range in $(^{230}Th/^{232}Th)_a$ of the HPTh basanites, which suggests the presence of a variety of different sized deep magma chambers or magma chambers in different states of evolution, rather than a single, large, well stirred chamber that would result in Th contaminants showing uniform Th residence times in the phonolitic layer. However, three of the samples do need a magma chamber with a long lived phonolitic layer (>200Ka). This represents a *minimum* model age for the life span of the phonolite layer and hence the magma chamber as a whole. In comparison, Halliday et al. (1989) have argued that large, zoned silicic magma chambers have existed over periods of millions of years. The calculations above however,

whilst requiring a fairly long lived system do not put strong constraints on the temporal evolution of deep magma chambers because of the large uncertainties, and approximations in both the model and monazite composition.

An alternative explanation for the variation in $(^{230}Th/^{232}Th)_a$ could be that the basanites themselves stagnate at depth for different lengths of time before eruption. Fig. 3.13a shows isochrons through the data set indicating that in this model basanitic magmas show differences of ~30,000a in their transit times to the surface. This model in itself does not account for the HPTh lavas showing lower $(^{230}Th/^{232}Th)_a$, but it might be argued that longer stagnation periods enable a magma batch to establish a phonolitic cap, and consequently become contaminated by crystal settling from this layer.

It is difficult to chose between models because of a large number of potential variables, a small number of samples, additional primary compositional differences due to differences in degree of partial melting and relatively small differences in $(^{230}Th/^{232}Th)_a$. However the association of lower $(^{230}Th/^{232}Th)_a$ with the HPTh basanites argues for stagnation of segregated melts at depth beneath La Palma, for periods of at least tens of thousands of years.

3.8.3 U/Th Disequilibrium Constraints on Partial Melting

Disequilibrium shown by the LPTh lavas is assumed to have been unaffected by magma transit to the surface and can thus used be to constrain degrees of melting. It is further assumed that no $(^{230}Th/^{232}Th)_a$ fractionation occurs during partial melting (as envisaged by the conventional U-Th disequilibrium model), and that consequently the degree of disequilibrium records the absolute incompatible element fractionation between source and melt :

$$(^{230}Th/^{232}Th)_a^{liquid} = (^{238}U/^{232}Th)_a^{source} \qquad (2)$$

$$(^{230}Th/^{238}U)_a^{liquid} = \frac{(^{230}Th/^{232}Th)_a^{liquid}}{(^{238}U/^{232}Th)_a^{liquid}} = \frac{(C_U^{source}/C_U^{liquid})_a}{(C_{Th}^{source}/C_{Th}^{liquid})_a} \qquad (3)$$

$$(C_U^{source}/C_U^{liquid})_a = (C_U^{source}/C_U^{liquid}) = D_o^U + X(1-P^U) \qquad (4)$$

$$(C_{Th}^{source}/C_{Th}^{liquid})_a = (C_{Th}^{source}/C_{Th}^{liquid}) = D_o^{Th}+X(1-P^{Th}) \qquad (5)$$

$$\text{Hence} \qquad (^{230}Th/^{238}U)_a^{liquid} = \frac{D_o^{U}+X(1-P^{U})}{D_o^{Th}+X(1-P^{Th})} \qquad (6)$$

$$X = \frac{D_o^{U} - D_o^{Th}.(^{230}Th/^{238}U)_a^{liquid}}{(^{230}Th/^{238}U)_a^{liquid}.(1-P^{Th}) - (1-P^{U})} \qquad (7)$$

Consequently no source U and Th concentrations need to be inferred, unlike the forward modelling approach used for the rare earth elements. However, a knowledge of partition coefficients is required and these vary widely for U and Th, since they are very small and difficult to determine accurately. Partition coefficients used here are from Meijer et al. (1990), in which previous data are assessed, together with their own results, to derive preferred values of K_{cpx}^{Th} =0.01 and K_{cpx}^{U}=0.02, and $K_{opx}^{Th}/K_{cpx}^{Th}$=0.25 and K_{opx}^{U}/K_{cpx}^{U}=0.05. Degrees of melting are calculated for the two LPTh basanites that were analysed for $(^{230}Th/^{232}Th)_a$, using the same source mineralogy and melt norms as those used for the forward modelling in Fig. 3.11b. Results of 0.3-0.4% partial melting are obtained, which are somewhat smaller than the values of 1-2% melting suggested from REE modelling (Fig. 3.13b). The two LPTh samples with disequilibrium data are the two most incompatible element rich LPTh lavas, and therefore represent the lowest degrees of melting for the LPTh group as a whole, although even considering this, the two approaches do not give coincident results, which is perhaps not surprising given the large uncertainties, particularly in the U & Th distribution coefficients. However, both results stress that the La Palma basanites are small degree melts, somewhere between 0.3 and 2%.

Since the melt fractionation process that results in U-Th disequilibrium must be recent (<350ka), by inference, the other elemental fractionations observed in the basanites are also a result of the melting event, rather than recent (i.e.between ~500-0.5Ma) source enrichment processes.

3.9 Source Characteristics of the Historic Basanites

The composition of asthenospheric mantle sources provides important constraints on the differentiation, enrichment and recycling processes experienced by the convecting mantle. Since radiogenic isotopic ratios are unfractionated on melting, isotopic studies have been important in inferring source composition of OIBs (e.g. O'Nions et al. 1977, Hawkesworth et al. 1979, White and Hofmann 1982, Zindler & Hart 1986). However radiogenic isotope ratios reflect only the time-intergrated parent daughter ratios and a full range of incompatible element concentrations give additional constraints on the processes that have resulted in the mantle composition prior to melting (Weaver 1991). Incompatible element ratios *may* be fractionated on melting and not represent source ratios, but the *range* of compositions produced by partial melting in the cogenetic La Palma basanites enables inversion of highly incompatible element data to yield information on source concentrations. This section assesses information on source characteristics reflected in both incompatible element ratios and radiogenic isotope ratios and their implication for the evolution of the La Palma mantle source.

3.9.1 Incompatible element characteristics of the La Palma source

Fig. 3.16a shows a primitive mantle normalised plot of incompatible elements for the LPTh basanites. All lavas display significant negative anomalies for potassium and rubidium. The previous sections have shown that the basanites are small (0.3-2%) degree melts that fractionate incompatible element ratios on melting, and so it is important to establish whether these anomalies are source features or the result of the melting process. Fig. 3.10 shows that Rb is the *most incompatible* element during melting (since all Rb/C_i ratios plotted against Rb have positive slopes) and therefore is not buffered relative to other incompatible elements, as would be expected if the low Rb concentrations were produced during this, most recent, melting event, and likewise K does not seem to vary less with respect to other incompatible elements (e.g. with Rb in Fig. 3.8b). This strongly suggests that the negative Rb and K anomalies observed in Fig. 3.16a are source features, but this can be tested more quantitatively using the inversion technique of Hofmann & Feigenson 1983. Manipulation of the batch melting equation (1), leads to the expression in equation 8,

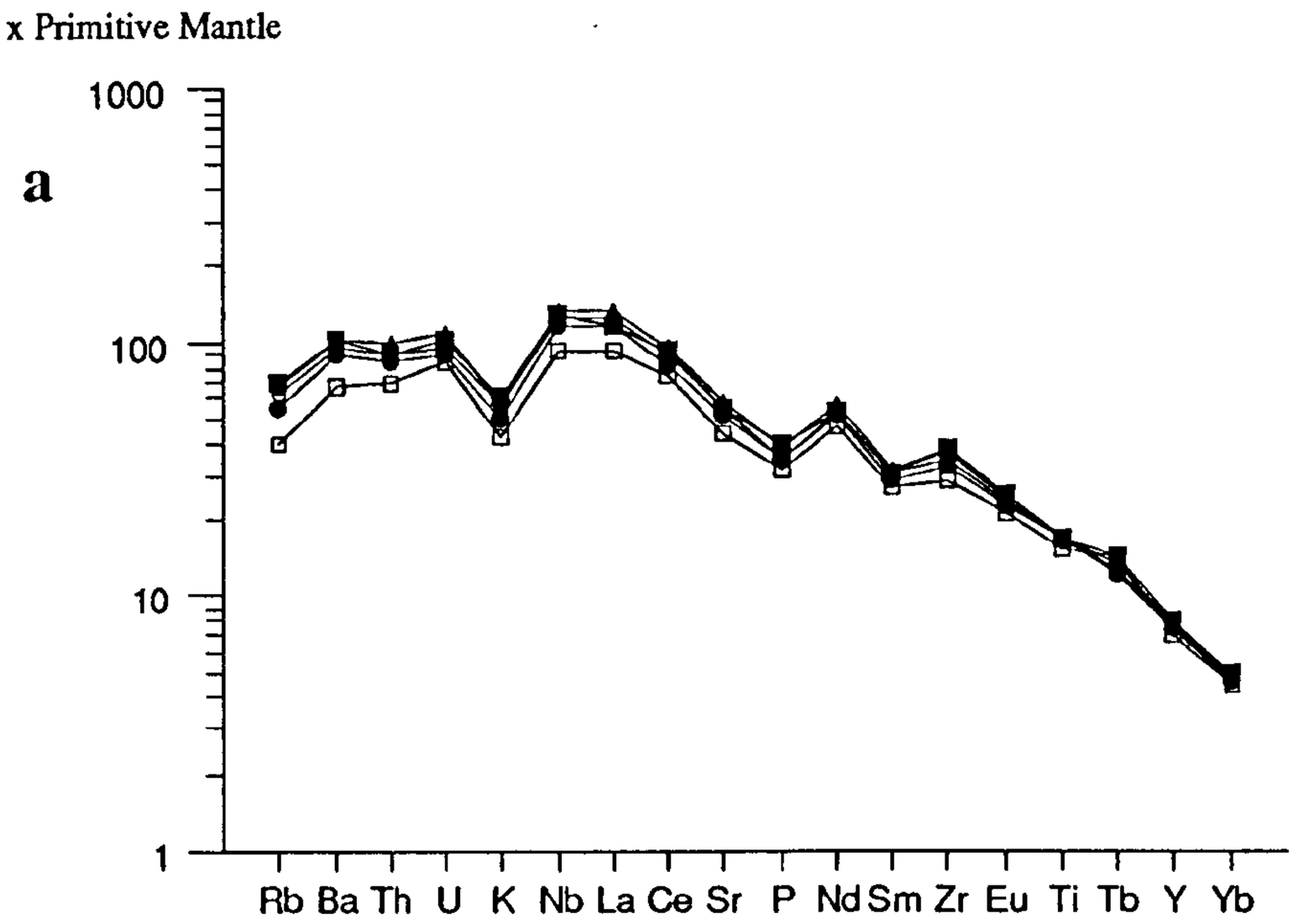

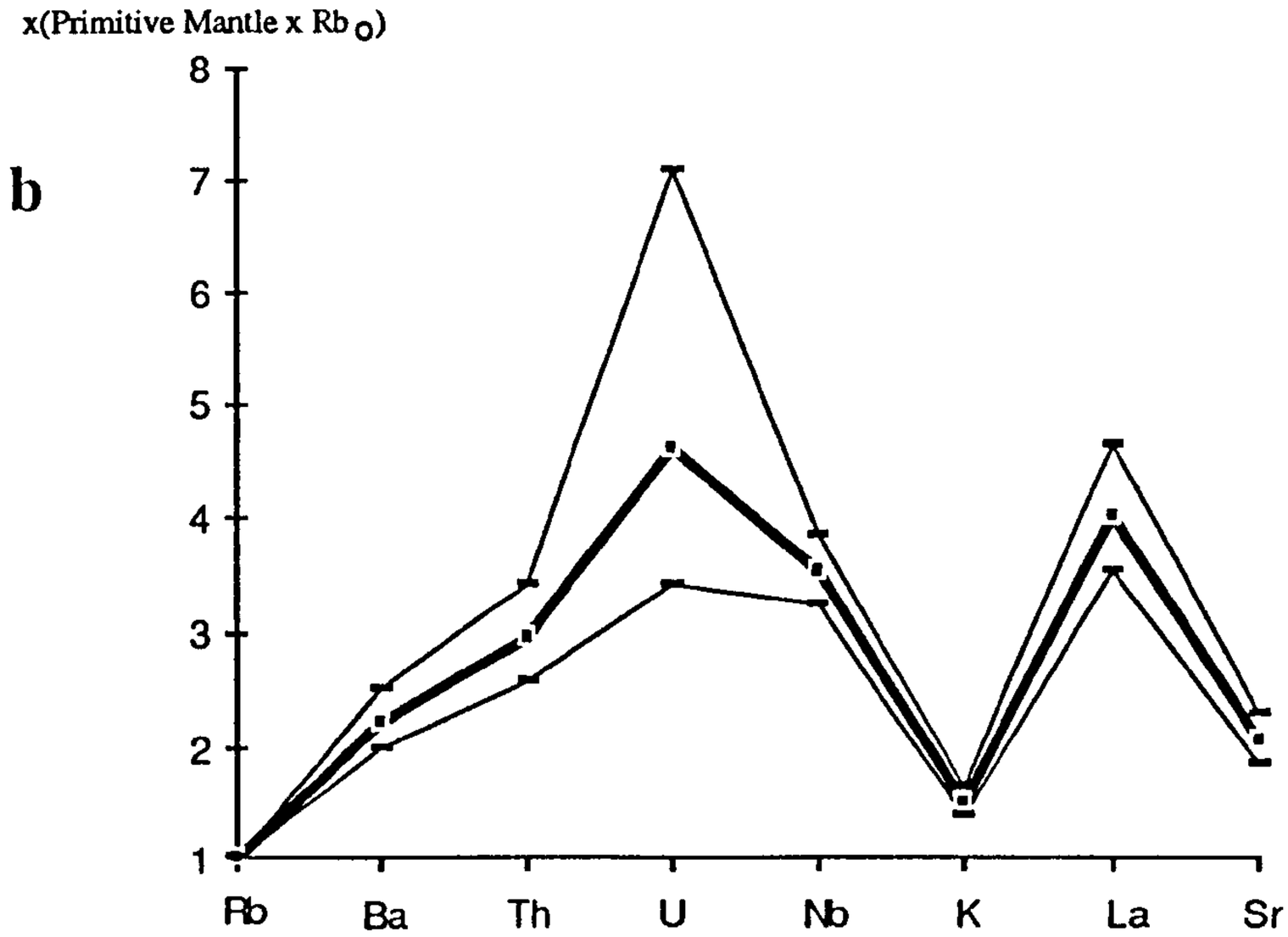

Figure 3.16 a) Incompatible element contents of the LPTh lavas normalised to primitive mantle values. **b)** Incompatible element contents of the mantle source of the historic basanites, inferred from inversion of data from the LPTh basanites. Concentrations are normalised to primitive mantle values *and* to the Rb concentration of the mantle source. Errors shown are 1σ uncertainties from the intercept values calculated by regressing data from plots such as Fig. 3.10a.

$$I^i = \frac{C_o^H}{C_o^i}.(1-P^i) \qquad (8)$$

where C_o^H is the source concentration of the most incompatible element in the lava suite (Rb in this study), which is assumed to be completely incompatible ($D^{Rb}=0$, $P^{Rb}=0$). C_o^i is the source concentration of an incompatible element i, P^i is the bulk distribution coefficient of the melt norm for element i (as in equation 1), and I^i is the intercept of the straight line defined in a plot of (C^H/C^i) against C^H (e.g. Fig. 3.10a) for the lava suite. This model assumes constant P^i and hence a constant major element composition for all primary melts. The La Palma basanites show little major element variation, and as small degree melts they are quite likely to approximate to invariant melts. It is argued by Hofmann & Feigenson (1983) that if a data set define good straight lines that the assumptions of the invariant batch melting model are valid, and indeed the LPTh basanites meet this requirement.

As discussed earlier, this inversion approach was not used for rare earth element modelling because of the dependence on the poorly independently constrained P^i for less incompatible elements (MREE and HREE), but for highly incompatible elements uncertainties in melt norms are much less significant since distribution coefficients become very small, and for highly incompatible elements $(1-P^i)\sim1$ (Ormerod et al. in press). Thus the source ratios of highly incompatible elements may be approximated by:

$$\frac{C_o^1}{C_o^2} \sim \frac{I^2}{I^1} \qquad (9) \qquad \text{and} \quad \frac{C_o^i}{C_o^{Rb}} = \frac{1}{I^i} \qquad (10)$$

Table 3.5 shows I^i values for the highly incompatible elements from the LPTh basanites, derived from plots similar to Fig. 3.10, and regressed using the method of York (1969) to obtain 1 σ errors on the intercepts (using the analytical uncertainties for the data points from values reported in Table 3.1). Rb concentrations were nominally corrected for 15% olivine fractionation in these calculations. The inverse each of these intercepts gives the primitive mantle normalised source concentration of an incompatible element relative to Rb (equation 10), and these are shown, with associated errors, in Fig. 3.16b, in which the comparative *source* depletion in Rb and K is quite evident.

This analysis can be used to calculate a source Th/U ratio and a value of 2.5 is obtained which is similar to the value of 2.75 inferred from the $(^{230}Th/^{232}Th)_a$=1.1 for the

$(Rb/C^i)_n$	r^i	1σ error
Rb/Ba	0.451	0.053
Rb/Th	0.342	0.047
Rb/U	0.218	0.077
Rb/Nb	0.286	0.025
Rb/K	0.664	0.051
Rb/La	0.251	0.034
Rb/Sr	0.491	0.053
Rb/Nd	0.277	0.096
Rb/Sm	0.485	0.100

Table 3.5 Calculated intercepts and associated uncertainty, from York (1969), for plots of primitive mantle normalised Rb contents against primitive mantle normalised ratios of Rb over other incompatible elements, such as in Fig. 3.10. This data is used to produce Fig. 3.16b.

LPTh lavas (assuming no $(^{230}Th/^{232}Th)_a$ fractionation during melting). However the errors on the Th/U ratio obtained by the inversion technique are large and cannot be used to verify the assumption of no $(^{230}Th/^{232}Th)_a$ fractionation during melting. However the Rb/Sr ratio calculated has smaller associated errors since it is derived from a single intercept value (i.e. equation 10), rather than a ratio of two intercepts (i.e. equation 9) needed to calculate Th/U.

The calculated source Rb/Sr is 0.015±0.0016 which is as low as some of the lowest time intergrated Rb/Sr ratios required to account for the $^{87}Sr/^{86}Sr$ of MORB by closed system evolution from 4.55Ga. This is a minimum value since Sr is not totally incompatible during melting, and so the true source Rb/Sr ratio is given by $I^{Sr}/(1-P^{Sr})$, equation 8, although for Sr, $(1-P^{Sr})$ is still not very significant (~0.9), and the source Rb/Sr is still very low ~0.017. The Sm/Nd of the source may also be approximated, though as with Sr neither Sm nor Nd are totally incompatible and the (1-P) term will have some effect. However the primitive mantle normalised Sm/Nd ratio is given by the expression;

$$\frac{I^{Nd}.(1-P^{Sm})}{I^{Sm}.(1-P^{Nd})}$$

and since P^{Sm} will be greater than P^{Nd}, a ratio of I^{Nd}/I^{Sm} will give a maximum Sm/Nd. A maximum primitive mantle normalised Sm/Nd is hence calulated to be 0.80±0.03, which reinforces the light rare enriched nature of the La Palma source, inferred from modelling of Ce and Yb concentrations.

3.9.2 Isotopic Constraints on Source Composition

Having inferred incompatible element ratios for the La Palma source from trace element inversion, it is of interest to compare the characteristics of the present day source with time integrated information represented by radiogenic isotope ratios.

Fig. 3.17 shows the radiogenic isotope data of the La Palma basanites relative to other Atlantic oceanic magmas. The data of this study plot within the existing fields for Canary Islands samples, which are characterised by a fairly small range of $^{87}Sr/^{86}Sr$ and $^{143}Nd/^{144}Nd$ ratios, that are slightly enriched with respect to Atlantic MORB (Fig. 3.17a), but with a wide variation of Pb isotopic compositions (Fig. 3.17b & c), that trend towards the very radiogenic values of the so-called high μ component, $^{206}Pb/^{204}Pb>20.5$ (Zindler

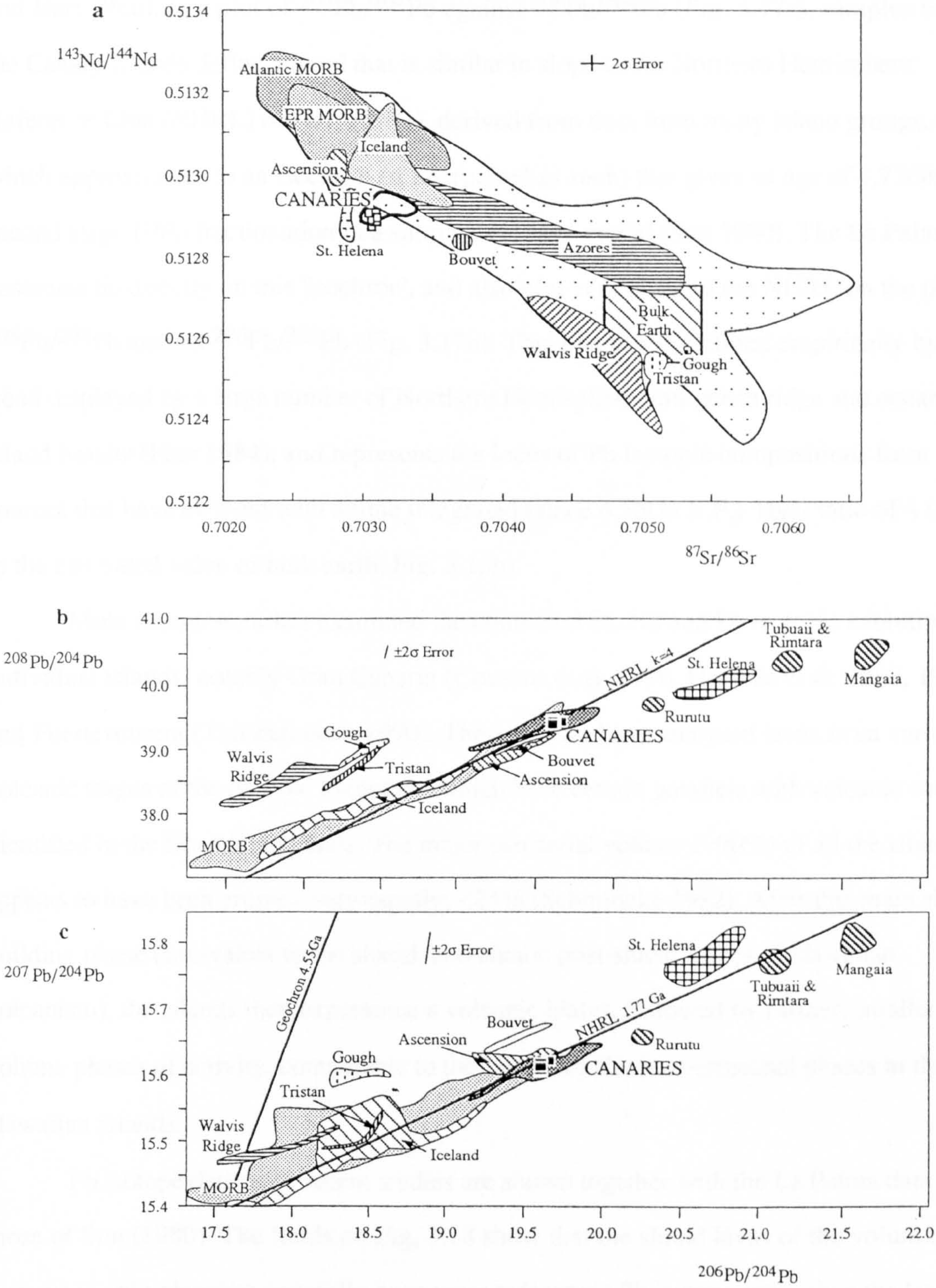

Figure 3.17 Sr, Nd and Pb isotopic compositions of the La Palma basanites compared with data for MORB and other oceanic islands. **a)** $^{87}Sr/^{86}Sr$ against $^{143}Nd/^{144}Nd$, after Zindler & Hart (1986), showing data for Atlantic ocean islands (other ocean island data indicated by lightly shaded field). Data from the historic La Palma basanites is shown as open squares and falls within the Canary Islands field defined by recent data from Cousens et al. (1990) and Hoernle et al. (1988). **b)** & **c)** show the Pb isotopic data of the historic La Palma basanites (filled squares) compared with data from other Atlantic Islands and also with oceanic 'high μ' lavas. The NHRL (Northern Hemisphere Reference Line, Hart 1984) in **b)** represents the locus of samples that have evolved in a closed system since 4.55Ga B.P., with a Th/U ratio (κ) of 4, and in **c)** it defines a secondary isochron of 1.77Ga for samples that have experienced a simple two stage U/Pb fractionation through earth history, whilst the Geochron represenents the locus of samples that experienced a single stage U/Pb fractionation at 4.55Ga B.P. **b)** & **c)** are after Zindler & Hart (1986) but with additional data from Palacz & Saunders (1986), Nakamura & Tatsumoto (1988) and Chaffey et al. (1989).

and Hart 1986). In a plot of $^{207}Pb/^{204}Pb$ against $^{206}Pb/^{204}Pb$ (Fig. 3.17c), samples from all the Canary Islands define a trend that is similar in slope to the Northern Hemisphere Reference Line (NHRL) of Hart (1984), derived from data from many island groups, and which approximates to an isochron (if interpreted as such) that gives an age of 1.77Ga for a second stage U/Pb fractionation in a simple two stage model (Sun 1980). The La Palma basanites lie directly on this 'isochron', and also plot very close to the NHRL on the plot of $^{208}Pb/^{204}Pb$ against $^{206}Pb/^{204}Pb$ (Fig. 3.17b). This line is also defined empirically by the trend displayed by a large number of Northern Hemisphere mid-ocean ridge and ocean island basalts (Hart 1984), and represents the locus of Pb isotopic compositions from sources that have evolved with a time integrated (since 4.55Ga B.P.) Th/U ratio of 4 (similar to the estimated value of bulk earth, Fig. 3.13b).

More recent work has examined the combined Sr, Nd and Pb isotopic evolution of individual islands, notably Gran Canaria (Cousens et al. 1990, Hoernle et al. 1988, 1990) and Fuerteventura (Thirwell et al. 1990). These studies have analysed lavas from various volcanic stages of the islands' evolution, which have certain parallels with volcanic stages identified in the Hawaiian Islands. The major sub aerial volume (~90%) of all the islands appears to have been erupted very rapidly; <2Ma (Schmincke 1982). After this main shield building phase (equivalent to the shield, and alkalic post-shield stages of Hawaiian volcanism), the islands then experience a volcanic hiatus, followed by further, smaller volume phases of activity, comparable to the highly alkalic post-erosional phases in the Hawaiian islands.

Pb isotope data from recent studies are shown together with the La Palma data and those of Sun (1980). The fields on Fig. 3.18 show that the shield lavas of the voluminous, main phase of volcanism generally have more radiogenic Pb isotope ratios than the later, volumetrically less significant, post-erosional lavas on both Gran Canaria and Fuerteventura. The data for Gran Canaria post-erosional lavas plot significantly off the NHRL (Fig. 3.18) and this has lead Hoernle (1990) to argue against an age implication of the Pb isotope data, invoking instead a mixing of various isotopic components hosted in the upwelling plume, asthenosphere and overlying lithosphere ($^{207}Pb/^{204}Pb$ ratios make interaction with the sediment layer at the base of the islands unlikely). Hoernle et al. (1990) have suggested that

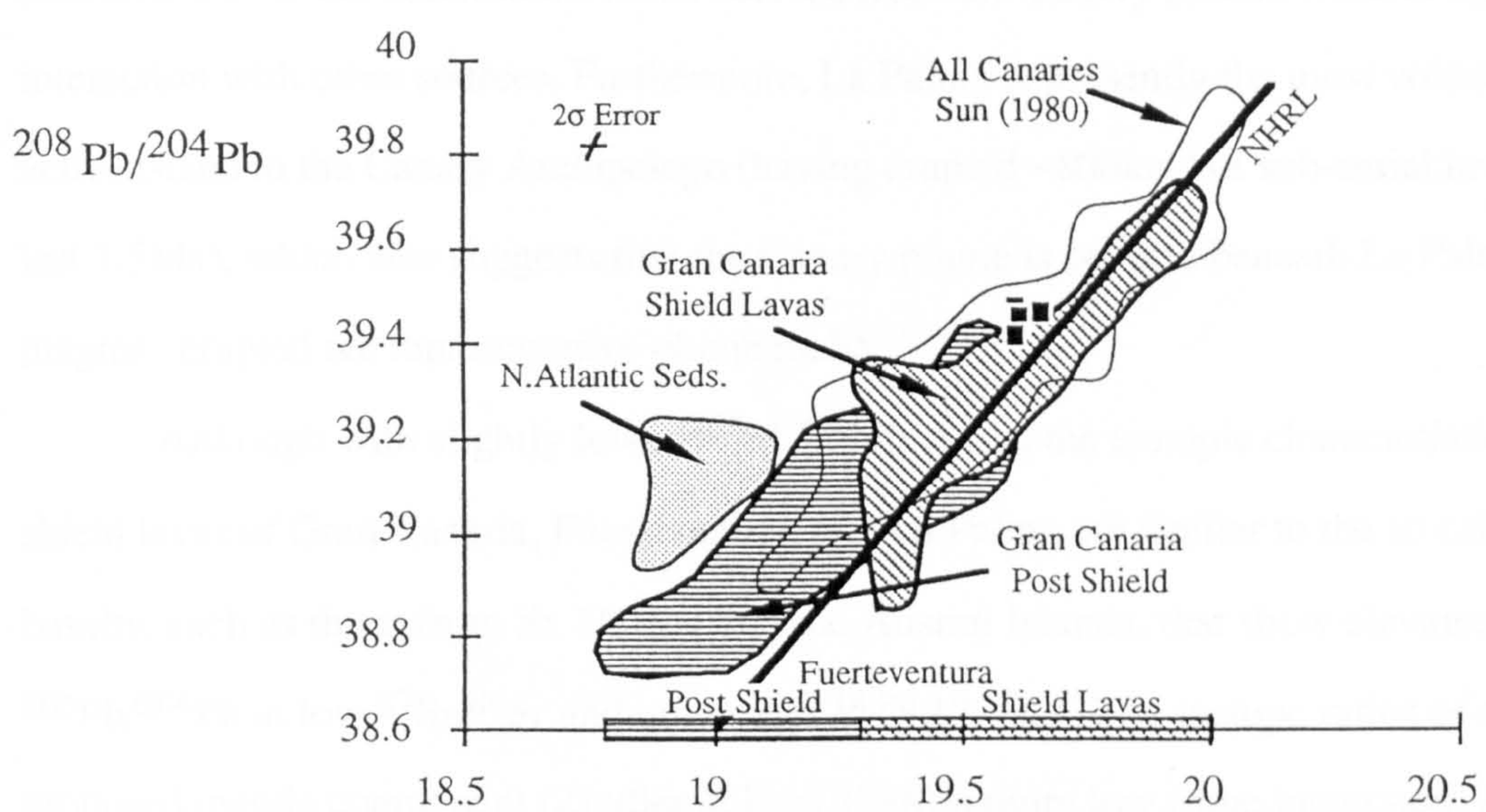

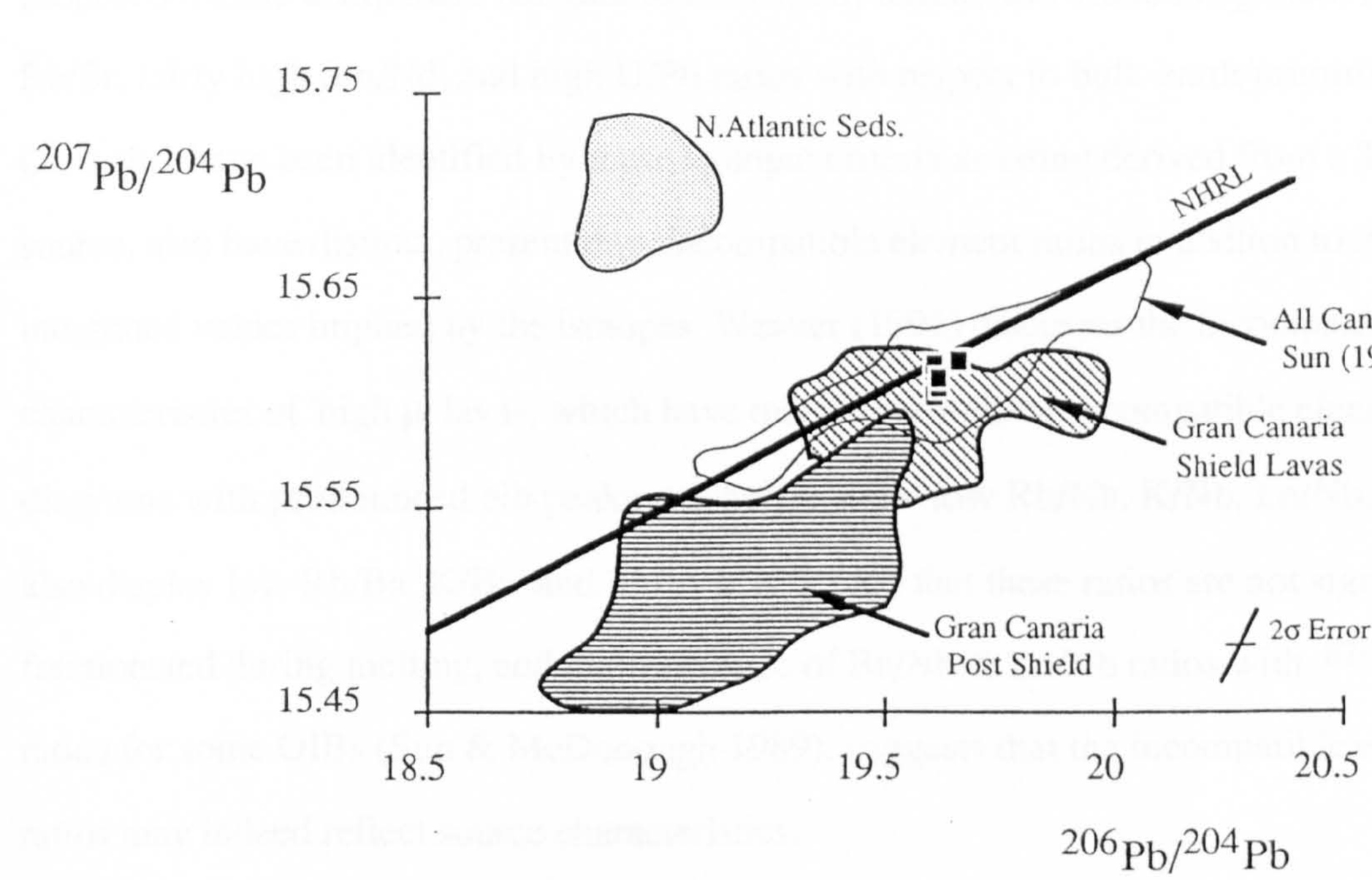

Figure 3.18 Plots of **a)** $^{208}Pb/^{204}Pb$ vs. $^{206}Pb/^{204}Pb$ and **b)** $^{207}Pb/^{204}Pb$ vs. $^{206}Pb/^{204}Pb$ for the historic basanites of La Palma (filled squares) and other Canary Island volcanics (after Cousens et al. 1990). Data from Fuerteventura lavas ($^{206}Pb/^{204}Pb$ only) is from Thirwell (1990). The NHRL is defined in Fig. 3.17.

lavas with the most radiogenic Pb isotopic ratios represent largely uncontaminated plume melts, and that mixing with other isotopic components in the post-erosional stages of volcanism lowers the Pb isotope ratios of these lavas. The historic basanites of La Palma have lead isotope ratios that plot within the radiogenic fields of the shield building lavas of both Gran Canaria and Fuerteventura (Fig. 3.18), and this suggests that they are characteristic of the voluminous melts derived from the Canary plume, without significant interaction with other sources. Furthermore, La Palma is presently the most volcanically active island in the Canary Archipelego (having erupted ~800km^3 of sub-aerial lavas in the last 1.5Ma), which also suggests that the Canary plume is centred beneath La Palma and that magmas erupted are representative plume melts.

Although with slightly lower $^{206}Pb/^{204}Pb$ ratios, the isotopic characteristics of the shield lavas of Gran Canaria, Fuerteventura and La Palma are similar to the so called high μ basalts, such as those from St. Helena and the Austral Islands, that show elevated $^{206}Pb/^{204}Pb$ at low $^{87}Sr/^{86}Sr$ and quite high $^{143}Nd/^{144}Nd$. The isotope ratios of this proposed mantle component (Zindler & Hart 1986) require low (time integrated) source Rb/Sr, fairly high Sm/Nd, and high U/Pb ratios with respect to bulk-earth/primitive mantle. OIBs that have been identified by these isotopic criteria as being derived from a 'high μ' source, also have distinct, present day, incompatible element ratios in addtion to the time-integrated values implied by the isotopes. Weaver (1991) discusses the incompatible element characteristics of 'high μ' lavas, which have mantle normalised incompatible element diagrams with pronounced Nb peaks and hence show low Rb/Nb, K/Nb, La/Nb, Ba/Nb, also display low Rb/Ba, K/Ba and Th/U. It is argued that these ratios are not significantly fractionated during melting, and the coherence of Ba/Nb & La/Nb ratios with $^{87}Sr/^{86}Sr$ ratios for some OIBs (Sun & McDonough 1989), suggests that the incompatible element ratios may indeed reflect source characteristics.

The La Palma basanites show many incompatible element ratios similar to those identified by Weaver (1991) as typical of 'high μ' lavas, namely low Rb/Nb, K/Nb, Ba/Nb, Ba/Rb,Th/U (Fig. 3.19) and importantly, from inversion of incompatible element data (Fig. 3.16b) and $(^{230}Th/^{232}Th)_a$ ratios (Fig. 3.13b), it is inferred that these are source features in addition to being characteristic of the basanites themselves (Fig. 3.16a). The combined

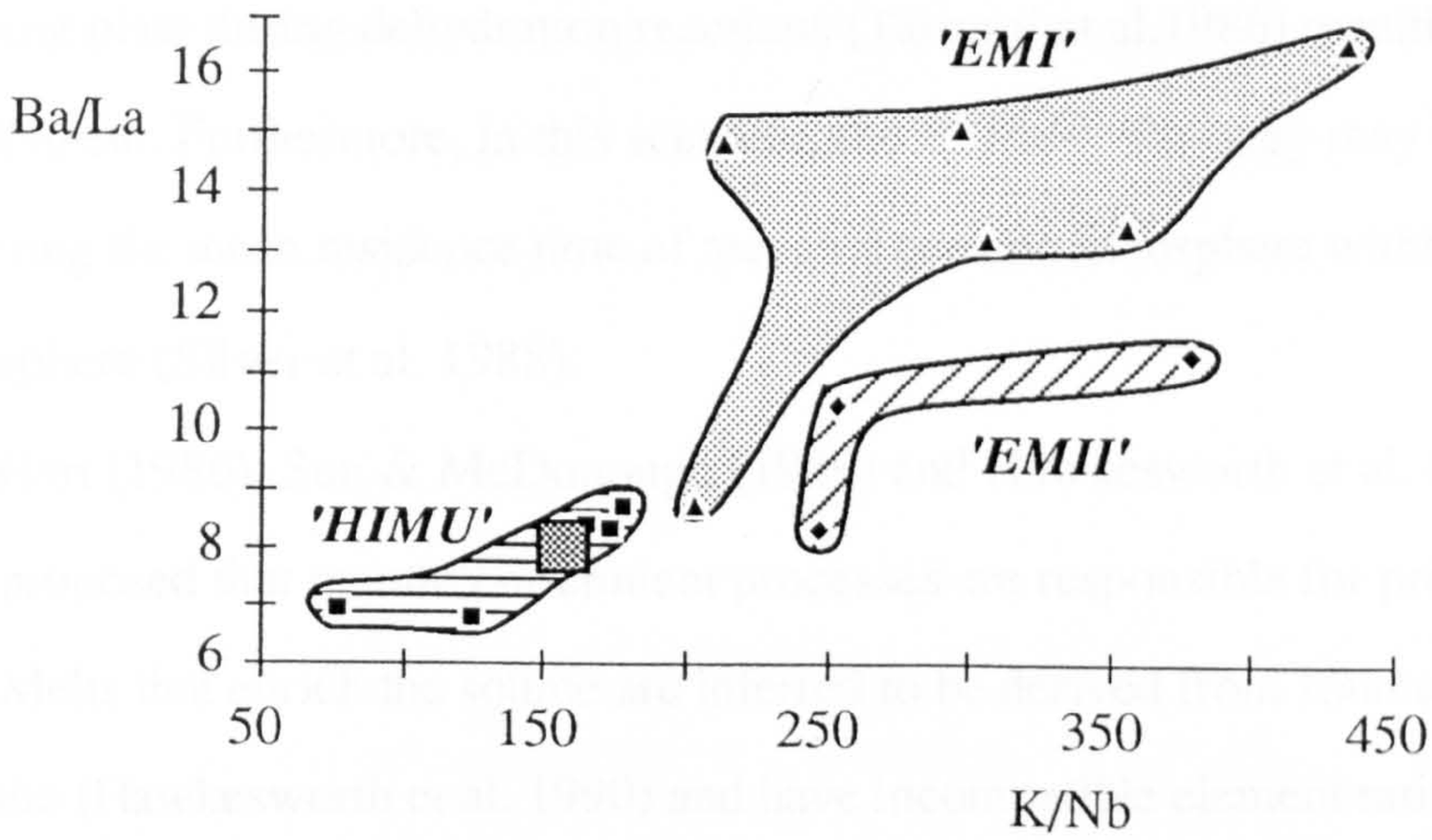

Figure 3.19 Ba/La and K/Nb ratios for oceanic basalts from the isotopically defined HIMU, EMI and EMII groups. The mean value of the LPTh basanites of this study is shown as a shaded square. Each of the points on the diagram represent an average of analyses from an island group (Weaver 1991).

isotopic and incompatible element ratios typical of 'high μ' lavas has lead to two main suggestions of processes that produce a high μ source. Altered oceanic crust is strongly enriched in U (Michard et al. 1983) and recycled subducted crust, if it retains such a elevated U/Pb ratios will generate the characteristic high $^{206}Pb/^{204}Pb$ (Hofmann & White 1982, Palacz & Saunders 1986). The incompatible element fractionations experienced by a descending plate in a subduction zone is a matter of much debate, but if the process occurs under reducing conditions, elevated U concentration may be retained, whilst large ion lithophile elements, such as Rb, K and Ba are likely to be preferentially removed from the downgoing plate during dehydration reactions (Tatsumi et al.1986) resulting in a source with low Rb/Nb etc. Furthermore, in this scenario, the $^{207}Pb/^{206}Pb$ array may be interpreted as representing the mean residence time of recycled oceanic lithosphere within the asthenosphere (Silver et al. 1988).

Hart (1986), Sun & McDonough (1989) and Hawkesworth et al. (1990) have instead proposed that mantle enrichment processes are responsible for producing a 'high μ' source. Melts that enrich the source are inferred to be derived from sources with residual phlogopite (Hawkesworth et al. 1990) and have incompatible element ratios very similar to those of the high μ lavas, as is compatible with measured distribution coefficients of phlogopite (Rogers et al. in press). A source enriched with such small degree melts would evolve towards the isotopic compositions observed in high μ lavas. An important difference betwen the two mechanisms for producing 'high μ' sources is that dehydration reactions in a down-going slab are likely, to preferentially deplete the LREE elements, if the REE of the slab are affected at all, and since the downgoing slab has flat or already LREE depleted normalised rare earth element profiles, this should result in a LREE depleted 'high μ' source, whilst small degree melts from a phlogopite bearing source will be LREE enriched and result in a LREE enriched 'high μ' source. In modelling the melting trends of the LPTh basanites it is inferred that the La Palma source is LREE enriched and hence for the La Palma source, the 'high μ' signature may be best explained by an intra-mantle enrichment process. This does not necessarily imply that all high μ sources are generated in this way, but inferences of the source REE patterns of other high μ sources may be an important tool in ascertaining the process that lead to their formation.

High μ lavas (sensu stricto) from St. Helena and the Austral islands have higher $^{206}Pb/^{204}Pb$ ratios, but lower $^{87}Sr/^{86}Sr$ and $^{208}Pb/^{206}Pb$, relative to the La Palma source and yet in terms of their characteristic 'high μ' incompatible element signatures, they are very similar to the La Palma basanites (Fig. 3.19). This suggests similar elemental ratios in the source for the various island groups, but differences in the time between enrichment and eruption, over which the sources evolved. This implies that the high μ component is not a single point in multi-dimensional isotope space, but a range of endmembers that have expeienced similar enrichment processes, but at different times in earth history. That 'mantle components' are not defined by extensive reservoirs of similar isotopic composition has been recently stressed by Barling & Goldstein (1990), who find that a well defined isotopic mixing curve for Heard island does not trend towards any of the acronym compositions of Zindler & Hart (1986).

3.10 Conclusions

Historic basanites from La Palma evolve from primitive compositions by fractionation of an olivine, clinopyroxene, titanomagnetite assemblage. The presence of clinopyroxene but not plagioclase on the liquidus implies depths of fractionation of >4kbar, perhaps at the crust/mantle boundary. Fractionation occurs in zoned magma chambers, and the complex, disequilibrium phenocryst assemblage of individual lavas reflects settling of phenocrysts from upper, evolved, phonolitic layers of the magma chamber into the basanites. Some basanites have accumulated monazite by crystal settling, as documented by their elevated Th, U, LREE and P_2O_5 contents of relative to uncontaminated basanites, at a given Rb content. The lower $(^{230}Th/^{232}Th)_a$ ratios of some of these contaminated basanites suggests lifespans of >200ka for some of these deep magma chambers.

Basanites show variations in incompatible element concentrations that are attributable to differences in degree of partial melting from a homogeneous mantle source. Modelling of rare earth element contents of the LPTh lavas suggests that melting occurred within the spinel stability field, without the presence of residual garnet, from a LREE enriched source. REE modelling further implies the basanites represent a range of melts from 1-2% melting, although U-Th disequilibrium data suggests a lower bound of 0.3%. Inversion of the highly incompatible trace elements of the LPTh lavas indicates that anomalously low Rb/Nb and

K/Nb ratios of the basanites are source characteristics, and argued to result from intra-mantle enrichment by melts from a phlogopite bearing source. These source features are very similar to incompatible element signatures of isotopically defined, high μ basalts, yet the La Palma basanites show less extreme isopic ratios. This is argued to result from the La Palma source being more recently enriched relative to the other high μ ($^{206}Pb/^{204}Pb>20.5$) sources.

Chapter 4

Dynamic Melting of the Iceland plume.

Icelandic high MgO basalts show striking correlations between major element abundances and incompatible element and radiogenic isotope ratios. The highest MgO lavas have the most depleted incompatible element ratios and among the least radiogenic Pb isotopes recorded in Atlantic MORB, highlighting a decoupling of major and trace element characteristics expected of plume melts. This paradox can be explained by the process that mixes melts segregated from different depths of the melting column. The resulting model offers new insights into processes governing melt compositions at spreading ridges.

4.1 Introduction

Advances in the understanding of the physics of partial melting (McKenzie 1984) have enabled quantitative modelling of mantle melt production during extension (McKenzie & Bickle 1988). The volume of melt produced depends on the amount of extension and the temperature of the mantle induced to upwell during extension. The relation between these parameters is most readily quantified for mid-oceanic rifting, since the stretching factor is infinite and the volume of melt produced is manifest in the thickness of oceanic crust. Thus oceanic crustal thickness should be principally dependent on the temperature of the underlying, upwelling mantle. Moreover since melt composition is dependent on the degree of melting and thus the volume of melt produced beneath any rift, there should be a relationship between oceanic crustal thickness and its chemistry, as observed by Klein & Langmuir (1987).

The thickest segment of actively rifting oceanic crust is beneath Iceland, formed as a result of high degrees of melting of mantle some 200°C hotter than mantle upwelling beneath 'normal' oceanic ridges. Since high degree melts are MgO rich (Jaques & Green 1980, Stolper 1980, Takahashi & Kushiro 1983, Falloon & Green 1988), high MgO contents should be characteristic of lavas erupted on Iceland.

The mantle source beneath Iceland is however not only hotter, but also geochemically 'enriched' in comparison to the mantle beneath 'normal' spreading ridges (N-

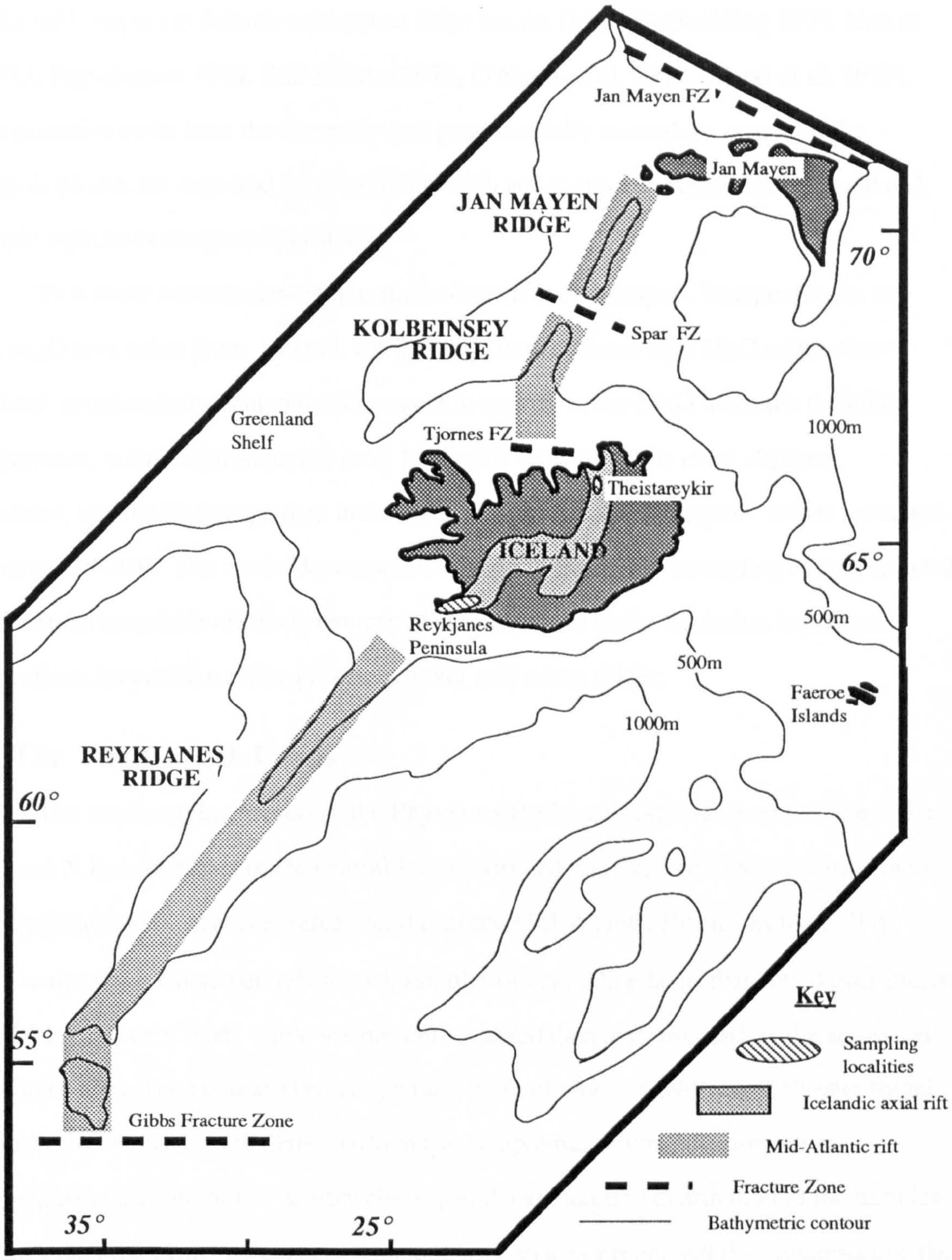

Figure 4.1 Bathymetry and location of Iceland, sampling localities and adjacent segments of the Mid-Atlantic Ridge.

MORB source). Numerous studies have shown Icelandic basalts to have more radiogenic Pb and Sr isotope ratios, less radiogenic $^{143}Nd/^{144}Nd$ ratios and incompatible element ratios reflecting higher concentrations of the more incompatible element (e.g. higher La/Sm and Rb/K), with respect to Atlantic mid-ocean ridge basalts (MORB) (Schilling 1973, Hart et al.1973, Sigvaldason 1974, Sun & Jahn 1975, O'Nions et al. 1977, Wood et al. 1979). Thus primitive melts from the thermally and geochemically anomalous mantle of the Icelandic plume, are expected to be both MgO rich and to have enriched trace element and isotopic signatures compared to MORB.

This study presents new major, trace element and radiogenic isotope data on two high MgO lava suites from Iceland. Intriguingly, both of these high MgO suites show *depleted* geochemical signatures with respect to typical, lower MgO Icelandic tholeiites. Furthermore, within each suite, the most MgO rich lavas show the *most depleted* signatures, and the Pb isotope data include some of the most unradiogenic values measured in Atlantic MORB. The model developed to explain this striking decoupling of the predicted major and incompatible element characteristics expected of plume melts has important implications for partial melting processes along mid ocean ridges.

4.2 The High MgO Lavas

The two sampling locations, the Reykjanes Peninsula and Theistareykir, are at the S.W. and N.E. extremities of the central Iceland rift and represent onshore continuations of the Reykjanes and Kolbeinsey ridge sections of the Mid-Atlantic Rift respectively (Fig. 4.1). Analyses were made on whole rock samples of crystalline lavas that are all post-glacial (<10,000a) and very fresh. Table 4.1 presents selected data and summarises the analytical techniques used. The lavas studied are picrites (with olivine, Fo 88-91, and chrome spinel phenocrysts), and olivine tholeiites (which can be aphyric, olivine, plagioclase or olivine/plagioclase phyric). The very close spatial and temporal distribution of the samples in each suite minimises any changes in source over space or time, and thus suggests that the geochemical variations are largely process controlled.

There is a large range in MgO content, 19–8% ($Mg\# = Mg^{2+}/(Mg^{2+}+Fe^{2+}) = 82\text{-}58$, Table 4.1), which correlates inversely with SiO_2 and FeO (Figs. 4.2a and b). The effects of crystal fractionation for such high MgO tholeiitic compositions are quite easy to assess,

Sample	*Suite*	*Latitude*	*Longitude*	*Modal Phenocryst Content*	*MgO*	*FeO*	*Mg#*	*K_2O*
D2/11	R	63°48'N	22°39'W	20% Ol (+Cr Sp.)	19.64	7.46	82	0.006
D6	R	63°51'N	22°34'W	Aphyric	10.30	8.98	67	0.102
D7	R	63°53'N	22°32'W	8% Ol (+Cr Sp.)	12.88	7.39	76	0.009
D8A	R	63°52'N	22°23'W	10% Ol, 3%Plag	9.30	9.64	63	0.093
D8B	R	63°53'N	22°23'W	8% Ol (+Cr Sp.), 4% Plag	14.62	7.69	77	0.031
D18	R	63°52'N	21°42'W	5% Ol (+Cr Sp.)	11.73	9.11	70	0.040
D26	R	63°54'N	21°28'W	5% Ol (+Cr Sp.)	11.21	8.42	70	0.033
D27	R	63°55'N	21°24'W	5% Ol (+Cr Sp.)	13.08	7.57	75	0.017
IT1	T	65°53'N	17°09'W	2% Plag	9.19	8.96	65	0.061
IT2	T	65°53'N	17°03'W	4% Plag	8.07	9.77	60	0.113
IT3A	T	65°49'N	16°54'W	3% Ol, 3% Plag	9.07	9.86	62	0.127
IT4	T	65°50'N	16°50'W	2% Ol, 2% Plag	7.91	10.24	58	0.144
IT5	T	65°52'N	17°03'W	20% Ol (+Cr Sp.)	15.84	8.92	76	0.035
IT6	T	65°52'N	17°03'W	4% Ol (+Cr Sp.)	10.60	8.65	69	0.045
IT7	T	65°48'N	16°58'W	4% Ol (+Cr Sp.)	11.45	8.30	71	0.053
TH8	T	65°57'N	17°05'W	5% Ol (+Cr Sp.)	12.40	8.46	72	0.033
TH13	T	65°54'N	16°52'W	4% Ol (+Cr Sp.)	9.78	9.24	65	0.055
TH29	T	65°55'N	17°04'W	15% Ol (+Cr Sp.)	15.73	7.39	79	0.011

Sample	*$^{143}Nd/^{144}Nd$*	*$^{87}Sr/^{86}Sr$*	*$^{206}Pb/^{204}Pb$*	*$^{207}Pb/^{204}Pb$*	*$^{208}Pb/^{204}Pb$*
D2/11	0.513178±20		18.197	15.401	37.741
D6			18.556	15.412	37.984
D7			18.268	15.432	37.859
D8A	0.513089±12	0.703188±8	18.525	15.453	38.035
D8B	0.513117±24		18.422	15.460	38.005
D18	0.513110±16		18.298	15.439	37.957
D26	0.513064±22		18.411	15.436	37.959
D27			18.323	15.439	37.862
IT1			18.058	15.417	37.685
IT2	0.513085±14	0.703225±4	18.035	15.374	37.574
IT3A		0.703238±6	18.060	15.410	37.704
IT4	0.512986±14	0.703071±5	18.005	15.335	37.475
IT5	0.513070±12	0.703044±5	17.980	15.352	37.441
IT6	0.513071±10		17.983	15.367	37.491
IT7	0.513062±14		17.988	15.380	37.518
TH8	0.513088±22	0.703025±7	17.957	15.363	37.452
TH13	0.513077±16	0.703020±10	18.064	15.399	37.643
TH29	0.513106±20	0.702928±8	17.800	15.344	37.263

Table 4.1 Selected geographical, chemical and petrographic data for the high MgO basalts.
R indicates samples from the Reykjanes Peninsula and T indicates samples from Theistareykir. Major elements were analysed by XRF on fused pellets with a heavy La absorber (Fitton & Dunlop 1985). FeO was calculated from total Fe_2O_3 assuming $Fe^{3+}/(Fe^{2+}+Fe^{3+}) = 0.1$. Nd was run as metal with $^{143}Nd/^{144}Nd$ normalised to $^{146}Nd/^{144}Nd = 0.72190$ within run, and the final $^{143}Nd/^{144}Nd$ renormalised to $^{142}Nd/^{144}Nd=1.142025$, using the mean, Ce corrected $^{142}Nd/^{144}Nd$ of the sample. $^{87}Sr/^{86}Sr$ was normalised to $^{86}Sr/^{88}Sr = 0.1194$. Errors quoted are within run $2\sigma/\sqrt{N}$ statistics and replicate standard runs indicate a reproducibility of 0.007% for $^{143}Nd/^{144}Nd$ (2σ on 4 runs) and 0.005% for $^{87}Sr/^{86}Sr$ (2σ on 3 runs). These techniques give $^{143}Nd/^{144}Nd = 0.512638$ for BCR-1 and 0.710329 for NBS 987. Blanks are less than 2ng and 0.3ng for Sr and Nd respectively, and thus insignificant. Pb was run at a controlled temperature of 1200°c using an adaptation of the silica gel technique of Manhès et al. (1978). Reproducibility of standards and samples is better than 0.04%/amu (2σ on 8 runs of NBS 981). Pb isotope ratios have been corrected using a fractionation factor of -0.06% as indicated from the mean values obtained for NBS 981. Pb blanks vary between 0.1-0.2ng and represent less than 0.5% of total sample load for the lowest Pb (low FeO) samples, and so are insignificant. A full data set is given in Appendix D.

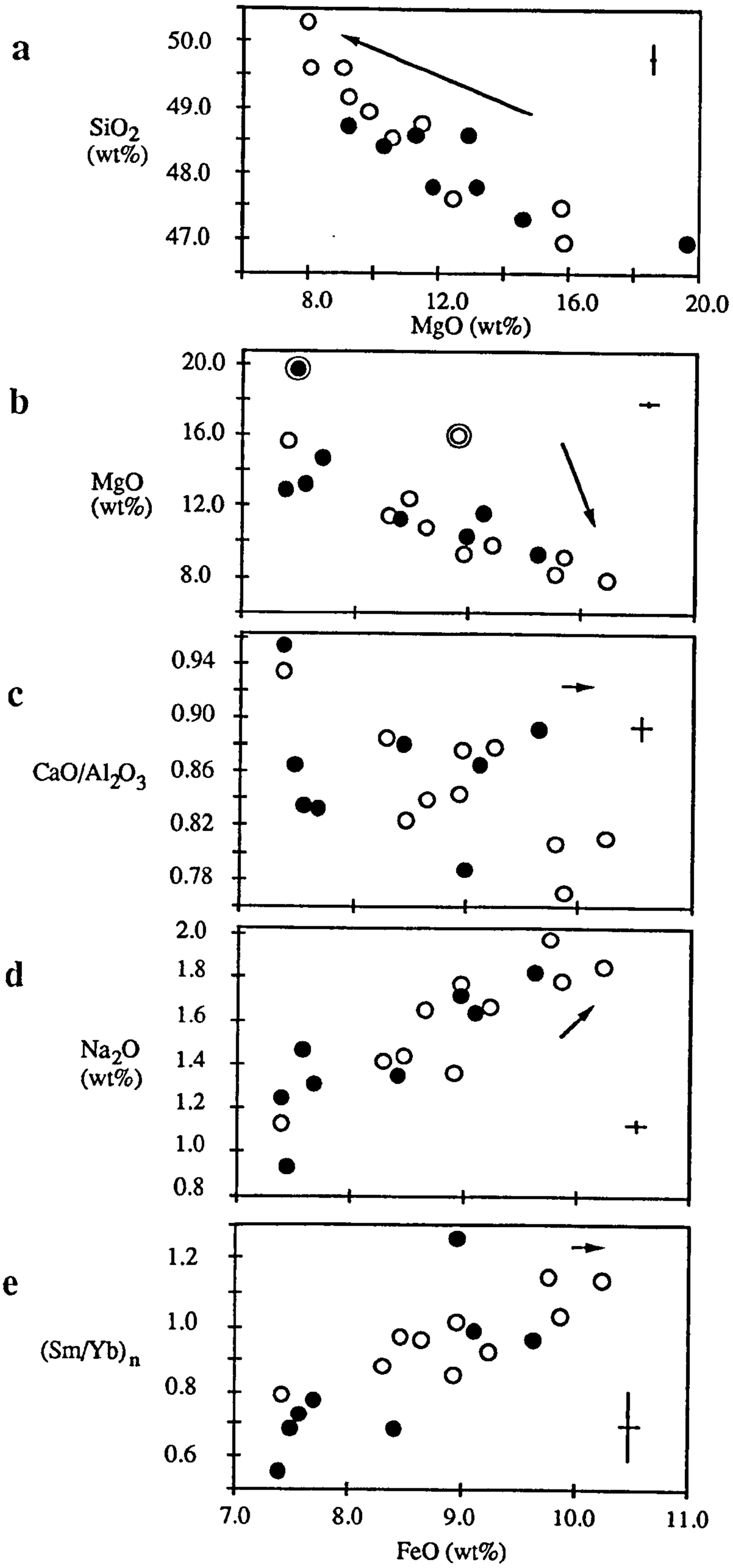

Figure 4.2 Major and trace element variation. **a)** MgO verses SiO_2; and FeO verses **b)** MgO, circled symbols are petrographically identified as olivine cumulates; **c)** CaO/Al_2O_3; **d)** Na_2O; **e)** Sm/Yb normalised to chondritic abundances (Sun & McDonough 1989). Data from the Reykjanes Peninsula samples are plotted as closed symbols, data from the Theistareykir samples are plotted as open symbols. Analytical techniques are summarised in Table 4.1 except for Sm and Yb which were measured by INAA (Potts et al. 1985). Analytical uncertainties assessed from 2σ deviation of triplicate sample runs are shown by crosses. Vectors show the effect of 15% fractional olivine crystallisation for which olivine compositions are calculated to be in equilibrium with the evolving liquid at the start each 0.1% increment.

since only olivine (+chrome spinel) is expected to fractionate until plagioclase becomes cotectic at Mg#~65 (Bender et al. 1978, Maaløe & Jakobsson 1980). Vectors for 15% olivine fractionation are shown in Fig 4.2, and it is clear that this can account for increasing SiO_2 with decreasing MgO (Fig. 4.2a). Similarly, *addition* of olivine can explain the departure of the two aberrant points from the main trend in Fig 4.2b, which is also consistent with the abundant olivine phenocrysts present in these two samples (Table 4.1). However, to generate the main negative FeO–MgO trend in Fig. 4.2b by fractional crystallisation would implausibly require plagioclase to be cotectic with olivine for the *whole* range of lava compositions. Furthermore, such fractionation of olivine and plagioclase would cause an increase in CaO/Al_2O_3 with increasing FeO. Although the trend is scattered, the opposite is observed (Fig. 4.2c). Thus variations in FeO do not appear to be a result of crystal fractionation, and FeO may be used as an index of primary major element composition.

FeO correlates with both incompatible element contents and incompatible element ratios (Figs. 4.2d and e). The variations of incompatible element contents within the high MgO lavas are very large (e.g. K_2O contents vary by over an order of magnitude, Fig. 4.3), and are greatest for elements with the lowest inferred distribution coefficients for melts in equilibrium with a mantle source (Sun & McDonough 1989). Thus the lowest FeO (highest MgO) lavas have the lowest incompatible element concentrations and the most depleted incompatible element ratios. This is unexpected since if the highest MgO melts are most representative of high degree melts from the plume they should have enriched incompatible element ratios, characteristic of the plume source.

If the lower FeO (higher MgO) melts are thought to represent higher degree melts, it would be expected that they should have lower incompatible element contents. However the variations in incompatible element contents between the highest and lowest FeO lavas of this study are greater than could reasonably be explained by differences in degrees of partial melting using simple melting models (Jakobsson et al. 1978), and additionally, differences in degree of melting for such high degree tholeiitic melts are unlikely to fractionate incompatible trace element ratios significantly.

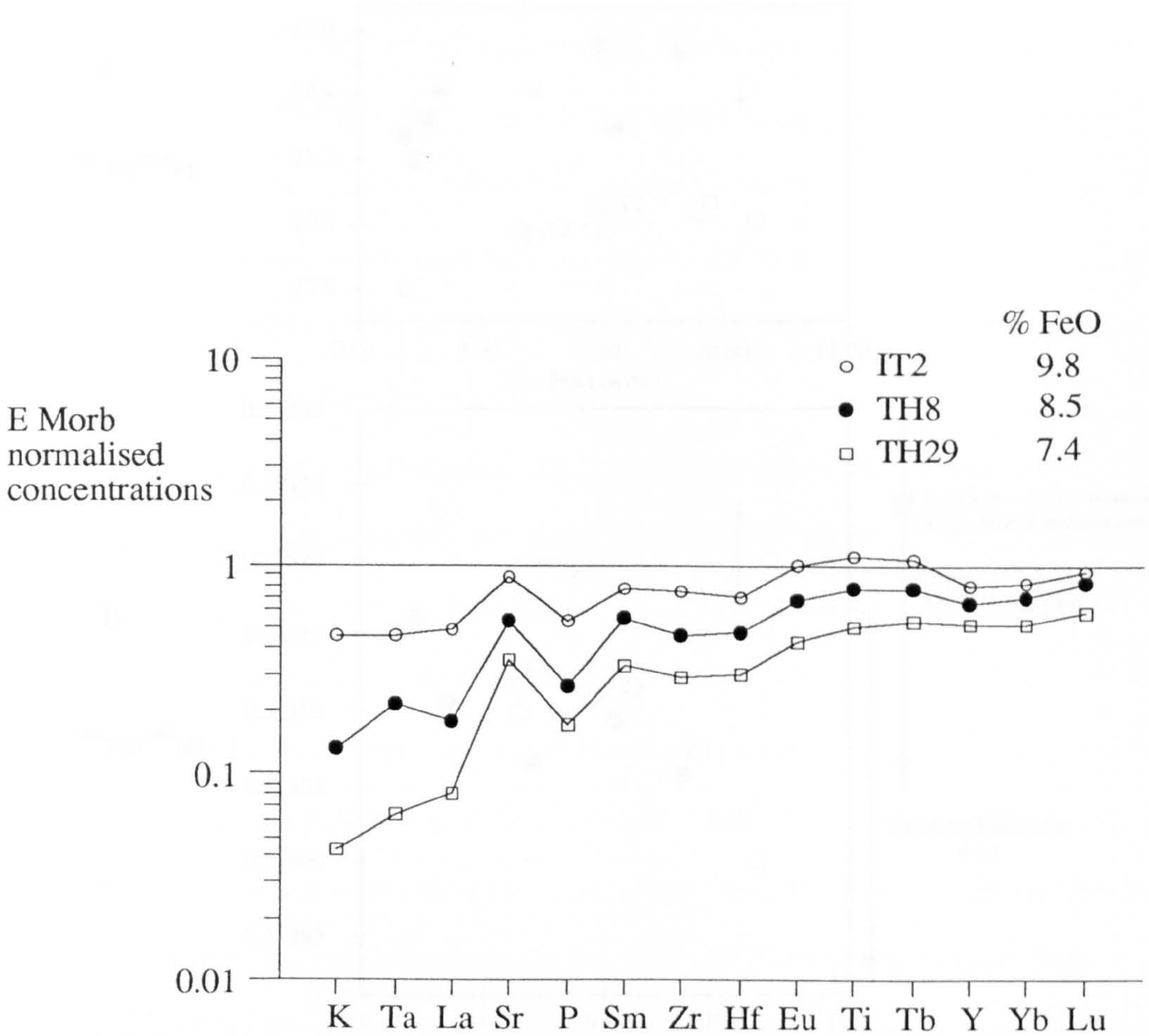

Figure 4.3 E-MORB normalised (Sun & McDonough 1989) incompatible element concentration diagrams. Elements on abscissa plot from left to right in decreasing order of inferred incompatiblity during mantle melting (Sun & McDonough 1989). Three lavas from Theistareykir that cover the range of FeO in the high MgO suites. (Several elements frequently used in such normalised incompatible element plots are excluded because of analytical difficulties in their measurement at low concentration in the high MgO suites). K, P and Ti were measured by XRF on fused beads; Sr, Zr and Y by XRF on pressed powder pellets (Fitton & Dunlop 1985); and the rare earth elements, Ta and Hf by INAA (Potts et al. 1985).

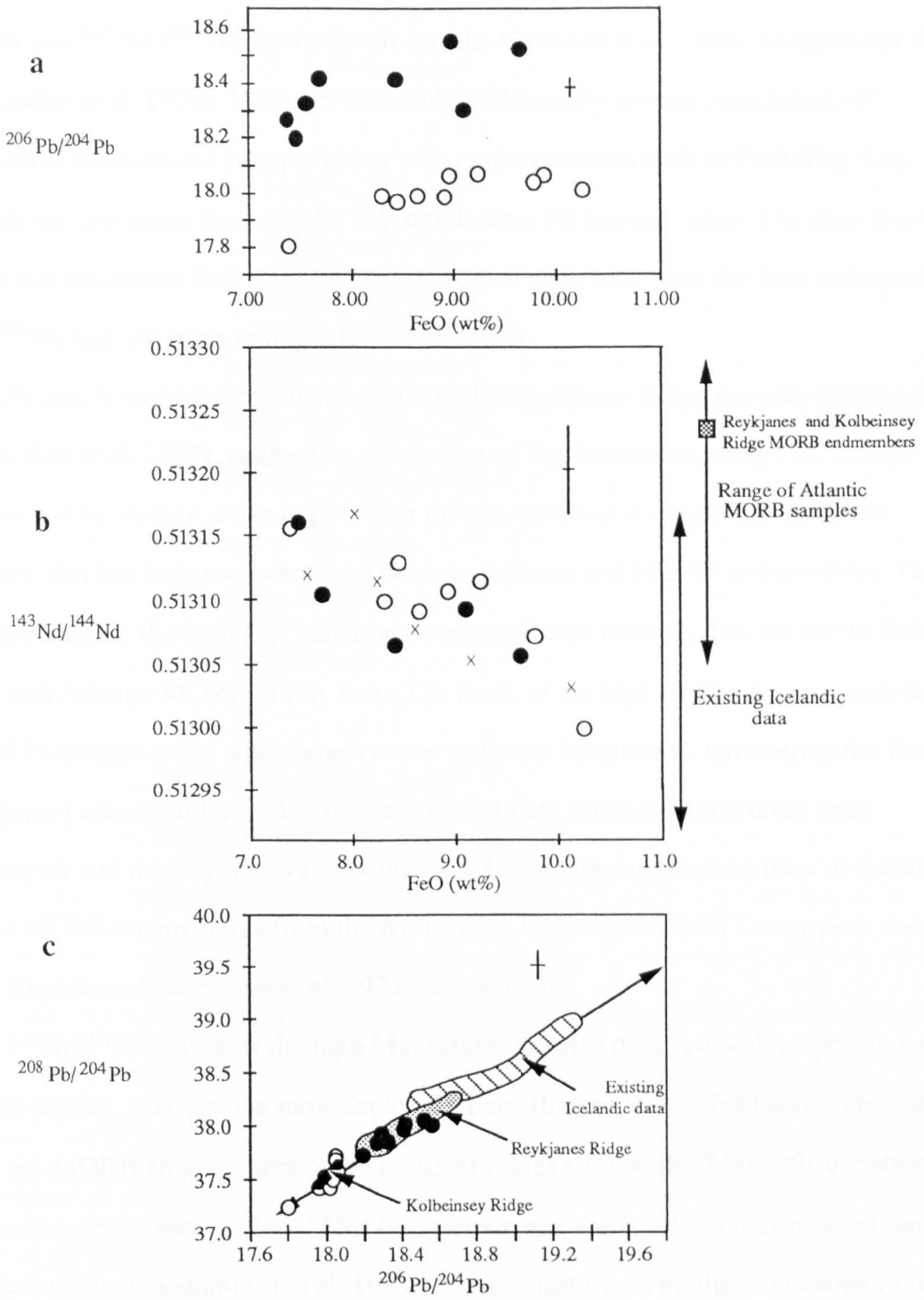

Figure 4.4 FeO verses **a)** $^{206}Pb/^{204}Pb$ and **b)** $^{143}Nd/^{144}Nd$. Range of Atlantic MORB $^{143}Nd/^{144}Nd$ data from O'Nions et al. (1977), Cohen et al. (1980), Cohen & O'Nions (1982b), White & Hofmann (1982). Crosses show data for other similar Reykjanes Peninsula lavas taken from Jakobsson et al. (1978) and Zindler et al. (1979). MORB endmembers for Reykjanes Ridge and Kolbeinsey Ridge from Cohen et al. (1980) and Mertz and Devey (pers.comm.) respectively. **c)** $^{206}Pb/^{204}Pb$ verses $^{208}Pb/^{204}Pb$. The hatched field shows existing data for post-glacial Icelandic basalts (Sun & Jahn 1975), the shaded field shows data for the submarine Reykjanes Ridge basalts (Sun et al. 1975), and the bar shows the range of Pb isotope values for samples from the Kolbeinsey Ridge (Mertz and Devey, pers. comm.). The double headed arrow shows the range of Atlantic MORB Pb isotope values (Sun et al. 1975, Cohen et al. 1980, Cohen & O'Nions 1982b, Tatsumoto 1978, Sun 1980, Dupré & Allègre 1980) and is aligned to best fit the data. Symbols for Reykjanes Peninsula and Theistareykir suites as in Fig. 4.2. Analytical techniques described in Table 4.1. Analytical uncertainies, as assessed by 2σ deviation of replicate analyses of standards, are shown by crosses.

Previous studies have noted variations of incompatible element ratios with both $^{87}Sr/^{86}Sr$ and $^{143}Nd/^{144}Nd$ for Icelandic basalts (O'Nions et al. 1976, Langmuir et al. 1978, Zindler et al. 1979). However this study additionally reveals correlations of incompatible element and isotopic ratios with major elements such as FeO (Fig. 4.4). Although the two suites have similar Nd, but distinct Pb isotope ratios, it is clear from Fig. 4.4a &b that the lowest FeO (highest MgO) lavas of each suite have the least radiogenic $^{206}Pb/^{204}Pb$, and the most radiogenic $^{143}Nd/^{144}Nd$.

Pb and Sr isotope ratios increase along the Reykjanes Ridge towards Iceland (Hart et al. 1973, Sun et al. 1975), suggesting a coupling of the thermal anomaly (i.e. crustal thickness and by isotacy, ridge depth) with the geochemical anomaly (i.e. enriched signature), that has been explained as a mixing of plume and MORB endmembers. The new Pb isotope data for the high MgO lavas are compared with existing data for recent Icelandic basalts, and Atlantic MORB in Fig. 4.4c. The lavas of the high MgO suites not only have depleted Pb isotope ratios with respect to the Icelandic basalt field, but overlap the fields for their adjacent oceanic ridges. Moreover the lowest FeO (highest MgO) lavas from Theistareykir and the Reykjanes Peninsula have Pb isotope ratios *as depleted* as the most depleted MORB endmembers from the Kolbeinsey Ridge (Mertz and Devey pers. comm.) and the Reykjanes Ridge (Sun et al. 1975) respectively.

$^{143}Nd/^{144}Nd$ ratios of the high MgO suites are also depleted with respect to typical Icelandic basalts, although the most depleted values (for the lowest FeO lavas) are *not* as high as the MORB endmembers of the adjacent ridges (Fig. 4.4b). $^{87}Sr/^{86}Sr$ variation correlates inversely with $^{143}Nd/^{144}Nd$ (not shown, see Table 4.1) as is consistent with other recent data (Condomines et al. 1983), and similarly, as with the Nd isotope ratios, the most depleted $^{87}Sr/^{86}Sr$ of the high MgO suite (0.7029) is not as low as has been observed in MORB endmembers of the Kolbeinsey and Reykjanes Ridges (0.7028, Mertz and Devey pers. comm. and 0.7026, Hart et al. 1973). Nevertheless, all three isotopic tracers, as with the incompatible element ratios, highlight a decoupling of the geochemical signatures of plume melts inferred from major and incompatible elements respectively.

4.3 Dynamic Melting Processes

The geochemical variations observed in the Icelandic high MgO suites cannot be explained by fractional crystallisation or variable degrees of batch melting. The variations in FeO content of the high MgO lavas suggest a polybaric melting process, since at constant pressure the FeO content of a basaltic melt from a mantle source is little affected by the degree of melting (Jaques & Green 1980, Stolper 1980, Falloon & Green 1988). However, at higher pressures, partial melts have higher FeO contents than at lower pressure (Jaques & Green 1980, Stolper 1980, Falloon & Green 1988). The FeO variations shown by the high MgO lavas could thus be the result of mixing FeO rich melts from depth with shallower FeO poor melts. Dynamic melting models invoke melting over a depth (pressure) range, and have been used successfully, for both geophysical and geochemical reasons, to explain MORB genesis (McKenzie & Bickle 1988, Klein & Langmuir 1987, Langmuir et al. 1977, McKenzie 1985).

Dynamic melting is more fully described elsewhere (McKenzie 1984, Klein & Langmuir 1987, McKenzie 1985), but a sketch model is shown in Fig. 4.5. Adiabatically upwelling mantle intersects its solidus, and melts along its flow-line for the rest of its ascent. Estimated rates of melt extraction in silicates suggest that the melt produced will be extracted continuously during ascent and that the porosity of the melting column will be small (< 2%, McKenzie 1984). It is envisaged that all 'instantaneous' melts are continuously extracted from all levels, mixed and erupted as an average (termed 'point and depth average' in McKenzie & Bickle 1988) of the entire column production. The system is in steady state, with unmelted mantle entering the bottom of the melting column as the mantle residue leaves the top of the column.

In such a model the deeper, FeO rich magmas represent the first melts of 'fertile' mantle entering the bottom of the melting column and so they will have the highest incompatible element contents. Conversely the FeO poor magmas from higher in the melting column are derived from mantle that has already undergone melt extraction throughout the underlying melting column, and so the FeO poor magmas have very depleted incompatible element contents. Such depletion will be greatest for the most incompatible elements. This model readily explains the variations incompatible elements in the high MgO

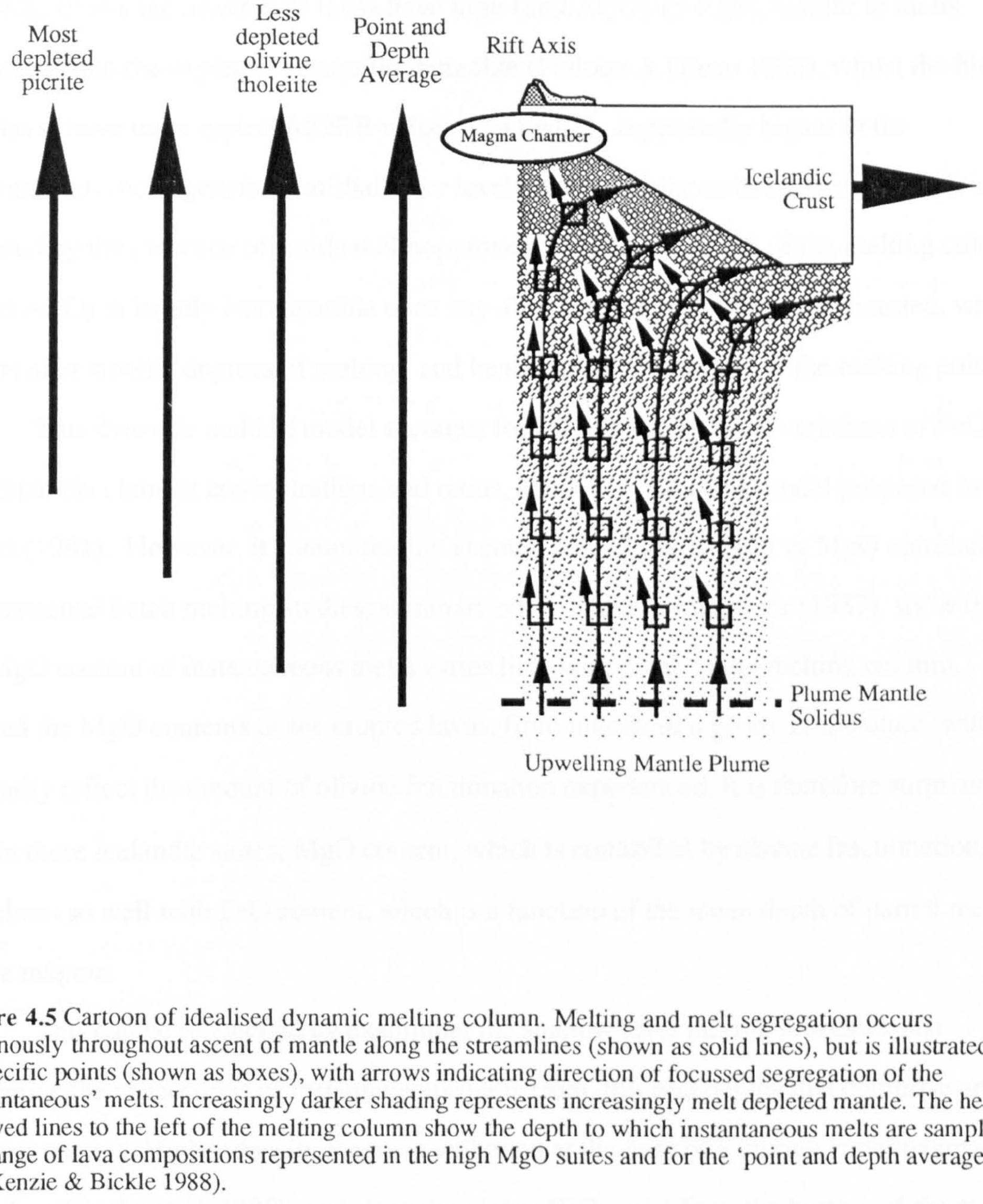

Figure 4.5 Cartoon of idealised dynamic melting column. Melting and melt segregation occurs continously throughout ascent of mantle along the streamlines (shown as solid lines), but is illustrated only at specific points (shown as boxes), with arrows indicating direction of focussed segregation of the 'instantaneous' melts. Increasingly darker shading represents increasingly melt depleted mantle. The heavy arrowed lines to the left of the melting column show the depth to which instantaneous melts are sampled for the range of lava compositions represented in the high MgO suites and for the 'point and depth average' (McKenzie & Bickle 1988).

suite shown in Figs. 4.2&4.3. Notably, *all* the lavas of the high MgO suites are depleted with respect to an E-MORB composition (Sun & McDonough 1988, Fig. 4.3a), that is typical of the more abundant, lower MgO Icelandic tholeiites (Meyer et al. 1985). This suggests that none of the high MgO lavas sample the most enriched instantaneous melts from the bottom of the melting column, as illustrated in Fig. 4.5.

Indices of major element depletion are also related to the FeO content of the lava. Fig. 4.2c shows the lower FeO lavas have high CaO/Al_2O_3 (> 0.85), similar to melts produced from the depleted Tinaquillo lherzolite (Falloon & Green 1988), whilst the higher FeO lavas have more typical MORB values. CaO/Al_2O_3 is generally higher in the instantaneous melts generated at shallower levels in the melting column, because CaO is buffered by the presence of residual clinopyroxene throughout much of the melting column, whilst Al_2O_3 is largely incompatible once any aluminous mantle phase is exhausted, which occurs after smaller degrees of melting, and hence nearer the bottom of the melting column.

This dynamic melting model accounts for the large, correlated variations of FeO with incompatible element concentrations and ratios, and it is similar to a model proposed by Wood (1981). However, it cannot readily account for the strong FeO vs MgO correlation. Experimental batch melting studies, summarised by Klein & Langmuir (1987), show that the MgO content of instantaneous melts varies little with depth in the melting column. Instead the MgO contents of the erupted lavas, from mantle of a given temperature, will primarily reflect the amount of olivine fractionation experienced. It is therefore surprising that in these Icelandic suites, MgO content, which is controlled by olivine fractionation, correlates so well with FeO content, which is a function of the mean depth of partial melting of the magma.

This can be reconciled by examining the shallow level mixing processes that determine the proportions of instantaneous melts from different depths that comprise any erupted magma. Higher density magmas will pond at the base of a mixing zone/magma chamber (Sparks et al. 1980), and since the higher FeO melts from the bottom of the melting column will be denser than those with lower FeO (at similar MgO) produced from the top of the melting column, they will not mix readily. Sparks et al. (1980) argued that picritic melts would be trapped at the base of a more evolved, basaltic mid-oceanic magma chamber until

they had fractionated sufficient olivine to reduce their density enough to mix with the other magmas. The situation envisaged for the Icelandic high MgO suites is similar, but with more FeO rich picrites being trapped beneath less FeO rich picrites. The deepest, highest FeO instantaneous melts are the densest melts and must thus fractionate the most olivine to mix and erupt. Since the highest FeO lavas must have the greatest proportion of such deep dense melts, these magma mixtures must have undergone the greatest net amount of olivine fractionation prior to eruption and hence have the lowest MgO contents. In contrast, the lowest FeO (highest MgO) magmas which have experienced little fractionation, represent almost primitive instantaneous melts from *higher* in the melting column.

4.4 Plume/MORB Interaction

Although the correlations between major elements and incompatible element contents and ratios within the high MgO suites can be modelled by melting and mixing processes of melts from a homogeneous source, the isotopic variations require contributions from isotopically distinct sources. The depleted isotopic signatures of the high MgO lavas with respect to the typical Icelandic tholeiites suggest the involvement of an N-type MORB source, and recent models show entrainment of MORB source mantle into a rising plume (Griffiths & Campbell 1990), that will subsequently melt as it upwells beneath a ridge axis.

For a given degree of MORB contamination, the most incompatible element depleted lavas will show the greatest isotopic change. Additionally, such contamination will have a greater effect on Pb than Nd isotope ratios, since the former element is more incompatible in the upper mantle, and hence more depleted in the high MgO lavas. This explains why the Pb isotope ratios in the lowest FeO basalts of the Theistareykir and Reykjanes Peninsula suites are as *unradiogenic* as the MORB endmember of the Kolbeinsey Ridge and Reykjanes Ridge respectively, whilst the corresponding highest $^{143}Nd/^{144}Nd$ are *not* as depleted as Nd in the adjacent MORB. A quantitative treatment of these mixing processes is attempted in Chapter 5.

Since MORB from the Kolbeinsey and Reykjanes Ridges have distinct Pb, but similar Nd isotopic compositions, contamination of the high MgO lavas by their respective adjacent MORB reservoirs results in distinct Pb isotope fields for the Theistareykir and Reykjanes Peninsula, but just one Nd isotope array. What is less clear is why the Pb values

of the two suites do not converge towards a single plume isotopic composition at high FeO, but towards apparently distinct endmembers (Fig. 4.4a), suggesting Pb isotope heterogeneity within the plume over the scale of several hundred kilometers. Although they analysed samples of various ages, Welke et al. (1968) also observed that the Pb isotope ratios in samples from the south and west of Iceland, were more radiogenic than those from the north and east.

Whilst mixing between plume and small amounts of MORB melts is required to explain the isotopic variation observed in the high MgO suite, it is important to stress that the principal control on the geochemical variation is nevertheless the melting processes described in the previous section, and not simple mixing between MORB and an FeO, incompatible element rich plume. For example, in such a mixing scenario, the Pb isotopic ratios of the lowest FeO lavas of the suites would suggest that they represent pure MORB endmember compositions, however the $^{143}Nd/^{144}Nd$ (and $^{87}Sr/^{86}Sr$) data of the same samples is incompatible with this (Fig 4.4).

4.5 Implications of the Melting Model

The parameterisations of McKenzie & Bickle (1988) and more recent refinements of Watson & McKenzie (1991) suggest that the high degree melts required to generate the thickness of the Icelandic crust must have a composition that has MgO> 15% . Their calculations estimate the sum of all the instantaneous melts from the *whole* melting column, and so such a calculated high MgO melt is also expected to possess enriched incompatible element ratios, characteristic of the enriched plume. In Meyer et al.'s (1985) comprehensive data set of Icelandic rift basalts, whilst the majority have enriched, E-MORB like incompatible element ratios, none of these enriched lavas has MgO>9%. Conversely, the high MgO basalts of this study all have depleted incompatible element ratios with respect to E-MORB (Fig 4.3a).

It is argued above that the FeO, MgO and SiO_2 variations within the high MgO suite suggest that the dense, FeO and incompatible element rich melts from the bottom of the melting column fractionate olivine in order to be sampled at the surface (as mixtures with shallower melts from the column). Thus, although a theoretical 'parental' melt from the Iceland plume is both enriched in incompatible element ratios and has high MgO content

(>15%), this is never realised in practice because in order to mix all of the independently segregated instantaneous melts to produce a point and depth average, some olivine fractionation must occur. Thus the more common, fractionated (MgO<9%) Icelandic basalts sample instantaneous melts from the whole of the melting column, and so erupt with a full complement of incompatible elements from the melting column (and hence enriched incompatible element ratios), but without the full budget of olivine compatible elements. More rarely, as observed in this study, melts from the upper portion of the melting column can erupt as lavas with more primitive MgO contents, by escaping mixing (and attendant fractionation) with the complementary enriched melts from the bottom of the melting column, but they carry only a small proportion of the incompatible elements expected for a point and depth average of the whole melting column.

Hence although the high MgO lavas have primitive Mg#, their compositions cannot be inverted to deduce information about the Iceland plume source. However, if as believed, the MgO contents of instantaneous melts remain constant throughout the melting column, the least fractionated lavas of this study provides an important constraint on the MgO content of plume derived melts. It might be argued that the composition of the lavas with the highest MgO contents of the Theistareykir and Reykjanes Peninsula suites do not represent liquid compositions, but indicate cumulus olivine (as for the Réunion picrites, Alberède & Tamagnan 1988). However, while two samples clearly are olivine cumulates (Fig. 4.2b), the other samples all lie on coherent geochemical trends that cannot be explained by olivine addition. Moreover, the forsterite contents of the olivine phenocrysts of the most magnesian lavas imply equilibrium with liquids of 12-14% MgO. Hence it is reasonable to argue that the high MgO endmember of these trends represents a liquid composition, with 14-16% MgO (Fig. 4.2b). This is similar to the values based on geochemical and theoretical estimates for primitive MgO contents of Hawaiian plume melts (Watson & McKenzie 1991, Nicholls & Stout 1988, Rhodes 1990) and hence suggests a similar potential temperature for both plumes.

Although melts from beneath Iceland are derived from hotter and geochemically enriched mantle, geophysically similar processes occur beneath all spreading ridges. Noticeably, the correlation of FeO vs Na_2O in the high MgO suites is consistent with the

vector of local variation observed in individual ridge segments from a global MORB database by Klein and Langmuir (1987).

Trends of decreasing CaO/Al_2O_3 with increasing TiO_2 contents and decreasing Mg# observed in some MORB suites have been explained by clinopyroxene fractionation even though no clinopyroxene phenocrysts are observed, or even predicted for such melt compositions (Dungan & Rhodes 1978, Rhodes et al. 1979). However, for the Icelandic high MgO suites it is argued that CaO/Al_2O_3 variation is a partial melting effect with decreasing CaO/Al_2O_3 correlating with increasing TiO_2, thus mimicking a fractionation trend involving clinopyroxene. Furthermore, the lavas with lower CaO/Al_2O_3 are also those which represent a melt mixture with a larger proportion of melts from the bottom of the melting column, that had to fractionate more olivine before mixing could occur. Thus, the partial melting effects controlling CaO, Al_2O_3 and TiO_2 are accompanied by a decrease in MgO resulting from the removal of olivine. This combination generates the chemical features which might be attributed to clinopyroxene fractionation without the involvement of this phase.

The Icelandic high MgO suites display large variations in incompatible element contents and ratios as a result of mixing various proportions of instantaneous melts from different depths of the melting column. It is argued that most MORBs may represent a similar 'cocktail' of melts segregated from different depths and mixed in an axial chamber. Though a local average of numerous MORB compositions will reflect the incompatible element ratios of the point and depth averaged melt of the underlying mantle, chemical variability of individual lavas is likely to result from different mixes of melts, segregated from various levels, feeding the magma chamber at any given instant.

Chapter 5

Modelling the Dynamic Melting Column beneath Iceland.

In the last chapter it was argued that the correlated major and incompatible element variations within high MgO tholeiites of the main Icelandic rift can be explained by the sampling of instantaneous melts to various depths within a dynamic melting column, and that isotopic variation within these lavas is the result of mixing these melts with MORB melts. This chapter quantitatively models these processes, which initially requires an assessment of the various mantle sources involved and the physical parameters of the Icelandic melting column. Potential mantle sources beneath Iceland are constrained by a requirement to account for the geochemical variation within *all* recent Icelandic lavas, rather than just the high MgO lavas, and the melting column is modelled from geophysical considerations. The synthetic dynamic melts generated from a primitive mantle source, mixed with some 20% MORB, reproduce reasonably well the range of chemical variation observed within the high MgO lavas.

5.1 Diversity of Icelandic Lava Types

The variety of sources and processes operating beneath Iceland are well illustrated by the variety of lava types observed. Jakobsson (1972) identified important variations of lava chemistry with geographical position and tectonic setting within Iceland (Fig 5.1). By studying only the post-glacial lavas (<10,000a), which are clearly identifiable in the field, reasonable estimates of the comparative volumes of the different lava types erupted within this period can be made, and hence the relative rates of production can be constrained. Some 85% of post-glacial lavas are tholeiites and hence these lavas represent the principal product of melting in the Icelandic plume. Tholeiitic lavas are erupted along the central rift zone, the onshore continuation of the mid-Atlantic Rift (Fig 5.1). There is variation within the tholeiitic lavas from picrites, olivine tholeiites, quartz tholeiites through to rhyolites (Jakobsson 1972, Jakobsson et al 1978). Lavas more evolved than the olivine tholeiites have undergone fractionation and frequently have assimilated older, altered crust (Oskarsson 1982, Hemond et al 1988, Nicholson et al. in press). In the interior of Iceland

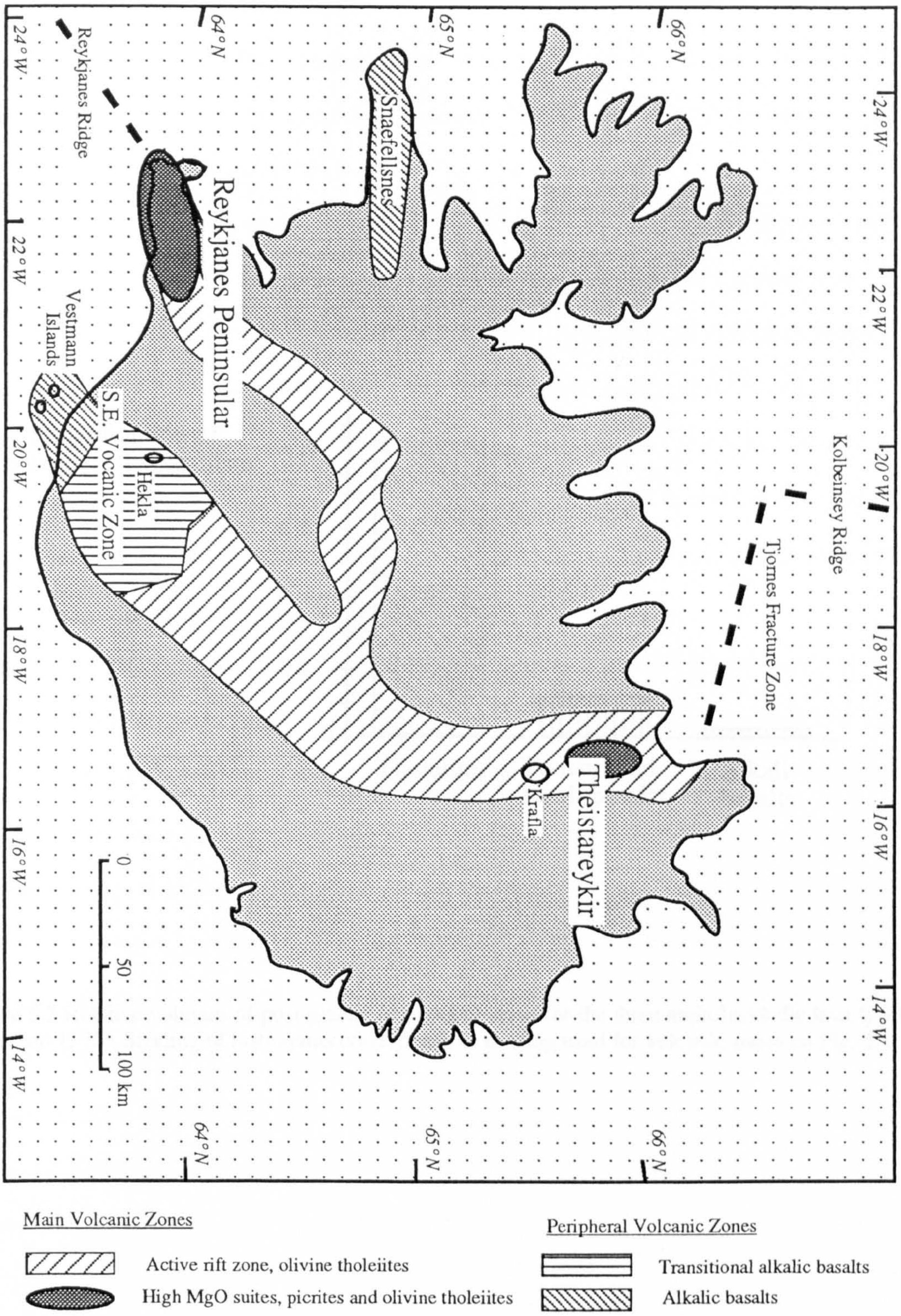

Figure 5.1 Sketch map of the major zones of volcanic activity on Iceland.

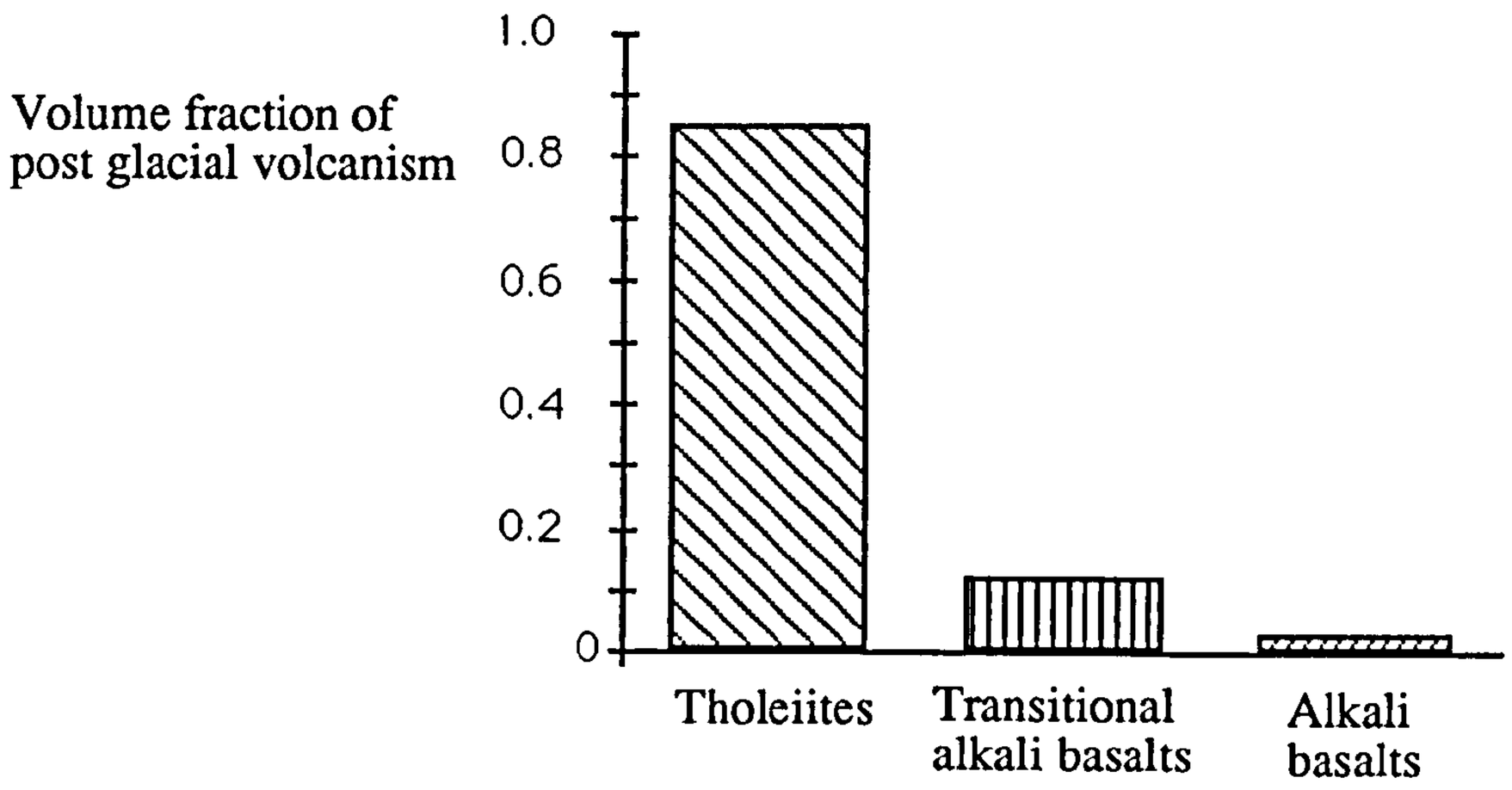

Figure 5.2 Relative volumes of post-glacial (<10,000a) lavas for the three main Icelandic lava types (after Jakobsson 1972). Shading of histograms corresponds to shading used for volcanic zones on Fig. 5.1.

the products of rift volcanic centres are generally more evolved, but within the more basic volcanic zones of the central rift, the Reykjanes Peninsula for example, the parental nature of the olivine tholeiite magmas is suggested by the volumetric dominance of such lavas, locally 74% (Jakobsson et al. 1978). The apparently more primitive picrites are not only rare (<3% total volume), but as discussed in the last chapter, they do not sample the whole melting column and cannot be considered 'parental'.

Alkalic and transitional alkali basalts occur in zones peripheral to the central rift. Transitional alkali basalts were erupted in the S.E. volcanic zone, in a region which is thought to represent an onshore analogue of a propagating ridge tip (Oskarsson et al. 1982), and they represent ~12% of the total volume of post glacial lavas (Jakobsson 1972). Alkali basalts were erupted in the Vestmann Islands at the very south of the S.E. volcanic zone and also in the Snaefellsnes Peninsula, the tectonic setting of which is less clear. In total they account for a mere 3% of post-glacial volcanism and Fig. 5.2 summarises the relative volumes of post-glacial lavas (after Jakobsson 1972).

The clear variations of the major element composition of Icelandic lavas with geographic position are also reflected in different primitive mantle normalised rare earth element (REE) ratios (Fig 5.3 & 5.4). (All primitive mantle normalisations in this chapter use the values from Sun & McDonough 1989). Although the tholeiites have a wide range of rare earth element patterns, from the strongly depleted picrites to slightly LREE enriched olivine tholeiites (e.g. Fig. 5.3a), the *majority* of the tholeiites have flat or slightly LREE enriched profiles (Fig. 5.4). Much of the variation of REE patterns in the tholeiites (Fig. 5.3a) is represented in volumetrically minor lavas (such as most of the high MgO lavas of this study), that do not sample the whole of the melting column (as discussed in the last chapter). The transitional and alkali basalts are more LREE enriched than the tholeiites (Figs. 5.3 & 5.4), and this contrast is readily explained in terms of their geographical location with respect to the plume and crustal rifting.

The thermodymanics of adiabatically upwelling mantle requires that the thick oceanic crust at Iceland (Palmason & Saemundsson 1974, Gebrande et al. 1980) results from melting of hot mantle. Such anomalously hot mantle has been modelled by McKenzie & Bickle (1988) to be ~200°C hotter than MORB source mantle, and to intersect its solidus at a

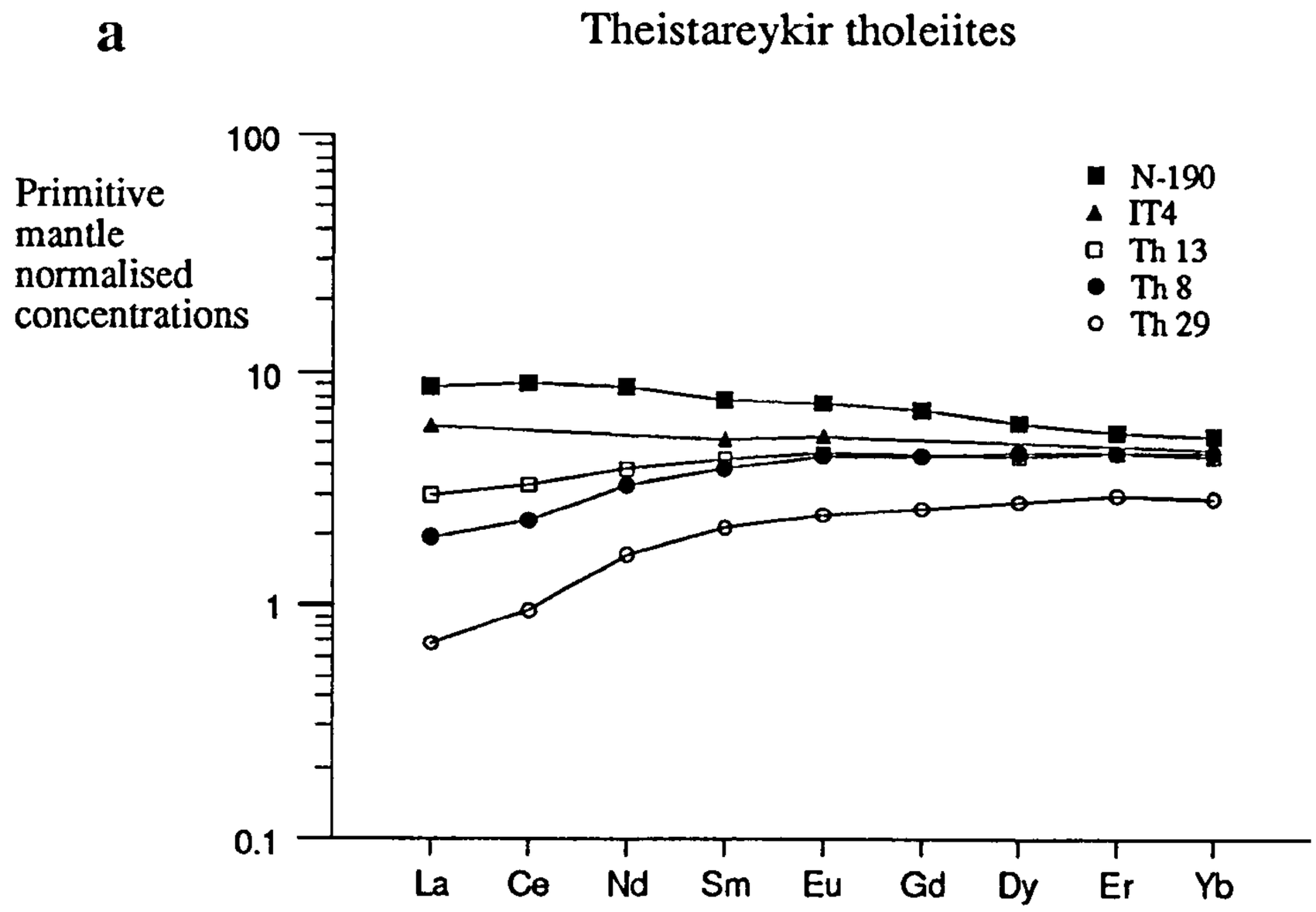

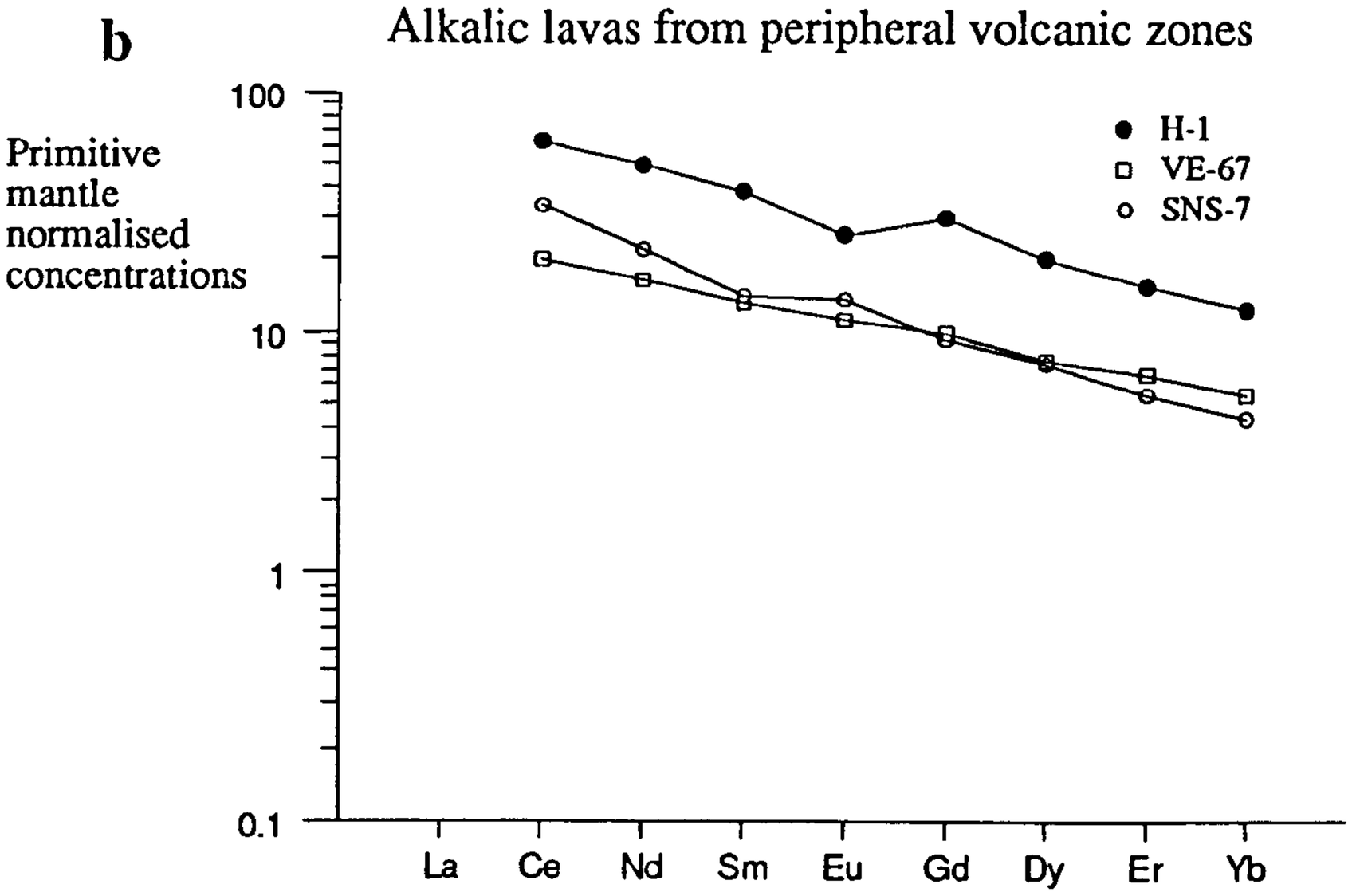

Figure 5.3 Representative, primitive mantle normalised rare earth element patterns for **a)** 'primitive' tholeiites (olivine tholeiites and picrites) and **b)** transitional alkali basalts and alkali basalts. Tholeiitic samples Th 29, Th 8, Th 13 (O'Nions et al 1976) and IT4 (this study) are from Theistareykir, N-190 is from Namafjall (O'Nions et al 1976) near Krafla, and cover the *range* of rare earth element profiles shown by 'primitive' tholeiites. However, the highly depleted patterns are uncommon, and the profiles of IT4 and N-190 are typical of the more volumetrically significant tholeiites (see Fig. 5.4). The two alkali basalts SNS-7 and VE-67 are from Snaefellsnes (O'Nions et al 1976) and the Vestmann Islands (O'Nions et al 1973) respectively, and the transitional alkali basalt HE-1 is an Icelandite from Hekla (O'Nions & Grönvold 1973). HE-1 is more evolved than the other samples, and shows a negative Eu anomaly and elevated Yb contents, but clearly still has a steep REE pattern, that is not a funcytion of crystal fractionation.

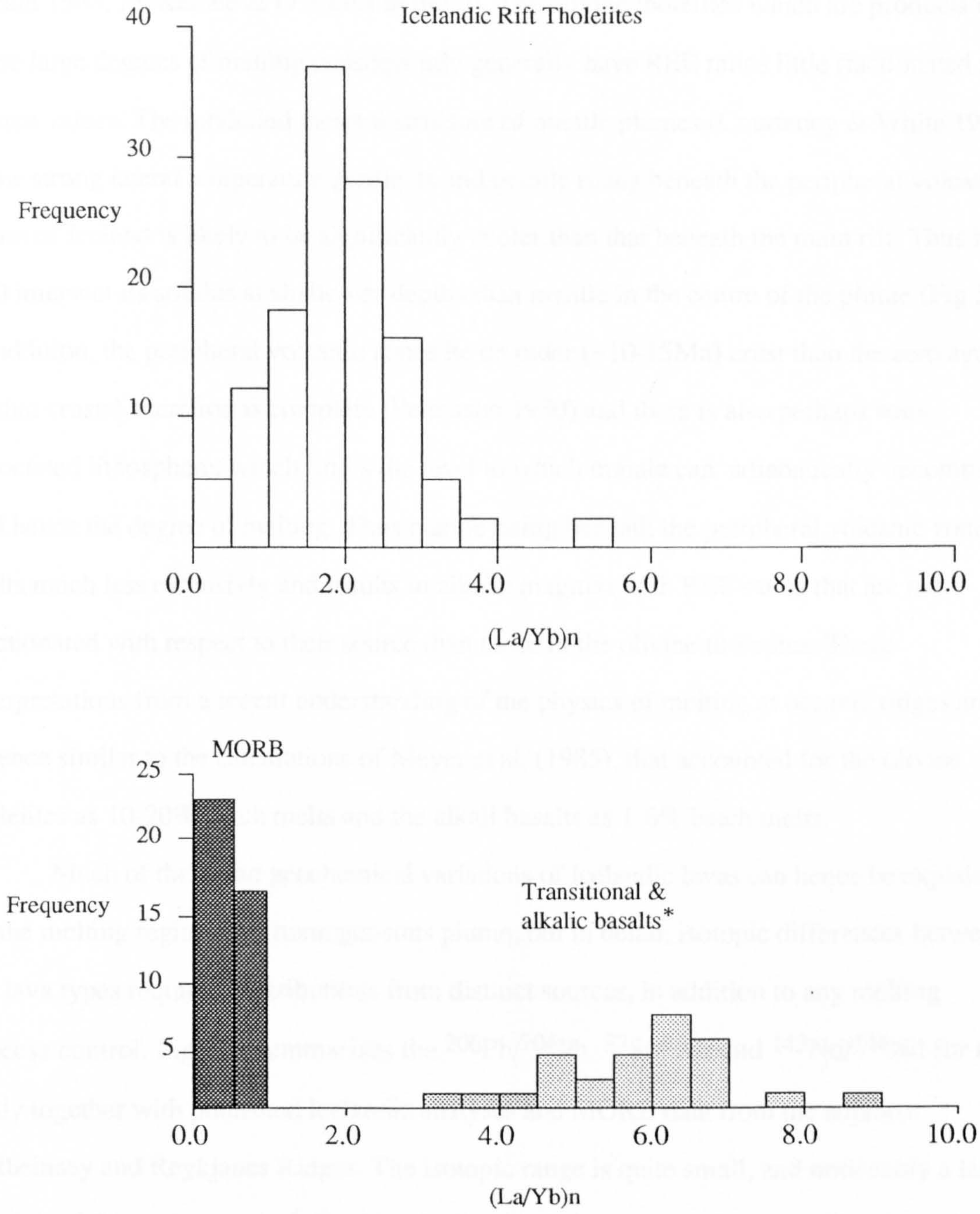

Figure 5.4 Histograms for primitive mantle normalised La/Yb ratios for **a)** tholeiites from the main rift (Schilling et al. 1978, Meyer et al. 1985), and **b)** MORB, from Kolbeinsey and southern-most Reykjanes Ridge (darkest stipple, Mertz & Devey, pers comm. and Schilling 1973 respectively), transitional alkali basalts (lightest stipple, Meyer et al 1985) and alkali basalts (medium stipple, O'Nions et al 1973 and O'Nions et al. 1976). *The lowest three values plotted for alkali basalts are $(Ce/Yb)_n$ not $(La/Yb)_n$, since no La data are available for these alkali basalts (O'Nions et al. 1973), and hence their $(La/Yb)_n$ ratios are probably higher.

depth of 120km (Fig 5.5). Such hot mantle rising beneath the central rift upwells to within a few kilometeres of the surface, and undergoes large degrees of melting, ~20% (McKenzie & Bickle 1988, McKenzie & O'Nions in press). The olivine tholeiites which are products of these large degrees of melting consequently generally have REE ratios little fractionated from source values. The modelled thermal structure of mantle plumes (Courteney & White 1986) show strong lateral temperature gradients and mantle rising beneath the peripheral volcanic zones of Iceland is likely to be significantly cooler than that beneath the main rift. Thus it will intersect its solidus at shallower depths than mantle in the centre of the plume (Fig 5.5). In addition, the peripheral volcanic zones lie on older (~10-15Ma) crust than the zero age rift so that crustal accretion is complete (Palmason 1980) and there is also perhaps some associated lithosphere, which limits the level to which mantle can adiabatically decompress, and hence the degree of melting. Thus mantle rising beneath the peripheral volcanic zones melts much less extensivly and results in alkalic magmas with REE ratios that are more fractionated with respect to their source than those in the olivine tholeiites. These interpretations from a recent understanding of the physics of melting at oceanic ridges are in essence similar to the calculations of Meyer et al. (1985), that accounted for the olivine tholeiites as 10-20% batch melts and the alkali basalts as 1-6% batch melts.

Much of the broad geochemical variations of Icelandic lavas can hence be explained by the melting regime of a homogeneous plume, but in detail, isotopic differences between the lava types requires contributions from distinct sources, in addition to any melting process control. Fig. 5.6 summarises the $^{206}Pb/^{204}Pb$, $^{87}Sr/^{86}Sr$ and $^{143}Nd/^{144}Nd$ for this study together with published Icelandic analyses and MORB data from the adjacent Kolbeinsey and Reykjanes Ridges. The isotopic range is quite small, and noticeably a large fraction of the total range is defined by the isotope ratios of the volumetrically minor picritic and alkalic lavas. The olivine tholeiites not only have more enriched LREE contents than adjacent MORB (Fig. 5.4) but they are also relatively isotopically enriched (higher $^{206}Pb/^{204}Pb$, $^{87}Sr/^{86}Sr$ and lower $^{143}Nd/^{144}Nd$). Likewise, the alkalic basalts are more LREE enriched than the tholeiites and they also tend to have more enriched isotopic ratios and, conversely, the very LREE depleted picrites have the most depleted isotopic ratios. This makes it more difficult to distinguish between incompatible element fractionation that is

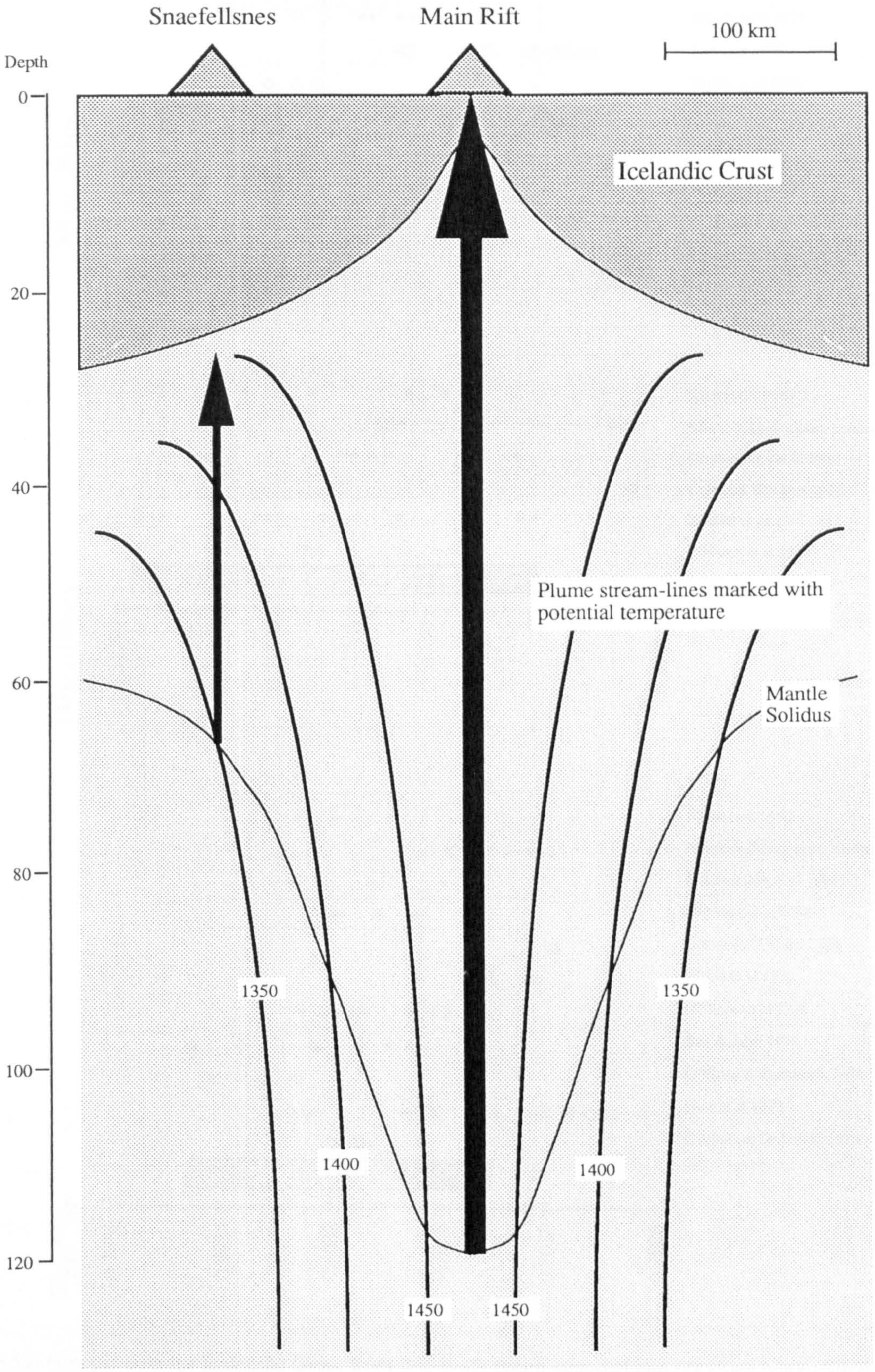

Figure 5.5 Sketch of mantle structure beneath Iceland. The thermal structure of the up-welling plume determines the depth of the mantle solidus beneath Iceland, which becomes shallower radially away from the plume centre that lies beneath the rift axis. The thickness of the overlying, accreting crust (and lithosphere?) also affects the length of melting columns, which are indicated by arrowed lines. The thickness of the arrowed lines reflects the relative overall degree of melting produced by the column.

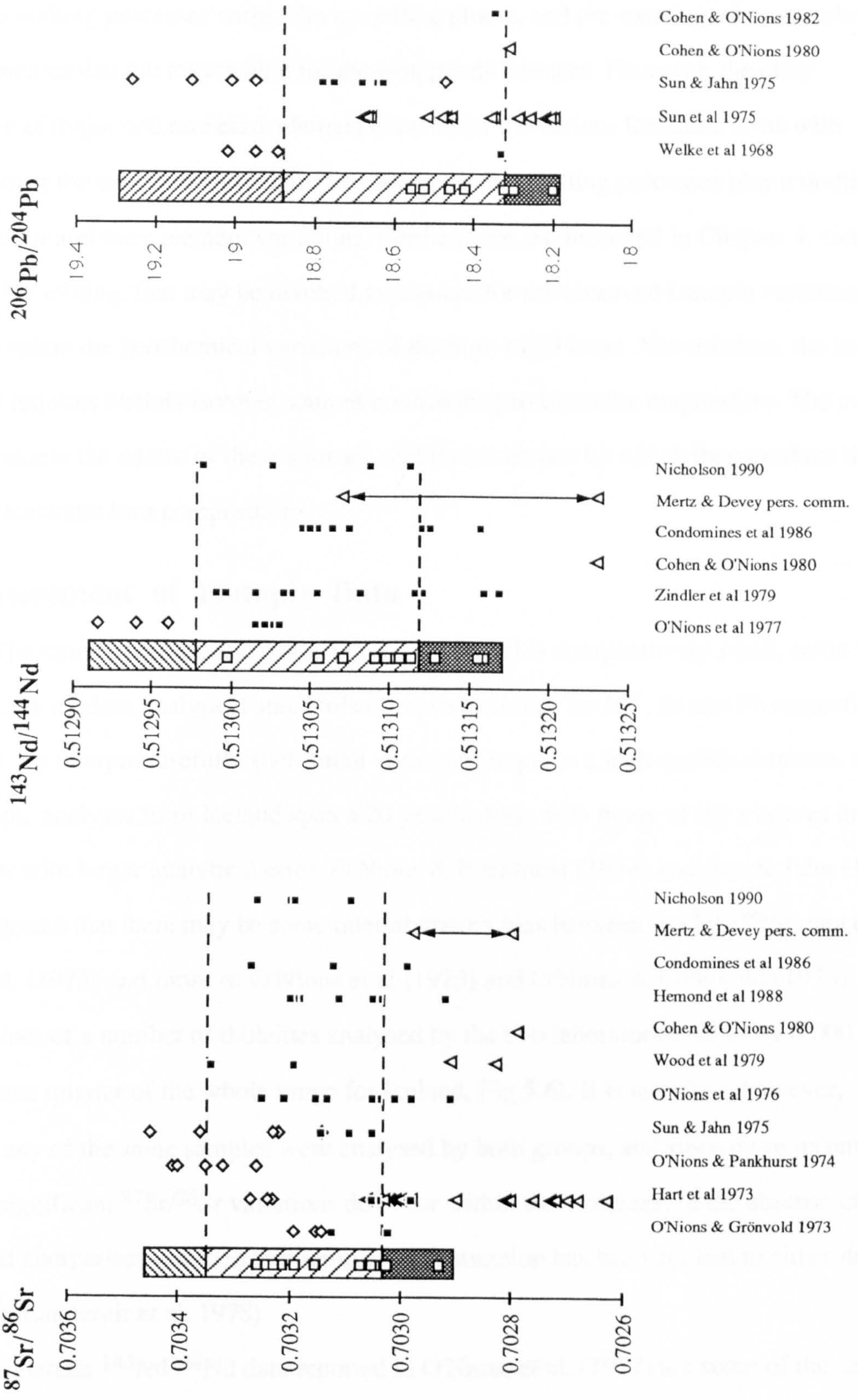

Figure 5.6 Isotopic data for Icelandic lavas, from this study (open squares) and previous work (filled squares are tholeiites from the main rift, open diamonds are alkali basalts and open triangles are MORBs from adjacent ridges). The box at the left side of each diagram shows the complete range recorded in Icelandic lavas, with that part of the range defined only by picritic (MgO>10%) and alkali basalt samples shown as dark stipple and close diagonal shading respectively. The dashed lines show the isotopic range of olivine tholeiites, the volumetrically most important lava type. Some $^{87}Sr/^{86}Sr$ analyses from the literature in which crustal assimilation is suspected have been excluded from the data set.

related to melting processes within the upwelling plume, and pre-existing, old trace element heterogeneities that are responsible for the isotopic differences. However, the clear coherence of major and rare earth element contents of the various Icelandic lavas with position over the expected melting regime, suggests that melting processes play a dominant role in major and trace element variations. Furthermore, as discussed in Chapter 4, simple endmember mixing, that may be invoked to account for the observed isotopic variations, cannot explain the geochemical variations of the high MgO lavas. Nevertheless, the isotopic variation requires distinct isotopic sources contributing to Icelandic magmatism. The next sections assess the nature of these sources, and the processes by which they produce the range in Icelandic lava compositions.

5.2 Assessment of Isotopic Data

The range of radiogenic isotope ratios in Iceland is comparatively small, some 6x, 11x and 36x modern analytical standards of reproducibility for Nd , Sr and Pb respectively (Fig 5.6). To interpret usefully such small variations requires a high quality database, and yet isotopic analyses from Iceland span a 20 year history, with many of the analyses made in the 1970s with larger analytical error. O'Nions & Pankhurst (1974) and Sun & Jahn (1975) also suggested that there may be some interlaboratory bias between the $^{87}Sr/^{86}Sr$ data of Hart et al. (1973) and those of O'Nions et al (1973) and O'Nions & Grönvold (1973). The *mean* values of a number of tholeiites analysed by the two laboratories differ by 0.00011 (almost one quarter of the whole range for Iceland, Fig 5.6). It is not clear, however, whether any of the same samples were analysed by both groups, and since more recent data suggest significant $^{87}Sr/^{86}Sr$ variations do occur within the tholeiites, in the absense of published comparisons of the same samples, no correction has been applied to either data set (unlike in Langmuir et al. 1978).

Icelandic $^{143}Nd^{144}Nd$ data reported in O'Nions et al. (1977) are some of the earliest published Nd isotope measurements, and in the light of more recent analyses, appear unreliable at the level of precision needed in studying Iceland. For example, Th 29 is one of the most incompatible element depleted samples from Iceland, and for Sr (also Pb and Nd in this study, Table 4.1) is clearly isotopically depleted (O'Nions et al. 1976), yet the $^{143}Nd/^{144}Nd$ reported in O'Nions et al. (1977) is no more radiogenic than other Icelandic

samples measured in the same study which are much less depleted than Th29 in different isotopic and incompatible element tracers. In the same study (O'Nions et al. 1977), the $^{143}Nd/^{144}Nd$ of a Reykjanes Ridge basalt (R 40) is much lower (and plots within the Icelandic field) than a sample from a similar location (A59°46'N) reported in a later paper by Cohen et al. (1980). Unfortunately the lowest $^{143}Nd/^{144}Nd$ ratios reported for Iceland are from O'Nions et al. (1977), which places uncertainty on the accuracy overall Icelandic range in $^{143}Nd/^{144}Nd$.

Analytical problems aside, $^{87}Sr/^{86}Sr$ ratios have also been shown convincingly to increase by assimilation of hydrothermally altered Icelandic crust, even in basaltic quartz tholeiites (Hemond et al. 1988, Nicholson et al. in press). The very primitive lavas of this study are unlikely to have assimilated crust, but for many samples reported in the literature, it is difficult to assess the effects of possible contamination, and thus whether or not the $^{87}Sr/^{86}Sr$ ratios reported are primary signatures. Additionally, even young (<10,000a) lavas from the Reykjanes Peninsula have been shown to suffer contamination from sea spray (acid washed powders have lower $^{87}Sr/^{86}Sr$ ratios, K.Grönvold pers. comm.) and this casts doubt on the reliability of the Sr isotope data from unwashed Reykjanes powders (e.g. Zindler et al. 1979). There are few lead isotope data for Iceland, and the results from Chapter 4 indicate a major cross-Iceland Pb isotope variation, as was suggested by Welke et al. (1968). Thus it is unlikely that there is a single 'plume' endmember composition for Pb, and so the high Mgo suites from the N.E. and S.W. are treated seperately (Fig. 5.6 includes only data from the S.W of Iceland, since there are very few data on recent tholeiites from the N.E. section of the main rift zone).

5.3 Icelandic Plume Source

In Chapter 4, the 15 fold variation in K_2O and the correlation of incompatible trace element ratios with FeO content in the high MgO lavas was attributed to the primary control of a dynamic melting process on their melt composition. In order to model this process, the source which is melting to produce these variations must be assessed. The isotopic variations in Icelandic lavas shown in Fig. 5.6 requires that at least two source materials contribute to Icelandic magmatism. However the volumetric dominance of olivine tholeiites (Fig 5.2) with an average $^{87}Sr/^{86}Sr$ of 0.70317±0.0015 and $(La/Yb)_n$ of 2±1 (Figs. 5.6 and

5.4) requires that the net contributions from various sources produce such compositions.

Two endmember scenarios can be envisaged to explain these observations:

1. The plume is a heterogeneous on a small scale, in which enriched and depleted portions of mantle coexist. Olivine tholeiites represent the mean melt product of the heterogeneous plume, but sampling of various proportions of enriched and depleted plume mantle, results in the small variabilty of $(La/Yb)_n$ and $^{87}Sr/^{86}Sr$ in the olivine tholeiites. Melting of the more enriched portions alone can account for the alkali basalts.

2. The plume is characterised by enriched isotopic compositions, at least as enriched as those observed in the alkali basalts, but extensive mixing with depleted MORB melts results in the major products having the less enriched isotopic compositions of the olivine tholeiites. Isotopic variabilty results from different mixing proportions of plume and MORB, although given the fairly small range of isotopic variation within the olivine tholeiites, mixing processes generally mix similar amounts of enriched plume and depleted MORB. Melting of the plume endmember alone results in the alkali basalts.

Mixing of plume and MORB melts was initially suggested from the isotopic studies of Hart et al (1973) and Sun et al. (1975), and the rare earth element data from Schilling et al. (1973), which show increasingly MORB-like signatures in submarine basalts dredged from the Reykjanes Ridge, with distance from Iceland (Fig. 5.7). In particular, lead isotope ratios and (La/Sm) correlate well with latitude and hence increasing axial ridge depth (Fig. 4.1). Klein & Langmuir (1987) demonstrated that axial ridge depth is largely dependent on crustal thickness, which in turn reflects the degree of melting and hence temperature of the upwelling mantle below a ridge axis. Thus both the chemical and thermal signatures of the plume appear to decrease systematically along the Reykjanes Ridge providing strong evidence for MORB/plume mixing. However, the studies demonstrating such a mixing relation beneath the Reykjanes Ridge (Schilling 1973, Sun et al. 1975) include only data from olivine tholeiites as the Icelandic plume endmember. If all the geochemical variation on Iceland is to be explained by simple mixing of an enriched plume and MORB, the alkali basalts must also be included.

Langmuir et al (1978) examined the mixing relationships for all Icelandic and Reykjanes Ridge data, and found that *the full range* of data could not be modelled by simple

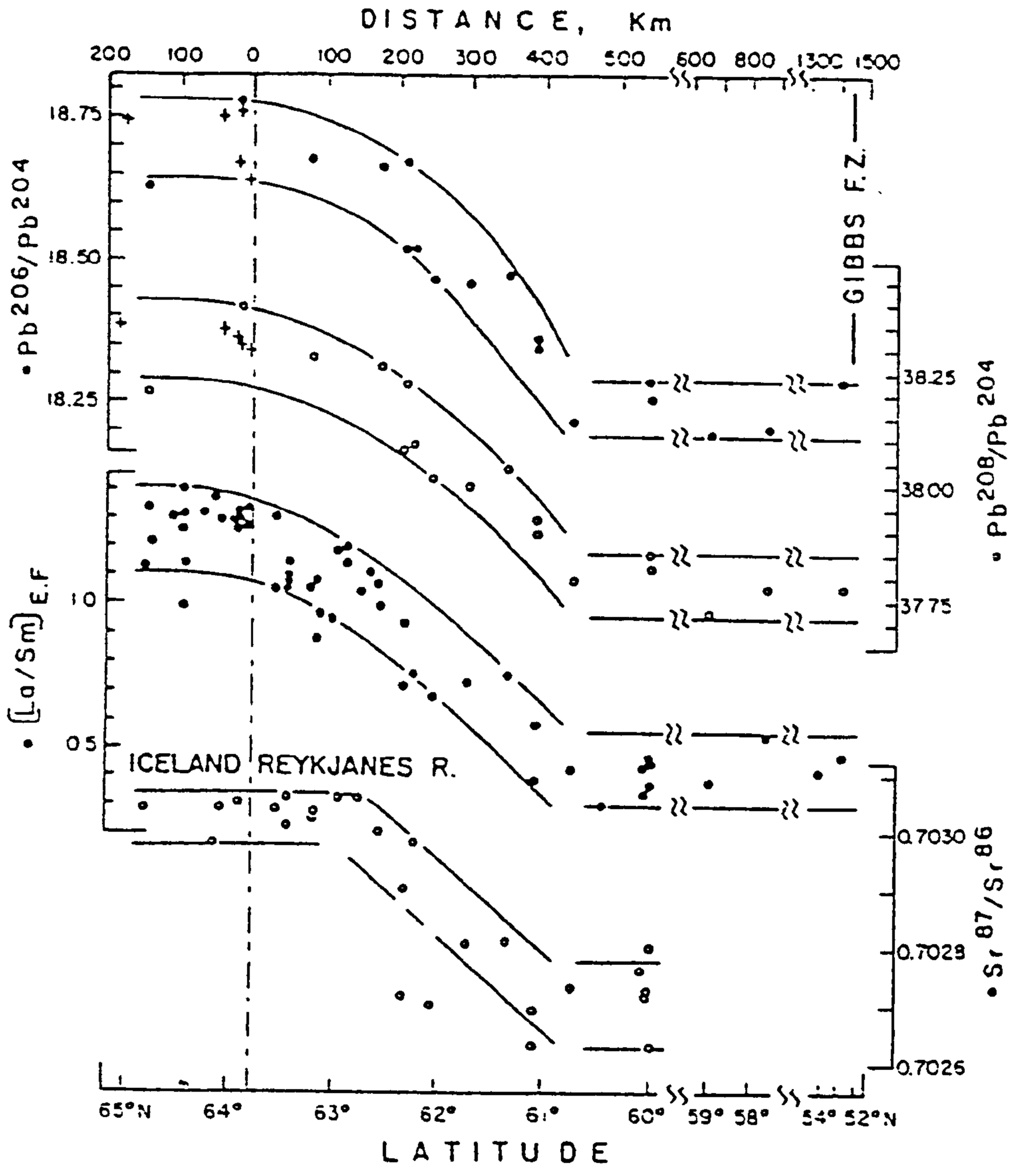

Figure 5.7 Variation with latitude of $^{206}Pb/^{204}Pb$, $^{208}Pb/^{204}Pb$, chondrite normalised La/Sm and $^{87}Sr/^{86}Sr$ in MORBs dredged from the Reykjanes Ridge. Decreasing latitude corresponds to increasing distance from Iceland and increasing depth of the ridge axis (see Fig. 4.1). Figure taken from Sun et al. (1975).

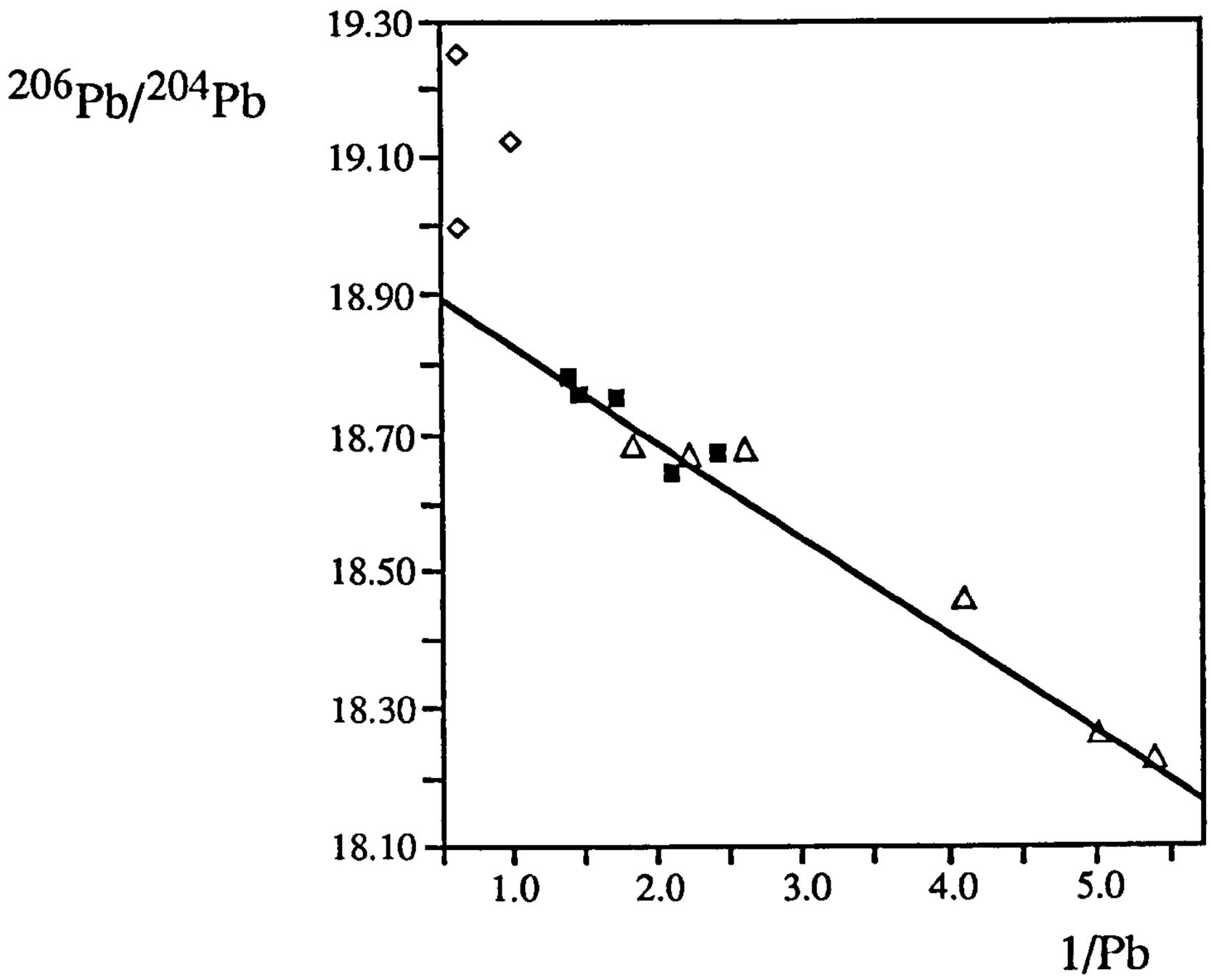

Figure 5.8 Variation of $^{206}Pb/^{204}Pb$ with 1/Pb for a range of Icelandic and Reykjanes Ridge basalts (after Langmuir et al. 1978). Symbols show Reykjanes Ridge MORBs as open triangles, Icelandic rift tholeiites as closed squares and alkali basalts as open diamonds. The line indicates a potential, simple mixing line for the Icelandic tholeiites and Reykjanes Ridge MORBs, but the alkali basalts clearly do not lie on the simple mixing trend.

two component mixing of plume and MORB. Although Langmuir et al. (1978) suggested that some mixing trends may be masked by dynamic melting effects (indeed in the light of this study that is now thought to be increasingly likely), it is clear in Fig 5.8 (taken from Langmuir et al. 1978, Fig.8) that the Icelandic alkali basalts do not lie on a simple mixing trend involving Icelandic tholeiites and Reykjanes Ridge samples. The abscissa of this plot is 1/Pb and it will be affected by the degree of melting, but since the alkali basalts are likely to be smaller degree melts (section 5.5.1) than the tholeiites, for similar degrees of melting 1/Pb would be larger and the fit worse.

Thus it appears that the olivine tholeiites are essentially the mean melt product of the plume alone (scenario 1, above). A rough assessment of the mean plume source may be made from using average trace elements contents of the olivine tholeiites and estimating the degree of melting beneath Iceland. The thick Icelandic crust suggests high degrees of melting beneath Iceland, and from two different approaches, Klein & Langmuir (1987) and McKenzie & Bickle (1988) estimate the chemistry and crustal thickness of Iceland to be consistent with ~20% melting. At such degrees of melting, the *residual* mantle will have very low bulk distribution coefficients for a large range of trace element ratios, and to a first approximation all the REE, for example, may be considered as totally incompatible. Mean primitive mantle normalised La and Yb contents from a large database of olivine tholeiites (Schilling et al. 1978, Meyer et al 1985) are 10 and 5 respectively, implying, at 20% melting for the tholeiites a mean plume source with 2x and 1x primitive mantle contents of La and Yb respectively.

However, the small but significant variations in isotopic ratios between the olivine tholeiites (Fig 5.6) require a heterogeneous source. The distinct lead isotope field for the Reykjanes Peninsula and Theistareykir discussed in Chapter 4 were argued to show a large scale Pb isotope heterogeneity between north and south Iceland, as has also been suggested by Welke et al (1968). Additionally, variations of $^{87}Sr/^{86}Sr$ ratios (and Nd and Pb isotopic ratios, although these are less extensively documented) of olivine tholeiites, further to the variation observed in the higher MgO lavas, occurs within individual volcanic zones on the scale of <10km. Likewise, although Fig 5.4 shows a strong peak at a mean $(La/Yb)_n$ for olivine tholeiites of 1.5-2, there is clearly greater a range of values, that also presumably

reflects differences in source composition. There may be a continous range in source compositions, but such variations can also be modelled in terms of mantle sources with different relative proportions of two plume 'components'.

In such a scenario, the most enriched component must have isotopic values as enriched as the alkali basalts, but the more depleted component is less well constrained. Two endmember compositions for the depleted component may be envisaged:

i) the depleted component is very depleted, and melts of the pure depleted component result in the compositions of the extremely depleted picrites.

ii) the depleted component has isotopic ratios similar to those of the less enriched olivine tholeiites (e.g. with $(La/Yb)_n \sim 1$), such that the more enriched tholeiites represent mixtures with small amounts of the enriched component, and the depleted picrites represent mixtures with MORB.

In both options, the enriched component must have LREE contents greater than 2x primitive mantle in order to account for the an average plume source with La~2x primitive mantle. However, since the most depleted picrites have melt La contents of ~0.5x primitive mantle and presumably a source with even lower values, to produce a mean plume source of 2x primitive mantle in option i), from mass balance arguments, the plume would have to consist predominantly of highly depleted mantle. If the bulk of the plume consisted of highly depleted mantle this may be reflected in the major element compositions of the average melts, although their incompatible element concentrations would be dominated by the enriched component. A depleted plume would be expected to give rise to average melts with high Ca/Al_2O_3 (Ellam & Cox 1991), as is observed in the picrites (Fig. 4.3c), but not in the dominant olivine tholeiites.

Furthermore, it is quite striking how the Pb isotopic compositions of the very depleted high MgO lavas from Theistareykir and the Reykjanes Peninsula approach the very different Pb isotopic ratios of the MORBs from Kolbeinsey and Reykjanes Ridges respectively (Chapter 4). This suggests that their Pb isotopic ratios reflect some interaction with MORB, and it would seem strangely fortuitous for this to arise if the highly depleted picrites were plume melts alone.

It is thus likely that the *more* depleted component of the plume is not highly depleted,

as in option i above. A reasonable model is that the plume consists mainly of mantle with incompatible element contents similar to primitive mantle, but with a small proportion of more enriched veins. The 'primitive mantle' plume matrix dominates the geochemical signature of the olivine tholeiites, but different proportions of contributions from vein melts result in the small isotopic and La/Yb variations observed within the olivine tholeiites. In this model, the alkali basalts are dominated by a signature from the plume veins.

From these conceptual arguments, the most reasonable set of isotopic 'components' to explain the range of isotopic variation on Iceland are:

i) the plume matrix, which represents the bulk of the plume and melts to produce the volumetrically dominant olivine tholeiites. Its isotopic ratios are enriched with respect to adjacent Atlantic MORB values, and probably are close to those of the less enriched olivine tholeiites.

ii) the plume veins, which are isotopically and incompatible element enriched with respect to the plume matrix. They dominate the incompatible element signature of the alkali basalts, and contribute to the overall signature of the more enriched olivine tholeiites, but they are a small proportion of the total plume volume.

iii) MORB, which is inferred to mix with the plume from the isotopic ratios of dredged basalts along the Reykjanes Ridge (Hart et al. 1973, Sun et al. 1975) and from the depleted, sub-aerial high MgO suites (Chapter 4). MORB mixing, may also play a role in the genesis of the olivine tholeiites, but this is not necessary from the arguments above.

5.4 Mixing of isotopic components within a dynamic melting column

The last sections examined all the Icelandic post-glacial volcanics in order to assess their range in composition and hence the probable nature of source 'components' beneath Iceland that may contribute to any given Icelandic melt. This is an important preliminary to modelling the high MgO lavas (discussed qualitatively in Chapter 4) that is the main aim of this chapter, since although it is argued in Chaptert 4 that the melting process strongly controls the composition of the high MgO lavas, contributions from distinct sources are clearly required to account for isotopic variation. Thus the analysis in section 5.3 is useful in choosing suitable source 'components' in the modelling of the high MgO lavas.

However, mixing of source components to produce the isotopic signatures observed within the Icelandic high MgO lavas is not a simple mixing of melt endmembers but is strongly affected by the melting and segregation processes in the melting column beneath Iceland. The most depleted high MgO lavas have Pb isotope ratios as low as those of the most depleted MORB sampled from adjacent ridge segments, apparently suggesting that these lavas represent the pure MORB endmember. However these lavas have higher $^{87}Sr/^{86}Sr$ and lower $^{143}Nd/^{144}Nd$ ratios than those of adjacent MORB (Fig 4.4, Fig. 5.6), and so clearly they are not pure MORB melts. This suggests that MORB melts are not mixed with a single plume composition, but an array of plume melts, the incompatible element contents of which are determined by the melting process. The most incompatible element depleted lavas of the high MgO suite are depleted because they did not sample instantaneous melts from the bottom of the melting column (which are the most incompatible element enriched), rather than because they are mixed with greater proportions of MORB. The more incompatible elements are more depleted in these shallower level plume melts than the less incompatible elements, and since Pb is more incompatible than Sr or Nd in mantle melting, mixing with MORB causes a greater shift in Pb isotope ratios than for $^{87}Sr/^{86}Sr$ and $^{143}Nd/^{144}Nd$ ratios (Chapter 4).

5.4.1 MORB mixing and melting

Not only can incompatible element fractionation in the melting column affect the composition of the plume melts, but also potentially the composition of melts from a MORB source, that mix with the plume melts. From the anomalous crustal thickness of Iceland, it is apparent that mantle of elevated temperature (i.e. plume), rather than MORB mantle (that melts to produce ~7km of oceanic crust) is upwelling beneath the Icelandic rift, and hence MORB melts may only be present beneath Iceland if MORB-source mantle is entrained into the rising plume (e.g. Griffiths & Campbell 1990). The melting behaviour of the entrained MORB-source material will depend critically on heat transfer from the plume mantle to the colder MORB-source mantle. This is a function of the size of the portions of MORB-source mantle entrained, the depth at which they are entrained and the rate of rise of the plume. The first two parameters are particularly poorly constrained and consequently it is difficult to predict the melting behaviour of the entrained MORB-source material. However two limiting

situations are clear (Fig 5.9). If small packets of MORB-source mantle are entrained at depth within a slowly rising plume, these packets may be heated to near ambient plume temperature by the time they reach ~120km below the rift (the depth at which plume temperature mantle intersects its solidus). Consequently they will start to melt at this depth, along with the plume mantle, and undergo high degrees of melting (~20%). Alternatively packets of MORB-source may experience negligible conductive heating and thus only intersect their solidus nearer the top of the melting column (80-50km depth) and produce normal degrees of melting for MORB (~8%), Klein & Langmuir (1987) and McKenzie & Bickle (1988).

These two scenarios have important implications for the mixing of the isotopic MORB component into plume melts. The very depleted high MgO lavas cannot have sampled the incompatible element enriched instananeous melts from the bottom of the melting column. If the entrained MORB-source melts simultaneously with plume mantle (Fig. 5.9b) then its incompatible elements will be concentrated, together with those from the plume, in the instantaneous melts at depth in the melting column. Thus there will be no *preferential* MORB isotopic contribution to the very depleted melts, which sample later, depleted instantaneous melts from *both* the already partially melted plume and entrained MORB mantle, and hence the high MgO basalts will not show the depleted isotopic signatures observed. The entrained MORB-source mantle is therefore constrained geochemically to melt at shallower depths, so that its first instantaneous melts, that carry much of its incompatible element budget are sampled by even the very depleted high MgO lavas. Modelling in a later section tries to quantify the depth to which the high MgO melts sample instantaneous melts and hence the depth at which entrained MORB-source materialstarts to melt, which from these arguments, must be shallower than the plume mantle solidus. To a first approximation it is assumed that all the lavas erupted in the central rift sample *all* the instantaneous melts of any entrained MORB-source, and ranges in lava composition are purely the result of sampling the instantaneous melts of the *plume* to various depths. This is equivalent to a single MORB composition being added to a range of plume melts.

Such a model explains why although the MORB source is more depleted in

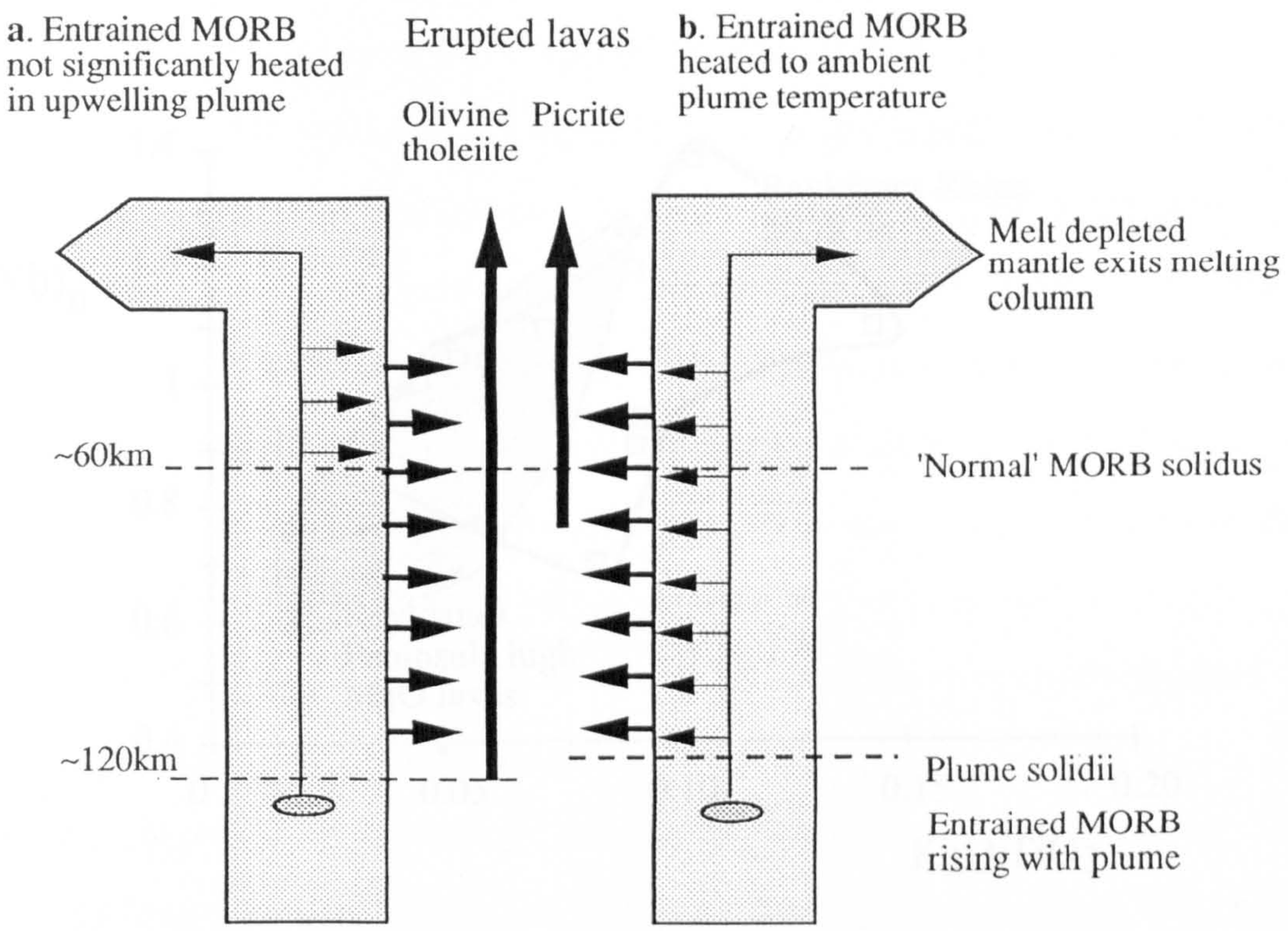

Figure 5.9 Schemtaic representation of the endmember scenarios for melting of entrained MORB material. Instantaneous melts are shown as horizontal arrows, that segregate at all depths once melting commences. Instantaneous melts are shown for both the plume mantle and entrained MORB. Thick vertical arrows schematically represent the depth in the melting column to which olivine tholeiite and picritic lavas sample instantaneous melts, and are of reference for both scenarios shown. **a**) The MORB material is not significantly heated by the hot plume after entrainment and starts melting at the depth of the 'normal' MORB solidus. Thus the picritic melts sample all the instantaneous melts from the entrained MORB material. **b**) Entrained MORB material is heated to the ambient temperature of the up-welling plume and hence starts melting at the plume solidus at ~120km. Hence the picritic melts do not sample the earliest instantaneous melts of the MORB material that carry the largest proportion of its incompatible elements.

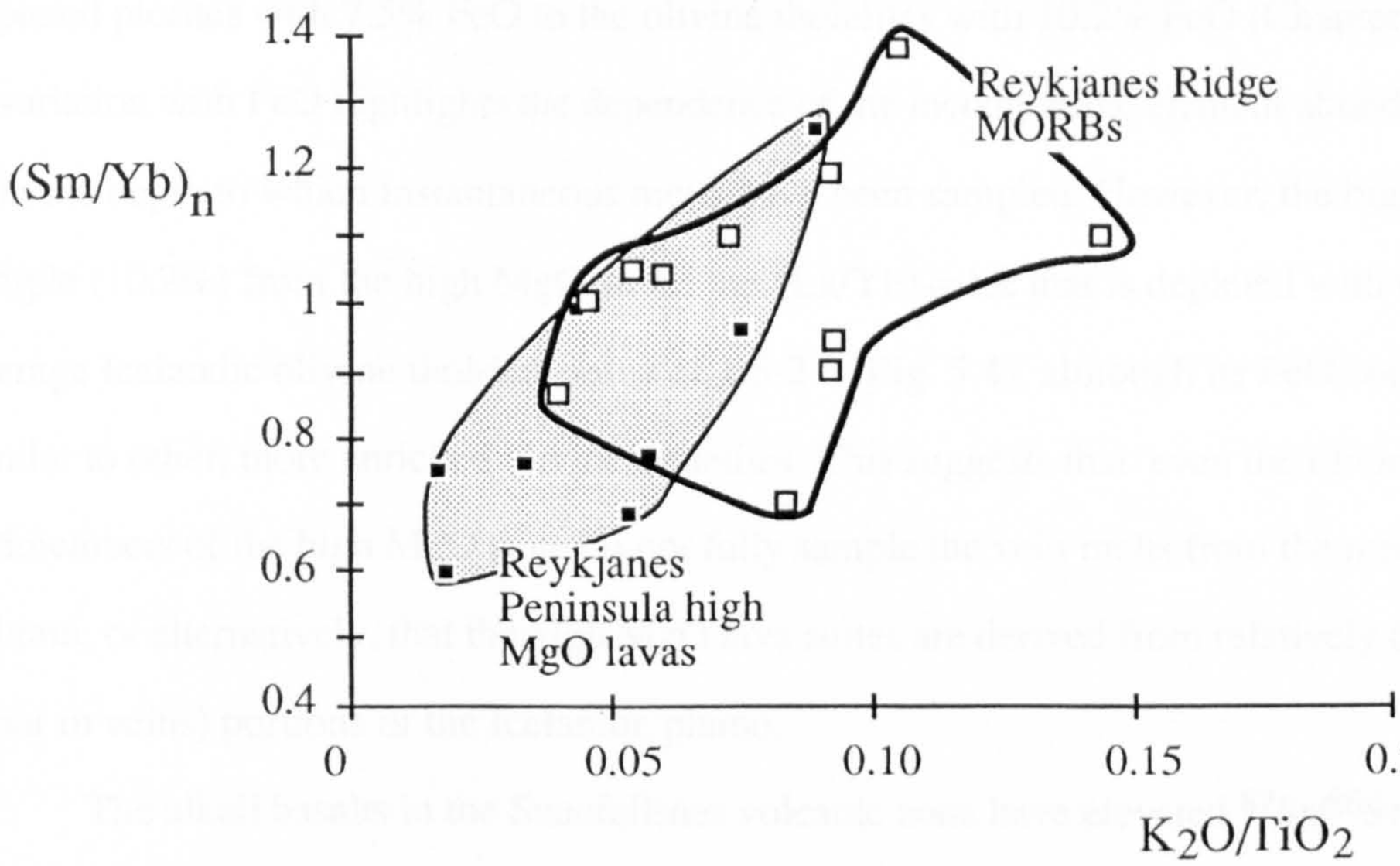

Figure 5.10 K_2O/TiO_2 vs. primitive mantle normalised Sm/Yb for the Reykjanes Peninsula lavas of this study (solid symbols and shaded field) and for Reykjanes Ridge basalts >200km from Iceland (open symbols, Schilling 1973). The most depleted lavas of this study show more depleted incompatible element ratios than the most depleted MORBs of the Reykjanes Peninsula.

incompatible element contents and ratios than the plume matrix, a MORB melt does not lie at the depleted end of the array of the high MgO suite lavas on plots such as Fig. 5.10, as would be expected for simple mixing. MORB melts are mixed with a range of plume derived melts whose incompatible element abundances have been controlled by melting column processes.

5.4.2 Involvement of veins within the tholeiites

Large variations of incompatible element abundances in the high MgO suites (e.g. 15x for K_2O contents) are clearly related to the FeO contents of the lavas, from the very depleted picrites with 7.5% FeO to the olivine tholeiites with 10.2% FeO (Chapter 4). The covariation with FeO highlights the dependence of the incompatible element abundances with the depth to which instantaneous melts have been sampled. However, the highest FeO sample (10.2%) from the high MgO suites has $(La/Yb)_n$=1.2 that is depleted with respect to average Icelandic olivine tholeiite value of 1.5-2.0 (Fig. 5.4), although its FeO content is similar to other, more enriched olivine tholeiites. This suggests that even the olivine tholeiite endmembers of the high MgO suite do not fully sample the vein melts from the melting column, or alternatively, that the high MgO lava suites are derived from relatively depleted (poor in veins) portions of the Icelandic plume.

The alkali basalts in the Snaefellsnes volcanic zone have elevated $^{87}Sr/^{86}Sr$ that suggests that the lower degree of melting expected beneath such a peripheral zone (Fig 5.5) results in the preferential encorporation of enriched vein melts within these lavas. This implies that the veins have a lower solidus temperature than the plume 'matrix', and consequently beneath the rift axis, the veins also probaly melt before the general onset of melting in the matrix. Thus, just as sampling to different depths in the melting column can produce the variations observed in the high MgO lavas, differences in the depth to which the *very bottom* of the column is sampled may result in the variations in isotopic ratios and incompatible element ratios between olivine tholeiites of similar FeO. However this scenario is difficult to distinguish from a lateral variation in the proportion of matrix/vein proportion on a small scale within the plume.

5.4.3 Isotopic Mixing Patterns

This section assesses the probable range of MORB melt involved in producing the range of isotopic compositions of the high MgO lavas. It is not an attempt to determine rigorously the precise fractions of MORB/plume mixing but an estimate of the amount of MORB involved in their genesis. As discussed in section 5.4.1, it is assumed that all instantaneous melts from the entrained MORB source are sampled (Fig 5.9a), and hence mixing can be modelled simply as mixing of a single MORB melt with a range of plume melts.

Mixing calculations are shown graphically on Fig 5.12, in which the high MgO lavas are plotted on a grid of various amounts of mixing between a range of plume melts and MORB. In these plots, a suitable MORB melt is taken from endmember compositions from adjacent ridges (see figure caption for data sources). The elemental concentrations used for the plume melts are simply chosen to span a suitable range of elemental concentrations, from depleted to enriched melts, and are not intended to signify any particular depth in the melting column to which instantaneous melts are sampled. Isotopic compositions of plume melts are variable (Fig 5.6), because of different contributions from matrix and veins, but isotope ratios of some of the more enriched olivine tholeiites are used in these calculations to estimate the *maximum* probable amounts of MORB mixing. In Fig. 5.11 all elemental concentrations are expressed relative to primitive mantle.

No attempt was made to determine precisely Pb and Nd concentrations in the high MgO lavas. Nd concentrations are not precisely measured at the low levels found in the high MgO tholeiites, by the INAA technique used to measure other REE in this study, and so values were estimated by interpolating between La and Sm concentrations. Pb concentrations were determined on the same selection of samples (Table 5.1) for which Ce had been determined by isotope dilution (O'Nions et al 1976). These show no systematic variation of Ce/Pb ratios and consequently interpolated (from La and Sm), primitive mantle normalised Ce contents are used as analogues for primitive mantle normalised Pb concentrations.

The plots in Fig 5.11 display several important features, although in detail no consistent MORB/plume mixing array is apparent for all isotopic systems, presumably due

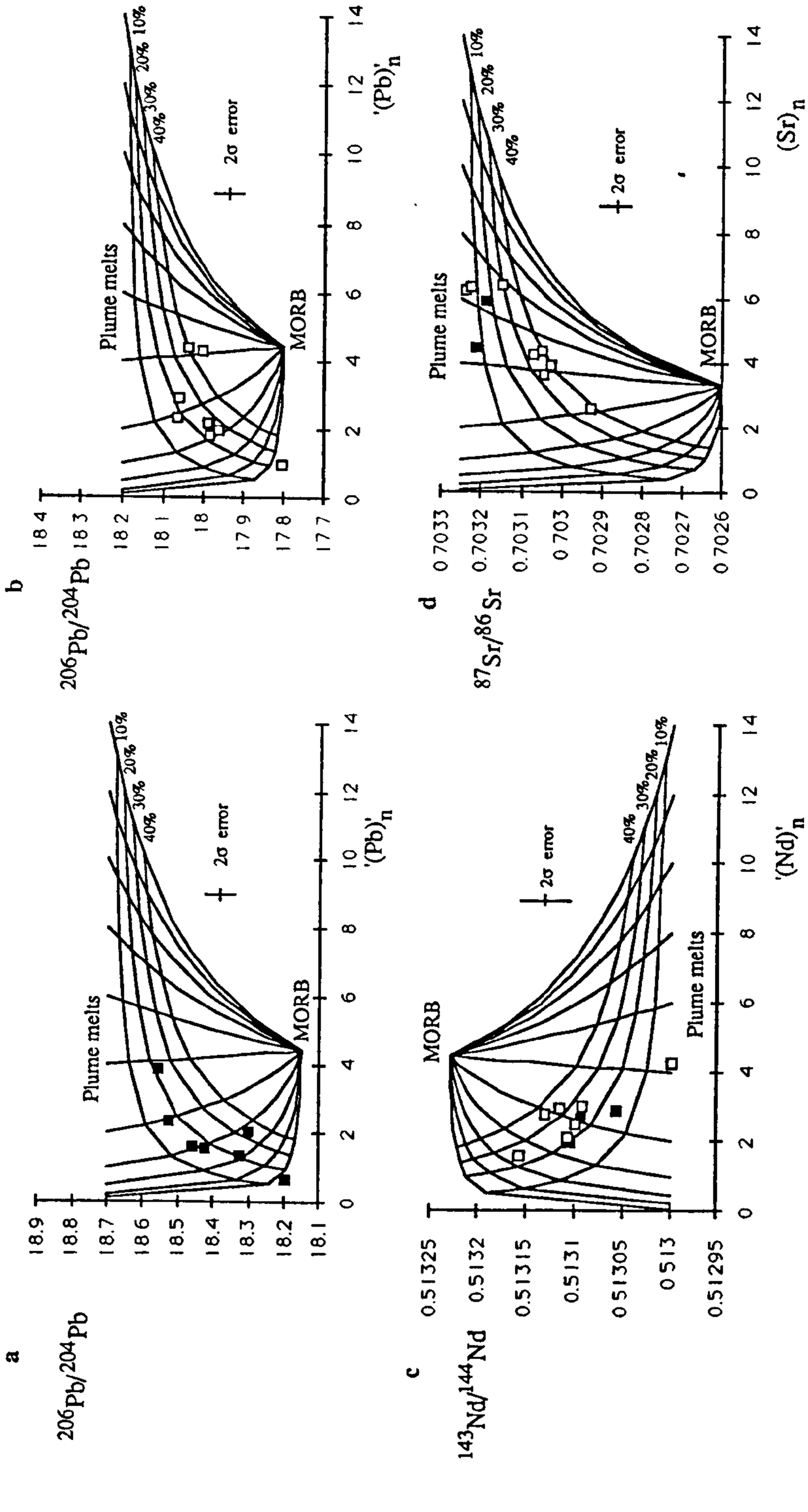

Figure 5.11 Mixing grids to assess the degree of plume/MORB mixing in the genesis of the high MgO lavas (Reykjanes Peninsula suite as filled squares, Theistareykir suite as open squares). A range of elemental contents for various plume melts, from 0.1-14x primitive mantle, are chosen to represent melts that sample the melting column to various depths. These plume melts are mixed with a single MORB composition to produce a series of vertical mixing lines, which are contoured for 10, 20, 30 and 40% mixing with MORB. Isotopic compositions of the plume were taken from some of the more enriched olivine tholeiites (Fig. 5.6) in order to maximise the amount of MORB mixing. Elemental and isotopic compositions of MORB were taken from depleted endmembers of Reykjanes and Kolbeinsey Ridges (Hart et al. 1973, Sun & Jahn 1975, Cohen et al. 1980, Mertz & Devey pers. comm.). Pb isotopes from the Reykjanes suite and Theistareykir are shown seperately in a) and b) because of the major heterogeneity in Pb isotope ratios between N & S Iceland. Pb and Nd contents of the high MgO lavas were estimated from interpolated Ce and Nd contents respectively, and hence the axes are marked as '(Pb)' and '(Nd)', see text.

Sample	Ce	Pb	Ce/Pb
Th13	5.81	0.246	23.6
Th8	4.06	0.163	24.9
Th29	1.66	0.092	18.0

Table 5.1 Ce and Pb concentrations for three Thestareykir samples. Ce concentrations from O'Nions et al. (1976), Pb from isotope dilution measurements of this study.

to associated uncertainties in the data and approximations in the modelling. Firstly, it can be seen that the most isotopically depleted melts are not necessarily mixtures containing higher proportions of a MORB melt, but rather they reflect mixing with an incompatible element depleted plume melt, as argued qualitatively in Chapter 4. Secondly, these diagrams can help constrain the incompatible element contents of the plume derived melts before mixing with MORB melts. In the plots of Nd and Pb isotope data (Figs 5.12 a-c), plume melts with elemental contents as low as 0.5x and 0.1x primitive mantle respectively are implied, although the actual incompatible element contents of the mixed, i.e. erupted lava are only as low as ~1x primitive mantle, and so such mixing relationships limit the most depleted compositions of the plume derived melts prior to mixing. The melts modelled in Fig 5.11d have higher Sr contents relative to primitive mantle (8x-2x) than Pb or Nd, which reflects the 'Sr spikes' seen on spidergrams of Icelandic lavas e.g. Fig 4.3, reflecting a comparatively Sr rich plume source. Finally, such diagrams suggest that in general the tholeiites record some 20-30% mixing of MORB melt with plume melts.

5.5 Forward Modelling of the Geochemical Variation produced in the Melting Column Beneath Iceland

In this section, a melting column has been modelled to generate synthetic plumes melts, in order to assess the geochemical variations expected from mixing variously summed instantaneous melts from a plume with entrained MORB, and also to examine the depth range over which geochemical variation occurs. However, such synthetic melts may only be reliably forward modelled if independent constraints on melting column parameters may be obtained.

5.5.1 Constraints on the degree of melting and depth of the Icelandic melting column

The modelling is not aimed at constraining the overall degrees of melting but to assess the affects of sampling to different depths within the melting column. Thus a framework of depth and degree of melting beneath Iceland must be obtained to use melting equations to model the within-column incompatible element variations in the instantaneous melts. The depth of the melting column has important constraints on the mineralogy of the source, i.e. whether garnet or spinel peridotite, and hence on the bulk distribution coefficients of the system. The major control on the depth at which melting starts, and hence the depth of the melting column, is the *potential temperature* of the adiabatically upwelling mantle, with hotter mantle intersecting its solidus at greater depth.

The depth of the melting column and the overall degree of melting are also closely linked since, although the amount of melting per unit of pressure release (i.e. depth interval in the melting column) is a complex function, it may reasonably be approximated to a constant degree of melting per unit of pressure release (Ahren & Turcotte 1979). Klein & Langmuir (1987) used such a relationship to estimate the depth of the melting column beneath spreading ridges, by inferring the degree of melting from fractionation corrected sodium contents of ridge lavas (assuming derivation from a mantle with chondritic sodium content). Icelandic lavas represent an endmember composition in their calculations, which suggests that they represent a maximium of 20% mean degree of melting, from a melting column of 120km resulting in a crustal thickness of 22.5km. McKenzie & Bickle (1988) used a theoretically more rigorous approach of combining parameterised mantle melting experiments with thermodynamic melting equations to relate the volume of melt production with melting column depth. By equating crustal thickness to the volume of melt production they inferred that the Icelandic crust was the result of a mean of 22.5% melting from a melting column 100km deep, assuming that the Icelandic crust is 26km thick. Furthermore, the low FeO contents and the high, fractionation-corrected MgO contents of Icelandic lavas are consistent with estimates of magmas compositions calculated by combining experimental melting data to simulate the products of a dynamic melting column ~100km deep (Klein & Langmuir 1987, McKenzie & Bickle 1988, Watson & McKenzie 1991).

Thus for the forward modelling in this section, the Icelandic melting column is assumed to be 120km deep and to result in a mean degree of melting of 20%. From these constraints on the melting column, the source mineralogy may be assessed. The pressure (depth) and temperature dependence of the spinel/garnet transition has been most recently studied in experiments by Nickel (1986). McKenzie & Bickle (1988) calculate that the potential temperature of upwelling mantle that melts to produce the Icelandic crust is 1480°C, and McKenzie & O'Nions (in press) extrapolate the data of Nickel (1986) to this temperature to estimate depths of 100km and 80km for the garnet-in and spinel-out reactions respectively. These values are used in the forward modelling, and within the garnet-spinel transition, garnet is assumed to react with olivine to produce spinel by the reaction (Johnson et al 1990):

$$0.34\text{Olivine} + \text{Garnet} = 0.6\text{Orthopyroxene} + 0.34\text{Spinel} + 0.39\text{Clinopyroxene}$$

(in which the minerals are expressed in weight proportions), such that all garnet has reacted once a mantle segment has upwelled to 80km.

5.5.2 Constraints on partition coefficients and source composition

Partition coefficients for the rare earth elements are among the most reliably known for incompatible elements, and hence in the forward modelling only rare earth elements are used. Partition coefficients were taken from the compilation of McKenzie & O'Nions (in press), and they are very similar to the values used by Johnson et al (1990). In attempting to assess radiogenic isotopic variation by mixing of various plume melts with MORB, clearly Sr and Pb contents within the synthetic melts need to be calculated, in addition to REE contents. However, it is assumed that Sr and Pb are analogous to Pr and Ce respectively during melting, rather than attempting to choose other partition coefficients for these elements. This is a reasonable approximation, since melting within the plagioclase stabilty field (that may fractionate Pr and Sr) occurs only after a mantle segment has been essentially stripped of all incompatible elements and as discussed above, Ce/Pb contents for a range of tholeiites show no systematic variations.

As discussed in section 5.3 the Icelandic source is heterogeneous and, although on average the plume composition is quite well constrained, the actual incompatible element contents of any given segment is variable. However, since the most enriched tholeiite in this

study (IT4, Fig 5.3) has an essentially flat REE pattern with $(La/Yb)_n$=1.2, it is assumed that the high MgO lavas were derived from a source with primitive mantle REE abundances.

The major element contents of the mantle are reasonably well known by planetary mass balance considerations (O'Nions et al. 1981). From a knowledge of the major element contents, the mineralogy may be calculated by least squares mixing of the minerals expected for given pressure and temperature conditions. Since the upwelling mantle plume is expected to start melting within the garnet stability field, the major elements are distributed between olivine, orthopyroxene, clinopyroxene and garnet, using mineral compositions appropriate for nodules that appear not to have undergone melt depletion (McKenzie 1989). Using this approach a starting mantle mineralogy of Ol62%, Opx20%, Gnt10% and Cpx8% is obtained (McKenzie & O'Nions 1991 in press). However, as discussed below, once melting starts the proportions of these phases change.

5.5.3 The melting model

As mantle passes through a melting column it melts continuously and hence becomes increasingly depleted as it upwells, resulting in instantaneous melts that reflect its changing composition. Thus, in order to calculate instantaneous melt compositions an incremental melting calculation is required. Incremental melting calculations only approximate to the continuous melting process of the real melting column if increments are small with respect to the overall degree of melting (Williams & Gill 1989, Johnson et al 1990). By comparing the mean composition calculated from the incremental melting column (i.e. the average of all the instananeous melts) with an accumulated fractional melt ($C_l=C_o.(1-(1-P.X/D)^{1/P})/X$) for the same mean degree of melting (X), any artifacts produced by increment size can be assessed. Calculations using 0.4% increments were found accurately to reproduce accumulated fractional melt compositions, and so they have been used in the modelling.

During melting within a melting column it is likely that not all melt is completely extracted and that a residual melt porosity is retained (McKenzie 1984). A value of 0.5% is used here, which is probably the greatest porosity expected for a basaltic melting column (McKenzie 1989). By maximising the porosity, the depletion of highly incompatible elements in the upwelling residue is minimised, and thus the depth range over which chemical variation occurs is maximised.

To make modelling simpler it is assumed that the first melt increment melts to produce the 0.5% porosity. In subsequent melt intervals the amount of melt increases by the melt increment (0.4%) to a total melt fraction of 0.9% (the melt increment + porosity). The composition of the residual source is then recaluated, allowing for the change in source mineralogy that is associated with 0.4% melting using typical mineral melt norms (Appendix E). The new bulk distribution coefficients of the solid phase and hence the new equilibrium incompatible element concentrations of both coexisting liquid and solid can be computed. A 0.4% melt increment is then assumed to segregate from the system, and the mantle segment rises, together with the residual 0.5% melt porosity, to undergo the next 0.4% melting increment, until the top of the melting column is reached after a given degree of melting: a *mean* degree of melting of 20% is assumed from the constraints in 5.5.1. The *total* number of 0.4% increments represents the degree of melting that a given mantle segment has experienced as it leaves the melting column, however the *mean degree of melting* represented by the averaged compositions of the instantaneous melts (equivalent to the degree of melting in single stage melting model), is only half the total number of melt increments (Klein & Langmuir 1989).

The *average* composition of all the 0.4% melt increments represent the mean melt product of the whole melting column (similar to the 'point and depth' average of McKenzie & Bickle 1988). In Chapter 4 it was argued that the high MgO lavas sampled instantaneous melts down to various depths within the melting column. In simulating these melts, incremental 0.4% batch melts are summed from the most depleted (i.e. last calculated composition, corresponding to instantaneous melts from the top of the melting column) down to increasingly more enriched compositions (calculated earlier and representing melts from deeper in the melting column), and then averaged to give the REE contents of various 'synthetic lavas'. It is assumed that the degree of melting per unit of pressure (depth) release is constant throughout the melting column, so that the number of melt increments sampled is proportional to the depth to which melts are sampled.

The spreadsheet used to calculate the synthetic melts is reproduced in Appendix E, which also includes the details of mineral fractions, melt norms and distribution coefficients used in the melting model.

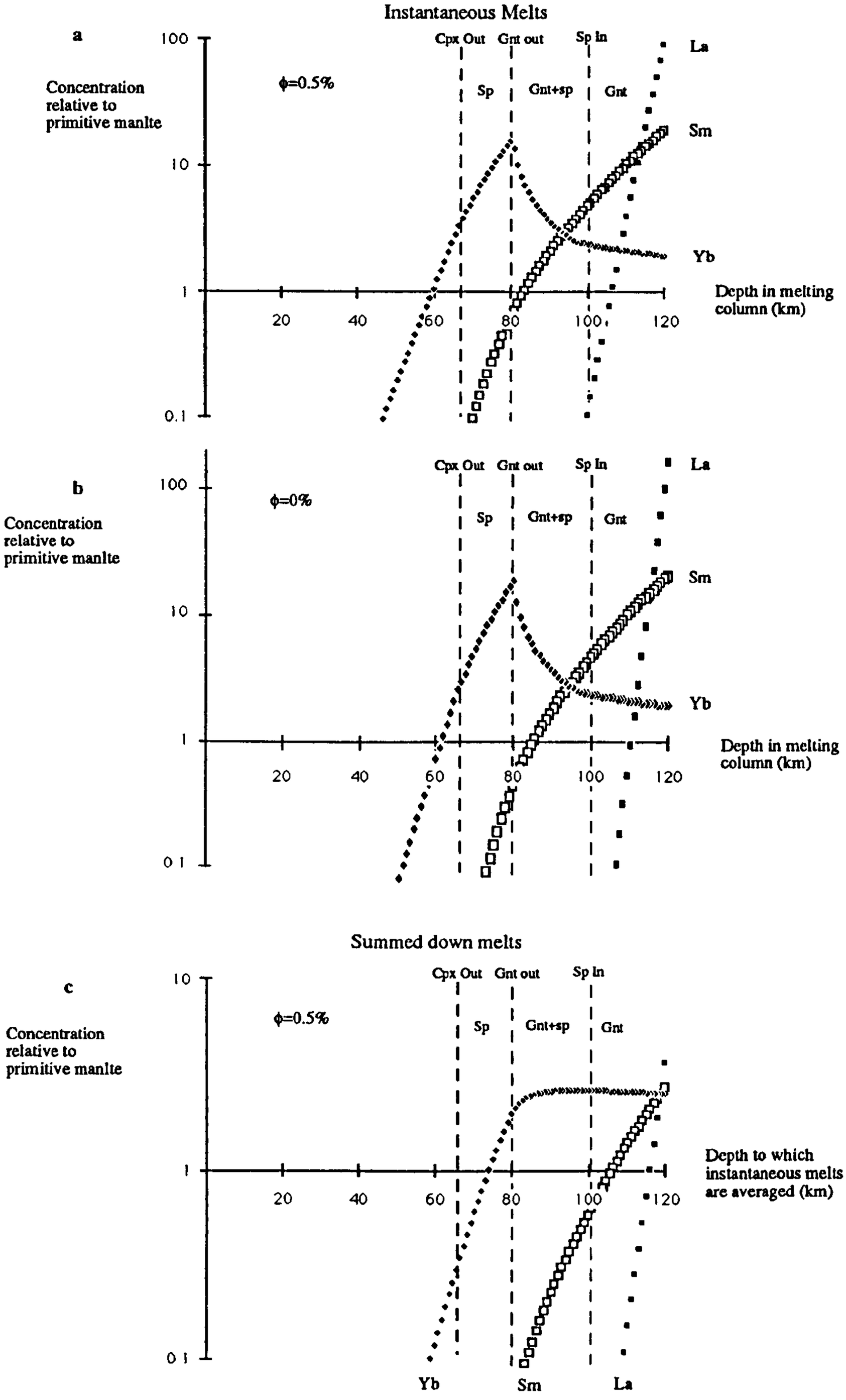

Figure 5.12 The modelled behaviour of La, Sm and Yb during dynamic melting. The garnet/spinel transition used in the calculation, together with the depth of cpx exhaustion are shown. **a)** and **b)** show the REE concentrations in the instantaneous melts with varying depth, i.e. the concentrations of each 0.4% melt increment. Concentrations below 0.1x primitive mantle are not shown. **a)** has a column melt porosity of 0.5% whilst **b)** is modelled with no porosity and hence shows more rapid depletion of incompatible elements. **c)** shows REE concentrations in the 'summed down' melts, i.e. the synthetic analogues to the high MgO lavas in which instantaneous melts are averaged from the top of the melting column down to increasing depth (in 0.4% increments), such that the summed down melt at 120km is the average product of the whole melting column. A porosity of 0.5% is used for this diagram and in all subsequent calculations.

5.5.4 Synthetic lava compositions

Fig 5.12a shows how the concentrations of La, Sm and Yb in instantaneous melts vary with depth in the melting column, down to concentrations of 0.1x primitive mantle, below which concentrations are assumed to be negligible. La (and also other LREE) becomes very rapidly depleted and the upwelling mantle is effectively stripped of La well before the exhaustion of clinopyroxene, but even the Yb content of instantaneous melts is insignificant for instantaneous melts produced at depths less than 60km in the column. The same plot is shown with no column melt porosity (Fig 5.12b), to illustrate the even more rapid depletion that occurs if there is no residual porosity to buffer the highly incompatible elements (all other calculations in this chapter use a porosity of 0.5%). Fig 5.12c shows a similar plot to Fig 5.12a, except that it displays the contents of the summed down melts which are used to simulate the high MgO lavas (i.e. the depth axis represents the depth down to which instantaneous melts are sampled and averaged, so that the composition at 120km is the average melt of the whole column).

Fig 5.13 compares calculated $(Sm/Yb)_n$ and $(La/Yb)_n$ ratios in the synthetic summed down melts with those from the high MgO lavas. The range in $(La/Sm)_n$ and $(Sm/Yb)_n$ is quite well modelled in Fig 5.13a, where the depth in the melting column to which instantaneous melts are sampled is shown with the synthetic lava composition. As was clear from Fig 5.12, the LREE rapidly become very depleted, and to model the variation of La/Sm and Sm/Yb within the high MgO lavas, *differences* in the depths to which instantaneous melts are sampled are small, and so it appears that even the depleted melts sample a large proportion of the melting column.

However the isotopic variation within the high MgO lavas implies mixing with MORB melts, and such mixing will also have an effect on REE contents and ratios. Fig 5.11 suggests that mixing with some 20% MORB to all melts of the suite can roughly model the radiogenic isotope variations. Hence an average N-MORB melt (Sun & McDonough 1989) was added to the synthetic melting column melts in the proportion1:4. The results of this calulation are shown in Fig. 5.13b. Although the MORB composition is depleted with respect to a melt from the whole column, the synthetic melts that sample instantaneous melts to progressively shallower levels in the melting column, become so rapidly LREE depleted

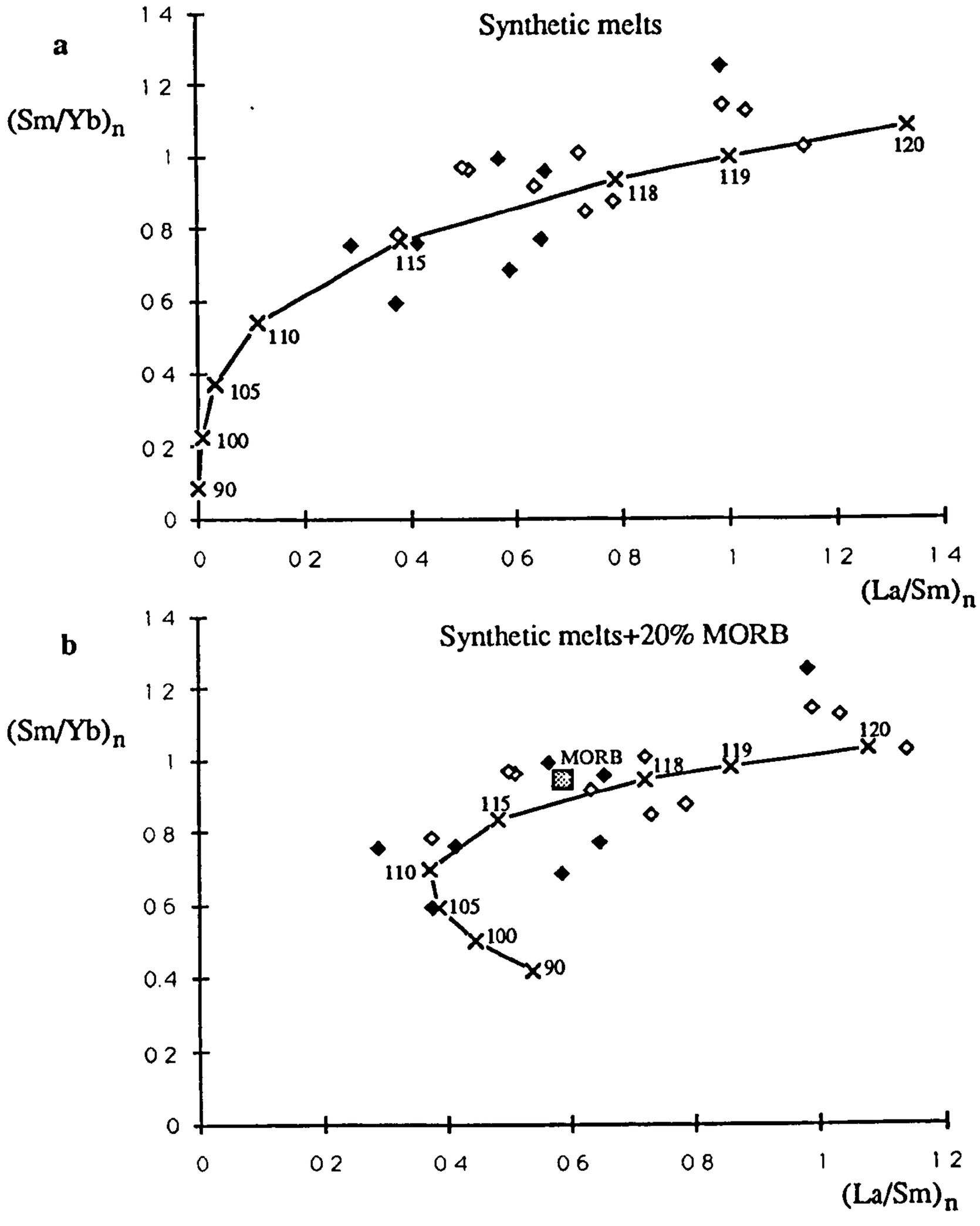

Figure 5.13 Variation of primitive mantle normalised Sm/Yb and La/Sm in the high MgO lavas (Reykjanes Peninsula samples as closed symbols, Theistareykir samples as open symbols) and **a)** the synthetic (summed down) melts, **b)** the synthetic summed down melts mixed with 20% MORB (from N-MORB average, Sun & McDonough 1989, shown on the figure as shaded square). Specific synthetic melt compositions are shown as crosses, next to which are given the depths to which instantaneous melts have been averaged to produce these compositions. A line links these points to indicate a continuous range in possible melt compositions from the melting column.

that the addition of a MORB melt significantly increases their LREE contents and buffers the degree of depletion. As the synthetic melts become very depleted, the MORB contribution completely dominates the LREE budget, and the La/Sm ratio for example increases from the highly depleted values back to MORB ratios. However it is important to note that even with the addition of 20% of MORB melt, the synthetic melts still model the Sm/Yb and La/Sm ratios observed in the most depleted high MgO lavas, which are more depleted than MORB and must predominantly reflect melting rather than mixing processes.

The synthetic melts appear to model quite well the variations in rare earth element ratios of the high MgO lavas in Fig 5.13. Because the LREE are so rapidly depleted with the onset of melting, the most rapid changes in La/Sm occur within instantaneous melts from the garnet stabilty field. Thus, the REE ratios of the synthetic melts are dominated by melting in the garnet stability field, and thus have Yb contents that are buffered by the presence of garnet. Fig 5.14a shows Sm/Yb against Yb for the high MgO lavas and the synthetic melts, and clearly the variation in Yb in the high MgO lavas is not reproduced by the synthetic melts. Although Yb contents of the lavas may have been affected by fractional crystalisation (and accumulation), the variation in Yb content is too great for the probable maximum difference of 20% fractional crystallisation between the high MgO lavas (Chapter 4).

Nicholson & Latin (in review) present data for a set of olivine tholeiites from Krafla with MgO contents of 8-10%. As with the high MgO lavas of this study, good correlations of incompatible element variations with FeO content are observed in the Krafla olivine tholeiites (Nicholson & Latin, in review), which indicates that the lavas represent instantaneous melts sampled to different depths within the melting column. Additionally, the high MgO lavas of Krafla also show a systematic increase of Yb with increasing Sm/Yb (Fig 5.14b). The Krafla lavas have a smaller range in MgO content than lavas of this study and hence the maximum degree of crystal fractionation, and associated Yb variation, between samples is probably even smaller.

Not only is the range in Yb for the data sets in both Fig. 5.14 a&b too great for the degrees of fractional crystallisation estimated from major element considerations (Chapter 4 and Nicholson & Latin, in review), but there is a positive variation of Sm/Yb with Yb that cannot simply be explained by crystal fractionation. However, in Chapter 4 it is argued that

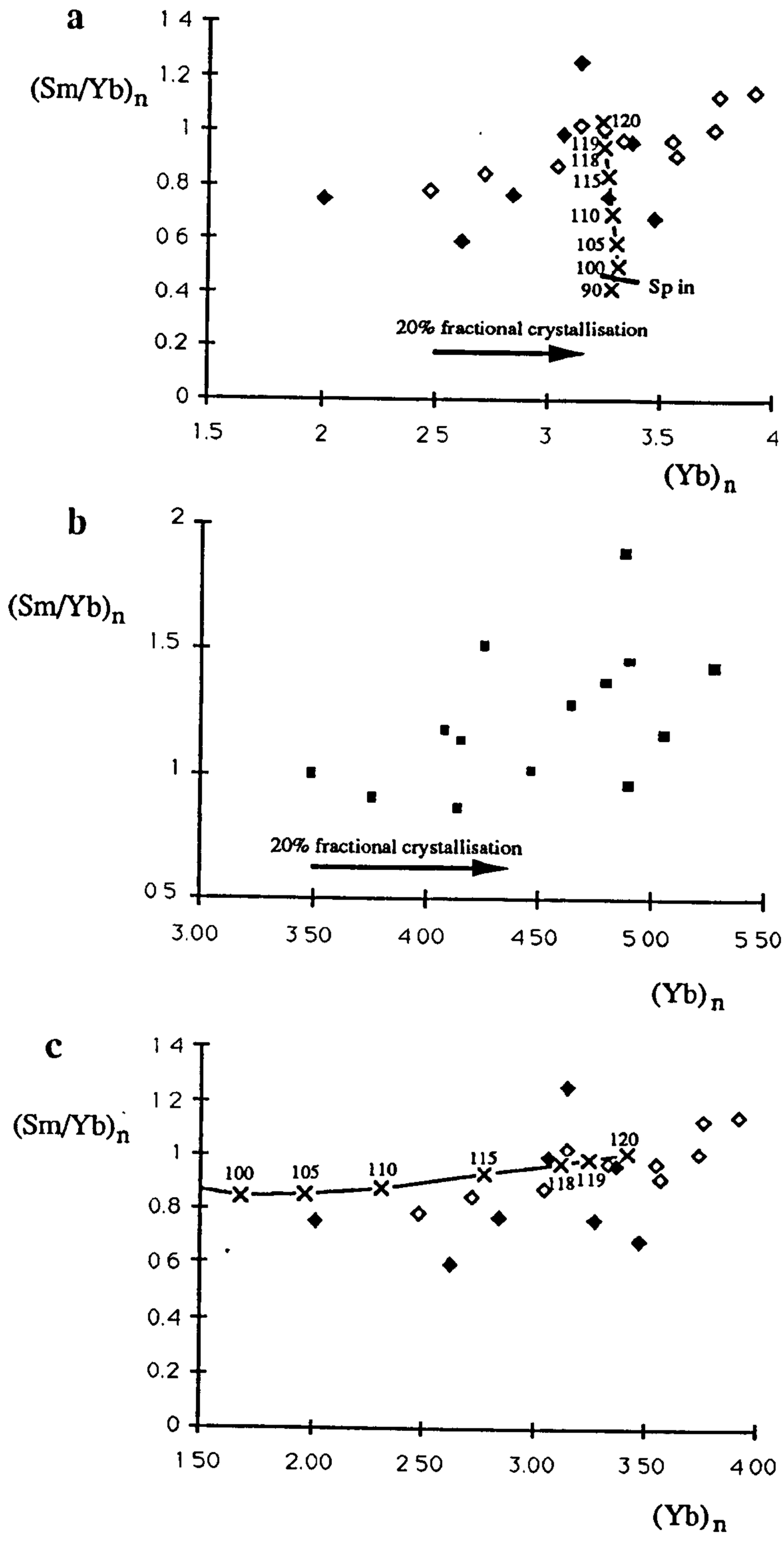

Figure 5.14 Variation of primitive mantle normalised Sm/Yb ratios and Yb contents in, **a&c)** synthetic melts (mixed with 20% MORB) compared to the high MgO lavas of this study (symbols as Fig. 5.13) , and **b)** for recent high MgO lavas from Krafla (Nicholson & Latin in review). In **a)** melting is modelled to start in the garnet stability field (as predicted from independent constraints). Synthetic melt compositions are dominated by the composition of instantaneous melts produced in the garnet stabilty field, which results in a buffering of Yb contents in the summed down melts. The effect of 20% fractional crystallisation (estimated in Chapter 4 as a maximum value evident from variations in major element compositions of the high MgO lavas) is shown by an arrow. In **c)** it is assumed that no garnet is stable in the melting column and the Yb contents of instantaneous melts are controlled by clinopyroxene. This results in a rapid depletion of Yb contents but little fractionation of Sm/Yb in synthetic melts that sample instantaneous melts from shallower depths.

the more enriched (e.g. high Sm/Yb) instantaneous melts from the bottom of the melting column are denser (as a result of higher FeO contents), relative to shallower, more depleted melts, and undergo greater degrees of crystal fractionation in order to mix and erupt. Hence more enriched *lavas*, with a higher proportion of FeO and incompatible element rich instantaneous melts from the bottom of the melting column, have experienced greater net degrees of crystal fractionation. Furthermore, Langmuir (1990) suggests that in-situ crystal fractionation of magmas can produce greater increases in incompatible element concentrations than implied by major element variation. Hence some of the Yb variation observed in Figs 5.14a&b may be attributable to crystal fractionation, although the melting process produces the variations in Sm/Yb, and controls the density of instantaneous melts, which results in the most enriched lavas erupted having undergone highest degrees of fractional crystallisation.

Although the process of fractional crystallisation described above may account for some correlation of Sm/Yb with Yb contents, this process results in *higher* Yb contents than the 'primitive' melts. In Fig. 5.14a it is clear that Yb contents of many lavas of this study are *lower* than the 'primitive' synthetic melts and hence cannot be accounted for by fractional crystallisation from such synthetic melts.

An alternative explanation for the correlation of Sm/Yb with Yb is that the position of the garnet stability field with respect to the melting regime is not accurately represented in the model, and that variations in Yb are a result of melting alone. The independent constraints used to assess the physical parameters of the melting column were described in 5.5.1, but small differences in the depth at which melting starts, and the position of the spinel-in reaction can have large effects on the Yb composition of the melts, since as discussed above, the greatest changes in incomptible element ratios occur within a small melting interval at the bottom of the melting column. In the McKenzie & Bickle (1988) model the depth of the melting column is assessed from the crustal thickness of Iceland which, however, is poorly known. Although the Icelandic crust is significantly thicker than 'normal' oceanic crust, estimates vary from 15-30km (Palmason & Saemundsson 1974, Bjornsson 1984, Gebrande et al. 1980, and reinterpretation of the latter by McKenzie & O'Nions 1991, in press). The variations in these values result in differences in the length of

associated melting columns of 70-120km. The approach of Klein & Langmuir (1987) to model the length of the melting column length relies on a good knowledge of the degree of melting and Na content of mantle beneath Iceland, and they estimated 120km to be the *maximum* probable length, rather than necessarily the true length. Furthermore, the depth of the garnet-spinel transition (as discussed in Chapter 3) is extrapolated for the probable temperature of the Icelandic plume, and hence also not well known.

Thus, although the constraints outlined in 5.5.1 were the best *a priori* estimates on physical melting column parameters, the chemical variations within the high MgO lavas suggests that melting may not start below the spinel-out reaction. McKenzie & O'Nions (in press) and Latin & Waters (1991) have also used a geochemical approach to try to constrain better both the depth at which melting starts and the variation of melt fraction with depth, although as discuused in Chapter 3, the model used in the above studies does not account for melt depletion of the mantle as it rises through the melting column. In amending the melting model of this study to better fit the results from the high MgO lavas, the absolute depth of the melting column is most significant only in respect to how this depth corresponds to the garnet-spinel transition, and so all parameters (including mixing with 20% MORB) have been kept constant but the depth of the transition itself has been varied. For melting only within the spinel stability field, Yb is incompatible, and not buffered as it is in the presence of garnet. Hence, Yb contents become depleted in instantaneous melts produced higher in the melting column. Thus the trend in synthetic melts produced in a melting column in which melting starts above the garnet-out reaction reproduce the similar variations in Yb to those observed within the high MgO lavas (Fig. 5.15c).

However, melting only within the spinel peridotite facies (i.e. above the garnet-out reaction) models the variation in Sm/Yb less well than in models with garnet present (compare Figs. 5.13b & 5.14c), since clinopyroxene does not sufficiently fractionate Sm and Yb to produce the very depleted Sm/Yb values observed within the high MgO lavas. There is apparently a very fine balance in the interplay of melting with garnet present and absent that is not totally resolved by the modelling here, and may also be complicated by some fractional crystallisation. Allowing the melt fraction per unit of pressure release to vary through the melting column and varying the depth at which the garnet-spinel transition

occurs may help to produce a better fit to the data. However, these adjustments are beyond the scope of simple forward modelling, and are currently being investigated using minimisation of an inverse model.

Another puzzling aspect of the results of the melting model is the very small depth interval over which variations in the incompatible element ratios observed in the high MgO lavas are controlled. As discussed by McKenzie & Bickle (1988), no existing major element melting experiments provide data that is suitable for assessing variation within a true dynamic melting column. However, the depth interval (the bottom 10km of a 120km melting column) that controls the incompatible element variation from the modelling in this chapter (Fig. 5.13b) seems somewhat small to produce the correlated variations in FeO. This may partially be explained if smaller degrees of melting per unit of pressure release occur at depth, so that a greater pressure range occurs for a given degree of melting and incompatible element fractionation. However, there are no independent constraints that may readily be applied to this.

5.5.5 Isotopic variation modelled using the synthetic melts

Radiogenic isotope variation of the high MgO suite can also be modelled from mixtures of synthetic plume melts and MORB, using Ce and Pr content from the synthetic melts as analogues for Pb and Sr respectively, and using the isotopic values for plume & MORB melts from section 5.4.3. The problems associated with modelling the involvement of garnet in the melting column is not significant for Ce, Pr and Nd since clinopyroxene is the dominant controlling phase for these elements, irrespective of whether melting occurs in spinel or garnet peridotite facies. The major heterogeneity in lead isotope compositions across Iceland prevents the Reykjanes Peninsula and Theistareykir high MgO suites being considered together, and since more $^{87}Sr/^{86}Sr$ and $^{143}Nd/^{144}Nd$ results have been obtained on the Theistareykir samples only these are modelled. Hence a MORB endmember from the Kolbeinsey Ridge is used in this section (Mertz & Devey pers. comm.).

Isotope-isotope variation diagrams are shown for the data from Theistareykir (Fig 5.15) and for synthetic melts (that sample instantaneous melts over the same range of depths as the those synthetic melts shown in Figs 5.13 & 5.14). The effect of adding variable amounts of MORB, within the range suggested by Fig 5.11, to the range of plume melts is

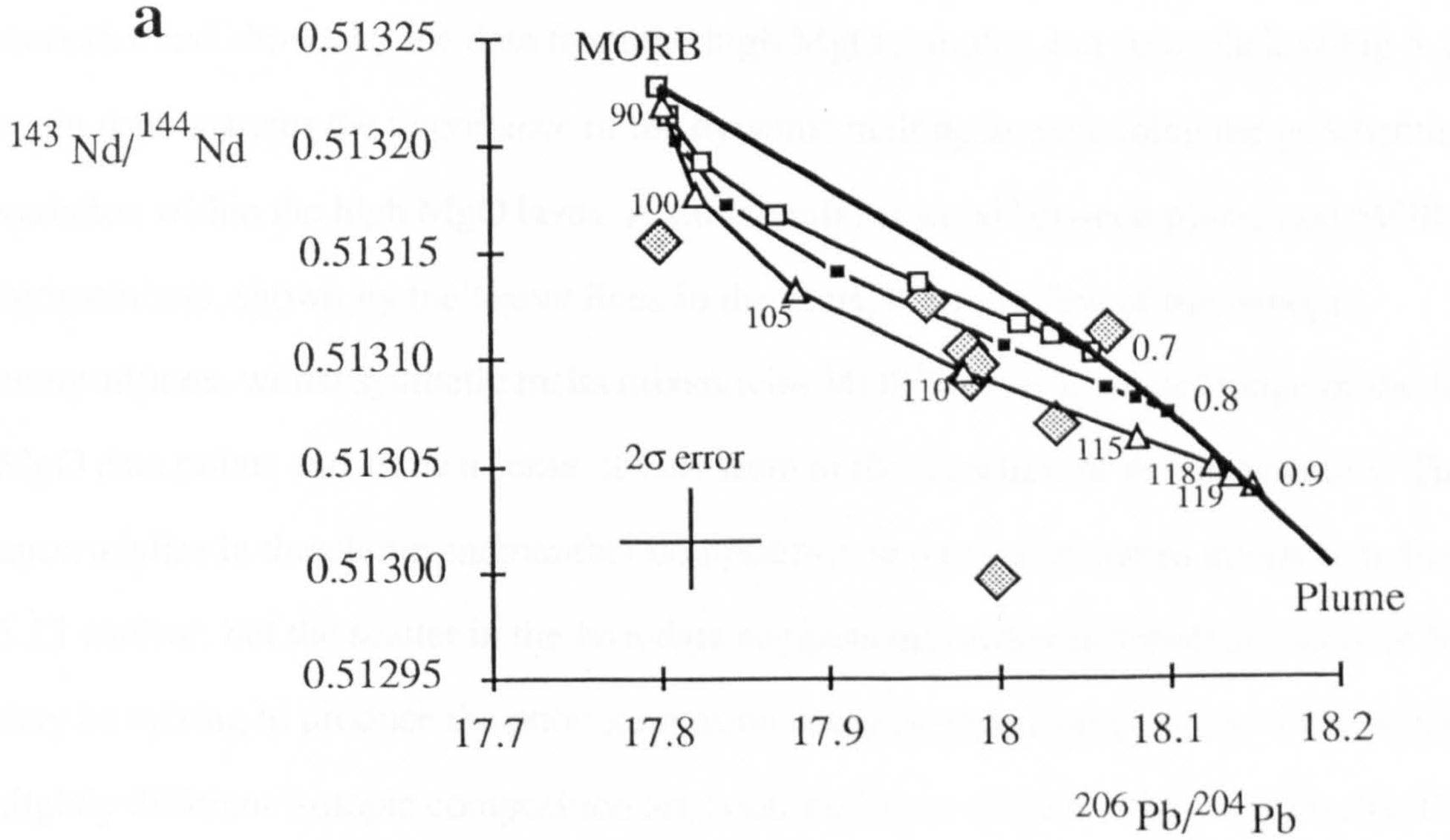

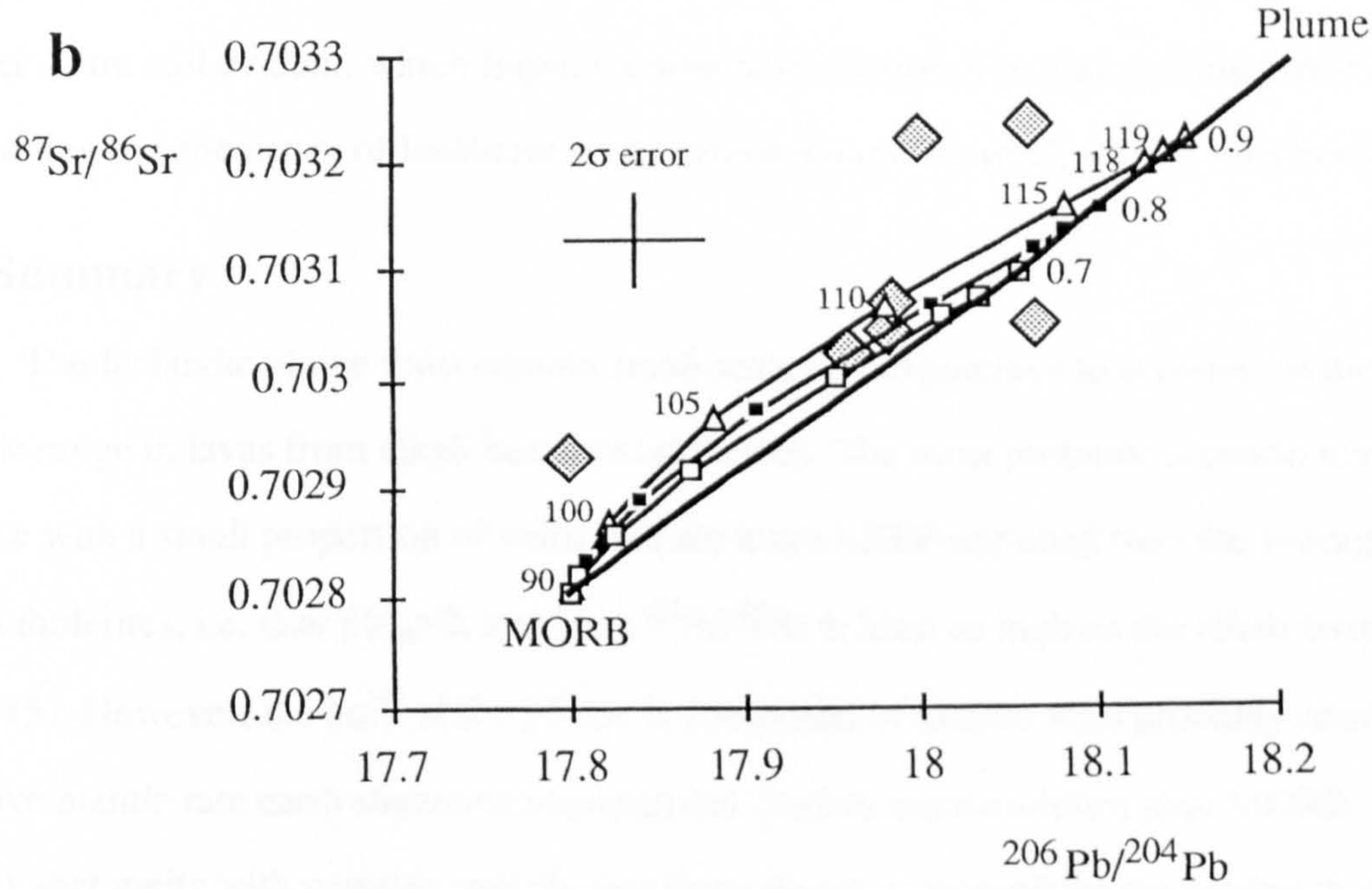

Figure 5.15 Comparison of isotopic variation of the Theistareykir high MgO lavas (large shaded diamonds) with synthetic summed-down melts mixed with various amounts MORB. The compositions of the synthetic melts are shown as open squares, filled squares and open diamonds for melts mixed with 30, 20 and 10% MORB respectively. As in Figs. 5.13 & 5.14, the depths to which instantaneous melts are sampled in the melting column are shown, and are the same for all three mixing scenarios. Elemental MORB compositions are taken from an average N-MORB (Sun & McDonough 1989), using Ce and Pr as Pb and Sr analogues respectively. Isotopic ratios are $^{143}Nd/^{144}Nd=0.51300$, $^{87}Sr/^{86}Sr=0.7033$ and $^{206}Pb/^{204}Pb=18.2$ for the plume (Fig. 5.11), and $^{143}Nd/^{144}Nd=0.51323$, $^{87}Sr/^{86}Sr=0.7028$ and $^{206}Pb/^{204}Pb=17.8$ for Kolbeinsey Ridge MORB (Mertz & Devey pers. comm.). A heavy line indicates a simple mixing curve for plume and MORB melts.

shown. No single mixing trend explains all the data, and modelling is fraught with uncertainties on endmember compositions. Furthermore it is clear that there is actually no smooth trend shown by the data from the high MgO samples, but nevertheless Fig 5.15 again demonstrates the importance of the dynamic melting in explaining the geochemical variation within the high MgO lavas. A simple mixing trend between plume and MORB endmembers, shown by the heavy lines in the plots, recovers few of the isotopic compositions, whilst synthetic melts mixed with MORB cover a greater range of the high MgO data points and show a sense of curvature in the direction of the other points. The uncertainties in the plume endmember composition in particular makes inferrences from Fig. 5.15 unclear, but the scatter in the lava data suggests that either different amounts of MORB may be mixing to produce the poor correlation in the isotope/isotope plots or that veins of slightly different isotopic composition are contributing to different high MgO melts. Despite these potential complications, it is striking that coherent trends, as those discussed in Chapter 4, are still evident, which implies a dominant control of partial melting process in determining the chemistry of Icelandic lavas, which overprints small source variations.

5.6 Summary

The Icelandic plume must contain small scale heterogeneities to account for the isotopic range in lavas from alkali basalts to tholeiites. The most probable scenario involves a source with a small proportion of veins that are more LREE enriched than the average of the rift tholeiites, i.e. $(La/Yb)_n>2$, and have $^{87}Sr/^{86}Sr$ at least as high as the alkali basalts (0.70345). However, the bulk of the plume is composed of mantle with probably near primitive mantle rare earth element concentrations (and so more enriched than MORB source), that melts with variable contribution from the veins to produce the olivine tholeiites, the volumetrically dominant lava type on Iceland, with a fairly small range in $(La/Yb)_n$ and $^{87}Sr/^{86}Sr$.

Modelling of the melting a of mantle source with primitive rare earth element contents in a dynamic melting column, together with ~20% MORB melt contribution can adequately reproduce many of the features observed within the high MgO lavas. Uncertainties, particularly in the isotopic composition of the melting plume source make more detailed modelling difficult. The large variations in incompatible element ratios appear

to be produced at the very bottom (10km) of the melting column, in which the presnce or absence of garnet is important in modelling Sm/Yb ratios and Yb contents. The involvement of garnet is suggested by significant variation in the Sm/Yb ratios of the high MgO lavas, but argued against by variation of Yb contents to depleted values. This paradox suggests that understanding the behaviour of the garnet/spinel transition is of great importance in modelling the geochemical behaviour of plume melts.

Chapter 6

Synthesis of plume melting processes.

Iceland and La Palma are both the manifestations of plume magmatism, however, they have been developed on two extremes of oceanic lithospheric thickness. The Icelandic plume impinges on a spreading ridge axis, at which oceanic crust is being formed, and thus has no associated lithosphere. In contrast, La Palma lies on 150Ma oceanic crust, which is thought to be underlain by some 100km of lithosphere (Fig. 6.1). Degrees of melting by adiabatic upwelling are governed (assuming similar temperatures for all plumes e.g. Sleep 1990, Griffiths & Campbell 1990, Watson & McKenzie 1991), by the height to which the plume may rise. Thus the depth of the mechanical boundary layer of the lithosphere has a primary control on the degree of melting within plumes. This is evident in the contrasting chemistry of the main products of volcanism of Iceland and La Palma. Highly silica understaturated basanites erupt on La Palma with very high incompatible element concentrations (La~100x primitive mantle) as opposed to the olivine tholeiites of Iceland, that have much lower incompatible element contents (La ~10x primitive mantle). Differences in incompatible element contents may also be related to source variations, although from the sources inferred for La Palma and Iceland (Chapters 3 &5), there remains a strong effect from the overall degree of melting.

The higher degree melts from the longer Icelandic melting column will have a shallower *mean* depth of melting than the smaller degree melts from the shorter La Palma melting column (Fig. 6.1). Iron contents of melts increase with depth of melting, but they are not sensitive to the degree of melting (Jaques & Green 1980, Takahashi & Kushiro 1983), and so average Icelandic lavas are expected to show lower iron contents than average melts from the La Palma plume. This hypothesis is actually quite difficult to test, since the iron content of Icelandic lavas is highly variable, which results from two processes that can influence the iron content of erupted lavas. The incompatible element depleted, high MgO lavas of Iceland (Chapter 4) have low iron contents as they do not sample the iron and incompatible element rich instantanteous melts from the the bottom of the melting column

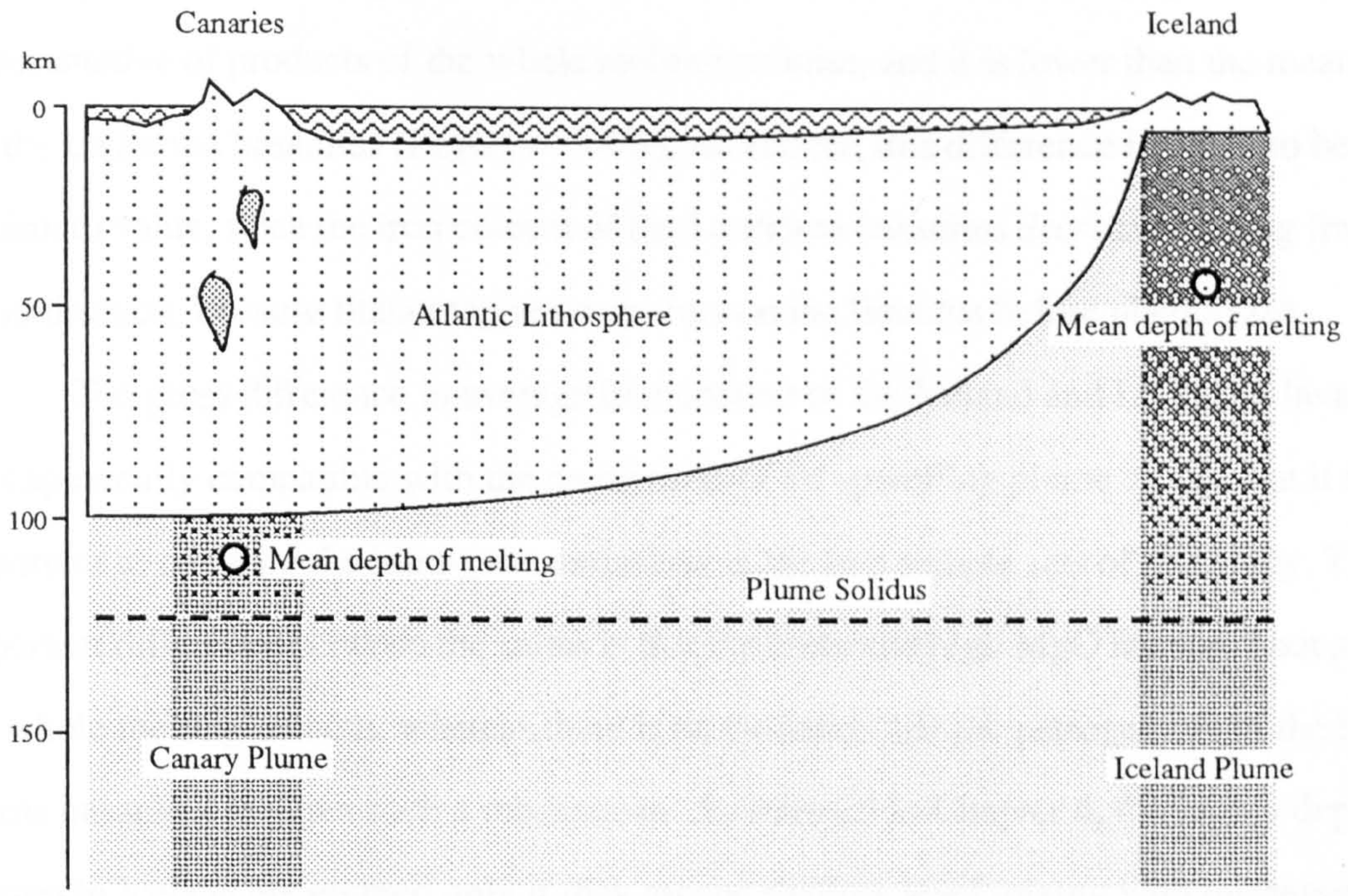

Figure 6.1 Representation of the effect of lithospheric thickness on degree, and mean depth of melting of the Canary and Iceland plumes.

and thus do not represent 'average' Icelandic melts. Conversely many tholeiites reported in the literature may have undergone plagioclase fractionation which will increase iron contents from 'primitive' values. Data from the olivine tholeiites of Nicholson & Latin (in review) may be compared with the La Palma basanites, as they have MgO contents of 8-10%, and are thus unlikely to have plagioclase on the liquidus (Bender et al. 1978), yet none of these olivine tholeiites is as highly depleted in incompatible elements as the low FeO picrites of this study. Thus the average iron content of these olivine tholeiites (Fe_2O_3 =11.7%), may be representative of products of the whole melting column, and it is lower than the mean value for the La Palma basanites (Fe_2O_3 =13.4%). Moreover, this difference is likely to be a minimum value, since the iron content of the La Palma basanites *decreases* during fractional crystallisation, because titanomagnetite appears on the liquidus before plagioclase.

The gross difference in average iron content of the Iceland and La Palma lavas is thus apparently compatible with the predictions of an upwelling plume model, but it is also important to compare the intra-suite variations in the two sample sets of this study. The most important difference between the suites is that the Icelandic high MgO lavas did not sample the whole melting column, whereas there is no evidence that the petrogenesis of the La Palma basanites requires such a mechanism. As stressed in Chapter 4, the highly depleted picrites in Iceland are erupted only if they escape shallow level mixing with instantaneous melts from the bottom of the melting column. This occurs rarely even on Iceland (only some 3% of post-glacial volcanics are picritic, Jakobsson et al. 1978), and for several reasons it is much more unlikely to happen on La Palma. The Icelandic crust is actively rifting, and hence pathways for magma to erupt, without ponding, mixing and fractionating, are more probable than for magma segregating beneath 100km of tectonically inactive lithosphere. Even beneath Iceland, however, it appears that more common olivine tholeiites have fractionated to some extent (effectively averaging the instantaneous melts from the underlying column during this process), and it is not surprising that all the La Palma basanites of this study have undergone significant fractionation (Chapter 3). Thus unlike the Icelandic high MgO lavas, the La Palma basanites represent averages of melting column products and can be modelled using simple, single-stage batch melting models.

Although the basanites represent averaged melting column products, they still reflect

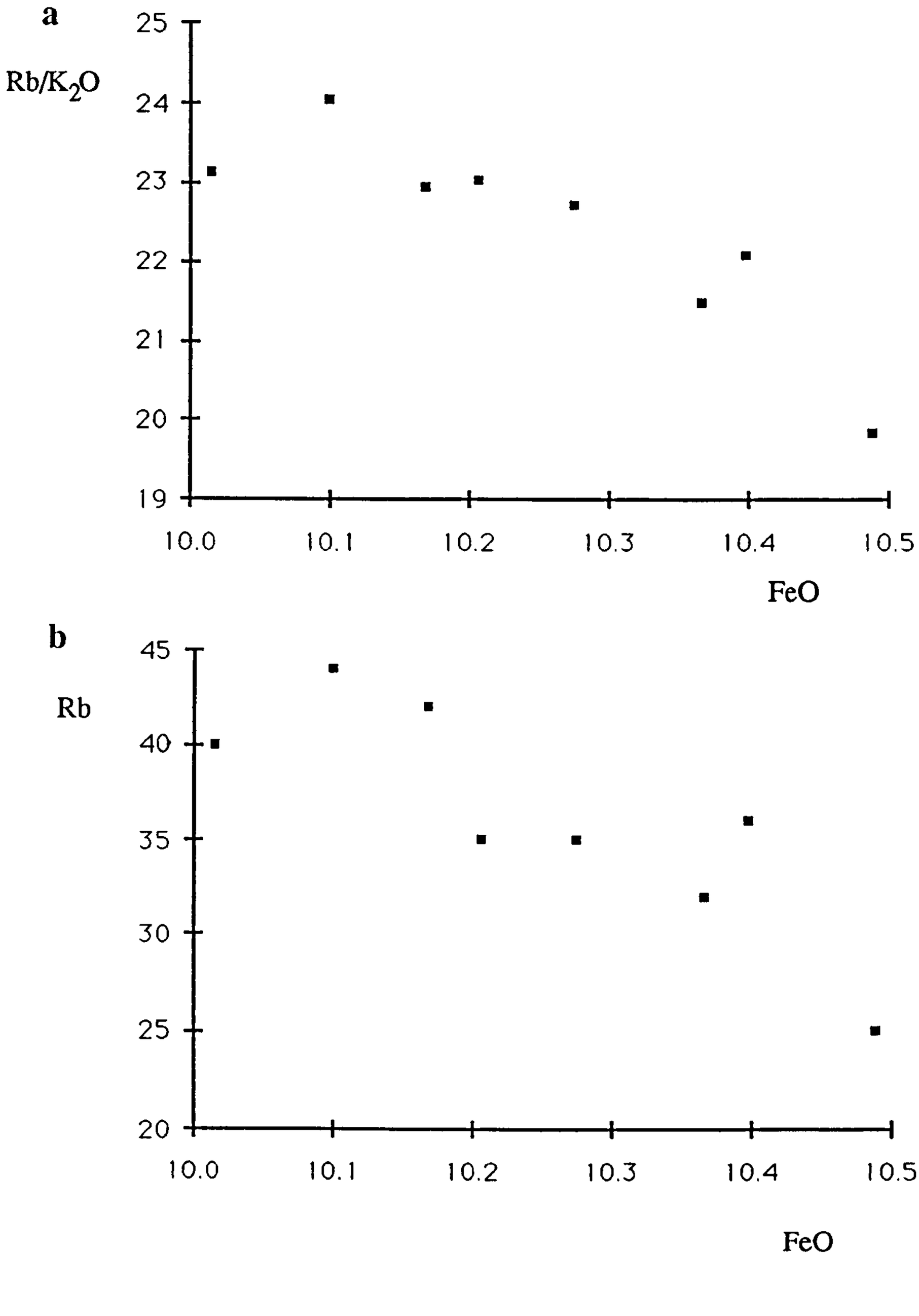

Figure 6.2 a) Rb/K_2O vs. FeO and **b)** Rb vs. FeO for the La Palma basanites that show little difference in degree of crystal fractionation (Fig. 3.7). A schematic explanation for these variations within a dynamic melting model is shown in Fig. 6.3.

different degrees of melting. In a dynamic melting scenario, differences in melting imply different mean depths of melting. FeO is used by both Klein & Langmuir (1987) and in Chapter 4 as an indicator of the mean depth of the melting column. However as mentioned above, unlike the the high MgO tholeiites of this study, which are thought to very largely have fractionated olivine alone and hence retain primary FeO contents, the fractionation assemblage in the La Palma basanites includes titanomagnetite that will have a significant effect on FeO content. Nevertheless, Fig. 3.7 illustrated, a group of basanites with very similar Ni contents, that cannot be related by fractional crystallisation, but in which primary differences in FeO between the lavas are thought to be preserved (after similar degrees of fractional crystallisation), even though their absolute FeO contents may not be primary. Fig. 6.2 shows FeO content plotted against Rb/K_2O and Rb (Rb and K_2O are both unaffected by monazite accumulation) for this group of basanites. There is a correlation between incompatible element contents (and ratios) and iron but in a different sense to that observed in the high MgO lavas, namely *more* enriched incompatible element ratios and *higher* incompatible element contents are associated with lavas with *lower* FeO.

The FeO and incompatible element variation within the La Palma basanites may result from differences in the lengths of melting column producing the lavas (Fig. 6.3), owing to small lateral temperature differences in the upwelling plume. Average melts from longer columns experience greater degrees of melting and have a greater mean melting depth, as discussed by Klein & Langmuir (1987) to explain global iron and sodium variations in MORB. This explanation of FeO and incompatible element covariation within the La Palma suite, clearly differs from that used to account for the variations within the Icelandic high MgO lavas, in which melts were sampled to different depths within a melting column of the same (or similar) length. Local, lateral variation in the overall depth of melting column may also affect the compositions of Icelandic olivine tholeiites, but such an effect is probably masked by source differences (unlike the La Palma basanites, the Icelandic tholeiites have variable radiogenic isotope ratios), and incomplete sampling of the melting column (which, as explained above, is more unlikely to occur beneath La Palma). Furthermore, for small degrees of melting beneath a thick lithosphere, small temperature heterogeneity within a plume will result in a much larger *relative* variation in melting column

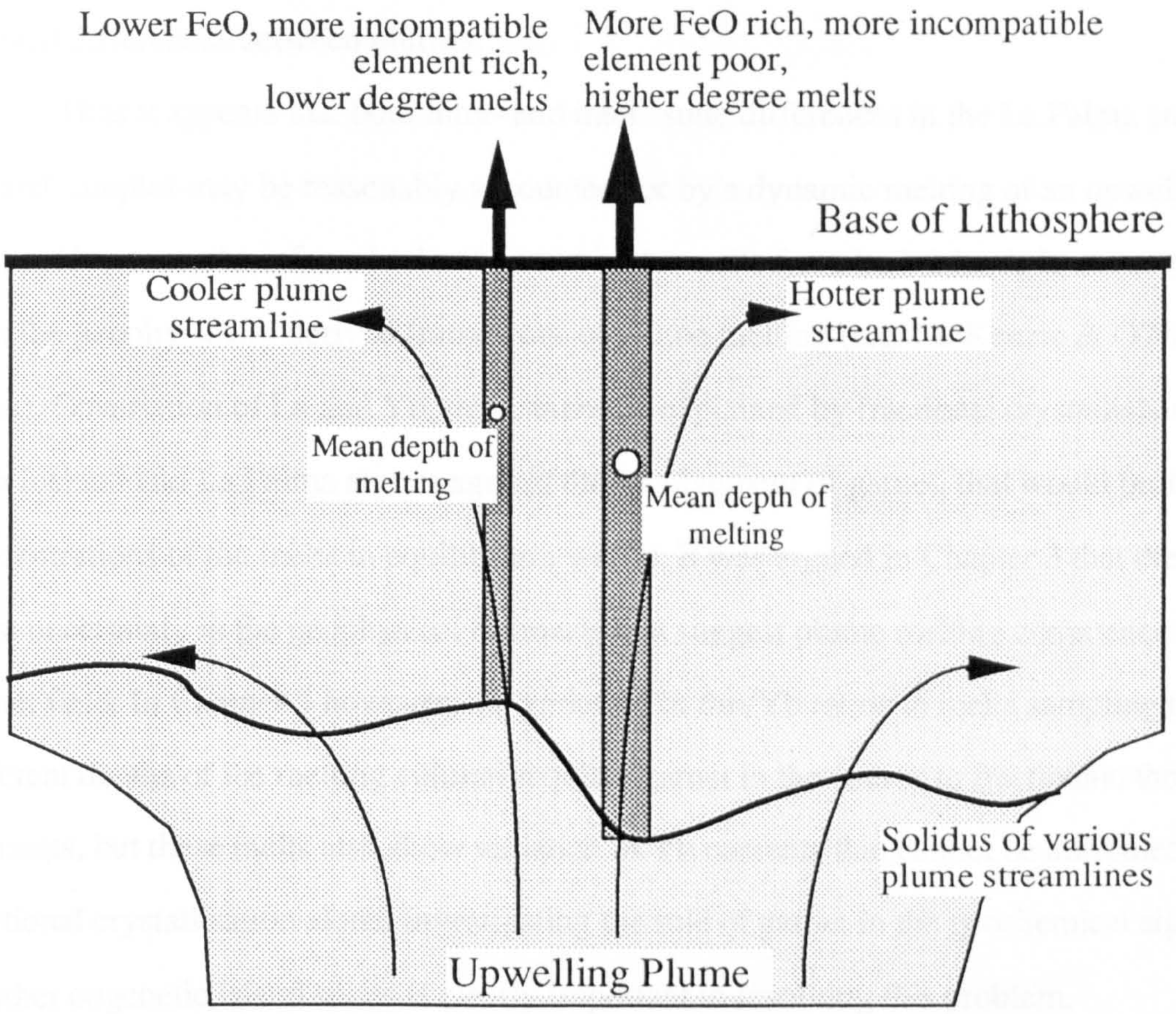

Figure 6.3 Schematic representation of the effect that thermal heterogeneity within an upwelling plume may have on melting column length, mean depth of melting and hence incompatible element and FeO content of resulting lavas.

length and hence chemistry, than for a much larger melting column, such as beneath Iceland. The large scale differences in FeO contents in lavas from Icelandic and La Palma, together with the smaller variations within the La Palma basanites, has parallels with the complementray global and local Fe_8 variations observed by Klein & Langmuir (1989). Analysis of other well categorised OIB suites may reveal if these trends are indeed globally applicable for plume magmas, and an absence of such a correlation might highlight major element differences between plumes.

Thus it appears that both intra- and inter- suite differences in the La Palma and Iceland samples may be reasonably accounted for by a dynamic melting of an upwelling plume. However, the inferred role of garnet in the melts from both islands is not compatible with the geophysically derived framework of plume melting (e.g. McKenzie & O'Nions in press). Covariation of La and Yb, that cannot be explained by fractional crystallisation, in both Iceland and La Palma argues against the involvement of garnet, that would buffer Yb concentrations of the melts in equilibrium with it. It was argued in Chapter 3 that there is a large uncertainty in the geophysical estimates that suggest plume melting commences in the garnet field. In Chapter 5 however, the variation in Sm/Yb ratios in melts sampling to different depths of the melting column requires garnet in the source to fractionate these elements, but these melts also show variation in Yb contents that cannot be attributed to fractional crystallisation alone. Investigating the role of garnet in the geochemical signatures of other cogenetic island suites is clearly important in resolving this problem.

Another intriguing issue raised by the geochemistry of the La Palma basanites is that, from the very limited sampling of older lavas in this study and from the major element classification of Hausen (1969), the small degree melts of historic eruptions seem to be representative of the island as a whole. This is in striking constrast to Gran Canaria, in which the major proportion of the island is constructed of tholeiitic lavas with higher SiO_2 contents and incompatible element contents that are generally some 2x lower (Schmincke 1982). Unless the composition of the sub-volcanic portion of La Palma is very different to that the sub-aerial lavas, this implies significantly different degrees of melting involved in the genesis of the main lavas of the respective the islands.The volumes of the islands of La Palma and Gran Canaria are estimated at 17 and 24 km^3 respectively by Schmincke (1982),

which may imply also some relation to the degree of melting, although La Palma is still active and may not have finished its main building phase. The inferred differences in degree of melting between the main island forming lavas of Gran Canaria and La Palma suggest important temporal changes in the melting regime and thermal structure beneath the Canaries in the last 14Ma, and it would be informative to investigate this problem in greater detail.

In summary, the study of temporally and spatially closely related lavas has enabled partial melting processes beneath two ocean islands to be examined. The quite different lava chemistry of the suites from Iceland and La Palma can be related, to first order, to the different tectonic setting beneath which the two plumes upwell. In detail however there inconsistencies with geophysical models that require further investigation of similar sample suites from other ocean islands.

References.

Abdel-Monem, A., Watkins, N.D., & Gast, P.W. (1971). Potassium-argon ages, volcanic stratigraphy, and geomagnetic polarity history of the Canary Islands: Tenerife, La Palma and Hierro. *Am. J. Sci.* **271**, 490-521.

Abdel-Monem, A., Watkins, N.D., & Gast, P.W. (1972). Potassium-argon ages, volcanic stratigraphy, and geomagnetic polarity history of the Canary Islands: Lanzarote, Fuerteventura, Gran Canaria, and La Gomera. *Am. J. Sci.* **272**, 805-825.

Ahren, J.L., & Turcotte, D.L. (1979). Magma migration beneath an ocean ridge. *Earth planet. Sci. Lett.* **45**, 115-122.

Albarède, F. (1983). Inversion of batch melting equations and the trace element pattern of the mantle. *J. Geophys. Res.* **88**, 10,573-10,583.

Albarède, F., & Tamagnan, V. (1988). Modelling the recent geochemical evolution of the Piton de la Fournaise volcano, Réunion Island, 1931-1986 . *J. Petrol.* **29**, 997-1030.

Allègre, C.J. (1968). ^{230}Th dating of volcanic rocks. A comment. *Earth planet. Sci. Lett.* **3**, 338.

Allègre, C.J., & Condomines, M. (1982). Basalt genesis and mantle structure studied through Th-isotopic geochemistry. *Nature* **299**, 21-24.

Allègre, C.J., Dupré, B., & Lewin, E. (1986). Thorium/uranium ratio of the earth. *Chem. Geol.* **56**, 219-227.

Araña, V., & Ibarrola, E. (1973). Rhyolitic pumice in the basaltic pyroclasts from the 1971 eruption of Teneguía volcano, Canary Islands. *Lithos* **6**, 273-278.

Arden, J.W., & Gale, N.H., (1974). Seperation of trace amounts of uranium and thorium and their determination by mass spectromeric isotopic dilution. *Anal. Chem.* **46**, 687-691.

Bard, E., Hamelin, B, Fairbanks, R.G., & Zindler, A. (1990). Calibration of ^{14}C timescale over the past 30,000 years using mass-spectrometric U-Th ages from Barbados corals. *Nature* **345**, 405-410.

Barling, J., & Goldstein, S.J. (1990). Extreme isotopic variations in Heard Island lavas and the nature of mantle reservoirs. *Nature* **348**, 59-61.

Ben Othman, D., Allègre, C.J. (1990). U-Th isotopic systematics at 13°N east Pacific Ridge segment. *Earth planet. Sci. Lett.* **98**, 129-137.

Bender, J.F., Hodges, F.N., & Bence, A.E. (1978). Petrogenesis of basalts from the project FAMOUS area: experimental study from 0 to 15kb. *Eath planet. Sci. Lett.* **41**, 277-302.

Bjornsson, S. (1984). Crust and upper mantle structure beneath Iceland, Structure and development of the Greenland-Scotland Ridge. *NATO Conf. Ser.* **4** (8), 31-61.

Booth, B., Crossdale, R., & Walker, G.P.L. (1978). A quantitative study of five thousand years of volcanism on San Miguel, Azores.. *Phil Trans. Soc. Lond.* **A288**, 271-319.

Booth, B., (1973). The Grandilla pumice deposit of southern Tenerife, Canary Islands. *Proc. Geol. Assoc.* **84**, 353-370.

Bosshard, E., & MacFarlane, D.J. (1970). Crustal structure of the Western Canary Islands from seismic refraction and gravity data. *J. Geophys. Res.* **75**, 4901-4918.

Campbell, I.H., & Turner, J.S. (1986). The influence of viscosity on fountains in magma chambers. *J. Petrol.* **27**, 1-30.

Chaffey, D.J., Cliff, R.A., & Wilson, B.M. (1989). Characteristation of the St. Helena magma source. *In: Saunders, A.D. & Norry, M.J. (eds) Magmatism in the Ocanic Basins. Geol. Soc. Lond. Special Publication* **42**, 257-276.

Chen, J.H., & Wasserburg, G.J., (1981). Isotopic determination of uranium in picomole and subpicomole quantities. *Anal. Chem.* **53**, 2060-2067.

Clague, D.A., & Dalrymple, G.B. (1987). The geology of the Hawaiian-Emperor volcanic chain. *U.S. Geol. Surv. Prof. Pap.* **1350**, 5-59.

Clark, S.P. Jr., Peterman, Z.E., and Heier, K.S., (1966). In: Handbook of physical constants, ed. S.P. Clark Jr., Geological Society of America, Boulder, Colorado. *Geol. Soc. America Memoir* **97**, .

Cohen, R.S., Evensen, N.M., Hamilton, P.J., & O'Nions, R.K. (1980). U-Pb, Sm-Nd and Rb-Sr systematics of mid-ocean ridge basalt glasses. *Nature* **283**, 149-153.

Cohen, R.S., & O'Nions, R.K. (1982a). Identification of recycled continental material in the mantle from Sr, Nd and Pb isotope investigations. *Earth planet. Sci. Lett.* **61**, 73-84.

Cohen, R.S., & O'Nions, R.K. (1982b). The lead, neodynium and strontium isotopic structure of ocean ridge basalts. *J. Petrol.* **23**, 299-324.

Condomines, M., Morand, P., & Allègre, C.J. (1981). ^{230}Th-^{238}U radioactive disequilibria in tholeiites from the FAMOUS zone (Mid-Atlantic Ridge, 36°50'N): Th and Sr isotopic geochemistry. *Earth planet. Sci.* **55**, 247-256.

Condomines, M., Tanguy, J.C., Kieffer, G., & Allègre (1982). Magmatic evolution of a volcano studied by ^{230}Th-^{238}U disequilibrium and trace elements systematics: the Etna case. *Geochim. Cosmochim. Acta* **46**, 1397-1416.

Condomines, M., Grönvold, K., Hooker, P.J., Muehlenbachs, K., O'Nions, R.K., Oskarsson, N., & Oxburgh, E.R. (1983). Helium, oxygen, strontium and neodynium isotopic relationships in Icelandic volcanics. *Earth planet. Sci.* **66**, 125-136.

Condomines, M., Hemond, Ch., & Allègre (1988). U-Th-Ra radioactive disequilibria and magmatic processes. *Earth planet. Sci.* **90**, 243-262.

Courtney, R.C., & White, R.S. (1986). Anomolous heat flow and geoid across the Cape Verde Rise: evidence foe dynamic support from a thermal plume in the mantle. *Geophys. J. R. astr. Soc.* **87**, 812-867.

Cousens, B.L., Spera, F.J., & Tilton, G.R. (1990). Isotopic patterns in silicic ignimbrites and lava flows of the Morgan and lower Fataga formations, Gran Canaria, Canary Islands: temporal changes in mantle source compositions. *Earth planet. Sci.* **96**, 319-335.

Dash, B.P., & Bosshard, E. (1968). Crustal studies around the Canary Islands. *Proc. Int. Geol. Congr. 23rd Session Czech* **1**, 249-260.

Davies, G.F. (1990). Mantle plumes, mantle stirring and hotspot chemistry. *Eath planet. Sci. Lett.* **99**, 94-109.

Devey, C.W., Albarède, F., Cheminée, J.-L., Michard, A., Mühe, R., & Stoffers, P. (1990). Active submarine volcanism on the Society Hotspot Swell (West Pacific): a geochemical study. *J. Geophys. Res.* **95**, 5049-5066.

Dietz, R.S., & Sproll, W.P. (1970). East Canary Islands as a microcontinent within the Africa-North America continental drift fit. *Nature* **226**, 1043-1045.

Donaldson, C.H., & Brown, R.W. (1977). Refractory megacrysts and magnesium-rich melt inclusions within spinel in oceanic tholeiites: indicators of magma mixing and parental magma composition. *Eath planet. Sci. Lett.* **37**, 81-89.

Duda, A., & Schmincke, H.-U. (1985). Polybaric differentiation of alkali basaltic magmas: evidence from green-core clinopyroxenes (Eifel, FRG). *Contrib. Mineral. Petrol.* **91**, 340-353.

Dungan, M.A., & Rhodes, J.M. (1978). Residual glasses and melt inclusions in basalts from DSDP legs 45 and 46: evidence for magma mixing. *Contrib. Mineral. Petrol.* **67**, 417-431.

Dupré, B., & Allègre, C.J. (1980). Pb-Sr-Nd isotopic correlation and the chemistry of the North Atlantic mantle. *Nature* **286**, 17-22.

Edwards, R.L., Chen, J.H., and Wasserburg, G.J., (1987). ^{238}U-^{234}U-^{230}Th-^{232}Th systematics and the precise measurement of time over the past 500,000 years. *Earth planet. Sci. Lett.* **81**, 175-192.

Ellam, R.M., & Cox K.G. (1991). An interpretation of Karoo picrite basalts in terms of interaction between asthenospheric magmas and the mantle lithosphere. *Earth planet. Sci. Lett.* **105**, 330-342.

Elliott, T.R., Hawkesworth, C.J., & Grönvold, K. (1991). Dynamic melting of the Iceland plume. *Nature* **351**, 201-206.

Falloon, T.J., & Green, D.H. (1988). Anhydrous partial melting of peridotite from 8 to 35kb and the petrogenesis of MORB. *J. Petrology Special Lithosphere Issue* , 379-414.

Feigenson, M.D. , Hofmann, A.W., & Spera, F.J. (1983). Case studies on the origin of basalt II. The transition from tholeiitic to alkalic volcanism on Kohala volcano, Hawaii. *Contrib. Mineral. Petrol.* **84**, 390-405.

Fisk, M.R., Upton, B.G.J., & Ford, C.E. (1988). Geochemical and experimental study of the genesis of magmas of Réunion Island, Indian Ocean. *J. Geophys. Res.* **93**, 4933-4950.

Fitton, J.G., & Dunlop, H.M. (1985). The Cameroon line, West Africa, and its bearing on the origin of oceanic and continental alkali basalt. *J. Petrol.* **72**, 23-38.

Frey, F.A. (1980). The origin of pyroxenites and garnet pyroxenites from Salt Lake Crater, Oahu, Hawaii: trace element evidence. *Am. J. Sci.* **280-A**, 427-449.

Galer, S.J.G., O'Nions, R.K. (1985). Residence time of thorium, uranium and lead in the mantle with implications for mantle convection. *Nature* **316**, 778-782.

Garner, E.L., Machlan, L.A., and Shields, W.R., (1971). Uranium isotopic standard reference materials. *U.S. Nat. Bur. Stand. Spec. Publ., Washington* **260-27**, pp133.

Gast, P.W. (1968). Trace element fractionation and the origin of tholeiitic and alkaline magma types. *Geochim. Cosmochim. Acta.* **32**, 1057-1086.

Gasteri, P., Hernandez-Pacheco, A., & Muñoz, M. (1966). Las rocas holocristallinas de la Caldera de Taburiente, Isla de La Palma (Canarias). *Estud. Geol.* **23**, 113-134.

Gebrande, H., Miller, H., & Einarsson, P. (1980). Seismic structure of Iceland along RRISP-profile I. *J. Geophys.* **47**, 239-249.

Gill, J.B., & Williams, R.W. (1990). Th isotope and U-series studies of subduction-related volcanic rocks. *Geochim. Cosmochim. Acta.* **54**, 1427-1442.

Goldstein, S.J., Murrel, M.T., & Janecky, D.R. (1989). Th and U isotopic systematics of basalts from the Juan de Fuca and Gorda Ridges by mass spectrometry. *Earth planet. Sci. Lett.* **96**, 134-146.

Green, T.H., & Pearson, N.J. (1987). An experimental study of Nb and Ta partitioning between Ti-rich minerals and silicate liquids at high pressure and temperature. *Geochim. Cosmochim. Acta* **51**, 55-62.

Griffiths, R.W., Campbell, I.H. (1990). Stirring and strucure in mantle starting plumes. *Earth planet. Sci. Lett.* **99**, 66-78.

Halliday, A.N.,, Mahood, G.A., Holden, P., Metz J.M., Dempster, T.J., & Davidson, J.P. (1989). Evidence for long residence times of rhyolite magma in the Long Valley magmatic system: the isotopic record in precaldera lavas of Glass Mountain. *Earth planet. Sci.* **94**, 274-290.

Harmon, R.S., and Rosholt, J.N., (1982). In: Uranium Series Disequilibrium in Environmental Problems, ed. Ivanovich, M, and Harmon, R.S.. *Clarendon Press, Oxford*, pp571.

Hart, S.R., Schilling, J.-G., & Powell, J.L. (1973). Basalts from Iceland and along the Reykjanes ridge: Sr isotope geochemistry. *Nature* **246**, 104-107.

Hart, S.R., & Davis, K.E. (1978). Nickel partitioning between olivine and silicate melt. *Earth planet. Sci. Lett.* **40**, 203-219.

Hart, S.R. (1984). A large-scale isotope anomaly in the Southern Hemisphere mantle. *Nature* **309**, 753-757.

Hart, S.R. (1986). A possible new Sr-Nd-Pb mantle array and consequences for mantle mixing. *Geochim. Cosmochim. Acta* **90**, 273-295.

Hausen, H. (1969). Some contributions to the geology of La Palma. *Comm. Phys. Math. Finn. Acad. Sci.* **35**, 1-140.

Hawkesworth, C.J., Norry, M.J., Roddick, J.C., & Vollmer,R. (1979). $^{143}Nd/^{144}Nd$ and $^{87}Sr/^{86}Sr$ ratios from the Azores and their significance in LIL-element enriched mantle. *Nature* **280**, 28-31.

Hawkesworth, C.J., Rogers, N.W., van Calsteren, P.W., and Menzies, M.A. (1984). Mantle enrichment processes. *Nature* **311**, 331-335.

Hawkesworth, C.J., Kempton, P.D., Rogers, N.W., Ellam, R.M., & van Calsteren, P.W. (1990). Continental mantle lithosphere, and shallow level enrichment processes in the Earth's mantle. *Earth planet. Sci.* **96**, 256-268.

Hayes, D.E., & Rabinowitz, P.D. (1975). Mesozoic magnetic lineations and the magnatic quiet zone off North West Africa. *Earth planet. Sci. Lett.* **28**, 105-115.

Hemond, Ch., Condomines, M., Fourcade, S., Allègre, C.J., Oskarsson, N., & Javoy, M. (1988). Thorium, strontium and oxygen isotopic geochemistry in recent tholeiites from Iceland: crustal influence on mantle derived magmas. *Earth planet. Sci. Lett.* **87**, 273-285.

Hoernle, K.A., Tilton,G. & Schmincke, H.-U. (1988). Pb, Sr and Nd isotopic study of post-erosional volcanism on Gran Canaria, Canary Islands. *EOS* **69**, 1510.

Hoernle, K.A., Tilton, G., & Scmincke, H.-U. (1990). The 15m.y. isotopic evolution of Gran Canaria, Canary Islans. *EOS* **71**, 1696.

Hofmann, A.W., White, W.M. (1982). Mantle plumes from ancient oceanic crust. *Earth planet. Sci. Lett.* **57**, 421-436.

Hofmann, A.W., & Feigenson, M.D. (1983). Case studies on the origin of basalts I. Theory and reassessment of Grenada basalts. *Contrib. Mineral. Petrol.* **84**, 382-389.

Hofmann, A.W., Feigenson, M.D., & Raczak, I. (1984). Case studies on the orogin of basalt: III. Petrogenesis of the Mauna Ulu eruption, Kilauea, 1969-1971. *Contrib. Mineral. Petrol.* **88**, 24-35.

Hofmann, A.W., Jochum, K.P., Seufert, M., & White, W.M. (1986). Nb and Pb in oceanic basalts: new constraints on mantle evolution. *Earth planet. Sci.* **79**, 33-45.

Hofmann, A.W., Feigenson, M.D., & Raczek, I. (1987). Kohala revisited. *Contrib. Mineral. Petrol.* **95**, 114-122.

Houseman, G., & McKenzie, D.P. (1982). Numerical models on the onset of convective instability in the Earth's manlte. *Geophys. J. R. Astron. Soc.* **68**, 133-164.

Huppert, H.E., & Sparks, R.S.J. (1980). The fluid dynamics of a basaltic magma chamber replenished by influx of hot, dense ultrabasic magma. *Contrib. Mineral. Petrol.* **75**, 279-289.

Huppert, H.E., & Sparks, R.S.J. (1984). Double diffusive convection due to crystallisation in magmas. *Ann. Rev. Earth Planet. Sci.* **12**, 11-41.

Irving, A.J., Frey, F.A. (1984). Trace element abundances in megacrysts and their host basalts: constraints on partition coefficients and megacryst genesis. *Geochim. Cosmochim. Acta* **48**, 1201-1221.

Ivanovich, M., & Harmon, R.S. (eds) (1982). Uranium series disequilibrium. *Clarendon Press, Oxford*, pp571.

Jackson, E.D. (1968). The character of the lower crust and upper mantle beneath the Hawaiian Islands. *Proc. Int. Geol. Congr. 23rd Session Czech* **1**, 135-150.

Jakobsson, S.P. (1972). Chemistry and distribution pattern of recent basaltic rocks in Iceland. *Lithos* **5**, 365-386.

Jakobsson, S.P., Jónsson, J., & Shido, F. (1978). Petrology of the western Reykjanes Peninsula, Iceland. *J. Petrol.* **19**, 669-705.

Jaques, A.L., & Green, D.H. (1980). Anhydrous melting of peridotite at 0-15kb pressure and the genesis of tholeiitic basalts. *Contrib. Mineral. Petrol.* **73**, 287-310.

Johnson, K.T.M., Dick, H.J.B., & Shimizu, N. (1990). Melting in the oceanic upper mantle: an ion microprobe study of diopsides in abyssal peridotites. *J. geophys. Res.* **95**, 2661-2678.

Joron, J.-L., Treuil, M. (1989). Hygromagmaphile element distributions in oceanic basalts. *In: Saunders, A.D. & Norry, M.J. (eds) Magmatism in the Ocanic Basins. Geol. Soc. Lond. Special Publication* **42**, 277-299.

Kaiser, C., & Schmincke, H.-U. (1987). Compositional and rheological evolution of the 1949 tephrite (AA) to basanite (pahoehoe) eruption on La Palma (Canary Islands). *Hawaii symposium on how volcanoes work* , 129.

Kent, D., & Gradstein, F.M. (1984). A Jurassic to recent chronology in the Western Atlantic Region. *In: Tucholke, P.R. & Vogt, P. (eds) The Geology of North America. Geol. Soc. America. Boulder, Colo.* M.

Klein, E.M., & Langmuir, C.H. (1987). Global correlations of oceanic ridge basalt chemistry with axial depth and crustal thickness. *J. geophys. Res.* **92**, 8089-8115.

Klein, E.M., & Langmuir, C.H. (1989). Local versus global variations in ocean ridge basalt composition: a reply. *J. geophys. Res.* **94**, 4241-4252.

Langmuir, C.H., Vocke, R.D., Hanson, G.N., & Hart, S.R. (1978). A general mixing equation with applications to Icelandic basalts. *Earth planet. Sci.* **37**, 380-392.

Langmuir, C.H., & Plank, T. (1988). Quantitative reevaluation of magma chamber processes and melting regime shape. *Chem. Geol.* **70**, 153-162.

Langmuir, C.H. (1990). Geochemical consequences of in situ crystallisation. *Nature* **340**, 199-205.

Lanphere, M.A., & Frey, F.A. (1987). Geochemical evolution of Kohala Volcano, Hawaii. *Contrib. Mineral. Petrol.* **95**, 100-113.

Latin, D., & Waters, F.G. (1991). Melt generation during rifting in the North Sea. *Nature* **351**, 559-562.

Le Roux, A.P. (1985). Geochemistry, mineralogy and magmatic evolution of the basaltic and trachytic lavas from Gough Island, South Atlantic. *J. Petrol.* **26**, 149-186.

Leeman, W.P., Budahn, J.R., Gerlach, D.C., Smith, D.R., & Powell, B.N. (1980). Origin of Hawaiian tholeiites: trace element constraints. *Am. J. Sci.* **280-A**, 794-819.

Li, W.X., Lundberg, J., Dickin, A.P., Ford, D.C., Schwarz, H.P., McNutt, R., & Williams, D. (1989). High-precision mass-spectrometric uranium -series dating of cave deposits and implications for palaeoclimate studies. *Nature* **339**, 534-536.

Liotard, J.M., Barsczus, H.G., Dupuy, C. & Dostal, J. (1986). Geochemistry and origin of basaltic lavas from Marquesas Archipelago, French Polynesia. *Contrib. Mineral. Petrol.* **92**, 260-268.

Loubet, M., Sassi, R., & Donato, G.D. (1988). Mantle heterogeneities: a combined isotope and trace element approach and evidence for recycled continental materials in some OIB sources. *Earth planet.Sci. Lett.* **89**, 299-315.

Maaløe, S., & Jakobsson, S.P. (1980). The PT phase relations of a primary oceanite from the Reykjanes Peninsula, Iceland. *Lithos* **13**, 237-246.

Maaløe, S., Sørensen, I.B., & Hertogen, J. (1986). The trachybasaltic suite of Jan Mayen. *J. Petrol.* **27**, 439-466.

Manhès, G., Minster, J.F., & Allègre, C.J. (1978). Comparative uranium-thorium-lead and rubidium-srontium study of the Saint Séverin amphoterite: consequences for early solar system chronology. *Eath planet. Sci. Lett.* **39**, 14-24.

McBirney, A.R., & Gass, I.G. (1967). Relations of oceanic volcanic rocks to mid-oceanic rises and heat flow. *Earth planet. Sci. Lett.* **2**, 265-276.

McDermott, F., & Hawkesworth, C.J. (1991). Th, Pb, and Sr isotope variations in young island arc volcanics and ocean sediments. *Earth planet. Sci. Lett.* **104**, 1-16.

McDougall, I. (1964). Potassium-argon ages from lavas of the Hawaiian Islands. *Geol. Soc. Am. Bull.* **75**, 107-128.

McKenzie, D. (1984). The generation and compaction of partially molten rock. *J. Petrology* **25**, 713-765.

McKenzie, D. (1985a). 230Th-238U disequilibrium and the melting process beneath ridge axes. *Earth planet. Sci. Lett.* **72**, 149-157.

McKenzie, D. (1989). The volume and composition of melt fractions in the mantle. *Earth planet. Sci. Lett.* **95**, 53-72.

McKenzie, D., & O'Nions, R.K. (in press). Partial melt distributions from inversion of rare earth element concentrations. *J. Petrol.*.

Meadows, J.W., Armani, R.J., Callis, E.L., and Essling, A.M., (1980). Half-life of ^{230}Th. *Phys. Rev.* **C22**, 750-754.

Meijer, A., Kwon, T.-T., & Tilton, G.R. (1990). U-Th-Pb partitioning behaviour during melting in the upper mantle: implications for the origin of high mu components and the 'Pb paradox'. *J. geophys. Res.* **95**, 433-448.

Menat, M. (1964). A quantitative study of scattering phenomena in an electromagnetic separator. *Can. J. Phys.* **42**, 164-192.

Meyer, P.S., Sigurdsson, H., & Schilling, J.-G. (1985). Petrological and geochemical variations along Iceland's neovolcanic zones. *J. geophys. Res.* **90**, 10,043-10,072.

Michard, A., Albarède, F., Michard, G., Minster, J.F., & Charlou, J.L. (1983). Rare earth elements and uranium in high temperature solutions for East Pacific Rise vent field (13°N). *Nature* **303**, 795-797.

Middlemost, E.A.K. (1970). San Miguel de La Palma- a volcanic island in section. *Bull. Volcanol.* **34**, 216-239.

Middlemost, E.A.K. (1972). Evolution of La Palma, Canary Archipelago. *Contrib. Mineral. Petrol.* **36**, 33-48.

Minster, J.F., & Allègre, C.J. (1978). Systematic use of trace elements in igneous processes. Part III: Inverse problem of batch partial melting in volcanic suites. *Contrib. Mineral. Petrol.* **68**, 37-52.

Nakamura, Y., & Tatsumoto, M. (1988). Pb, Nd, and Sr isotopic evidence for a multicomponent source for rocks of Cook-Austral Islands and heterogeneities. *Geochim. Cosmochim. Acta* **52**, 2909-2924.

Newman, S., Finkel, R.C., & MacDougall, J.D. (1983). 230Th-238U disequilibrium systematics in oceanic tholeiites from 21°N on the East Pacific Rise. *Earth planet. Sci. Lett.* **65**, 17-33.

Newman, S., Finkel, R.C., & MacDougall, J.D. (1984). Comparison of 230Th-238U disequilibrium systematics in lavas from three hot spot regions: Hawaii, Prince Edward and Samoa. *Geochim. Cosmochim. Acta* **48**, 315-324.

Nicholls, J., & Stout, M.Z. (1988). Picritic melts in Kilauea- evidence from the 1967-1968 Halemaumau and Hiiaka eruptions. *J. Petrol.* **29**, 1031-1057.

Nicholson, N., Condomines, M., Fitton, J.G., Fallick, A.E., Grönvold, K., & Rogers, G. (in press). Geochemical and isotopic evidence for crustal assimilation beneath Krafla, Iceland. *J. Petrol.*.

Nicholson, H., & Latin, D (in review). Olivine tholeiites from Krafla, Iceland: evidence for variations in melt fraction within a plume. *J. Petrol.*.

Nickel, K.G. (1986). Phase equilibria in the system SiO2-MgO-Al2O3-CaO-Cr2O3 (SMACCR) and their bearing on spinel/garnet lherzoite relationships. *Neues. Jahrb. Miner. Abh.* **155**, 259-287.

O'Nions, R.K., & Grönvold, K. (1973). Petrogenetic relationships of acid and basic rocks in Iceland: Sr-isotopes and rare-earth elements in late and postglacial volcanics. *Earth planet. Sci. Lett.* **19**, 397-409.

O'Nions, R.K., Pankhurst, P.J., & Fridleifsson, I.B. (1973). Strontium isotopes and rare earth elements in basalts from the Heimay and Surtsey volcanic eruptions. *Nature* **243**, 213-214.

O'Nions, R.K., Pankhurst, R.J. (1974). Petrographic significance of isotopic and trace element variations in volcanic rocks from the mid-Atlantic. *J. Petrol.* **15**, 603-634.

O'Nions, R.K., Pankhurst, R.J. , & Grönvold, K. (1976). Nature and development of basalt magma sources beneath Iceland and the Reykjanes Ridge. *J. Petrol.* **17**, 315-338.

O'Nions, R.K., Hamilton, P.J., & Evensen, N.M. (1977). Variations in $^{143}Nd/^{144}Nd$ and $^{87}Sr/^{86}Sr$ ratios in oceanic basalts. *Earth planet. Sci. Lett.* **34**, 13-22.

O'Nions, R.K., Carter, S.R., Evensen, N.M., & Hamilton, P.J. (1981). Upper mantle geochemistry. *In: C. Emiliani(ed.) The Sea Vol.7. The Oceanic Lithosphere, Wiley, N.Y.*, 13-22.

Omerod, D.S., Rogers, N.W., & Hawkesworth, C.J. (in press). Melting in the lithosphereic mantle: inverse modelling of alkali-olivine basalts from the Big Pine volcanic field, California. *Contrib. Mineral. Petrol.*.

Oskarsson, N., Sigvaldason, G.E., & Steinthórsson, S. (1982). A dynamic model of rift zone petrogenesis and the regional petrology of Iceland. *J. Petrol.* **23**, 28-78.

Oversby, V.M., & Gast, P.W. (1968). Lead isotopic compositions and uranium decay series disequilibrium in recent volcanic rocks. *Earth planet. Sci. Lett.* **5**, 199-206.

Overstreet, W.C., White, AM., & Warr, J.J. (1970). Uranium-rich monazites in the United States. *U.S. Geol. Surv. Prof. Paper* **700D**, 169-175.

Palacz, Z.A., & Saunders, A.D. (1986). Coupled trace element and isotope enrichment in the Cook-Austral-Samoa islands, southwest Pacific. *Earth planet. Sci. Lett.* **79**, 270-280.

Palmason, G., & Saemundsson, K. (1974). Iceland in relation to the Mid-Atlantic Ridge. *Ann. Rev. Earth Planet. Sci.* **2**, 25-50.

Palmason, G. (1980). A continuum model of crustal generation in Iceland: kinematic aspects. *J. Geophys.* **47**, 7-18.

Perrin, R.E., Knobeloch, G.W., Armijo, V.M., and Efurd, D.W., (1985). Isotopic analysis of nanogram quantities of plutonium by using a SID ionisation source. *Int. J. Mass Spectrom. Ion Processes* **64**, 17-24.

Potts, P.J., Williams Thorpe, O., Isaacs, M.C., & Wright, D.W. (1985). High-precision instrumental neutron-activation analysis of geological samples employing simultaneous counting with both planar and coaxial detectors . *Chem. Geol.* **48**, 145-155.

Rhodes, J.M., Dungan, M.A., Blanchard D.P., & Long, P.E. (1979). Magma mixing at mid-ocean ridges: evidence from basalts drilled near 22°N on the Mid-Atlantic Ridge. *Tectonphysics* **55**, 35-61.

Rhodes, J.M. (1990). The 1852 and 1868 Mauna Loa picrite eruptions: clues to parental magma compositions and magmatic plumbing system. *EOS* **71**, 1695.

Roedder, E. (1965). Liquid CO2 inclusions in olivine-bearing nodules and phenocrysts from basalts. *Am. Mineral.* **50**, 1746-1782.

Roesser, H.A., Hinz, K. & Plaumann, S. (1971). Continental margin structure in the Canaries. *Inst. Geol. Sci. Rep.* **70/16**, 27-36.

Rogers, N.W., Hawkesworth, C.H., & Palacz, Z.A. (in press). Isotope and trace element variations in olivine melilitites from Namaqualand, South Africa, and their implications for element fractionation processes in the upper mantle. *Lithos.*

Rokop, D.J., Perrin, R.E., Knobeloch G.W., Armijo V.M., and Shields, W.R., (1982). Thermal ionisation mass spectrometry of uranium with electrodeposition as a loading technique. *Anal. Chem.* **54**, 957-960.

Rothe, P., Schmincke, H.-U. (1968). Contrasting origins of the eastern and western islands of the Canary Archipelago. *Nature* **210**, 1152-1154.

Rogers, N.W., Hawkesworth, C.H., & Palacz, Z.A. (in press). Isotope and trace element variations in olivine melilitites from Namaqualand, South Africa, and their implications for element fractionation processes in the upper mantle. *Lithos*.

Rokop, D.J., Perrin, R.E., Knobeloch G.W., Armijo V.M., and Shields, W.R., (1982). Thermal ionisation mass spectrometry of uranium with electrodeposition as a loading technique. *Anal. Chem.* **54**, 957-960.

Rothe, P., Schmincke, H.-U. (1968). Contrasting origins of the eastern and western islands of the Canary Archipelago. *Nature* **210**, 1152-1154.

Rubin, K.H., & MacDougall, J.D. (1988). 226Ra excesses in the mid-ocean-ridge basalts and mantle melting. *Nature* **335**, 158-161.

Ruedenauer, F.G. (1970). Gas scattering as a limit to trace sensitivity in analytical mass spectrometers. *Rev. Sci. Instrum.* **41**, 1487-1488.

Schilling, J.-G. (1973). Iceland mantle plume: geochemical study of Reykjanes Ridge. *Nature* **242**, 565-571.

Schilling, J.-G., Sigurdsson, H., & Kingsley, R.H. (1978). Skagi and western neovolcanic zones in Iceland: 2. geochemical variations. *J. geophys. Res.* **83**, 3983-4002.

Schmincke, H.-U (1973). Magmatic evolution and tectonic regime in the Canary, Madeira and Azores Island Groups. *Geol. Soc. Am. Bull.* **84**, 633-648.

Schmincke, H.-U. (1982). Volcanic and chemical evolution of the Canary Islands. *In: U. von Rad, K. Hinz, M. Sarnthein and E. Seibold (eds.), Geology of the Northwest African margin. Springer-Verlag, New York* , 273-306.

Shaw, D.M. (1970). Trace element fractionation during anatexis. *Geochim. Cosmochim. Acta* **34**, 237-243.

Sigvaldason, G.R. (1974). Basalts from the centre of the assumed Icelandic mantle plume. *J. Petrology* **15**, 497-524.

Silver, P.G., Carlson, R.W. & Olson, P. (1988). Deep slabs, geochemical heterogeneity, and the structure of mantle convection: investigation of an enduring paradox. *Ann. Rev. Earth Planet. Sci.* **16**, 477-541.

Sleep, N.H. (1990). Hotspots and mantle plumes. *J. Geophys. Res.* **95**, 6714-6736.

Smith, D.H., and Carter, J.A., (1981). A simple method to enhance thermal emission of metal ions. *Int. J. Mass Spectrom. Ion Phys.* **40**, 211-215.

Smith, D.H., Walker, R.L., & Carter, J.A., (1982). Sampling and analysis of radio active solutions. *Anal. Chem.* **54**, 826A-832A.

Sparks, R.S.J., Meyer, P., & Sigurdsson, H. (1980). Density variation amongst mid-oceanic ridge basalts: implications for magma mixing and the scarcity of primitive lavas. *Earth planet. Sci. Lett.* **46**, 419-430.

Sparks, R.S.J., Marshall, L.A. (1986). Thermal and mechanical constraints on mixing between mafic and silicic magmas. *J. Volcanol. geotherm. Res.* **29**, 99-124.

Staudigel, H., & Schmincke, H.-U. (1984). The pliocene seamount series of La Palma/Canary Islands. *J. Geophys. Res.* **89**, 11,195-11,215.

Stolper, E. (1980). A phase diagram for mid-ocean ridge basalts: preliminary results and implications for petrogenesis. *Contrib. Mineral. Petrol.* **74**, 13-27.

Storey, M., Wolff, J.A., Norry, M.J., & Marriner, G.F. (1989). Origin of hybrid lavas from Agua de Pau volcano, Sao Miguel, Azores. *In: Saunders, A.D. & Norry, M.J. (eds) Magmatism in the Ocanic Basins. Geol. Soc. Lond. Special Publication* **42**, 161-180.

Sun, S.-S, Tatsumato, M., & Schilling, J.-G. (1975). Mantle plume mixing along the Reykjanes Ridge axis: lead isotope evidence. *Science* **190**, 143-147.

Sun, S.-S., & Jahn, B. (1975). Lead and strontium isotopes in post-glacial basalts from Iceland. *Nature* **255**, 527-530.

Sun, S.-S. (1980). Lead isotopic study of young volcanic rocks from mid-ocean ridges, ocean islands and island arcs. *Phil Trans. Soc. Lond.* **A 297**, 409-445.

Sun, S.-S. , & McDonough, W.F. (1989). Chemical and isotopic systematics of oceanic basalts: implications for mantle compositon and processes . *In: Saunders, A.D. & Norry, M.J. (eds) Magmatism in the Ocanic Basins. Geol. Soc. Lond. Special Publication* **42**, 313-345.

Takahashi, E., & Kushiro, I. (1983). Melting of a dry peridotite at high pressures and basalt magma genesis. *Am. Miner.* **68**, 859-879.

Tatsumi, Y., Hamilton, D.L., & Nesbitt, R.W. (1986). Chemical characteristics of fluid phase released from a subducted lithosphere and origin of arc magmas: evidence from high-pressure experiments and natural rocks. *J. Volcanol. Geotherm. Res.* **29**, 293-309.

Tatsumoto, M., (1978). Isotopic composition of lead in oceanic basalt and its implication to mantle evolution. *Earth planet. Sci. Lett.* **38**, 63-87.

Thirwell, M., (1990). Pb-Sr-Nd isotope geochemistry of basalts from Fuerteventura, Canary Islands, Spain: the development of the HIMU mantle. *Geol. Soc. Australia Abstracts* **27**, 100.

Watson, E.B. (1980). Apatite and phosphorus in the mantle source regions: an experimental study of apatite/melt equilibria at pressures up to 25kbar. *Earth planet. Sci. Lett.* **51**, 322-335.

Watson, S., & McKenzie, D. (1991). Melt generation by plumes: a study of Hawaiian volcanism. *J. Petrol.* **32**, 501-537.

Weaver, B.L., Wood, D.A., Tarney, J., & Joron, J.-L. (1987). Geochemistry of ocean island basalts from the South Atlantic; Ascension, Bouvet, St. Helena, Gough and Tristan da Cunha. *In: Fitton, J.G. & Upton, B.G.J. (eds) Alkaline Igneous Rocks. Geol. Soc. Lond. Special Publication* **30**, 253-267.

Weaver, B.L. (1991). Trace element evidence for the origin of ocean-island basalts. *Geology* **19**, 123-126.

Welke, H., Moorbath, S., Cumming, G.L., & Sigurdsson, H. (1968). Lead isotope studies on igneous rocks from Iceland. *Earth planet. Sci. Lett.* **4**, 221-231.

White, W.M., & Hofmann, A.W. (1982). Sr and Nd isotope geochemistry of oceanic basalts and mantle evolution. *Nature* **296**, 821-825.

Williams, R.W., & Gill, J.B. (1989). Effects of partial melting on the uranium decay series. *Geochim. Cosmochim. Acta.* **53**, 1607-1619.

Wolff, J.A. (1983). Petrology of Quaternary pyroclastic deposits from Tenerife, Canary Islands. *Ph.D. thesis, University of London*, 542pp.

Wolff, J.A. (1984). Zoning in highly alkaline magma bodies. *Geol. Mag.* **121**, 563-575.

Wolff, J.A. (1984). Variation in Nb/Ta during differentiation of phonolitic magma, Tenerife, Canary Islands. *Geochim. Cosmochim. Acta* **48**, 1345-1348.

Wood, D.A., Joron, J.L., Treuil, M., Norry, M.J., & Tarney, J. (1979). Elemental and Sr isotope variations in basic lavas from Iceland and the surrounding ocean floor. *Contrib. Mineral. Petrol.* **70**, 319-339.

Wood, D.A., (1981). Partial melting models for the petrogenesis of Reykjanes Peninsula basalts, Iceland: implications for the use of trace elements and strontium and neodynium isotope ratios to record inhomogeneities in the upper mantle. *Earth planet. Sci. Lett.* **52**, 183-190.

Wright, T.L., & Doherty, P.C. (1970). A linear programming and least square computer method for solving petrological mixing problems. *Bull. Geol. Soc. Am.* **80**, 1995-2008.

York, D. (1969). Least squares fitting of a straight line with correlated errors. *Earth planet. Sci. Lett.* **5**, 320-324.

Zindler, A., Hart, S.R., Frey, F.A., & Jakobsson, S.P. (1979). Nd and Sr isotope ratios and rare earth elemnt abundances in Reykjanes Peninsula basalts: evidence for mantle heterogeneity beneath Iceland. *Earth planet. Sci. Lett.* **45**, 249-262.

Zindler, A., & Hart, S.R. (1986). Chemical geodynamics. *Ann. Rev. Earth Planet. Sci.* **14**, 493-571.

Appendix A

Whole Rock Data from La Palma

This appendix contains all whole rock data for the La Palma samples. Tables A.1-A.4 contain data from different samples from the same flow or unit, for which a single analysis has been reported in Table 3.1. Multiple analyses of the same flow/unit were made in order to assess heterogeneity. However, all analyses from the same unit are very similar and generally within the analytical error given in Table 3.1. Table A.2 contains four replicate INAA analyses on historic basanites. Table A.5 contains data on nodules contained within basanites flows, and a single basement cumulate that were not discussed in Chapter 3. Petrographic descriptions of these samples are given, together with the other samples, in Appendix C and their locations are indicated in Fig. 3.2. Analytical techniques are described in section 3.4, except that the isotopic analyses in this appendix were made on a single collector VG-54e mass-spectrometer and have poorer reproducibility than the data reported in Table 3.1, which were analysed on a Finnigan 261 multi-collector. Mean NBS 987 and J&M Nd standards for the period of analysis on the 54e were 0.70173±90 and 0.511865±38 (2 sigma standard deviation) respectively.

Figs. A1-A3 show correlations of LREE concentrations measured by XRF and INAA techniques, and U&Th concentrations measured by INAA and isotope dilution techniques, for both just basanitic samples and for the data set as a whole. The regression lines obtained from these plots were used to correct LREE contents measured by XRF and U&Th contents measured by INAA, for samples not analysed by the more precise INAA and isotope dilution methods respectively, so that the whole data set reported in Table 3.1 is consistent.

Table A.1 Whole rock analyses for historic basanites.

		LP45C 1585	LP45D 1585	LP45D2 1585	LP45E 1585	LP43B 1646	LP43E 1646	LP43E2 1646	LP63C 1646 S	LP65B 1677	LP65C 1677	LP95A 1712 J	LP95C 1712 J	LP95D 1712 J	LP4 1712 SC	LP5 1712 SC	LP5T 1712 SC	LP29C 1712 CV	LP29D 1712 CV
SiO_2	XRF	43.21	43.15	43.14	42.99	42.5	42.7	42.22	42.45	43.57	43.29	43.41	43.56	44.01	43.04	42.79	42.81	42.47	42.69
Al_2O_3	XRF	13.78	13.91	14.04	13.8	13.01	13.11	12.94	12.84	13.78	13.75	13.8	13.86	13.99	14.62	14.45	14.56	14.11	14.18
Fe_2O_3T	XRF	13.24	13.2	13.14	13.32	13.48	13.43	13.42	13.55	13.12	13.29	13.3	13.27	13.09	13.06	13.17	13.09	13.4	13.4
MgO	XRF	7.43	7.29	7.24	7.56	8.3	8.24	8.21	8.48	7.79	7.81	7.63	7.63	7.65	6.39	6.38	6.4	6.92	6.91
CaO	XRF	10.63	10.6	10.52	10.62	12.15	12.22	12.19	12.26	10.83	10.8	10.9	10.9	10.9	10.84	10.9	10.89	11.07	11.15
Na_2O	XRF	3.88	4	4	3.84	3.5	3.54	3.43	3.39	3.75	3.95	3.64	3.53	3.71	4.39	4.13	4.06	3.82	3.98
K_2O	XRF	1.75	1.83	1.82	1.78	1.51	1.54	1.53	1.49	1.83	1.83	1.71	1.73	1.73	1.95	1.89	1.92	1.84	1.82
TiO_2	XRF	3.74	3.75	3.76	3.73	3.76	3.76	3.76	3.75	3.6	3.6	3.7	3.71	3.68	3.82	3.82	3.82	3.87	3.88
MnO	XRF	0.21	0.21	0.22	0.21	0.21	0.2	0.2	0.2	0.21	0.21	0.21	0.21	0.21	0.21	0.21	0.22	0.21	0.21
P_2O_5	XRF	0.83	0.87	0.86	0.83	0.87	0.87	0.86	0.84	0.85	0.84	0.79	0.76	0.76	1.1	1.09	1.09	1.02	1.02
TOTAL		98.71	98.81	98.72	98.69	99.28	99.61	98.76	99.25	99.34	99.37	99.09	99.15	99.72	99.42	98.83	98.86	98.75	99.25
Co	INAA		43.7				51.5		52.3		48.8			48.4	42				46.1
Ni	XRF	107	101	101	108	114	112	112	118	107	110	102	101	100	56	58	57	70	70
Cr	XRF	272	250	244	251	296	292	288	307	259	244	257	257	252	93	97	97	150	141
V	XRF	303	303	307	310	325	331	328	334	303	305	298	299	291	304	306	300	320	322
Sc	XRF	19	21	17	18	23	23	22	24	21	20	19	19	20	18	15	17	19	20
Cu	XRF	81	78	79	81	115	114	114	118	89	89	92	90	89	84	84	86	89	90
Zn	XRF	115	115	116	116	103	101	103	105	113	115	112	113	110	111	112	111	114	112
Sr	XRF	1142	1172	1167	1161	1165	1174	1169	1152	1238	1246	1154	1155	1166	1447	1437	1446	1352	1351
Rb	XRF	42	44	43	42	33	35	34	32	41	42	38	39	40	44	45	45	42	42
Ba	XRF	689	709	698	700	672	694	702	697	709	704	656	678	677	832	875	851	799	776
Cs	INAA		0.6						0.58										
Nb	XRF	88	91	91	91	76	79	78	76	89	90	88	89	89	100	99	99	95	94
Zr	XRF	418	427	427	425	380	354	351	348	395	399	385	384	387	459	453	455	426	433
Hf	INAA		7.82				6.83		6.86		7.42			7.53	8.02				7.56
Ta	INAA		5.95				5.1		5.15		5.67			5.68	6.27				5.75
Th	INAA		8.06				9.74		9.29		10.7			8.21	11.9				10.9
U	INAA		2.3				2.71		2.7		3.08			2.19	3.2				2.96
La	XRF	91	85	86	90	91	97	105	92	106	106	84	83	86	122	115	116	102	108
La	INAA		80.8				92.3		89.9		97.2			84.2	113				105
Ce	XRF	171	182	173	175	185	185	184	199	196	192	175	174	168	227	233	228	205	213
Ce	INAA		163				177		172		179			161	201				196
Nd	XRF	80	87	79	79	79	81	84	84	79	79	79	79	76	98	97	98	89	93
Nd	INAA		73				77.3		74.4		77.6			71.8	88.4				84.4
Sm	INAA		13.4				14.1		14		14.2			13.5	15.9				15.2
Eu	INAA		4.18				4.06		4.18		4.12			3.93	4.53				4.37
Tb	INAA		1.55				1.49		1.5		1.44			1.39	1.62				1.5
Yb	INAA		2.46				2.24		2.35		2.51			2.36	2.53				2.48
Lu	INAA		0.35				0.38		0.34		0.36			0.37	0.41				0.4
Y	XRF	36	37	36	36	34	35	34	34	35	36	35	35	35	39	39	39	37	38
$^{87}Sr/^{86}Sr$							0.70297							0.70302					
$^{143}Nd/^{144}Nd$							0.51291							0.51295					

Table A.2 Whole rock analyses for historic basanites.

		LP30A 1712 DM	LP30A Rep	LP30D 1712 DM	LP32B 1712 DM	LP51C 1712 G	LP51C Rep	LP51D 1712 G	LP51E 1712 G	LP48B 1712 PN	LP48B Rep	LP48C 1712 PN	LP69A 1949 E	LP69D 1949 E	LP40B 1971	LP40E 1971	LP40E Rep	LP41A 1971 S	LP41C 1971 S	LP41E 1971 S
SiO_2	XRF	42.68		42.7	42.34	43.57		43.73	43.51	43.37		43.17	43.96	44.06	43.95	43.99		42.99	42.96	42.96
Al_2O_3	XRF	12.93		12.87	13.87	14.26		14.38	14.29	13.51		13.63	13.87	13.98	15.34	15.35		13.63	13.76	13.8
Fe_2O_3T	XRF	13.59		13.53	13.49	13.31		13.08	13.03	13.34		13.31	13.71	13.59	13.09	13.07		14.03	14.05	14.01
MgO	XRF	8.68		8.8	7.47	7.15		6.91	7.18	7.97		7.67	8.35	8.3	5.85	5.84		7.95	8.14	7.97
CaO	XRF	11.47		11.43	11.19	10.68		10.63	10.6	11.28		11.22	10.83	10.83	10.19	10.15		11.1	11.04	11.06
Na_2O	XRF	3.57		3.52	3.83	4.08		4.05	3.93	3.72		3.7	3.47	3.5	4.2	4.28		3.53	3.54	3.49
K_2O	XRF	1.63		1.61	1.78	1.71		1.79	1.76	1.52		1.59	1.26	1.26	1.76	1.75		1.38	1.39	1.4
TiO_2	XRF	3.74		3.72	3.82	3.71		3.69	3.69	3.74		3.75	3.35	3.35	3.74	3.72		3.72	3.7	3.71
MnO	XRF	0.2		0.21	0.21	0.21		0.21	0.21	0.2		0.2	0.19	0.19	0.2	0.2		0.2	0.2	0.2
P_2O_5	XRF	0.87		0.87	1	0.83		0.8	0.8	0.76		0.78	0.7	0.71	0.97	0.97		0.79	0.82	0.82
TOTAL		99.35		99.26	98.99	99.51		99.28	99.01	99.43		99.03	99.69	99.78	99.28	99.31		99.32	99.6	99.41
Co	INAA	53.3	51.2			46.8	45.7			48.4	50.2		52.4			41.1	40		52.9	
Ni	XRF	124		126	87	89		88	89	105		95	122	119	47	49		100	102	102
Cr	XRF	297		295	206	195		208	203	260		257	307	311	66	66		199	207	207
V	XRF	321		318	322	291		296	291	309		308	296	298	274	278		312	307	311
Sc	XRF	22		17	18	21		17	20	20		18	26	25	17	17		22	22	19
Cu	XRF	102		101	96	83		83	81	101		102	96	97	77	75		98	99	102
Zn	XRF	105		104	113	109		114	112	103		104	113	113	116	114		108	109	108
Sr	XRF	1155		1143	1285	1243		1243	1227	1091		1113	924	925	1230	1224		1028	1018	1014
Rb	XRF	36		37	40	42		41	41	35		37	25	26	37	37		27	28	28
Ba	XRF	737		687	768	706		743	709	632		631	473	470	663	639		547	546	544
Cs	INAA	0.63	0.63										0.39				0.54			
Nb	XRF	80		79	90	94		96	95	82		83	66	66	82	81		67	66	66
Zr	XRF	379		376	411	416		424	422	369		375	320	320	428	427		366	361	361
Hf	INAA	7.09	6.93			7.8	7.74			7.29	7.05		6.47			7.77	7.62		6.81	
Ta	INAA	5.62	5			5.99	5.93			5.22	5.02		4.62			5.7	5.14		4.25	
Th	INAA	8.24	8.63			9.04	8.7			7.49	7.1		6.16			8.24	8.17		6.88	
U	INAA	2.46	2.49			2.81	2.37			1.98	2.09		1.83			2.12	2.5		1.98	
La	XRF	92		93	98	93		107	100	77		81	65	68	84	79		74	73	75
La	INAA	88.4	86.5			92	90.6			79.1	77.2		63.9			85.8	83.6		73.5	
Ce	XRF	188		189	200	176		191	194	162		168	132	134	181	182		151	165	157
Ce	INAA	174	158			168	162			143	142		133			176	157		134	
Nd	XRF	83		81	86	77		78	85	70		75	71	69	80	79		65	74	74
Nd	INAA	80.1	71.4			76.7	74			69.2	68.4		63.9			79.2	74.2		64.5	
Sm	INAA	14.3	12.3			14	12.8			12.9	12		11.8			14.7	13		12.3	
Eu	INAA	4.24	3.91			4.06	4.01			3.79	3.79		3.63			4.4	4.03		3.68	
Tb	INAA	1.71	1.38			1.46	1.41			1.34	1.31		1.55			1.75	1.45		1.37	
Yb	INAA	2.46	2.36			2.45	2.57			2.26	2.33		2.22			2.5	2.48		2.07	
Lu	INAA	0.41	0.34			0.4	0.39			0.35	0.37		0.33			0.37	0.38		0.3	
Y	XRF	34		33	37	36		37	36	34		35	32	31	36	35		32	32	32
$^{87}Sr/^{86}Sr$		0.70304											0.70303			0.70305				
$^{143}Nd/^{144}Nd$		0.51295											0.51289			0.51230				

		LP9 T1	LP11 T1	LP12 T2	LP14 T2	LP15 T3	LP16 T3	LP19 T4	LP20 T4	LP61D CD	LP68A CV3	LP68D CV3	LP73A CV1	LP73C CV1
SiO_2	XRF	48.31	48.49	43.31	43.21	41.11	41.15	42.68	42.54	42.82	43.26	43.49	45.36	45.34
Al_2O_3	XRF	16.6	16.66	14.7	14.71	12.09	11.66	13.92	13.81	16.82	14.43	14.55	14.66	14.59
Fe_2O_3T	XRF	11.2	11.26	13.6	13.77	14.08	13.98	15.78	15.62	9.14	13.34	13.31	12.08	11.99
MgO	XRF	3.52	3.64	6.09	6.14	9.68	10.27	7.23	7.28	3.62	7.02	6.94	7.03	6.88
CaO	XRF	8.3	8.31	10.16	10.21	12.84	13.11	10.94	10.8	8.58	10.77	10.73	10.2	10.27
Na_2O	XRF	4.5	4.71	3.56	3.27	2.76	2.49	2.85	2.8	6.71	3.87	4.09	3.99	4.16
K_2O	XRF	2.13	2.14	1.79	1.64	1.27	1.21	0.89	0.91	2.48	1.41	1.43	1.8	1.8
TiO_2	XRF	2.75	2.77	3.86	3.88	4.06	3.98	4.33	4.28	2.65	3.63	3.61	3.31	3.28
MnO	XRF	0.24	0.24	0.21	0.21	0.19	0.19	0.19	0.19	0.19	0.2	0.2	0.18	0.18
P_2O_5	XRF	1.26	1.27	1.07	1.05	0.67	0.63	0.52	0.52	0.77	1.24	1.26	0.77	0.79
TOTAL		98.79	99.48	98.36	98.09	98.75	98.68	99.33	98.76	93.79	99.17	99.59	99.38	99.28
Co	INAA	22		42.1			56.4	56.6		23.5				
Ni	XRF	6	6	48	47	127	140	89	89	17	75	72	96	94
Cr	XRF	2	3	59	56	339	342	115	117	20	126	131	211	211
V	XRF	137	136	287	278	369	354	373	356	245	262	259	252	249
Sc	XRF	7	8	20	15	25	26	25	22	5	15	19	16	19
Cu	XRF	25	28	71	73	52	53	98	103	34	77	76	91	89
Zn	XRF	136	137	124	124	93	90	116	113	97	104	101	96	100
Sr	XRF	1305	1287	1033	1081	866	839	679	664	1512	1286	1302	1078	1073
Rb	XRF	58	58	41	40	29	26	15	16	65	26	25	45	45
Ba	XRF	769	756	575	595	563	507	282	311	1123	667	674	716	684
Cs	INAA	0.72		0.45			0.4			1.33				
Nb	XRF	128	129	93	94	59	55	41	41	141	76	76	84	84
Zr	XRF	675	678	477	482	304	294	287	284	484	368	373	358	356
Hf	INAA	12.5		9.09			5.93	6.34		6.87				
Ta	INAA	8.8		6.31			3.64	2.91		8.29				
Th	INAA	10.8		6.82			4.67	2.71		11.7				
U	INAA	2.76		2.37			1.07	1.14		3.5				
La	XRF	109	112	77	73	45	53	38	37	81	106	107	74	76
La	INAA	109		75.4			44.4	34.4		87.6				
Ce	XRF	223	230	165	166	118	102	82	82	173	211	222	162	158
Ce	INAA	214		153			91.7	77.5		166				
Nd	XRF	97	96	77	76	57	52	45	46	70	87	94	64	70
Nd	INAA	92.1		72.4			50.8	44.2		68.3				
Sm	INAA	16		13.3			9.71	9.13		12.3				
Eu	INAA	4.87		4.13			3.1	2.95		3.7				
Tb	INAA	1.92		1.47			1.23	1.15		1.34				
Yb	INAA	3.13		2.33			1.92	2		2.31				
Lu	INAA	0.5					0.3	0.29		0.34				
Y	XRF	41	42	35	36	28	27	28	27	34	37	37	32	32
$^{87}Sr/^{86}Sr$		0.70301					0.70301			0.70293	0.70299			
$^{143}Nd/^{144}Nd$		0.51290					0.51292	0.51292		0.51302				

Table A.3 Whole rock analyses for older basanitic samples.

		LP34A CV2	LP34B CV2	LP34C CV2	PH64A CV3	PH64D CV3	LP74A CV4	LP74C CV4	LP71C CV5	LP71E CV5	LP72A CV6	LP72E CV6	LP95cn 1712 JE
SiO_2	XRF	50.89	51.47	53.33	54.93	54.88	56.7	56.55	52.52	52.27	49.38	49.67	55.18
Al_2O_3	XRF	18.31	18.52	19.25	20.39	20.35	20.45	20.34	19.53	19.71	17.97	17.94	20.37
Fe_2O_3T	XRF	7.04	7.07	5.77	4.31	4.32	3.77	3.88	6.24	6.17	8.35	8.36	4.63
MgO	XRF	2.55	2.45	1.85	0.92	1.05	0.63	0.77	1.57	1.74	2.91	2.85	0.94
CaO	XRF	4.89	4.86	3.84	2.77	2.79	2.83	2.91	4.78	5.09	6.51	6.47	3.95
Na_2O	XRF	8.07	7.63	8.09	8.92	8.81	8.66	8.65	7.98	7.69	6.64	6.87	8.27
K_2O	XRF	3.78	3.82	4.16	4.57	4.54	4.63	4.59	3.59	3.47	3.26	3.26	4.06
TiO_2	XRF	1.63	1.64	1.3	0.9	0.91	0.74	0.75	1.75	1.74	2.48	2.44	1.05
MnO	XRF	0.21	0.2	0.18	0.15	0.15	0.17	0.17	0.19	0.18	0.19	0.19	0.17
P_2O_5	XRF	0.58	0.57	0.42	0.21	0.21	0.21	0.2	0.47	0.46	0.78	0.77	0.24
TOTAL		97.92	98.22	98.18	98.08	98.02	98.79	98.8	98.62	98.52	98.47	98.81	98.5
Ce	INAA			11.5		6.2		4.5					6.1
Ni	XRF	18	16	13	8	9	4	5	8	8	13	13	7
Cr	XRF	15	12	11	7	9	1	*	1	3	4	11	1
V	XRF	96	93	75	58	57	42	45	97	100	147	146	67
Sc	XRF	3	1	2	1	1	*	*	1	2	3	3	2
Cu	XRF	23	22	17	7	9	2	4	8	6	29	29	10
Zn	XRF	117	115	111	116	115	105	106	107	105	95	94	100
Sr	XRF	1920	1949	1634	1978	1980	1013	1037	1468	1640	1548	1530	1633
Rb	XRF	141	144	162	165	166	147	146	109	103	101	99	125
Ba	XRF	1445	1467	1353	1733	1743	1457	1484	1184	1160	1152	1183	1277
Cs	INAA			1.85		2.1		1.81					1.85
Nb	XRF	248	251	246	218	219	117	117	184	175	173	172	120
Zr	XRF	906	919	972	1098	1099	801	806	660	643	675	676	741
Hf	INAA			16		16.2		12.6					11.4
Ta	INAA			11.4		9.09		4.07					5.04
Th	INAA			49.8		48.2		24.1					22.5
U	INAA			17.3		21.5		8.5					7.1
La	XRF	217	217	202	153	151	123	120	138	135	130	131	110
La	INAA			212		170		129					131
Ce	XRF	346	336	295	234	230	179	170	240	241	247	243	181
Ce	INAA			276		218		181					183
Nd	XRF	96	94	84	62	58	44	43	80	77	84	84	51
Nd	INAA			75.5		60		44.8					54.2
Sm	INAA			12.5		10.2		5.67					8.24
Eu	INAA			3.04		2.24		1.69					2.25
Tb	INAA			1.34		1.1		0.68					0.89
Yb	INAA			2.84		2.49		2.43					2.32
Lu	INAA			0.48		0.42		0.36					0.4
Y	XRF	38	38	35	29	28	24	23	38	37	39	38	26
$^{87}Sr/^{86}Sr$						0.70312	0.70306					0.70303	
$^{143}Nd/^{144}Nd$				0.51291		0.51300	0.51291					0.51292	

Table A.4 Whole rock analyses for more evoled samples.

		LP42E 1971/N5	LP42H 1971/N5	LP66A 1677	LP78 N1	LP84F N2	LP60A B	LP60C B	LP60D B
SiO_2	XRF	42.02	39.09	37.3	41.83	35.4	44.23	44.96	44.82
Al_2O_3	XRF	18.26	7.5	8.78	6.45	10.66	12.75	10.72	8.46
Fe_2O_3T	XRF	12.13	16.95	18.1	13.36	16.67	10.26	10.72	10.69
MgO	XRF	2.84	13.82	13.62	16.01	10.4	11.69	12.39	13.91
CaO	XRF	14.38	15.75	13.77	16.46	15.4	15.26	15.69	16.71
Na_2O	XRF	3.18	1.11	1.33	1.15	1.82	1.4	1.3	0.85
K_2O	XRF	0.25	0.34	0.58	0.29	0.88	0.29	0.37	0.31
TiO_2	XRF	4.21	4.33	4.42	2.99	5.13	1.94	2.17	2.12
MnO	XRF	0.19	0.19	0.19	0.16	0.19	0.14	0.15	0.16
P_2O_5	XRF	0.93	0.2	0.52	0.2	1.98	0.06	0.1	0.08
TOTAL		98.4	99.29	98.61	98.9	98.53	98.02	98.57	98.11
Co	INAA	17.7			62.2	59.4	55.3		
Ni	XRF	8	129	213	403	74	220	232	277
Cr	XRF	*	736	379	5295	215	547	645	774
V	XRF	170	472	423	351	468	274	282	308
Sc	XRF	0	44	38	60	37	41	46	57
Cu	XRF	37	66	63	66	55	102	72	36
Zn	XRF	65	92	98	80	98	47	55	53
Sr	XRF	3855	350	612	401	1010	577	464	290
Rb	XRF	*	6	5	2	5	4	7	6
Ba	XRF	546	137	276	169	511	117	114	68
Cs	INAA								
Nb	XRF	202	18	30	17	37	7	11	9
Zr	XRF	604	186	165	142	221	112	130	116
Hf	INAA	9.83			4.07	4.96	2.54		
Ta	INAA	25.2			1.25	2.6	0.49		
Th	INAA	8.31			0.6	2.27	0.5		
U	INAA	2.16				1.4			
La	XRF	117	15	22	21	57	5	8	8
La	INAA	153			25.5	54	8.3		
Ce	XRF	279	43	64	46	127	28	29	21
Ce	INAA	349			55.4	123	21.8		
Nd	XRF	135	40	45	49	74	18	24	23
Nd	INAA	175			32.3	66.5	13.7		
Sm	INAA	31.8			7.28	13.4	3.48		
Eu	INAA	9.9			2.41	4.25	1.31		
Tb	INAA	3.42			0.94	1.52	0.62		
Yb	INAA	4.52			1.4	1.4	0.99		
Lu	INAA	0.6			0.2	0.27	0.12		
Y	XRF	70	24	26	20	34	13	17	17
$^{87}Sr/^{86}Sr$		0.70311					0.70287		
$^{143}Nd/^{144}Nd$		0.51290	0.51290				0.51297		

Table A.5 Whole rock analyses for nodules found within basanitic flows, and a single basement cumulate.

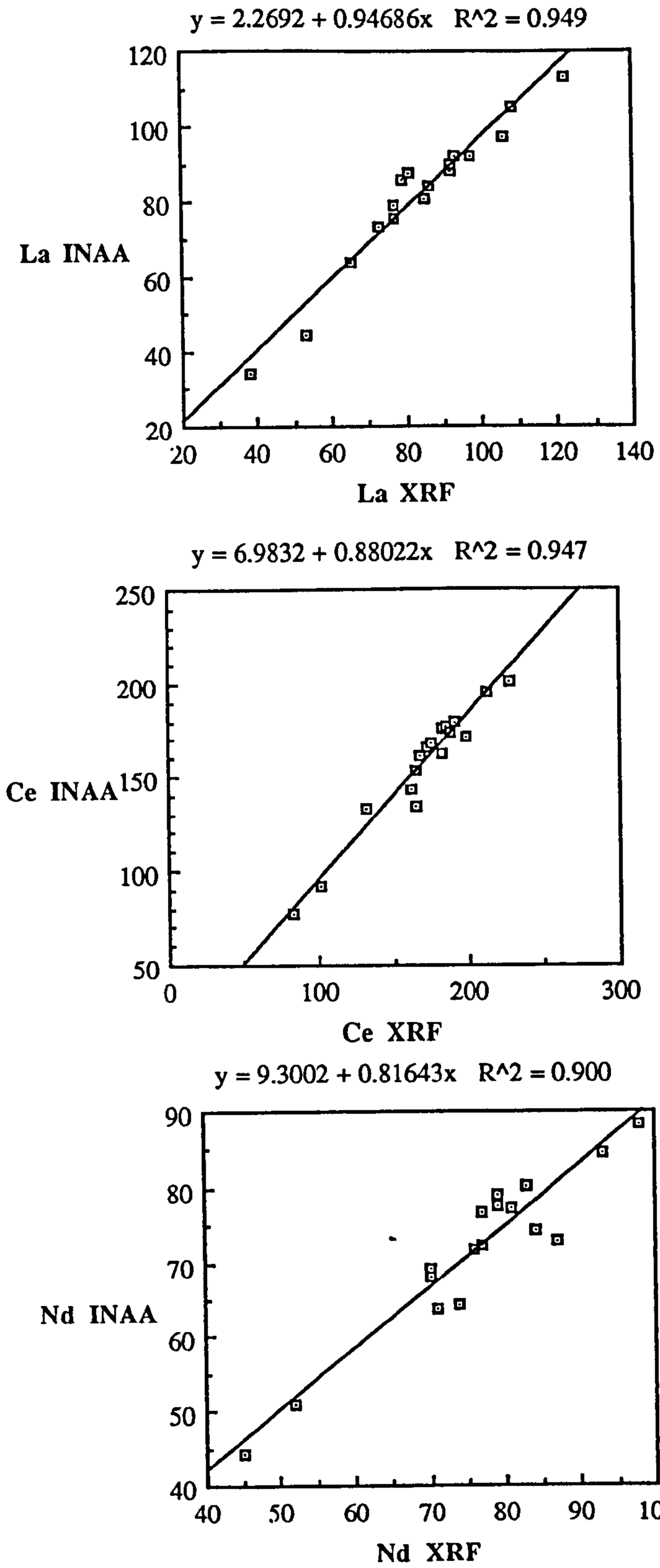

Figure A.1 Correlation of LREE contents of historic basanite samples measured by INAA and XRF techniques.

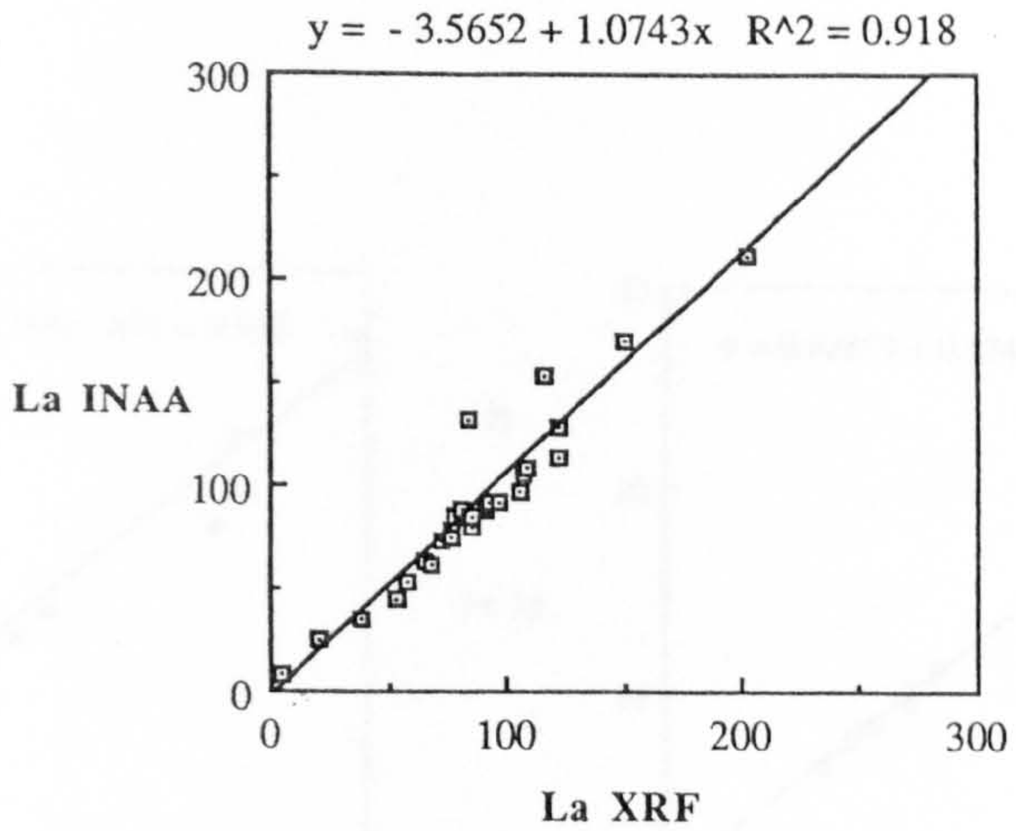

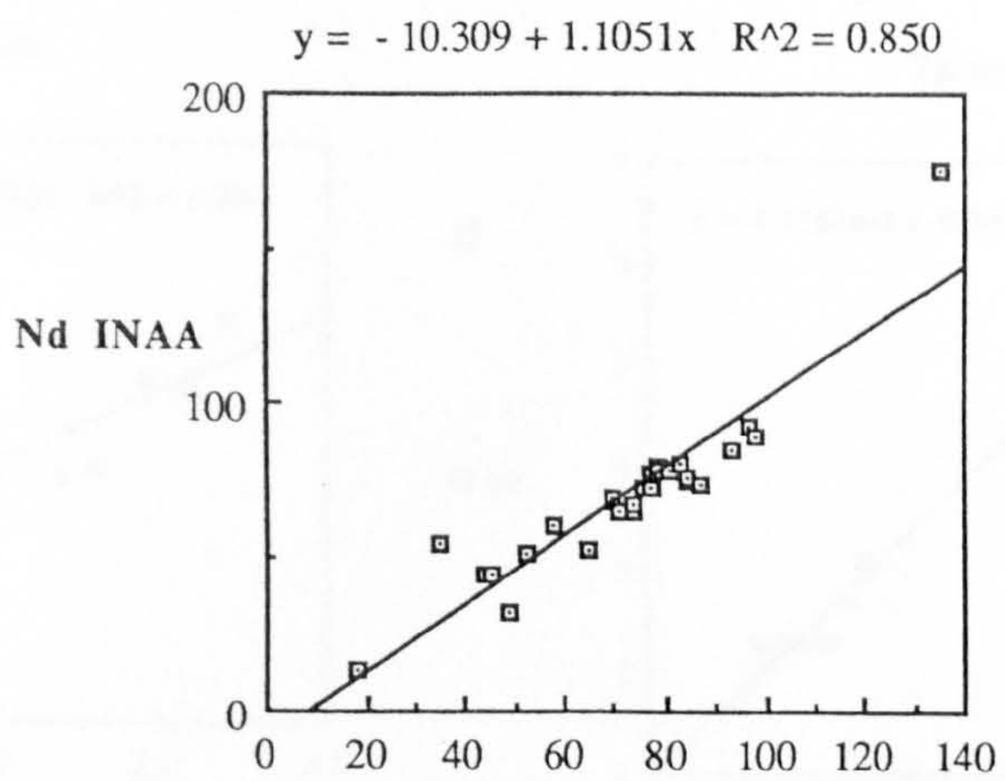

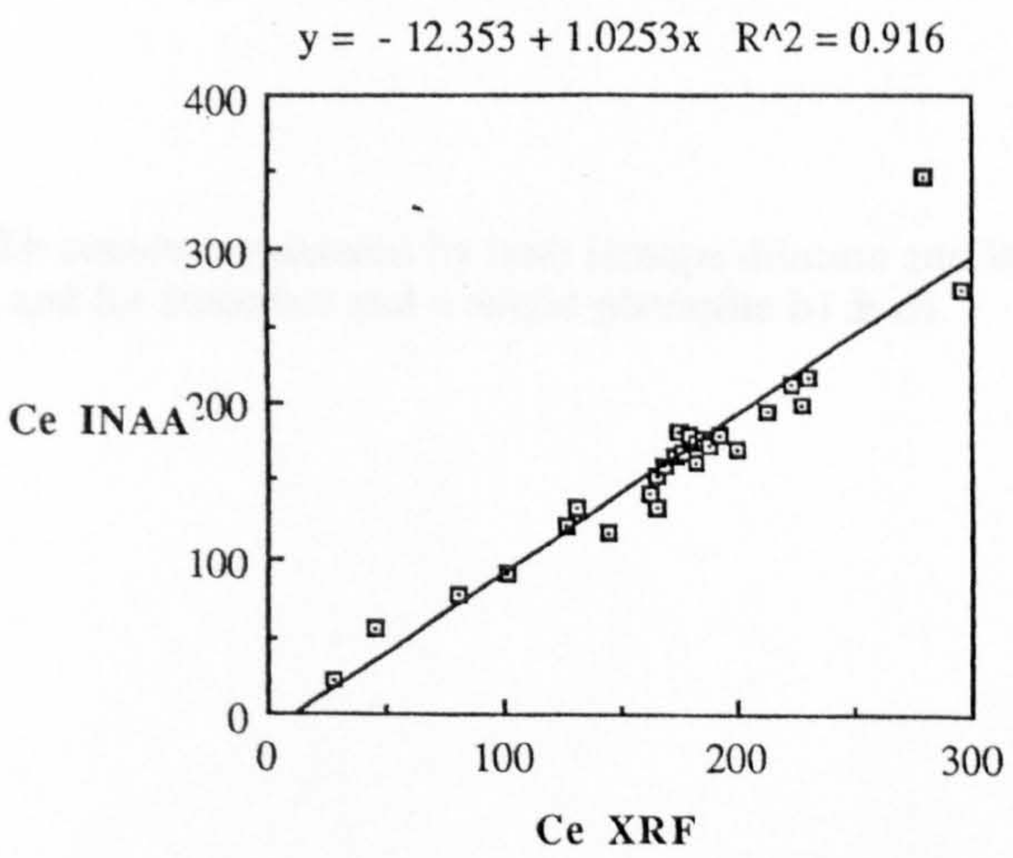

Figure A.2 Correlation of LREE contents of basanitic and evolved samples measured by INAA and XRF techniques.

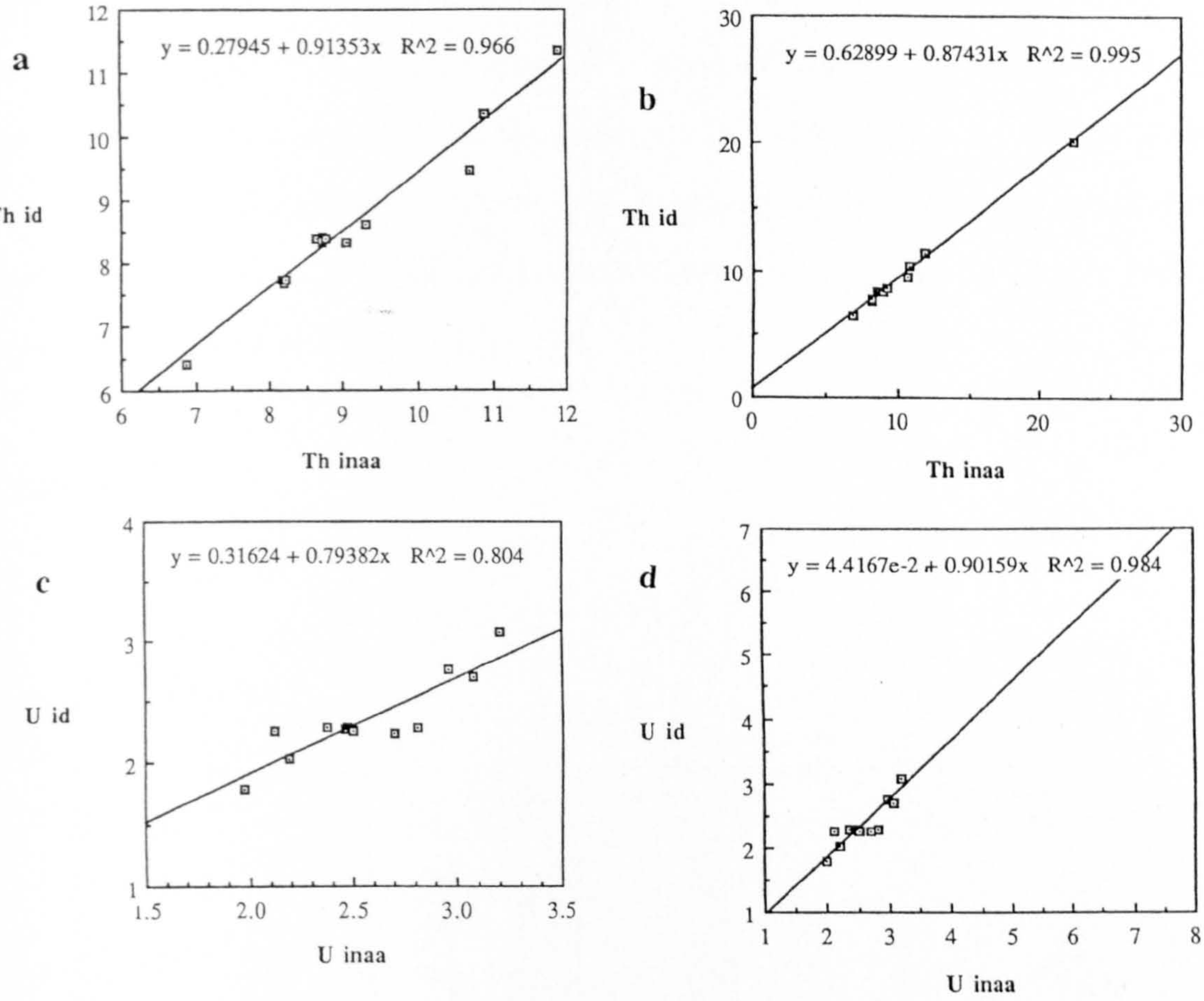

Figure A.3 Correlation of U&Th contents measured by both isotope dilution and INAA techniques for basanite samples only **a**) & **c**), and for basanites and a single phonolite **b**) & **d**).

Appendix B

Mineral Data from La Palma

Table B.1, below, contains all mineral analyses made on La Palma samples. The great majority of analyses are on minerals from rocks that have also been analysed for bulk chemistry, and hence have been documented in Appendix A. A few nodule samples do not have associated whole rock chemical analyses, but are located on Fig. 3.2 and described in Appendix C. All analyses were made on a Cambridge microscan Mk9 using the operating conditions described in section 3.4. The pyroxene analyses indicate where a core and rim from a single phenocryst have been probed.

Table B.1

Fe/Ti Oxides

	Phenocrysts from historic basanites				Phenocrysts from older, more evolved lavas					
Sample	LP70E	LP70E	LP29D	LP29D	LP34	LP34	LP64	LP71	LP71	LP71
Age/Location	1971	1971	1712CV	1712CV	CV2	CV2	CV3	CV5	CV5	CV5
SiO2	0.16	0.19	0.13	0.13	0.13	0.05	0.1	0.03	0.11	0.05
TiO2	15.49	15.58	12.61	15.81	16.41	14.34	10.25	14.11	14.29	14.28
Al2O3	7.02	7.4	3.21	5.94	1.56	2.13	1.43	3.04	2.91	2.86
Cr2O3	0.69	0.55		0.69		0.01	0.01	0.13	0.23	0.08
FeO	65.81	65.15	74.54	66.24	70.6	72.97	77.66	73.53	73.64	73.42
MnO	0.45	0.43	0.75	0.5	1.81	1.56	1.77	1.44	1.41	1.46
MgO	6.35	6.77	4.3	6.4	2.65	3.53	1.28	3.09	2.97	2.9
CaO					0.2	0.02	0.2	0.01	0.02	0.01
Total	95.97	96.07	95.55	95.71	93.36	94.72	92.7	95.38	95.61	95.09

Nodules

	Ultramafic		'Basic' cumulates	'Evolved' cumulates	
Sample	LP66E	LP66E	LP39A	LP76C	LP42E
Age/Location	1677	1677	1971	N3	1971/N5
SiO2	0.08	0.05	0.13	0.11	0.11
TiO2	0.28	0.33	12.54	11.32	11.81
Al2O3	20.5	20.62	4.28	3.35	3.17
Cr2O3	43.05	42.33	3.1		0.01
FeO	20.94	21.05	68.61	76.06	73.79
MnO	0.31	0.26	0.43	1.05	0.8
MgO	13.76	13.86	5.57	2.34	2.9
CaO	0	0	0.09		0.04
Total	99.06	98.63	94.75	94.24	92.63

Pyroxenes

Phenocrysts from historic basanites

Sample	LP 65D	LP 65D	LP 65D	LP 65D	LP 65D	LP 65D	LP 65D	LP 65D	LP 65D	LP 65D	LP 65D	LP 65D
Age/Location	1677	1677	1677	1677	1677	1677	1677	1677	1677	1677	1677	1677
Comments	Core1	Rim 1	Core2	Rim2		Core3	Rim3			Core4	Rim 4	
SiO2	46.11	47.57	46.93	43.92	46.22	44.91	46.04	48.55	49.74	46.87	44.07	45.45
TiO2	1.78	2.74	2.37	3.37	2.18	3.3	3.15	2.2	1.29	1.5	4.06	3.48
Al2O3	6.3	6.27	6.75	8.58	7.34	8.11	7.22	5.86	5.67	5.46	8.5	7.89
Cr2O3	0	0	0	0	0	0	0	0	0	0	0	0
FeOT	11.9	7.48	9.76	10.16	11.51	9.51	8.52	5.96	9.42	12.07	8.5	8.03
MgO	9.08	13.1	10.38	9.55	9.22	10.13	11.31	13.55	9.95	9.05	10.9	11.63
MnO	0.51	0.14	0.33	0.27	0.37	0.25	0.2	0.09	0.34	0.37	0.14	0.19
CaO	21.46	22.7	22.64	22.58	22.65	23	23.44	23.2	22.09	21.64	22.84	22.58
Na2O	1.45	0.53	0.98	0.92	1.3	0.95	0.73	0.47	1.8	1.73	0.7	0.71
Total	98.59	100.53	100.14	99.36	100.79	100.16	100.61	99.88	100.30	98.69	99.71	99.96

Sample	LP 65D	LP 65D	LP 65D	LP 65D	LP45E	LP45E	LP45E	LP45E	LP45E	LP45E	LP70E	LP70E
Age/Location	1677	1677	1677	1677	1585	1585	1585	1585	1585	1585	1971	1971
Comments									Core5	Rim5	Core6	Rim6
SiO2	45.86	48.25	49.95	52.93	48.54	46.51	49.58	46.41	45.64	47.13	47.11	48.92
TiO2	3.12	2.48	2.03	0.49	1.7	2.22	1.94	2.22	3.15	2.91	1.96	1.97
Al2O3	7.48	5.75	4.47	2.32	6.24	7.55	5.65	6.64	7.9	5.96	6.14	4.36
Cr2O3	0	0	0	0	0	0	0.05	0	0	0.09		
FeOT	8.29	7.12	6.43	6.69	9.79	11.06	6.6	10.73	8.17	7.2	10.47	7.08
MgO	11.23	12.83	14.4	14.29	10.62	9.45	13.75	9.74	11.44	13.02	10.32	14.09
MnO	0.2	0.17	0.13	0.27	0.41	0.42	0.11	0.36	0.14	0.13	0.39	0.17
CaO	22.33	22.86	22.67	22.7	22.29	22.32	22.62	23.03	23.13	22.94	22.39	22.66
Na2O	0.87	0.67	0.47	0.97	1.24	1.18	0.62	1.21	0.75	0.46	1.14	0.43
Total	99.38	100.13	100.55	100.66	100.83	100.71	100.92	100.34	100.32	99.84	99.92	99.68

Sample	LP70E	LP70E	LP70E	LP70E	LP29D	LP29D	LP29D	LP29D	LP29D	LP29D	LP29D
Age/Location	1971	1971	1971	1971	1712CV	1712CV	1712CV	1712CV	1712CV	1712CV	1712CV
Comments		Core7	Rim7				Core8	Rim8	Core9	Rim9	
SiO2	48.8	45.51	48.85	50.35	47.58	46.61	49.34	48.98	46.69	49.28	45.69
TiO2	1.86	2.86	1.97	1.17	2.54	2.82	1.96	2.15	2.68	2.09	3.09
Al2O3	5.2	7.32	4.76	4.32	6.19	6.87	4.31	4.54	6.96	4.69	7.27
Cr2O3				0.59			0.16	0.02		0.02	
FeOT	6.99	8.72	7.11	6.04	7.54	7.2	6.51	6.61	8.9	6.42	8.16
MgO	14.05	11.03	13.54	14.97	12.7	12.5	14.27	14.23	11.3	13.99	12.06
MnO	0.14	0.22	0.17	0.16	0.17	0.16	0.11	0.14	0.22	0.14	0.2
CaO	22.17	23.12	22.86	22.03	23.39	23.35	23.25	23.25	23.54	23.86	23
Na2O	0.57	0.82	0.51	0.5	0.71	0.62	0.39	0.46	0.75	0.49	0.66
Total	99.81	99.60	99.78	100.14	100.82	100.13	100.30	100.38	101.04	100.98	100.13

Sample	LP29D	LP29D	LP29D	LP29D
Age/Location	1712CV	1712CV	1712CV	1712CV
Comments	Core10	Rim10	Core11	Rim11
SiO2	47.64	48.97	45.91	49.12
TiO2	1.21	2.16	3.21	2.07
Al2O3	5.3	4.34	7.3	4.6
Cr2O3	0.02			
FeOT	12.9	6.92	7.65	6.49
MgO	8.84	14.05	12.02	14.11
MnO	0.72	0.19	0.17	0.17
CaO	22.39	23.44	23.56	23.64
Na2O	1.52	0.46	0.68	0.49
Total	100.54	100.53	100.50	100.69

Phenocrysts from older, evolved lavas

Sample	LP72	LP71	LP71	LP71	LP71	LP71	LP34	LP34	LP34	LP34	LP64	LP64
Age/Location	CV6	CV5	CV5	CV5	CV5	CV5	CV2	CV2	CV2	CV2	CV3	CV3
Comments					Core12	Rim12						
SiO2	48.09	47.19	46.65	46.75	47.28	48.58	50.23	50.01	50.2	50.97	49.04	48.87
TiO2	2.48	2.97	3.1	3.3	3.28	2.64	1.89	2.07	1.52	1.11	1.22	1.21
Al2O3	5.59	6.78	7.46	7.66	8.4	6.4	4.69	5.54	3.9	3.16	4.26	4.39
Cr2O3	0.02	0	0.02	0	0	0	0.02	0.02				
FeOT	6.54	9.12	9.2	8.07	7.41	8.77	9.9	7.98	8.55	8.61	13.78	12.67
MgO	13.31	11.18	10.89	12.2	12.83	12.11	11.33	13.06	11.98	12.05	8.19	8.86
MnO	0.14	0.34	0.3	0.23	0.14	0.36	0.34	0.27	0.38	0.42	0.75	0.61
CaO	23.19	22.51	22.69	22.87	22.85	22.9	21.98	23.13	22.12	22.15	20.42	20.92
Na2O	0	1.15	0.94	0.91	0.73	1.18	1.74	1.11	1.08	1.06	2.14	1.68
Total	99.36	101.24	101.25	101.99	102.92	102.94	102.12	103.19	99.73	99.53	99.80	99.21

Pyroxenes

	Nodules Ultramafic						'Evolved' cumulates		
Sample	LP66E	LP66E	LP66E	LP42C	LP42C	LP42C	LP42E	LP42E	LP76C
Age/Location	1677	1677	1677	1971/N5	1971/N5	1971/N5	1971/N5	1971/N5	N3
Comments		opx	opx	opx	opx	opx			
SiO2	54.52	57.45	56.48	56.36	56.11	56.47	45.53	43.57	44.86
TiO2	0.13	0.07	0.07	0.02	0.02	0.02	2.04	2.72	2.6
Al2O3	0.7	0.34	1.89	2.06	2.04	2.11	6.98	8.8	8.65
Cr2O3	1.21	0.27	0.55	0.7	0.7	0.7	0	0	
FeOT	2.73	6.03	6.28	5.48	5.64	5.62	11.02	10.44	10.98
MgO	17.26	33.7	32.43	32.37	31.79	32.43	9.37	8.91	9.12
MnO	0.09	0.16	0.14	0.14	0.17	0.14	0.33	0.34	0.37
CaO	21.06	0.8	1.13	1.62	2.31	1.76	20.96	21.53	21.78
Na2O	0.76	0.06	0.1	0.07	0.12	0.12	1.3	1.09	1.11
Total	98.46	98.88	99.07	98.82	98.90	99.37	97.53	97.40	99.47

	'Basic' cumulates										
Sample	LP42F	LP42F	LP42F	LP66C	LP66C	LP66C	LP66C	LP66C	LP66C	LP39A	LP39A
Age/Location	1971/N5	1971/N5	1971/N5	1677	1677	1677	1677	1677	1677	1971	1971
Comments									Exsolving opx		
SiO2	47.85	50.75	47.85	53.12	53.19	53.05	52.38	52.91	54.32	53.45	50.02
TiO2	2.16	0.81	2.16	0.28	0.32	0.23	0.21	0.15	0.13	0.38	1.68
Al2O3	5.3	3.28	5.3	1.63	0.81	2.51	1.58	1.13	0.9	2.41	4.81
Cr2O3	0.16	0.07	0.16		0.05					1.03	0.17
FeOT	6.33	6.75	6.33	7.4	8.25	7.03	6.77	6.69	16.02	3.32	6.14
MgO	13.27	13.67	13.27	14.95	15.32	13.8	14.11	14.68	26.59	15.83	13.67
MnO	0.11	0.22	0.11	0.24	0.34	0.27	0.25	0.25	0.43	0.08	0.16
CaO	21.8	21.51	21.8	21.27	19.63	20.82	22.92	22.22	1.1	22.22	22.47
Na2O	0.47	0.81	0.47	0.57	1.05	1.13	0.81	0.75	0.05	0.83	0.73
Total	97.45	97.87	97.45	99.48	98.96	98.86	99.03	98.78	99.54	99.55	99.85

Olivines

	Phenocrysts from historic basanites											
Sample	LP65D	LP65D	LP65D	LP65D	LP65D	LP65D	LP65D	LP45e	LP45e	LP29D	LP29D	LP29D
Age/Location	1677	1677	1677	1677	1677	1677	1677	1585	1585	1712CV	1712CV	1712CV
SiO2	38.87	39.64	39.36	39.19	39.85	40.12	39.77	39.66	39.97	39.63	39.76	39.28
TiO2	0.04	0.05	0.04	0.04	0.04	0.04	0.05	0.04	0.05	0.04	0.04	0.04
FeO	18.05	16.89	18.65	18.39	18.08	16.99	19.39	21.14	18.65	17.62	17.06	20.52
MnO	0.28	0.25	0.28	0.26	0.28	0.28	0.37	1.09	0.32	0.25	0.28	0.66
NiO	0.12	0.13	0.09	0.13	0.16	0.16	0.06	0.1	0.09	0.16	0.16	0.12
MgO	42.42	43.49	42.2	42.61	42.57	43.6	41.9	40.2	42.49	43.3	43.45	40.9
CaO	0.3	0.31	0.31	0.26	0.28	0.28	0.33	0.16	0.3	0.28	0.3	0.18
Total	100.08	100.78	100.93	100.88	101.28	101.47	101.87	102.39	101.87	101.3	101.07	101.7

	Nodules Ultramafic						
Sample	LP66E	LP66E	LP66E	LP66E	LP42C	LP42C	LP42C
Age/Location	1677	1677	1677	1677	1971/N5	1971/N5	1971/N5
SiO2	40.93	40.67	41.06	41	40.87	40.9	41.25
TiO2	0.02	0.02	0.02	0.02	0.02	0.02	0.02
FeO	9.19	9.35	9.34	9352	8.62	8.67	8.67
MnO	0.16	0.14	0.16	0.12	0.12	0.12	0.17
NiO	0.26	0.32	0.33	0.29	0.41	0.39	0.38
MgO	48.96	48.93	48.98	49.07	49.63	49.65	49.59
CaO	0.07	0.06	0.06	0.09	0.03	0.03	0.04
Total	99.59	99.49	99.95	100.11	99.7	99.8	100.14

	'Basic' cumulates					
Sample	LP42F	LP42F	LP42F	LP66C	LP39A	LP39A
Age/Location	1971/N5	1971/N5	1971/N5	1677	1971	1971
SiO2	38.97	38.93	39.41	38.45	39.73	39.99
TiO2	0.02	0.04	0.02	0.02		
FeO	20.8	20.97	17.21	25.91	19.29	19.84
MnO	0.51	0.46	0.34	0.87	0.37	0.39
NiO	0.06	0.07	0.06	0.06	0.13	0.13
MgO	40.09	40.05	42.42	35.82	41.9	41.56
CaO	0.11	0.13	0.23	0.13	0.14	0.16
Total	100.56	100.65	99.69	101.28	101.56	102.07

Amphiboles

Xenocrysts from historic basanites

Sample	LP45E	LP45E	LP45E	LP45E	LP45E	LP45E	LP45E	LP45E	LP45E	LP29D
Age/Location	1585	1585	1585	1585	1585	1585	1585	1585	1585	1712CV
SiO2	39.41	39.83	38.89	39.18	39.36	39.56	38.87	39.55	47.87	39.53
TiO2	5.88	6.12	6.14	6.38	5.92	5.74	6.02	6.03	2.26	5.9
Al2O3	13.07	12.81	13.54	13.6	12.95	13.5	14.23	13.71	6.27	13.02
Cr2O3	0.02	0	0.02	0	0	0	0	0.03	0.1	
FeO	11.34	10.05	9.9	9.77	10.13	9.68	11.89	10.18	9.28	10.49
MnO	0.19	0.12	0.12	0.11	0.14	0.12	0.16	0.14	0.28	0.14
MgO	11.83	13.27	12.74	13	13.22	13.3	11.51	12.8	10.91	12.87
CaO	12.19	12.35	12.35	12.24	12.1	12.1	12.11	12.06	22.23	12.53
Na2O	2.8	2.63	2.73	2.74	2.68	2.6	2.74	2.79	1.24	2.54
K2O	1.17	1.14	1.17	1.17	1.18	1.31	1.24	1.24	0	1.11
Total	97.90	98.32	97.60	98.19	97.68	97.91	98.80	98.58	100.47	98.14

Phenocrysts from older, more evolved lavas

Sample	LP64	LP64	LP64	LP64	LP34	LP34	LP34	LP71	LP71	LP71
Age/Location	CV3	CV3	CV3	CV3	CV2	CV2	CV2	CV5	CV5	CV5
SiO2	40.67	39.86	40.29	40.29	43.28	42.68	40.98	40.72	41.52	40.52
TiO2	5.03	3.73	4.89	4.89	4.81	4.95	4.41	5.84	5.71	6.1
Al2O3	13.01	12.38	12.43	12.43	12.12	13.93	11.85	12.95	13.69	13.8
Cr2O3	0	0			0	0.03		0	0	0
FeO	9.98	17.32	13.83	13.83	10	10.28	12.32	13.42	9.72	12.96
MnO	0.17	0.63	0.25	0.25	0.19	0.17	0.31	0.4	0.14	0.34
MgO	13.9	9.96	10.79	10.79	14.78	14.47	12.01	11.58	14.43	11.92
CaO	12.59	11.76	11.39	11.39	11.67	11.55	11.32	11.82	12.36	12.12
Na2O	3.04	3.48	3.32	3.32	4.1	3.5	2.92	3.32	3.33	3.48
K2O	1.37	1.38	0.99	0.99	1.13	1.29	1.17	1.08	1.05	1.02
Total	99.76	100.50	98.18	98.18	102.08	102.85	97.29	101.13	101.95	102.26

Nodules

	'Basic' cumulates			'Evolved' cumulates		
Sample	LP42F	LP66C	LP39A	LP83L	LP76C	LP76C
Age/Location	1971/N5	1677	1971	N4	N3	N3
SiO2	39.64	43.96	41.04	39.8	39.28	39.31
TiO2	5.25	1.84	4.67	5.37	4.86	4.58
Al2O3	12.82	10.29	12.12	12.97	13.5	12.91
Cr2O3	0.05					
FeO	9.25	11.08	9.66	10.06	14.92	15.14
MnO	0.11	0.23	0.11	0.14	0.37	0.39
MgO	13.33	14.7	13.93	12.59	9.96	10.06
CaO	11.72	11.25	11.48	11.9	11.64	11.42
Na2O	2.54	3.09	2.88	2.84	2.84	2.75
K2O	1.13	1.05	1.04	1.04	1.08	1.21
Total	95.85	97.49	96.93	96.71	98.45	97.77

Feldspars

Phenocrysts from older, more evolved lavas

Sample	LP64	LP64	LP64	LP71	LP71	LP71	LP71	LP71	LP71
Age/Location	CV3	CV3	CV3	CV5	CV5	CV5	CV5	CV5	CV5
SiO2	61.57	63.88	63.06	56.3	57.79	57.55	57.27	58.12	57.74
TiO2	0.17	0.15	0.13	0.11	0.09	0.11	0.11	0.09	0.11
Al2O3	23.14	21.59	23.34	26.89	26.31	26.32	26.98	26.67	28.02
FeO	0.38	0.31	0.34	0.48	0.39	0.38	0.42	0.41	0.46
CaO	2.8	1.39	2.95	9.39	8.4	8.6	9.02	8.55	9.64
Na2O	8.13	7.7	7.97	5.85	6.8	6.68	6.43	6.48	6.15
K2O	2.22	3.77	2.07	0.41	0.5	0.47	0.45	0.51	0.38
Total	98.41	98.79	99.86	99.43	100.28	100.11	100.68	100.83	102.50

Nodules

'Evolved' cumulates

Sample	LP42E	LP42E	LP42E	LP42E	LP42E	LP42E	LP42E
Age/Location	1971/N5	1971/N5	1971/N5	1971/N5	1971/N5	1971/N5	1971/N5
SiO2	53.06	56.63	54.18	53.23	52.56	54.31	55.14
TiO2	0	0	0	0	0	0	0
Al2O3	28.79	26.4	28	28.57	29.11	27.86	27.3
FeO	0.34	0.35	0.38	0.34	0.34	0.32	0.34
CaO	11.09	8.24	10.08	10.58	11.25	10.02	9.41
Na2O	4.56	6.09	5.27	4.9	4.58	5.24	5.65
K2O	0.22	0.48	0.28	0.23	0.23	0.32	0.42
Total	98.06	98.19	98.19	97.85	98.07	98.07	98.26

Appendix C

Petrography of the La Palma Samples

Table C.1 below summarises rock types and estimates of the proportions of minerals present (phenocrysts only for the volcanic samples) in all samples for which data is presented in Chapter 3 and Appendices A & B. The samples are located on Fig. 3.2 using the codes in the second column.

Table C.1

Sample	Age/Location	Rock-type	Mineralogy
LP45D	1585	Basanite	Cpx (2%), Ol (2%), Op (0.5%)
LP43E	1646	Basanite	Cpx (6%), Ol (6%), Op (2%)
LP63C	1646 S	Basanite	
LP65C	1677	Basanite	
LP95D	1712 J	Basanite	
LP4	1712 SC	Basanite	Cpx (12%) Ol (2%) Op (2%) + Kae
LP29D	1712 CV	Basanite	Cpx (15%), Ol (3%), Op (2%) +Kae
LP30A	1712 DM	Basanite	Cpx (7%), Ol (7%), Op (2%)
LP32B	1712 DM	Basanite	
LP51C	1712 G	Basanite	
LP48B	1712 PN	Basanite	Cpx (8%), Ol (5%0, Op (1%)
LP69A	1949 E	Basanite	Cpx (3%), Ol (3%), Op (0.5%)
LP40E	1971	Basanite	Cpx (10%), Op (2%) + Kae
LP41C	1971 S	Basanite	
LP95en	1712 en	Phonolite	Plag (10%), Cpx (3%), Kae (2%) +Hy, Sp
LP9	T1	Basanite	Aphyric
LP12	T2	Basanite	Ol (5%)
LP16	T3	Basanite	Cpx (35%), Ol(5%), Op (2%)
LP19	T4	Basanite	Cpx (3%), Ol (2%), Op (1%)
LP61D	CD	Basanite	Aphyric
LP73A	CV1	Basanite	Cpx (15%), Plag (8%), Op (2%)
LP34C	CV2	Phonolite	Cpx (2%), Kae (2%), Hy (2%)
LP64D	CV3	Phonolite	Cpx (3%), An (3%) +Kae, Hy, Op
LP74A	CV4	Phonolite	An (3%), Cpx (2%) +Kae, Hy, Op
LP71C	CV5	Phonolitic tephrite	Plag (7%), Kae (3%), Cpx (3%) +Hy, Sp, Op
LP72E	CV6	Phonolitic tephrite	Kae (4%), Plag (3%), Cpx (2%)+Hy, Op, Sp
LP39A	1971	Gabbro	Cpx (60%), Ol (30%), Plag (10%)
LP42C	1971/N5	Harzburgite	Ol(80%), Opx (20%)
LP42F	1971/N5	Pyroxenite	Cpx reacting to Kae
LP66C	1677	Gabbro	Cpx (50%), Plag (50%)
LP66E	1677	Harzburgite	Ol(80%), Opx (20%)
LP42E	1971/N5	Gabbro	Plag (60%), Cpx (25%), Sp (10%) +Op,Hy
LP42H	1971/N5	Pyroxenite	Cpx reacting to Kae
LP76C	N3	Gabbro	Plag (70%), Cpx (20%), Sp (10%) +Op,Hy
LP78	N1	Pyroxenite	Cpx reacting to Kae
LP83L	N4	Pyroxenite	Cpx reacting to Kae
LP84F	N2	Pyroxenite	Cpx reacting to Kae
LP66A	1677	Pyroxenite	Cpx reacting to Kae
LP60A	B	Gabbro	Cpx (75%), Ol (15%), Plag (10%)

Abbreviations

Cpx-clinopyroxene
Opx-orthopyroxene
Ol-olivine
Plag-plagioclase
Kae-kaersutite
Hy-Hauyne
Op-opaques
Sp-sphene
An-anorthoclase

Appendix D

Whole Rock Data of Icelandic High MgO Lavas

Table D.1, below, contains the complete data set for the high MgO lavas discussed in Chapters 4 and 5. The analytical techniques and sample localities are described in Chapter 4, and not reported here.

Table D.1

		D2/11	D6	D6I	D7	D8A	D8B	D18
Latitude		63°48'N	63°51'N	63°51'N	63°53'N	63°52'N	63°53'N	63°52'N
Longitude		22°39'W	22°34'W	22°34'W	22°32'W	22°23'W	22°23'W	22°42'W
SiO2	XRF	46.96	48.42	48.38	48.57	48.7	47.31	47.79
Al2O3	XRF	12.22	15.83	15.72	14.11	14.98	14.43	14.16
Fe2O3	Calc	0.921	1.139	1.109	0.912	1.19	0.95	1.125
FeO	Calc	7.46	9.22	8.98	7.39	9.64	7.69	9.11
Fe2O3T	XRF	9.21	11.39	11.09	9.12	11.9	9.5	11.25
MgO	XRF	19.64	10.65	10.3	12.88	9.3	14.62	11.73
CaO	XRF	10.58	12.36	12.36	13.48	13.33	12.01	12.24
Na2O	XRF	0.93	1.72	1.71	1.24	1.81	1.3	1.64
K2O	XRF	0.006	0.103	0.102	0.009	0.093	0.031	0.04
TiO2	XRF	0.353	1.163	1.145	0.486	1.244	0.543	0.916
MnO	XRF	0.153	0.183	0.177	0.148	0.195	0.157	0.184
P2O5	XRF	0.017	0.059	0.067	0.019	0.074	0.035	0.04
LOI		-0.34	-0.7	-0.46	-0.26	-0.57	-0.42	-0.49
Total		99.24	100.85	100.05	99.24	100.55	99.08	98.98
Co	INAA	73.2	54.2		52.8	52	63.5	60.1
Cr	XRF	2195.5	399.3	412.7	1524	358.4	1261	874.6
Ni	XRF	763	188.1	188.2	339.2	127.5	424.1	290.8
V	XRF	159.3	264.2	270.6	214.8	327.7	203.4	282.3
Sc	XRF	30.1	37.2	37.2	41.1	44.8	38.7	42.5
Cu	XRF	46	69.5	73.2	47	69.9	78.1	109.5
Zn	XRF	55.4	72.7	74.7	53.1	72.8	58.5	73.3
Sr	XRF	45.8	148	146.8	44.3	124.8	74.7	94.5
Y	XRF	8.3	11.4	13.6	10.6	15.7	12.2	14.7
Zr	XRF	14	54.8	55.1	17.6	36.3	22.8	29.4
La	INAA	0.3	2.66		0.4	1.45	0.97	1.18
Ce	INAA		8.5					
Nd	INAA		7.5					
Sm	INAA	0.67	1.75		0.69	1.43	0.97	1.35
Eu	INAA	0.32	0.84		0.4	0.7	0.52	0.68
Tb	INAA	0.24	0.47		0.26	0.45	0.38	0.42
Yb	INAA	0.99	1.55		1.29	1.66	1.4	1.51
Lu	INAA	0.15	0.23		0.23	0.27	0.22	0.26
Pb	I.D.							
Ta	INAA		0.33		0.04	0.16	0.08	0.09
Hf	INAA	0.4	1.49		0.59	1.08	0.68	0.91
87Sr/86Sr						0.70319	0.70326	0.70321
143Nd/144Nd		0.51316				0.51305	0.51310	0.51309
206Pb/206Pb		18.188	18.546			18.515	18.412	18.288
207Pb/204Pb		15.400	15.411			15.452	15.459	15.438
208Pb/204Pb		37.735	37.978			38.029	37.998	37.951

	D26	D27	IT1	IT2	IT3A	IT4	IT5
	63°54'N 22°28'W	63°55'N 22°24'W	65°53'N 17°09'W	65°53'N 17°03'W	65°49'N 16°54'W	65°50'N 16°50'W	65°52'N 17°03'W
SiO2	48.6	47.81	49.14	49.54	49.57	50.25	46.94
Al2O3	14.67	15.12	15.33	15.64	15.39	14.9	13.18
Fe2O3	1.04	0.935	1.107	1.207	1.218	1.265	1.101
FeO	8.42	7.57	8.96	9.77	9.86	10.24	8.92
Fe2O3T	10.4	9.35	11.07	12.07	12.18	12.65	11.01
MgO	11.21	13.08	9.19	8.07	9.07	7.91	15.84
CaO	12.92	12.62	13.43	12.62	11.83	12.06	11.12
Na2O	1.35	1.46	1.77	1.98	1.78	1.85	1.35
K2O	0.033	0.017	0.061	0.113	0.127	0.144	0.035
TiO2	0.62	0.509	0.96	1.107	0.914	1.035	0.721
MnO	0.174	0.161	0.187	0.198	0.202	0.216	0.169
P2O5	0.034	0.025	0.062	0.076	0.074	0.081	0.033
LOI	-0.38	-0.27	-0.59	-0.56	-0.66	-0.63	-0.55
Total	99.07	99.31	100.20	100.33	100.04	99.96	99.41
Co	53.1	55	51	52.1	56.9	52.7	70.8
Cr	853.7	910.4	254.7	98.7	84.7	89.7	1138
Ni	274.8	376.9	114	80.6	99.3	71.6	473.6
V	262	216.6	268.9	301.2	277.1	314.6	215
Sc	45.2	43	44.1	44	42.4	48.5	39.5
Cu	92.4	92.8	115.8	122.7	109	93.5	54.1
Zn	66.4	55.8	65.1	76.2	77.6	84.1	64
Sr	52.1	59.7	114.3	133.1	131.9	134	77
Y	14.6	13.9	17	17.4	16.3	18.5	12.2
Zr	25.1	20.2	47.4	53.1	46.5	54.7	32.4
La	0.95	0.7	1.86	3.04	2.52	3	1.15
Ce				8.5		8.5	
Nd						6.2	
Sm	1.05	1.1	1.67	1.99	1.43	1.88	1.02
Eu	0.52	0.48	0.82	0.89	0.74	0.82	0.59
Tb	0.29	0.37	0.54	0.56	0.43	0.45	0.34
Yb	1.71	1.61	1.84	1.93	1.55	1.85	1.34
Lu	0.27	0.28	0.29	0.33	0.27	0.3	0.22
Pb							
Ta	0.06	0.04	0.16	0.21	0.24	0.27	0.08
Hf	0.7	0.52	1.24	1.41	1.13	1.46	0.89
87Sr/86Sr					0.70324	0.70323	0.70304
143Nd/144Nd				0.51307		0.51300	0.51310
206Pb/206Pb	18.448	18.313	18.049	18.026	18.051	17.989	17.971
207Pb/204Pb	15.491	15.438	15.416	15.373	15.409	15.341	15.351
208Pb/204Pb	38.082	37.856	37.679	37.568	37.698	37.504	37.435

	IT6	IT7	TH8	TH13	TH16	TH29	TH40
	65°52'N 17°03'W	65°48'N 16°58'W	65°57'N 17°05'W	65°54'N 16°52'W	65°49'N 16°54'W	65°55'N 17°04'W	65°48'N 16°58'W
SiO2	48.54	48.76	47.62	48.91	49.4	47.47	46.96
Al2O3	15.66	14.98	14.96	15.11	15.56	13.41	11.34
Fe2O3	1.068	1.025	1.045	1.141	1.203	0.913	1.025
FeO	8.65	8.30	8.46	9.24	9.74	7.39	8.30
Fe2O3T	10.68	10.25	10.45	11.41	12.03	9.13	10.25
MgO	10.6	11.45	12.4	9.78	9.08	15.73	18.67
CaO	13.13	13.22	12.32	13.26	11.84	12.5	10.71
Na2O	1.64	1.42	1.44	1.65	1.81	1.13	1.1
K2O	0.045	0.053	0.033	0.055	0.119	0.011	0.035
TiO2	0.884	0.685	0.753	0.973	0.893	0.502	0.551
MnO	0.182	0.168	0.175	0.194	0.201	0.155	0.166
P2O5	0.043	0.045	0.037	0.05	0.062	0.024	0.039
LOI	-0.5	-0.24	-0.45	-0.51	-0.34	-0.34	-0.44
Total	100.44	100.11	99.25	100.36	99.91	99.24	98.90
Co	51	54.5	59.3	51.6		62.4	73
Cr	476.6	683.9	801.5	362.2	78	1802.6	1579.1
Ni	187.2	224.5	336.5	147.5	97.6	489	673.3
V	256.4	253.7	235.2	284.5	257.3	200.6	204.5
Sc	42.1	44.9	40.4	45.5	40.5	42.4	37.7
Cu	83.2	103.3	89.2	97.4	86.8	58.9	79.5
Zn	65.3	64.5	64.1	72.2	70.7	53.4	59.9
Sr	90.5	90.9	83.7	92.4	135.8	54.7	65.3
Y	20	13.4	14.3	16.3	14.3	11.3	11.6
Zr	54	29.6	33.2	44.5	45.3	20.9	25.2
La	1.2	1.43	1.1	1.42		0.5	1.2
Ce				7			
Nd				5.1			
Sm	1.52	1.18	1.43	1.45		0.86	1.21
Eu	0.68	0.58	0.61	0.72		0.38	0.47
Tb	0.41	0.41	0.4	0.45		0.28	0.32
Yb	1.75	1.5	1.64	1.76		1.22	1.31
Lu	0.29	0.24	0.29	0.3		0.21	0.2
Pb			0.163	0.246		0.092	
Ta	0.13	0.08	0.1	0.14		0.03	0.06
Hf	1.02	0.83	0.95	1.16		0.61	0.65
87Sr/86Sr	0.70307		0.70303	0.70305	0.70315	0.70293	
143Nd/144Nd	0.51309	0.51310	0.51313	0.51311		0.51316	0.51309
206Pb/206Pb	17.974	17.979	17.948	18.055		17.790	18.028
207Pb/204Pb	15.366	15.379	15.362	15.398		15.343	15.382
208Pb/204Pb	37.485	37.512	37.446	37.637		37.257	37.510

Appendix E

Calculation of Dynamic Melt Compositions

This appendix lists the spreadsheet used to calculate the synthetic melt compositions used in Chapter 5 to model the Icelandic high MgO lavas. As described in Chapter 5, instantaneous melts are calculated over small melting increments (0.4%) from the bottom to the top of the melting column accounting for changing source composition with melt extraction. The listing shown includes only the first five instantaneous melt compsitions (from the bottom of the melting column), but the full spreadsheet simply repeats the calculations shown for those melts produced higher up the melting column. The only changes with height in the melting column that are not evident from the segment of the spreadsheet shown here are the spinel-in and garnet-out reactions described later.

Input data are shown in italics. The partition coefficients (K_d phase) and starting mineralogy (F_{phase}) are taken from McKenzie & O'Nions (in press), and the melt norms (P_{phase}) are based on Johnson et al. (1990). The melting column porosity of 0.5% is used in all calculations and is a maximum probable value (McKenzie 1989). The depth of the melting column, and overall degree of melting are assessed in 5.5.1.

Except in Fig. 5.14c, all synthetic melts calculated start melting below the spinel-out reaction. Hence for instantaneous melts produced higher in the column, the garnet-spinel transition must be modelled. Given the melting column depth and overall degree of melting, the depth interval corresponding to production of a single 0.4% melt interval can be calculated (Column X). The number of melt intervals before and within the garnet/spinel transition can hence be calculated easily (using the depths of 80 and 100km for garnet-out and spinel-in reactions respectively from McKenzie & O'Nions, in press). The same melt norms were used within the transition as below the spinel-in reaction. The amount of garnet *melted* within the transition zone and hence any 'excess' garnet that would be present at 80km, if there were no solid state reaction, could be calculated.

Table E.1 Spreadsheet for calculation of synthetic dynamic melts.

	A	B	C	D	E	F	G	H	I	J	K	L	M	N
1	F cpx	F opx	F gnt	F ol	P cpx	P opx	P gnt	P ol	Element	Kd cpx	Kd opx	Kd gnt	Kd ol	D source
2	*0.08*	*0.2*	*0.1*	=1-C2-A2-B2	*0.4*	*0.15*	*0.5*	=1-G2-F2-E2	La	*0.054*	*0.002*	*0.01*	*0.0004*	=A2*J2+B2*K2+C2*L2+D2*M2
3	=(A2-E2*Q2)/(1-Q2)	=(B2-Q2*F2)/(1-Q2)	=(C2-G2*Q2)/(1-Q2)	=1-C3-A3-B3	=E2	=F2	=G2	=1-G3-F3-E3	Ce	*0.098*	*0.003*	*0.021*	*0.0005*	=A3*J2+B3*K3+C3*L2+D3*M2
4	=(A3-E3*Q3)/(1-Q3)	=(B3-Q3*F3)/(1-Q3)	=(C3-G3*Q3)/(1-Q3)	=1-C4-A4-B4	=E3	=F3	=G3	=1-G4-F4-E4	Pr	*0.15*	*0.0048*	*0.054*	*0.0008*	=A4*J2+B4*K2+C4*L2+D4*M2
5	=(A4-E4*Q4)/(1-Q4)	=(B4-Q4*F4)/(1-Q4)	=(C4-G4*Q4)/(1-Q4)	=1-C5-A5-B5	=E4	=F4	=G4	=1-G5-F5-E5	Nd	*0.21*	*0.0068*	*0.087*	*0.001*	=A5*J2+B5*K2+C5*L2+D5*M2
6	=(A5-E5*Q5)/(1-Q5)	=(B5-Q5*F5)/(1-Q5)	=(C5-G5*Q5)/(1-Q5)	=1-C6-A6-B6	=E5	=F5	=G5	=1-G6-F6-E6	Sm	*0.26*	*0.01*	*0.217*	*0.0013*	=A6*J2+B6*K2+C6*L2+D6*M2
7	=(A6-E6*Q6)/(1-Q6)	=(B6-Q6*F6)/(1-Q6)	=(C6-G6*Q6)/(1-Q6)	=1-C7-A7-B7	=E6	=F6	=G6	=1-G7-F7-E7	Yb	*0 28*	*0.04*	*4.03*	*0.0015*	=A7*J3+B7*K3+C7*L3+D7*M3

	O	P	Q	R	S	T	U	V	W	X
1	[La] source	[La] inst. melt	(rel)	Porosity	Ab. Fn. melted	(Ab.)	Top down			Depth
2	*1*		=R2	*0.005*			Ab. Fn.	La Ab.Inst. Fn.	[La]	
3	=N3*P3	=O2/(Q2+N3*(1-Q2))	*0.004*	=R2	=Q2	=S3	=T3+U4	=T3*P3+V4	=V3/U3	*120*
4	=N4*P4	=(O3*(1-R4)+R4*P3)/((Q3+R4)+N4*(1-(Q3+R4)))	=Q3	=R3	=S3+(1-S3)*Q3	=(S4-S3)	=T4+U5	=T4*P4+V5	=V4/U4	=X3-(0.004/0.4)*120
5	=N5*P5	=(O4*(1-R5)+R5*P4)/((Q4+R5)+N5*(1-(Q4+R5)))	=Q4	=R4	=S4+(1-S4)*Q4	=(S5-S4)	=T5+U6	=T5*P5+V6	=V5/U5	=X4-(0.004/0.4)*120
6	=N6*P6	=(O5*(1-R6)+R6*P5)/((Q5+R6)+N6*(1-(Q5+R6)))	=Q5	=R5	=S5+(1-S5)*Q5	=(S6-S5)	=T6+U7	=T6*P6+V7	=V6/U6	=X5-(0.004/0.4)*120
7	=N7*P7	=(O6*(1-R7)+R7*P6)/((Q6+R7)+N7*(1-(Q6+R7)))	=Q6	=R6	=S6+(1-S6)*Q6	=(S7-S6)	=T7+U8	=T7*P7+V8	=V7/U7	=X6-(0.004/0.4)*120

This excess must react within the transition zone (by the equation in 5.5.1) to produce spinel, so that no garnet remains at 80km. Thus the 'excess' garnet was reacted to other mineral phases incrementally over the transition zone, such that none remained at 80km. Above the garnet out reaction, melt norms of P_{cpx}=0.7, P_{opx}=0.2 and P_{ol}=0.1 were used, grouping spinel with olivine for simplicity. In practice, this rather complex procedure had little effect on the overall synthetic lava compositions, which were dominated by changes in instantaneous melts within the 120-110km depth range. As can be seen in Fig. 5.12, for La, instantaneous melts produced shallower than 105km have negligible effect on the summed-down synthetic melt composition.

Below, the function of each column within the spreadsheet is systematically explained to clarify the calculations. Only calculations for La are shown, since the procedure for other elements is identical.

Columns A-D calculates the new fractions of each of the minerals in the peridotite assemblage, after the removal of the 0.4% melt fraction. The melt norm multiplied by the melt increment is subtracted from the previous mineral fraction and the assemblage is then renormalised to unity.

Columns E-F the melt norms.

Columns I-M list the partition coefficients for different elements and minerals.

Columns N calculates the bulk distribution coefficent for each new mineral assemblage after removal of the melt increment.

Column O calculates the La concentration of the bulk solid assemblage in equilibrium after the increment of melting.

Column P line 3 calculates the La concentration of the first equilibrium melt which melts to produce the porosity. Lines 4 onwards calculates the La concentration of the instantaneous melts, by equilibrium partitioning of the La remaining in the solid and residual porosity after segregation of the last melt increment between the new source mineralogy and liquid (porosity + new melt increment).

Column Q the degree of melting of each melt increment, relative to remaining mass of solid.

Column R melting column porosity.

Column S total degree of melting experienced by source at a given depth, relative to the original mass of solid.

Column T the degree of melting for each melt fraction, relative to the original mass of solid.

Column U the total degree of melting represented by melt phase at a given depth, relative to the original mass of solid, if instantaneous melts are summed fom the top of the melting column downwards (i.e from the bottom of the spreadsheet upwards).

Column V the total mass fraction of La in the melt phase at given depth, for pooled instantaneous melts summed from the top of the melting column downwards.

Column W the concentration of La in pooled instantaneous melts from the top of the melting column down to given depth. These are the compositions of the synthetic analogues of the high MgO lavas, and are plotted in the Figs. in Chapter 5.

Column X depth within the melting column, calculated by assuming total melting column depth (120km), total degree of melting (i.e. total number of increments in column) and constant degree of melting per unit pressure release.